Search for Flavour Changing Neutral Currents in Single Top-Quark Production at $\sqrt{s} = 7$ TeV with the ATLAS Detector

Dissertation
zur
Erlangung des Doktorgrades (Dr. rer. nat.)
der
Mathematisch-Naturwissenschaftlichen Fakultät
der
Rheinischen Friedrich-Wilhelms-Universität Bonn

von
Muhammad Alhroob
aus
Hebron/Palestine

Bonn, July 2012

Dieser Forschungsbericht wurde als Dissertation von der Mathematisch-Naturwissenschaftlichen Fakultät der Universität Bonn angenommen und ist auf dem Hochschulschriftenserver der ULB Bonn `http://hss.ulb.uni-bonn.de/diss_online` elektronisch publiziert.

1. Gutachter:	Prof. Dr. Ian C. Brock
2. Gutachter:	Prof. Dr. Klaus Desch
Tag der Promotion:	14.08.2012
Erscheinungsjahr:	2013

Acknowledgements

This thesis would not be possible without the support of many people. I would like to gratefully acknowledge all of them, in particular those enthusiastic people that supervised my work, those that I have met and worked with and those who shared their knowledge with me.

First, I would like to express my sincere gratitude to Prof. Ian C. Brock for his invitation to me to join his research group, for accepting me to work on the analysis presented in this thesis, for his unlimited support and help throughout the last four years, and for his tremendous effort to give the thesis its final shape.

Special thanks must be given to the members of examining committee: Prof. Klaus Desch, Prof. Kirfel and Prof. Drees for kindly reading and providing valuable comments to my thesis.

I am very grateful to all my colleagues including, Thomas Loddenkötter, Robert Zimmermann and Peter Kövesárki from the Physikalisches Institut, University of Bonn, for being like a family to me during the four years I spent there and for their continued moral support thereafter. I would like to give special thanks to Dr. Detlef Bartsch for the warm welcome he gave me and the great discussions we had about various topics in physics and statistics. I should remember and thank Dr. Elizabeth Nuncio for the great help and support she gave to me and my wife; she really treated us as members of her family.

I should remember and thank Jan Stillings for being a good friend and for his great help and support he offered to me in Bonn. Jan and I shared an office at CERN for one and a half years which I very much enjoyed. This was mainly due to our extensive discussions on topics such as computer programming of which Jan came across as an expert, and we often engaged in friendly political and cultural debates!

One of my colleagues that I will never forget is Markus Jüngst from Bonn who is a great person in every aspect. Markus helped me in understanding physics, programming, statistics and data analysis at ATLAS. We worked together at Bonn and at CERN, and from time to time we would have lunch or go for a coffee to discuss various topics..

Antonio Onofre and Nuno Castoro both have had an impact on my PhD. Antonio advised me to work on a well defined project where it was clear where to start and to finish, which led me to choose the search for FCNC. Without Nuno the search for FCNC could not have been started. He helped me to make the full chain of FCNC signal events simulation, which took several months of labor. He helped me in validating the Monte Carlo generator and in writing code to apply the standard ATLAS event selections. Together with Antonio and Nuno we wrote the first conference note on the search for FCNC in single top-quark production and in top-quark decay. This note was prepared for the Moriond Conference in Winter 2011.

If the analysis could not have been started without the help of Nuno Castro, I would say that the analysis could not have been performed and published without the collaboration of various physicists at the University of Wuppertal. I would like to take the chance to thank Prof. Wolfgang Wagner for the help and support he offered during my PhD. Prof. Wagner suggested to me to study the FCNC in single top-quark production for the reasons presented in this thesis. He made excellent comments and gave me valuable ideas to improve the analysis. He stimulated the theoreticians to make the necessary calculations for this search. One man I will always remember is Dr. Dominic Hirschbühl who I met during a coffee break in 2010 and it was then we started our successful collaboration. We worked very closely together as if we were members of one group. Dominic supported me in many aspects, such as

programming, physics, statistics and he was the editor of the paper we published. I would like to say that he is clever, a hard worker and pragmatic, who knows how to deal with problems in the fastest, easiest and the most effective way. Two more people from the University of Wuppertal I would like to acknowledge: Philipp Sturm and Kathrin Becker for being good friends and for the multijet background estimation they delivered and for their contribution to our publication.

I would also like to thank my friend Sabri Masrie and his family for their help and limitless support during the last three years we spent in Saint-Genis-Pouilly. We often exchanged knowledge, experience, skills during my work at CERN. Sabri and his wife Nawal Sunallah are Palestinians who were expelled from their towns and forced to live outside the Holy Land, and both have made us feel as if we were living in our homeland, Palestine.

Last, but not least, I would like to thank my wife Mais Qaysia for her patience during the past few years. Her support, understanding and tolerance of my absence from home were in the end what made this achievement possible. I honour my sons Loay and Alwaleed for the joy they have brought to my life, who stay behind the doors waiting for me to return home. Although Mais and my sons often had to endure my absence they rarely complained. I hope they all enjoy the effort being completed.

Contents

Chapter 1

Introduction

Particle physics studies the elementary particles and their properties and the fundamental interactions in nature. Currently, particle physics is described by the Standard Model (SM) of particle physics, which is a framework that combines three of the fundamental forces in nature: the electromagnetic, the weak and the strong forces. The SM is very successful in describing and predicting the observed phenomena at the microscopic scale and has been verified by many experiments.

The Large Hadron Collider (LHC) at CERN is built to be a major step forward in understanding the fundamental interactions in nature. The ATLAS experiment is one of the general-purpose detectors for the LHC, whose design was guided by the need to study a wide spectrum of possible physics signatures. The major goal of the ATLAS experiment is to explore the new frontier of mass scale where groundbreaking discoveries are expected.

The discovery of the top quark in 1995 at Fermilab completed the third quark family of the SM. The mass of top quark m_{top}= 173.2±0.9 GeV [1] is of the order of the Electroweak Symmetry Breaking (EWSB) scale, υ =246 GeV, and therefore provides an excellent object to test the SM. The top quark can be produced in the SM either via the strong interaction in top-antitop quark pairs or singly via the electroweak interaction, through three different channels: the t-channel, Wt associated production and the s-channel.

The properties of the top quark can be studied with the LHC data in proton-proton collisions at $\sqrt{s}$ = 7 TeV. Top quark pair production via the strong interaction has been measured at the LHC [2, 3], and its cross section is in good agreement with the prediction of the SM. Single top-quark production has only been observed via the t-channel so far [4–7]. According to the corresponding values of the Cabibbo-Kobayashi-Maskawa (CKM) matrix, the top quark decays almost exclusively to a W boson and a b quark.

According to the SM of particle physics, flavour changing neutral current (FCNC) processes are forbidden at tree level and suppressed at higher orders due to the Glashow-Iliopoulos-Maiani (GIM) mechanism [8]. Extensions of the SM with new sources of flavour predict higher rates for FCNCs involving the top quark, for example new exotic quarks, new scalars, supersymmetry, or technicolour, [9]. If the new particles are heavy, which is consistent with the non-observation of low mass new particles at the Tevatron and LHC, their effects on top quark FCNC can be parametrised in terms of a set of dimension-six gauge-invariant operators [10]. The predicted branching fractions for top quarks decaying to a quark and a photon, Z boson, or gluon can be up to 10^{-3} to 10^{-5} for certain regions of the parameter space in such models. In any case, for heavy new particles these rates can also be large, if the new particles couple strongly to the SM particles.

FCNC in the top-quark sector can be studied either in top-quark decays [11, 12] or in top-quark production. However, the $t \to qg$ mode, where q denotes either an up quark (u quark) or a charm quark (c quark) and g denotes a gluon, is almost impossible to separate from generic multijets production via strong interaction processes. A much better sensitivity can be achieved in the search for anomalous single top-quark production.

In the process studied here, a u quark or c quark and a gluon coming from the colliding protons interact to produce a single top quark. The top quark is assumed to decay exclusively through the SM processes $t \to Wb$, where in this analysis only the leptonic decay of the W boson is considered. Selected events are characterised by an isolated high-energy lepton (electron or muon), missing transverse momentum from the neutrino and exactly one b-quark jet.

Given the large uncertainty of the expected background and the small number of expected signal events, a multivariate analysis technique is used to extract the signal events from background events. A neural network (NN) classifier [13] that combines a three-layer feed-forward neural network with a complex robust preprocessing, is used. The network infrastructure consists of one input node for each input variable plus one bias node, 13 nodes in the hidden layer, and one output node which gives a continuous output in the interval $[-1, 1]$.

Data collected with the ATLAS detector in 2011 corresponding to an integrated luminosity 2.05 fb^{-1} have been analysed. No evidence for anomalous FCNC single top-quark events has been observed. An upper limit at 95% C.L. was set on the corresponding cross-section using a Bayesian method, with a binned likelihood of the neural network output distribution. The signal prior is chosen to be flat. Systematic uncertainties and their correlations across channels are included with a direct sampling approach where the same Gaussian shift is applied to each process and all bins for a given systematic uncertainties. The observed upper limit at 95% C.L. including all uncertainties is 3.9 pb, which is converted to an upper limit on branching fraction using a NLO calculation, resulting limits on $\text{Br}(t \to ug) < 5.7 \cdot 10^{-5}$ assuming $\text{Br}(t \to cg) = 0$, and $\text{Br}(t \to cg) < 2.7 \cdot 10^{-4}$ assuming $\text{Br}(t \to ug) = 0$.

This analysis:

- is the first LHC analysis searching for FCNC in the top-quark sector [14],
- is the first physics analysis published by the ATLAS Collaboration done using a multivariate techniques,
- provides us with the world's best limit to date by improving the previous numbers [15] on the branching fractions of $\text{Br}(t \to ug)$ and $\text{Br}(t \to cg)$ by factors of 4 and 15, respectively.

This thesis contains three parts and is divided into ten chapters including the introduction:
the first part describes the theoretical framework of the analysis presented in this thesis. In Chapter 2 the SM of particle physics is introduced, the fundamental particles and their properties are summarised, top-quark physics is presented and the chapter is ended by introducing the needs of extending the SM. This is followed by the Chapter 3 where extensions to the SM are presented with their predictions of enhancing the production of top quark via FCNC processes. The production of single top-quarks via FCNC production is introduced and the theory of the model-independent approach is explained in detail. Finally the theoretical calculations at next-to-leading order allow us to convert the measured cross-sections to coupling constants and branching fractions.

The second part contains the description of the experimental setup and is divided into three chapters: in Chapter 4 the LHC machine is introduced. The ATLAS detector and its components with their parameters and functionalities are summarised. This is followed by explaining the luminosity measurement at ATLAS and the collision data samples used in this analysis. Chapter 5 describes the Monte Carlo (MC) simulation for ATLAS experiment and the MC generators used for simulating events. It also describes all MC samples with the corresponding cross-sections used in this analysis. Chapter 6 contains a summary about the particle identification procedures which are relevant in the analysis.

The third part explains the analysis methods used in the search for the single top-quark production via FCNC. This part is divided into four chapters: Chapter 7 explains in detail the selection criteria

applied to identify the particles coming from the signal events and to reject particles coming from the background. It also explains the selection criteria applied to reduce the number of background events in order to enrich the samples by expected signal events. This chapter also includes the corrections applied on MC events to achieve better description of the data. Finally the chapter ends with the event yield and a comparison between data and MC distributions. Chapter 8 starts by explaining the need to use advanced techniques to separate the signal events from the huge number of background events. This chapter includes a description in reasonable detail of the NN used in this analyses, variables used as an input to train the NN are described and a comparison between data and MC is shown. Finally the results of the NN training is shown demonstrating the good separation between the signal and background. Chapter 9 explains the sources of the systematic uncertainties and their effects on the results of this analysis. It also shows the effect on the event yield and a comparison between the nominal NN output and the NN output affected by systematic uncertainties. Chapter 10 contains an introduction to Bayesian statistics, and it explains the binned likelihood method used in this analysis. The way statistical and systematic uncertainties are included in likelihood is presented and the calculation of the posterior density function is shown. In this chapter the result is presented as well as the sensitivity of this analysis. A conversion from the observed limit on the single top-quark production via FCNC cross-section to a limit on the FCNC coupling constants and branching fractions is also given. The chapter gives an idea about the effect of each individual systematic uncertainty on the final result and ends with a discussion about the quality of the used statistical technique. Finally, Chapter 11 summarises the work done in this thesis.

Chapter 2

Introduction to the Standard Model

2.1 The Standard Model of Particle Physics

Matter is made from very small constituents called molecules, which consist of different atoms of elements that are made from electrons and nuclei. The atomic nucleus is made of protons and neutrons, both of which are made of elementary particles called quarks.

Quarks and electrons are elementary particles interacting via four fundamental forces in nature:

- gravitational force,
- electromagnetic force,
- weak force,
- strong force.

The gravitational force was well understood by Newton through his famous Newton's law of gravity, and gravity was later generalised by Albert Einstein through his general theory of relativity (GR). GR provides a unified description of gravity as a geometric property of space and time. The gravitational force can be seen as an interaction between massive objects, with an infinite range. Although it is still acts between any two light objects, it can be neglected, because it is extremely weak. The electromagnetic force (EM) was introduced by Maxwell through the Maxwell equations, which govern the dynamics of electricity and magnetism. The EM force acts over an infinite range. The strong interaction is a very short range force, which can be seen only inside the atomic nucleus. It is responsible for stability of the atomic nuclei by preventing them from fragmenting as a result of the electric repulsion of the protons. The weak force is an interaction that acts at very short distances, and is responsible for the beta decay of unstable atoms. The four forces with their characteristic features are shown in Table 2.1.

Force	Couples to	Effect	Strength	Range
Strong	Colour charge	Binds quarks and gluons	1	10^{-15} m
Electromagnetic	Electric charge	Interaction between el. charged particles	10^{-2}	infinite
Weak	Weak charge	Radioactive decay	10^{-5}	10^{-18} m
Gravity	Mass	Attraction	10^{-38}	infinite

Table 2.1: The four fundamental forces in nature with their important characteristics.

The three forces, electromagnetic, weak and strong are called the interactions that are combined and understood in a theory called the Standard Model (SM) of particle physics [16]. The SM is based on relativistic quantum field theory. It assumes that matter is built from elementary point-like particles of

spin-$\frac{1}{2}$, called fermions. Interactions between particles are mediated by spin-1 particles called bosons. The fermions are divided into leptons and quarks. Leptons can be either electrically charged with a charge of -$1.6 \cdot 10^{-19}$ C, or they can be an electrically neutral, neutrinos (ν). Quarks, unlike leptons, carry fractional charge, which can be either +$\frac{2}{3}$ e or -$\frac{1}{3}$ e, which were proposed by Gell-Mann [17, 18]. Additionally, every particle has an associated antiparticle, which has the same mass, but carries the opposite charge to its corresponding particle.

Leptons and quarks are grouped into three generations. Each generation differs from another generation in the flavour, i.e. the fermion type and the mass of the particles, the other corresponding quantum numbers are the same. Each generation comes in a doublet: in the lepton family, the doublet contains a charged lepton with its partner an uncharged neutrino, while in the quark family, the doublet comes with an up-type quark with a charge +$\frac{2}{3}$ e and a down-type quark with a charge -$\frac{1}{3}$ e.

There are three lepton doublets, the electron (e) with its partner electron neutrino, ν_e, muon (μ) with its partner muon neutrino, ν_μ, and finally the tau lepton (τ) with its partner tau neutrino, ν_τ. The electron doublet, muon doublet and the tau doublet belong to the first, second and third generations, respectively.

There are three quark doublets, the up quark (u) and down quark (d); the charm quark (c) and the strange quark (s); and finally the top quark (t) and bottom quark (b). The up doublet, charm doublet and top doublet belong to the first, second and third generations, respectively. Quarks carry an additional quantum number, the colour charge. This is of three different types (red, green or blue). Since free coloured particles have not been observed, quarks must be confined into colourless composite particles. These particles are either baryons consisting of three quarks or mesons consisting of a quark and an antiquark. Baryons and mesons are called hadrons, which consist of bound states of quarks. The fundamental particles are listed in Table 2.2.

	Leptons			Quarks		
Generations	Flavour	Q_{EM}(e)	Mass(MeV)	Flavour	Q_{EM}(e)	Mass
1st	$\begin{pmatrix}\nu_e\\ e\end{pmatrix}$	0 -1	0.511 0	$\begin{pmatrix}u\\ d\end{pmatrix}$	+2/3 -1/3	1.7-3.3 MeV 4.1-5.8 MeV
2st	$\begin{pmatrix}\nu_\mu\\ \mu\end{pmatrix}$	0 -1	105.658 0	$\begin{pmatrix}c\\ s\end{pmatrix}$	+2/3 -1/3	$1.27^{+0.07}_{-0.09}$ GeV $0.101^{+0.029}_{-0.021}$ GeV
3st	$\begin{pmatrix}\nu_\tau\\ \tau\end{pmatrix}$	0 -1	1776.82 0	$\begin{pmatrix}t\\ b\end{pmatrix}$	+2/3 -1/3	173.2 ± 0.9 GeV $4.19^{+0.18}_{-0.06}$ GeV

Table 2.2: The fundamental particles in Standard Model ordered in three generations [19].

In quantum field theory, all interactions occur via the exchange of particles which do not go faster than the speed of light (they are local and Lorentz invariant). The interaction strength is determined by a constant called the coupling strength.

In the SM, the interaction force carriers are bosons, and they are:

- The electromagnetic (EM) force carrier is the photon (γ), which is a massless particle with no electric charge. All electrically charged particles participate in the EM force.
- The weak interaction force carriers are the ($W^{\pm}$,Z). It was known before their discovery that they are massive. According to the Yukawa theory, a massive gauge boson leads to a short-range force.
- The strong force carriers are the gluons (g). They are massless particles and electrically neutral. Gluons carry colour charge with eight colour combinations, so they may interact among themselves, and they only couple to the strong charged (coloured) particles. Because gluons couple

only to the coloured particles, only quarks participate in the strong interaction. The strength of the strong interaction is determined by the running coupling strength; its value is determined by the energy and momentum of the interacting particles. At very high energy, the coupling becomes small which makes perturbation calculations possible, while at very low energy the coupling strength becomes big. This explains why it acts at very small range and can only be seen inside the atomic nucleus.

The relations of the gauge bosons to the three forces and some of their properties are summarised in Table 2.3.

Force	Boson	Electric charge [e]	Mass [GeV]
Strong	gluon	0	0
Electromagnetic	photon	0	$\leq 10^{-27}$
Weak	W	± 1	80.398±0.025
	Z	0	91.1876±0.0021

Table 2.3: The bosons, the related force they carry, and some of their properties [19].

2.2 Standard Model Lagrangian

In particle physics, physical systems are described by mathematical expressions called Lagrangians, which can be invariant under some kind of transformations, i.e. they contain a symmetry. The transformations can be either time and space independent called global transformations, or time and space dependent, called local gauge transformations. If a Lagrangian has a symmetry, then it describes a physical system which conserves one or more physical quantities, as stated by the Noether theorem [20]. The SM Lagrangian is Lorentz invariant, which limits speed of interactions to be within the speed of light (c). In addition to the Lorentz invariance, the SM Lagrangian is invariant under the non-abelian special unitary group gauge transformation SU(3)⊗SU(2)⊗U(1), where the strong interaction is described by SU(3) transformation group and the combined force of EM and weak interaction (the electroweak force) is described by the SU(2)⊗U(1) term.

Although the weak interaction bosons are known to be massive, the SM Lagrangian can not include explicit mass terms, since it will be no longer invariant under the gauge transformation. This was resolved by introducing a new complex scalar field, the Higgs doublet $\Phi = \begin{pmatrix} \phi^+ \\ \phi^0 \end{pmatrix}$ with non vanishing vacuum expectation value. The Higgs field is invariant under the SM gauge transformation, but once the vacuum expection value is chosen, the SM Lagrangian is spontaneously broken. This mechanism is called the Higgs mechanism [21, 22] or spontaneous symmetry breaking, where the electroweak symmetry is broken from SU(2)⊗U(1) to U(1). After the spontaneous symmetry breaking, the SM Lagrangian can be rewritten, and the mass terms for all fermions and the weak gauge bosons are generated automatically. According to the spontaneous symmetry breaking of SU(2) group transformation, the SM describes three massive gauge bosons, two of them are charged with the same mass ($W^{\pm}$) and the other one is neutral called the Z boson. The existence of these gauge bosons was confirmed later by the UA1 and UA2 experiments at CERN [23].

The Higgs mechanism also predicts the existence of a neutral spin-0 boson. Within the SM, the Higgs boson is the only particle which has a spin 0 (scalar), and it has not been discovered yet.

According to the SM, photons can only couple to electrically charged particles with their antiparticles from the same particle doublet. The Z boson can couple to a particle and its antiparticle: it can couple to quarks as well as charged leptons, it also can couple to neutrinos. In the lepton sector, the W boson can couple the charged lepton to a partner neutrino from the same doublet, but it can not change the lepton flavour. However, in quark sector, the W boson can couple the up-type quark to the down-type quark from the same doublet as well as to quarks from other doublets from different generations. When the W boson interacts, it violates parity to 100%, the W bosons couples only to left-handed particles and right-handed antiparticles.

The W boson can couple the up-type quarks with the down-type quarks from another generation changing the flavour of the quark, because the mass eigenstates of quarks are not the same as their flavour eigenstates. The mass eigenstate d, s, b is related to flavour eigenstates d', s', b' by the Cabibbo–Kobayashi–Maskawa matrix (CKM matrix or V_{CKM}) [24]. The CKM matrix is an $N \times N$ unitary matrix $V^\dagger V = 1$. For only three particle generations, the CKM matrix is a 3×3 matrix as shown in Equation 2.1. $V_{q_1 q_2}$ are proportional to the coupling of two quarks q_1, q_2 to a W boson. The single elements of the CKM matrix can be determined experimentally. The current values for the different elements $V_{q_1 q_2}$ are given in Equation 2.2.

$$\begin{pmatrix} d' \\ s' \\ b' \end{pmatrix} = \begin{pmatrix} V_{ud} & V_{us} & V_{ub} \\ V_{cd} & V_{cs} & V_{cb} \\ V_{td} & V_{ts} & V_{tb} \end{pmatrix} \begin{pmatrix} d \\ s \\ b \end{pmatrix} \tag{2.1}$$

$$V_{\mathrm{CKM}} = \begin{pmatrix} 0.97428 \pm 0.00015 & 0.2253 \pm 0.0007 & 0.00347^{+0.00016}_{-0.00012} \\ 0.2252 \pm 0.0007 & 0.97345^{+0.00015}_{-0.00016} & 0.0410^{+0.0011}_{-0.0007} \\ 0.00862^{+0.00026}_{-+0.00020} & 0.0403^{+0.0011}_{-0.0007} & 0.999152^{+0.000030}_{-0.000045} \end{pmatrix} \tag{2.2}$$

2.3 Measurements in Particle Physics

The goal of particle physics is to understand the elementary particles in nature, how many they are, their masses, their properties and the fundamental forces which govern the interactions between them. This can be done through colliding elementary particles and by looking and analysing the outcome. Cosmic particles originated in outer space, may collide and produce new particles when penetrating the earth's atmosphere. These collisions occur randomly all the time in the upper atmosphere and the particles coming out from the collisions can be detected on the ground providing physicists with very useful information. These cosmic particles have been studied for very long time and resulted for example in discovery of the positron, the discovery of antimatter.[1]

Since many of the searched phenomena occur with very small rate, it is very hard to rely on cosmic particles. Thus particle physicists build experiments in which they control most of the experimental aspects, such as the particle type, the energy of the colliding beams of particles and the rate of collisions. These experiments may be fixed-target experiments, where an incident beam of particles is sent to collide with atomic nuclei in a stationary block of matter, or colliding-beam experiments in which two beams of particles travelling in opposite directions collide at particular points. This method allows higher energy to be available to create new particles. The machine which delivers energy to accelerate particles is called a particle accelerator, and it can accelerate charged particles like leptons such as electrons, or hadrons such as protons or antiprotons.

[1] The positron which is the antimatter particle corresponding to electron was discovered in 1932 by Carl D. Anderson, for which he won the Nobel Prize for Physics in 1936.

The expected interaction rate between two colliding particles is determined by a quantity called the cross-section (σ). The cross-section depends on the coupling strength of the interacting force as well as the energy and momentum of the interacting particles. The SM Lagrangian can be split into a kinetic part and an interaction part. Interactions between particles can be described by Feynman diagrams. During an interaction process the forces couple to the interacting particles and gauge bosons are emitted and reabsorbed. The diagrams can be translated into a formula by using the Feynman rules. The formula provides the matrix element, $\mathcal{M}$, which is needed for the calculation of the differential cross-section or the decay rate of a process.

The cross-section is proportional to the probability that an interaction occurs. The differential cross-section $\frac{\mathrm{d}\sigma}{\mathrm{d}\Omega}$ is defined by the probability to observe a scattered particle in a unit solid angle Ω. The total cross-section (σ) is the integral of the differential cross-section over the whole sphere of observation. A cross-section is therefore a measure of the effective surface area seen by the colliding particles, and as such is expressed in units of area such as m^2. In particle physics, cross-sections are preferably quoted in picobarn, pb, where 1 pb = 10^{-40} m^2.

At hadron colliders such as the LHC and Tevatron, the composite nature of the protons has to be considered. Protons are a bound state of partons (quarks and gluons). In addition to the proton's quarks or the valence quarks, the proton has also the so-called sea quarks coming from gluon splitting into quark-antiquark pairs; and the proton's momentum is shared among all these constituents. The underlying scattering is between two partons, and the cross-section of the scattering process requires the knowledge of the individual parton's initial state. The momentum fraction carried by these partons is described by the parton distribution function (PDF), $f_i(x_i, Q^2)$. A PDF is defined as the probability density for finding a particle, i, with a certain longitudinal momentum fraction, x_i, at Q^2, where Q^2 is the negative four-momentum transfer squared at the interaction vertex, which describes the typical energy scale of the considered interaction. Figure 2.1 shows four PDF distributions for $u, \bar{u}, c$ quarks and gluon at $Q^2 = m_{\mathrm{top}}^2 = 172.5^2$ GeV^2. The cross-section of proton-proton scattering can be expressed in terms of the interaction between two incoming partons convoluted by the PDF as described in Equation 2.3

$$\sigma_{pp\to X} = \sum_{ij} \int \mathrm{d}x_1 \mathrm{d}x_2 f_i(x_1, Q_F^2) f_j(x_2, Q_F^2) \sigma_{q_i q_j \to X}(x_1, x_2, \alpha_s(Q^2), Q_F^2)\,. \tag{2.3}$$

The PDF cannot be derived from calculations, because of the non-perturbative nature of QCD bound states. It is extracted from data obtained at previous generations of collider experiments instead.

Another important quantity is the decay width, Γ_i, of an unstable particle into a specific final state i. It is very similar to the cross-section, which can be calculated through analogous integration over the partial width, $\mathrm{d}\Gamma_i$, related to the specific final state i. The total width Γ, gives a measure of the probability of a particle to decay to any state. Since a particle may decay into several other particles, a useful quantity to define is the branching fraction (Br). The Br is defined as the width of a particle decaying to a specific final state divided by the width of this particle decaying into all possible states. The Br of a decay mode is calculated by taking the ratio between the particle decay width in that mode and the full decay width.

The cross-section and the decay width can be calculated by considering only leading order from the perturbation expansion, also called a leading-order calculation (LO), or it can be done by considering the higher order radiative corrections, called next-to-leading-order calculations (NLO) or even next-to-next-to-leading order calculations (NNLO).

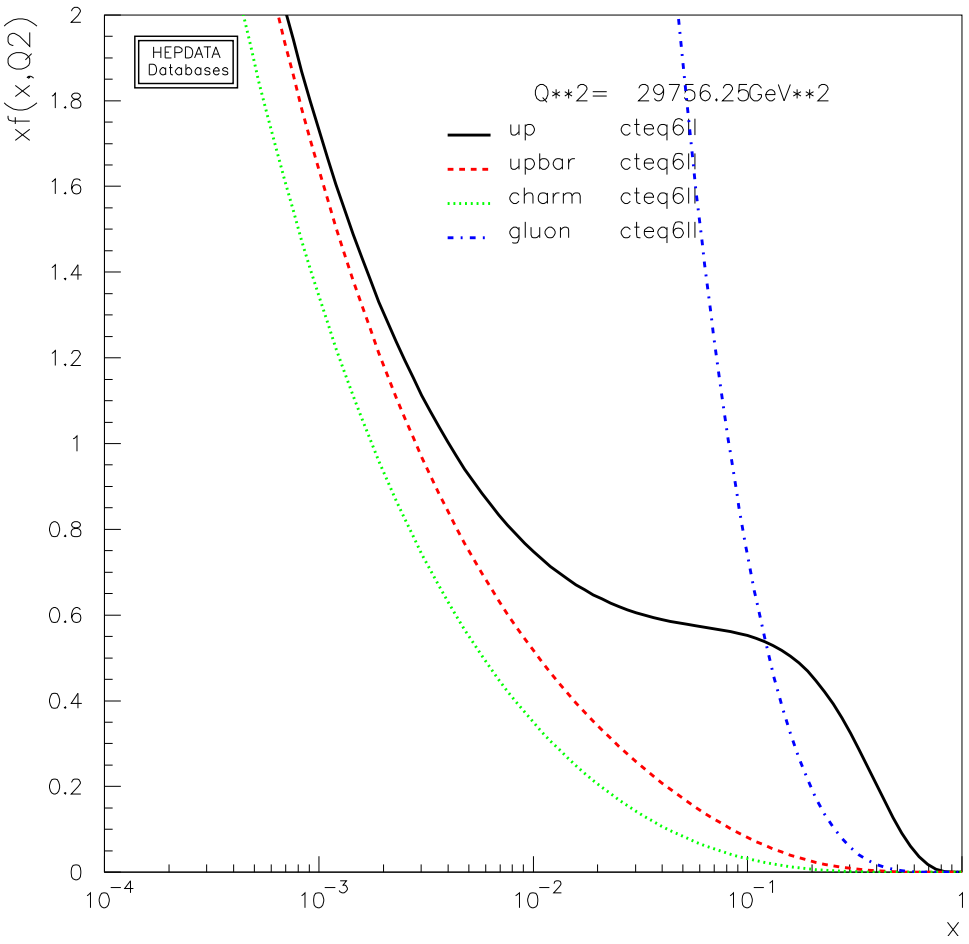

Figure 2.1: The CTEQ6ll parton distribution function at Q^2=172.5^2 GeV^2 [25].

2.4 Top-Quark Physics

The top quark was the last quark of the Standard Model (SM) to be discovered, The discovery was made at Fermilab in 1995 by the CDF [26] and DØ collaborations [27]. The top quark was rediscovered at CERN in 2010 [28] [29]. With the discovery of the top quark, the third generation structure of the SM was completed, and the new field of top-quark physics opened.

2.4.1 Top Quark in the Standard Model

The top quark is the heaviest elementary particle known so far, with a mass of 173.2±0.9 GeV [1] close to the electroweak symmetry breaking scale (EWSB), υ=246 GeV. The top quark has a very short lifetime $\sim O\,(10^{-25}$ s), and it is the only quark that decays before hadronising. As such it can be used to probe the properties of a bare quark.

In the SM, the top quark can be produced in top-quark antitop-quark pairs called $t\bar{t}$ production, or as a single top-quark associated with other particles. $t\bar{t}$ production occurs mainly via the strong interaction. At LHC, unlike at the Tevatron, the $t\bar{t}$ pair is produced dominantly through gluon fusion (90%). The predicted cross-section is 165^{+11}_{-16} pb at $\sqrt{s}$ =7 TeV [30, 31], assuming a top-quark mass, m_{top} of 172.5 GeV. Figure 2.2 and Figure 2.3 show the LO Feynman diagrams for $t\bar{t}$ production through gluon fusion and through quark-antiquark annihilation, respectively.

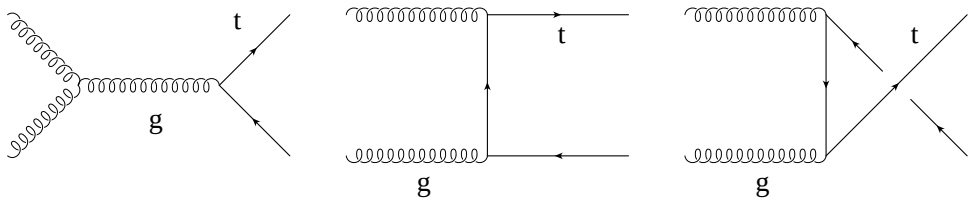

Figure 2.2: $t\bar{t}$ pair production through gluon fusion.

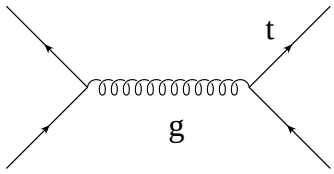

Figure 2.3: $t\bar{t}$ pair production through quark antiquark annihilation.

In single top-quark production, the top quark is produced via the weak interaction. There are three different channels: (a) W boson and gluon fusion which is called t-channel (b) associated production of a top quark and a W boson also called Wt-channel, (c) through the s-channel as shown in Figure 2.4. The cross-section values calculated at approximate NNLO at the LHC with $\sqrt{s}$ =7 TeV assuming m_{top}=171 GeV and using the MSTW2008 PDF, are $64.6^{+3.2}_{-2.6}$ pb [32], $15.7^{+2.6}_{-1.3}$ pb [33] and 4.6 ± 0.3 pb [34] for t-channel, Wt-channel and s-channel, respectively. Single top-quark production has been observed by the CDF [4] and DØ [35] collaborations based on a combination of the t-channel and s-channel processes in 2009. The observation of the t-channel production mode has also been recently reported [5] by the DØ collaboration. The ATLAS collaboration [6] has also presented a first measurement of the t-channel single top-quark production cross-section at the LHC in 2011.

Determined by the CKM mechanism, the decay of the top quark is dominated by one decay channel $t \rightarrow Wb$ with a branching fraction of approximately 100% [36]. The width predicted in the SM at

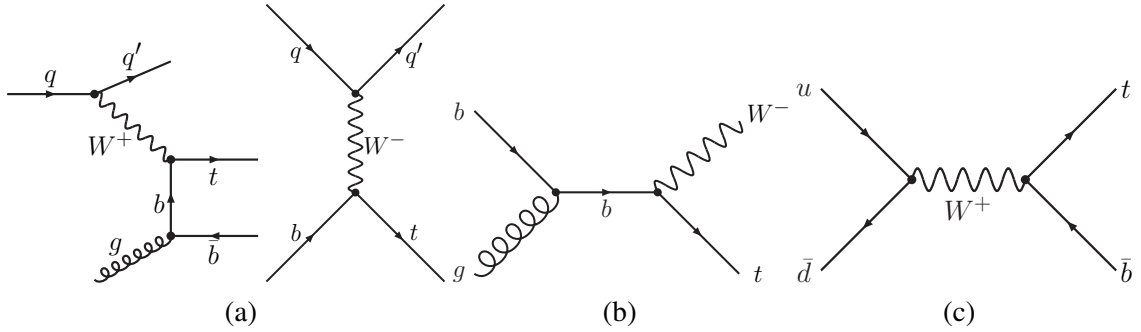

Figure 2.4: Single top-quark production at leading order: (a) t-channel (b) Wt associated production (c) s-channel.

next-to-leading order is given by Equation 2.4.

$$\Gamma = \frac{G_F m_{\text{top}}^3}{8\pi\sqrt{2}} \left(1 - \frac{M_W^2}{m_{\text{top}}^2}\right)^2 \left(1 - 2\frac{M_W^2}{m_{\text{top}}^2}\right) \left[1 - \frac{2\alpha_s}{3\pi}\left(\frac{2\pi^2}{3} - \frac{5}{2}\right)\right]. \tag{2.4}$$

where G_F is the Fermi coupling constant given by $G_F = \frac{\sqrt{2}g^2}{8M_W^2}$, M_W is the mass of the W boson and α_s is the strong coupling constant.

Because the top quark has a very large mass and a very short lifetime, it provides a good environment to test and to understand the SM, and it plays a key role in searches for physics beyond SM. By precise measurements of its properties, a deviation from the SM prediction can reveal new physics. For example, the single top-quark cross-section is proportional to the V_{tb}. With precise measurement, the unitarity of the CKM matrix can be tested, this gives a hint if a fourth generation or a heavier boson such as (W') exists. By measuring m_{top} precisely, the Higgs mass can be constrained. Many theories try to extend the SM, where the top quark is a possible decay product of the introduced particles. In many of those models, the introduced particles have masses at the TeV scale, the new particles may be too heavy to be produced even at the LHC, and the only observable effects may be the indirect ones, i.e. the modification of SM particle properties.

2.4.2 Standard Model FCNC in the Top-Quark Sector

Flavour changing neutral currents (FCNC) stands for an interaction, in which a fermion (quark or lepton) flavour in the initial state changes to another in the final state, through emitting or absorbing neutral bosons. In the SM, there is no vertex that directly couples neutral currents (g,Z,γ,H) with two fermions from different generations, in other words, the process is not allowed at tree level. On the other hand, the quark flavour may change, if the interaction occurs at higher order correction or loop-level. This can happen because $W^{\pm}$ changes the quark flavour which is allowed by the CKM mechanism. Figure 2.5a shows a forbidden vertex in the SM, while Figure 2.5b shows a top quark coupled to a u or c quark through a loop diagram.

To calculate the amplitude of possible top-quark decays through FCNC process at loop-level, all possible loop diagrams have to be considered. Since m_{top} is of the order of the electroweak scale, and all internal quarks (d, s, b) in the loops have very small masses, the amplitude suffers from destructive interference. This cancellation is called the Glashow, Iliopoulos and Maiani (GIM) mechanism [8]. The branching fraction of top-quark decay via FCNC suffers from the small decay width through FCNC (the effect of GIM mechanism), as well as the large tree-level rate for top-quark decay to bW. This leads to

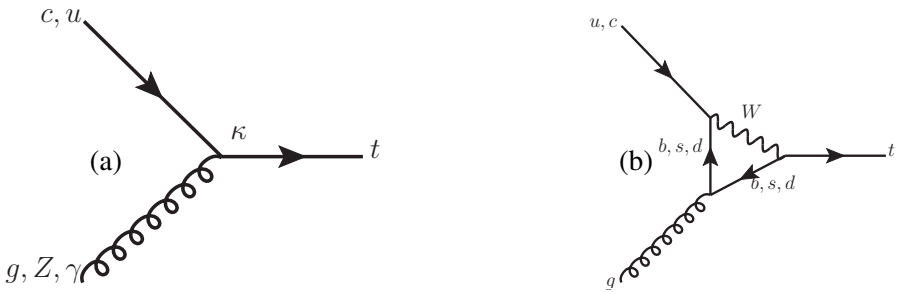

Figure 2.5: a)Non-allowed vertex in SM, where $u(c)$ quarks change their flavour to a top quark by interacting with an electrically neutral boson(g, Z, γ). b) Possible FCNC process in the SM through a loop process.

an extremely suppressed branching fraction of the order of 10^{-13}[37].

2.5 Beyond the Standard Model

The Standard Model successfully describes all aspects of fundamental particles physics from atomic scales down to the shortest length scales probed in experiments so far. It unifies the electromagnetic and weak forces together with the strong interaction force, by a detailed set of mathematical equations derived from general principles.

The SM predicted the existence of the W and Z bosons, the gluon, the charm, bottom and the top quark, all these have been subsequently found with precisely the predicted properties. Despite the fact that the SM is well tested, many fundamental questions remain unanswered and there are indications that the SM is unable to describe physics at ever smaller length scales, at least based on the structure it has today. A summary of all issues that particle physicists would like to answer is mentioned below.[2]

The SM predicts the existence of the Higgs boson, while its existence is not confirmed yet by experiments[3]. In case the Higgs boson will not be discovered in the future, new theories are needed to explain the spontaneous symmetry breaking, and how particles acquire their masses. In the SM, particles have mass by interacting with Higgs field, but the SM does not predict the very special forms that the Higgs interactions must take.

One of the SM problems is that neutrinos are described as massless particles, although they have a finite, albeit small, mass. The particle masses are very different, the mass varies from the eV scale for the neutrino to the top quark mass ~173 GeV; again the SM does not provide an answer.

There are three particle families or generations observed by experiments. The SM does not predict the number of generations, and does not constrain the possible number of generations.

The other problem which has not been solved is the quantisation of gravity. The quantum field theory for gravitation has not yet been accomplished. Although gravity is a very weak force on the small scales, it becomes significant at very small length scales quantified by the Planck scale, $M_{\text{Planck}} \sim 10^{19}$ GeV.

The universe began in the big bang as a huge burst of energy, which expected to have evolved in equal parts of matter and antimatter. But instead the universe now is made only from matter. The SM does not have a mechanism that explains this matter asymmetry (CP violation).

There is evidence that in the first fraction of a second of the big bang the universe went through a

[2] All the given points are mentioned and well explained in "The dawn of physics beyond the standard model." article written by Gordon Kane, which was published by the Scientific American Magazine in May 11, 2003.

[3] On 14^{th} of July 2012, while I was preparing the final version of this thesis, ATLAS and CMS Collaborations announced the discovery of the Higgs-like particle.

stage of extremely rapid expansion called inflation. The forces responsible for inflation cannot be SM ones. The expansion of the universe was long believed to be slowing down because of the gravitational attraction of all the matter in the universe. But instead, it was found that the expansion is accelerating and that whatever causes the acceleration is not a part of SM physics.

It is know to astronomers and cosmologists, that 96% of the universe is dark matter and dark energy, a matter that neither emits nor scatters light or other electromagnetic radiation. Its existence is inferred from gravitational effects on visible matter. The SM has no candidate constituents which can fit and answer this mysterious astronomical observation.

Considering all the above points, one comes to the conclusion that extensions to the SM are inevitable. Many theories try to answer the above questions by introducing new particles such as heavy bosons i.e. W', others introduce new symmetries, for example the Supersymmetry (SUSY) theory, which extends the Lorentz transformation to a Poincare transformation. Some theories assume that nature has more than four space-time dimensions (extra dimension models), and other theories like string theory go far beyond SM by trying to find one solution for all unresolved questions.

The branching fraction of neutral current top-quark decay is predicted to be enhanced by the beyond SM theories, which makes FCNC a signature of these extension models. The prediction of FCNC in the top-quark sector is discussed in Chapter 3, a search for this signature is explained in detail in this thesis.

Chapter 3

Introduction to FCNC

As discussed in Chapter 2, FCNC processes are extremely suppressed within the SM and within that framework they are too small to be observed at the CERN Large Hadron Collider (LHC).

Nevertheless, several Standard Model extensions predict new physics at a scale above a few TeV. The new states may be too heavy to be produced at the LHC, and the only observable effects may be indirect ones e.g. a modification of SM particle properties. Top quark FCNC interactions provide an excellent way to probe the new physics.

Examples of SM extensions which predict the FCNC signals are: the quark-singlet model (QS) [38–40], the two-Higgs doublet model with (FC 2HDM) or without (2HDM) flavour-conservation [41–46], the minimal supersymmetric model (MSSM) [47–53], SUSY with R-parity violation [54] or the topcolour-assisted technicolour model (TC2) [55]. For a review see [9]. Table 3.1 shows the predicted branching fraction values for these models as well as those from the Standard Model.

Process	SM	QS	2HDM	FC 2HDM	MSSM	$\not{R}$ SUSY	TC2
$t \to u\gamma$	3.7×10^{-16}	7.5×10^{-9}	—	—	2×10^{-6}	1×10^{-6}	—
$t \to uZ$	8×10^{-17}	1.1×10^{-4}	—	—	2×10^{-6}	3×10^{-5}	—
$t \to ug$	3.7×10^{-14}	1.5×10^{-7}	—	—	8×10^{-5}	2×10^{-4}	—
$t \to c\gamma$	4.6×10^{-14}	7.5×10^{-9}	$\sim 10^{-6}$	$\sim 10^{-9}$	2×10^{-6}	1×10^{-6}	$\sim 10^{-6}$
$t \to cZ$	1×10^{-14}	1.1×10^{-4}	$\sim 10^{-7}$	$\sim 10^{-10}$	2×10^{-6}	3×10^{-5}	$\sim 10^{-4}$
$t \to cg$	4.6×10^{-12}	1.5×10^{-7}	$\sim 10^{-4}$	$\sim 10^{-8}$	8×10^{-5}	2×10^{-4}	$\sim 10^{-4}$

Table 3.1: The theoretical values for the branching fractions of FCNC top-quark decays predicted by the Standard Model (SM), the quark-singlet model (QS), the two-Higgs doublet model (2HDM), the flavour-conserving two-Higgs doublet model (FC 2HDM), the minimal supersymmetric model (MSSM), SUSY with R-parity violation and the topcolour-assisted technicolour model (TC2). These values were calculated assuming some values of the predicted new particles masses which might be different from the current experimental limits.

The present experimental limits on the branching fractions of FCNC top-quark decay channels established by experiments at the LEP, HERA and Tevatron accelerators are shown in Table 3.2. The CDF collaboration has published limits derived from the search for FCNC direct top-quark production, where gluon interacts with a $u(c)$ quark to produce one top quark without being associated to other particles, $\mathrm{Br}(t \to ug) < 3.9 \times 10^{-4}$ and $\mathrm{Br}(t \to cg <) 5.7 \times 10^{-3}$ [56], where DØ published the current limits derived from the search for FCNC through single top-quark production in t-channel, where a gluon interacts with a u or c quark to produce one top-quark associated with another quark [15].

	LEP	HERA	Tevatron
$Br(t \to q\gamma)$	2.4% [57–61]	0.64% ($tu\gamma$) [62]	3.2% [63]
$Br(t \to qZ)$	7.8% [57–61]	49% (tuZ) [64]	3.2% [12]
$Br(t \to qg)$	17% [65]	13% [64, 66, 67]	2.0×10^{-4} (tug), 3.9×10^{-3} (tcg) [15]

Table 3.2: Present experimental limits on the branching fractions of FCNC top-quark decay channels.

3.1 FCNC Within a Model Independent Approach

In order to study the anomalous FCNC couplings in the top-quark sector, it is not necessary to create a whole new theory. FCNC can be approached through an effective Lagrangian [68]. The data can be analysed in a model-independent way. For example, consider the possible SUSY Feynman diagram in Figure 3.1. A gluon interacts with a $u(c)$ quark to produce a single top quark. This process occurs through a loop, where the exchanged particles are a squark ($\tilde{q}$) and a gluino ($\tilde{g}$). To calculate the cross-section of such a process, the mass of the exchanged particles and the coupling strengths are needed. In the model-independent approach this diagram looks like the one in Figure 3.2. The SUSY loop looks like a vertex, and this vertex can be parametrised by a coupling constant, kappa (κ), which does not require any prior knowledge of the particle masses or vertex values in a certain model. The drawback of the approach is that the coupling has a mass dimension.

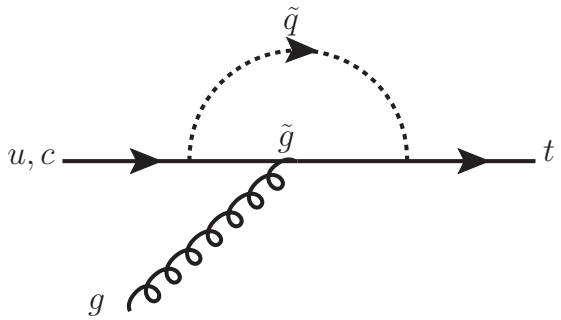

Figure 3.1: SUSY Feynman diagram for $q + g \to t$.

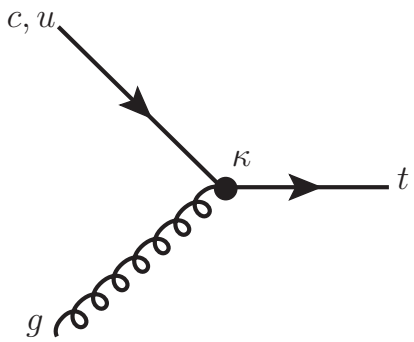

Figure 3.2: FCNC Feynman diagram for $q + g \to t$ through model independent approach.

Within this approach, the new physics is described by an effective Lagrangian density,

$$\mathcal{L}^{\text{eff}} = \mathcal{L}_0 + \mathcal{L}_1, \tag{3.1}$$

Since the possibility of FCNC through a gluon interaction is considered, $\mathcal{L}_0$ is the QCD Lagrangian and can be written as

$$\mathcal{L}_0 = -\frac{1}{4} G^a_{\mu\nu} G^{a\mu\nu} - i\bar{q}\gamma^\mu D_\mu q - m_q \bar{q} q\,, \tag{3.2}$$

where $D_\mu = \partial_\mu - i g_s \frac{\lambda_a}{2} A^a_\mu$ is the covariant derivative, g_s is the strong coupling strength, λ_a are eight $SU(3)$ 3×3 matrices that follow the commutation relations of

$$[\lambda_\beta, \lambda_\gamma] = i C^a_{\beta\gamma}, \tag{3.3}$$

where $C^a_{\beta\gamma}$ are the $SU(3)$ algebra structure constants, γ^μ are the Dirac matrices and $G^a_{\mu\nu}$ is the gluon field tensor given by

$$G^a_{\mu\nu} = \partial_\mu A^a \nu - \partial_\nu A^a_\mu + C^a_{\beta\gamma} A^\beta_\mu A^\gamma_\nu. \tag{3.4}$$

The $\mathcal{L}_1$ term contains operators of dimension higher than four, multiplied by coefficients with appropriate dimensions of mass to ensure that the dimension of the Lagrangian as a whole remains four. Including terms of this kind leads us to call this an "effective Lagrangian". Since the resultant theory is not valid to an arbitrarily high energy scale, it is not a fundamental physical theory. Instead, it represents the theory that is "effective" at a lower energy scale where the energy is too low to allow us to see the full details of the underlying physics. The coefficients with dimensions of mass in front of the effective terms characterise the mass scale at which new physics must enter the theory if any non SM effect is to be found.

In the analysis presented in this thesis, an up quark, or a charm quark, and gluon coming from the colliding protons interact directly to produce a single top quark without being associated to other particles. In this case the Lagrangian $\mathcal{L}_1$ can be written as follows [69]:

$$\mathcal{L}_1 = g_s \sum_{q=u,c} \frac{\kappa_{gqt}}{\Lambda} \bar{t}\sigma^{\mu\nu} \lambda^a (f^L_q P_L + f^R_q P_R) G^a_{\mu\nu} q + \text{h.c.}\,, \tag{3.5}$$

where the $\kappa_{gqt} (q = u, c)$ is a dimensionless parameter that relates the strength of the new coupling to g_s. Λ is the new physics scale, related to the mass scale above which the effective theory breaks down, λ^a are the Gell-Mann matrices, $\sigma^{\mu\nu} = \frac{i}{2}[\gamma^\mu \gamma^\nu, \gamma^\nu \gamma^\mu]$. $f^{L,R}_q$ are the chiral parameters normalised such that: $|f^L_q|^2 + |f^R_q|^2 = 1$. The operator $P_L = \frac{1}{2}(1 - \gamma^5)$ performs a left-handed projection, while $P_R = \frac{1}{2}(1 + \gamma^5)$ performs a right-handed projection, where γ^5 represents the chirality operator. The h.c. is the hermitian conjugate of the first part of the Lagrangian.

The tree-level cross-sections for direct top-quark production considering only the SM decay of top quark to bW, where W boson decays leptonically ($g + u(c) \to bW \to bl\nu_l$) is given as follows,

$$\mathrm{d}\sigma = \frac{1}{4(4\pi)^5} \frac{\hat{s} - M^2_{l,\nu_l}}{\hat{s}^2} |\bar{\mathcal{M}}|^2 \mathrm{d}\Omega_b \mathrm{d}\Omega_l \mathrm{d}M^2_{l,\nu_l}\,, \tag{3.6}$$

where $\mathrm{d}\Omega_b$ and $\mathrm{d}\Omega_l$ are the solid angles for b quark and lepton, respectively, M^2_{l,ν_l} is the invariant mass squared of the W boson, not necessarily on shell, defined by

$$M^2_{l,\nu_l} \equiv (p_l + p_{\nu_l})^2\,, \tag{3.7}$$

and $|\bar{\mathcal{M}}|^2$ is the spin-averaged squared matrix element defined by

$$|\bar{\mathcal{M}}|^2 = \frac{256\pi^3\alpha^2\alpha_s}{3\sin^4\theta_W}\frac{\kappa_{ugt}^2}{\Lambda^2} \times \frac{\hat{s}(p_b \cdot p_{\nu_l})[\hat{s}(q_u \cdot p_l) + m_{\text{top}}^2(q_g \cdot p_l)]}{[(\hat{s} - m_{m_{\text{top}}}^2)^2 + m_{\text{top}}^2\Gamma_t^2][(M_{l,\nu_l}^2 - M_W^2)^2 + M_W\Gamma_W^2]}. \tag{3.8}$$

The quantities p_{b,l,ν_l} are the four-momenta of the outgoing b quark, lepton and neutrino, respectively, and q_u, q_g are the four-momenta of the incoming quark and gluon. Γ_W is the decay width of the W boson, $\hat{s}$ is the parton centre-of-mass energy, α is the fine structure constant, θ_W is the weak mixing angle, also known as Weinberg angle, and Γ_t is the total top-quark decay width including the anomalous top quark decay to u or c quark and gluon. Γ_t is defined as

$$\Gamma_t = \Gamma_{t\to bW} \times \left[1 + \frac{128M_W^2\alpha_s}{3\alpha^2\left(1 - \frac{M_W^2}{m_{\text{top}}2}\right)^2\left(1 + \frac{M_W^2}{m_{\text{top}}^2}\right)}\left(\frac{\kappa_{ugt}^2}{\Lambda^2}\right)\right], \tag{3.9}$$

$\Gamma_{t\to bW}$ is the SM top-quark decay width to a b quark and W boson, given by

$$\Gamma_{t\to bW} = \frac{G_f m_{\text{top}}^3|V_{tb}|^2}{8\pi\sqrt{2}}\left[1 - \frac{M_W^2}{m_{\text{top}}^2}\right]\left[1 + 2\frac{M_W^2}{m_{\text{top}}^2}\right]. \tag{3.10}$$

The new FCNC processes would affect the top-quark intrinsic width, and when calculating the branching fraction of the top-quark decay via the anomalous processes such as $t \to qg$ ($q = u, c$), the total top-quark decay width should be considered. It can be calculated simply by taking the fraction between the top-quark decay width through FCNC and the total top-quark decay width,

$$\text{Br}(t \to qg) = \frac{\Gamma_{t\to qg}}{\Gamma_{t\to bW} + \Gamma_{t\to qg}}. \tag{3.11}$$

For very small anomalous couplings, the top-quark decay width is not expected to change and it will be the same as the width through the SM top quark decay to bW. Thus the Equation 3.11 can be rewritten as follows:

$$\text{Br}(t \to qg) \approx \frac{\Gamma_{t\to qg}}{\Gamma_{t\to bW}}. \tag{3.12}$$

The branching fraction and the couplings are retrieved from the cross-section measurement by using the effective theory calculations. The calculation of the cross-section as a function of the coupling strength is done in reference [70] for the LHC at $\sqrt{s} = 7$ TeV, using the CTEQ6L1 parton distribution function (PDF), and setting the normalisation and factorisation scales to the top quark mass, m_{top} =173.1 GeV, The cross-section for single top-quark production can be written as

$$\sigma_{\text{signal}} = \sum_{q=u,c}\left(\frac{\kappa_{tqg}}{\Lambda}\right)^2 (b_{qL}|f_q^L|^2 + b_{qR}|f_q^R|^2), \tag{3.13}$$

where the b_{qL} and b_{qR} constants depend on centre-of-mass energy of the proton-proton collision, and the $f_q^{L,R}$ are the chiral parameters as they are defined for Equation 3.5. Since we are interested in the top-quark decays as predicted by the SM, the coupling is assuming to be pure left-handed and f_q^R is set to 0. Equation 3.13 can be written by using LO calculation as shown in Equation 3.14 and by using NLO

it can be written as in Equation 3.15. The results can be graphically presented as shown in Figure 3.3.

$$\sigma_{qg\to t} = 6.15\times10^{4}\left(\frac{\kappa_{ugt}}{\Lambda}\right)^{2} + 9.77\times10^{3}\left(\frac{\kappa_{cgt}}{\Lambda}\right)^{2}\ \text{pb}. \tag{3.14}$$

$$\sigma_{qg\to t} = 8.21\times10^{4}\left(\frac{\kappa_{ugt}}{\Lambda}\right)^{2} + 1.48\times10^{4}\left(\frac{\kappa_{cgt}}{\Lambda}\right)^{2}\ \text{pb}. \tag{3.15}$$

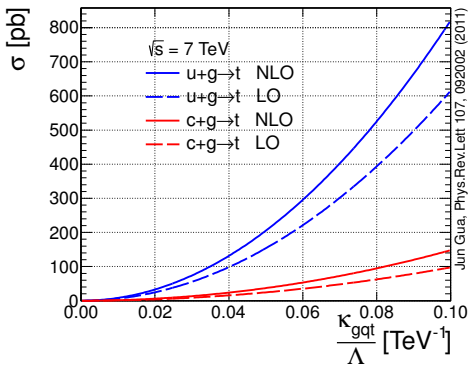

Figure 3.3: The cross-section for single top-quark production as a function of the coupling constant for the $ug \to t$ (blue) and $cg \to t$ (red). The NLO calculation is shown with solid lines, the LO cross sections with hatched lines.

The calculation of the branching fraction of the top-quark decay to a $u(c)$ quark and gluon has also been done at NLO in reference [71]. The normalisation and factorisation scales are taken to be the top quark mass m_{top} =173.1 GeV. The top-quark decay width and the branching fraction are given in Equation 3.16, where the dimension of coupling constant $\frac{\kappa_{qgt}}{\Lambda}$ is in units of TeV^{-1}. It was shown in [71] that the NLO correction increases the LO branching fraction by about 20% for $t \to u(c)g$, while the NLO correction for the decay width is just 10%. Figure 3.4a shows the branching fraction as a function of the coupling constant for both LO and NLO calculations, while Figure 3.4b shows the branching fraction of the SM top quark decays to $b + W$ as a function of the anomalous coupling. It is easily seen that for very small κ_{gqt}, the top quark decays purely to $b + W$.

$$\begin{aligned} \Gamma_{t\to qg} &= 1.577\times\left(\frac{\kappa_{gqt}}{\Lambda}\right)^{2}\ \text{GeV} \\ \text{Br}(t\to qg) &= 1.1964\times\left(\frac{\kappa_{gqt}}{\Lambda}\right)^{2} \end{aligned} \tag{3.16}$$

FCNC anomalous couplings through a gluon current can be searched for via single top-quark production, or top-quark decays. However, this brings us back to the problem of using top-quark decays to determine the magnitude of a coupling: the decay can provide information about the relative branching fraction of the exotic decay compared to the SM top decay $t \to bW$, but since it does not allow one to measure the top-quark decay width, it cannot provide a limit on the size of the exotic operator without first making an assumption concerning the nature of the Wtb interaction[1]. In addition, the search for FCNC top-quark decays remains a very challenging task at LHC from the experimental point of view, even if the branching fraction is enhanced by some exotic models to reach the level of 10^{-3} to 10^{-5}.

[1] There is very nice discussion in [72] about FCNC in single top-quark production and why FCNC search through the top-quark production is preferred over a FCNC search in top-quark decay.

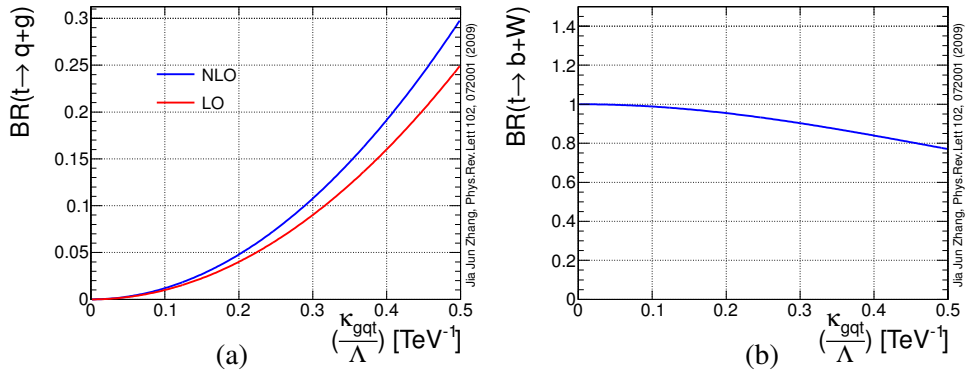

Figure 3.4: (a) The branching fraction of the anomalous top-quark decay, (b) the branching fraction of the top quark decay to W boson and b quark as a function of $\frac{\kappa_{gqt}}{\Lambda}$.

First, top quarks should be firstly produced (mostly by SM process), and then decay through the FCNC process. This means that one should expect to construct a few top-quark events, and in addition, the most promising mode, $t \to u(c)g$, is very difficult to separate from multijet production background.

The search for FCNC processes through a gluon current can be done via single top-quark production, $u(c)g \to t$, assuming that top quarks decay dominantly via the SM decay modes ($t \to Wb$), see Figure 3.5. This assumption is valid, because the anomalous top quark decay rates are expected to be

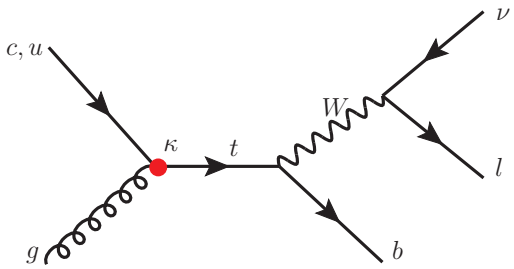

Figure 3.5: Feynman diagram for single top-quark production through FCNC, and the subsequent decay through SM process ($t \to bW$), with W boson decays to lepton and neutrino.

extremely small, and high values of the branching fraction and coupling constants have already been excluded by experiments [15].

Chapter 4

ATLAS Detector

4.1 The Large Hadron Collider

The Large Hadron Collider (LHC)[1] is a proton-proton collider located between 45 and 170 m below the ground near Geneva at the CERN laboratory. It is built into the tunnel of the former LEP accelerator which has eight straight sections and eight arcs resulting in a 26.7 km circumference.

The LHC accelerates two beams of protons in opposite directions in two separated beam pipes within one cryostat system. It is designed to accelerate each beam up to 7 TeV, but during the 2010-2011 operation period each beam was accelerated up to 3.5 TeV for safety reasons.

The proton beams used in the LHC are extracted from a hydrogen source and pre-accelerated by the Linear Accelerator (LINAC2) to an energy of 50 MeV. Then they are transferred to BOOSTER where the energy is raised to 1.4 GeV, before they are transferred first to the Proton Synchrotron (PS) (26 GeV) and then to the Super Proton Synchrotron (SPS) where the beam energy reaches 450 GeV. They are then injected into the LHC itself (see Figure 4.1).

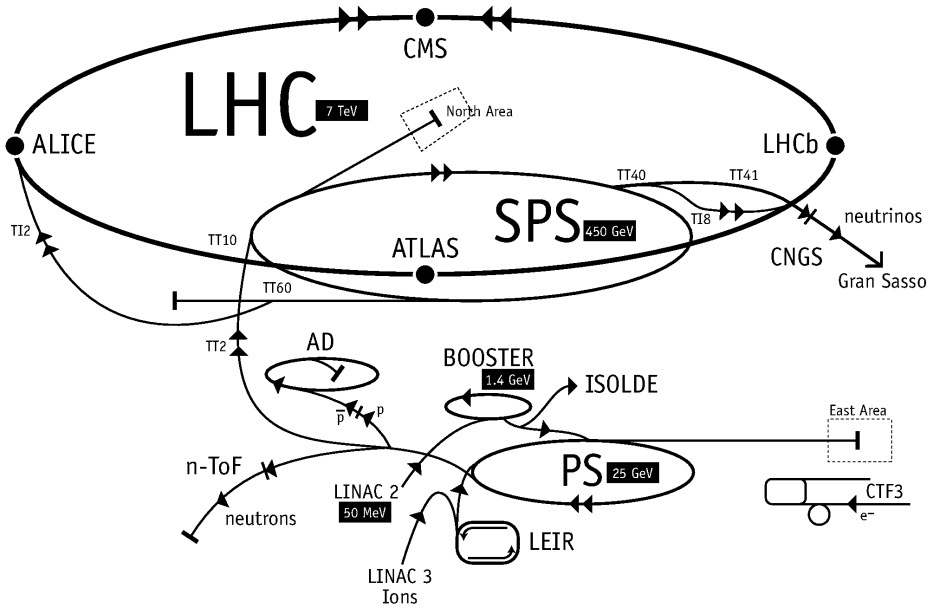

Figure 4.1: Layout of the LHC accelerator complex.

In the LHC the particles are accelerated by radio-frequency cavities (RF) which operate at a temperature of 4.5 K and at 400.8 MHz. To keep the protons running along a circular ring, the LHC is

[1] For detailed information about the LHC accelerator, see [73]

equipped with 1232 high-field superconducting dipole magnets. The magnets are cooled down to 1.9 K with super-fluid liquid helium to achieve the superconductivity. To focus the proton beams, the LHC is equipped with 392 quadrupole magnets.

Four large experiments have been constructed at the LHC. Two of them are general purpose experiments, the ATLAS and CMS experiments at Point 1 and Point 5, respectively. The other two experiments are ALICE and LHCb designed to explore the quark-gluon plasma and B hadrons, respectively.

The proton beams at the LHC are not continuous but rather they are organised in bunches or packets. Each beam can have 2808 bunches by design, where the number of protons per bunch is around $\sim 1.15 \cdot 10^{11}$. Every bunch has a length of ~32 cm and is separated from the next bunch by 25 ns. The LHC beams travel in opposite directions in separate beam-pipes, but when they come to collide they share a common beam-pipe. At the interaction point (IP), the beams are squeezed to 16 μm in diameter and the distance between the two beams vanishes to zero, with a crossing angle of 285 μrad. Table 4.1 shows the LHC design parameters.

Number of bunches	2808
Bunch intensity	$1.15 \cdot 10^{11}$
Bunch length	1.06 ns
Bunch spacing	25 ns
Beam size at IP	16 μm
Crossing angle	285 μrad
$\sqrt{s}$	14 TeV

Table 4.1: The LHC design parameters.

4.2 The ATLAS Detector

A Toroidal LHC AparatuS (ATLAS) [74] is not only the largest of the LHC detectors, but also the largest experiment of its type ever built. It is 44 m long and 25 m high and weighs 7000 tonnes.

It was built upon the knowledge learned from previous particle detectors. ATLAS has a multilayer structure (see Figure 4.2). It consists of many sub-detectors, each of them designed for a different kind of measurement. The sub-detectors from the inside to the outside are: the inner detector (see Section 4.2.3), the calorimeter (see Section 4.2.4), and finally the outer-most detector is the muon system (see Section 4.2.5).

4.2.1 ATLAS Coordinate System

The coordinate system used in ATLAS is defined by the beam direction, with the z-axis pointing along the LHC beam-pipe. The transverse plane to the z-axis is defined by the x-axis which points to the centre of the LHC ring and the y-axis which points upwards. The (0,0,0) point is defined as the nominal interaction point. The polar angle, θ, is the angle between the z-axis and the $x - y$ plane while the azimuthal angle, ϕ, is the angle between the x-axis and the y-axis. The polar angle is defined within $\theta \in [0, \pi]$ and the azimuthal angle within $\phi \in [-\pi, \pi]$, respectively.

The particle momenta P_x, P_y and P_z are defined along x, y and z-axis, respectively. The transverse momentum, P_T, is defined by

$$P_T = \sqrt{P_x^2 + P_y^2}. \tag{4.1}$$

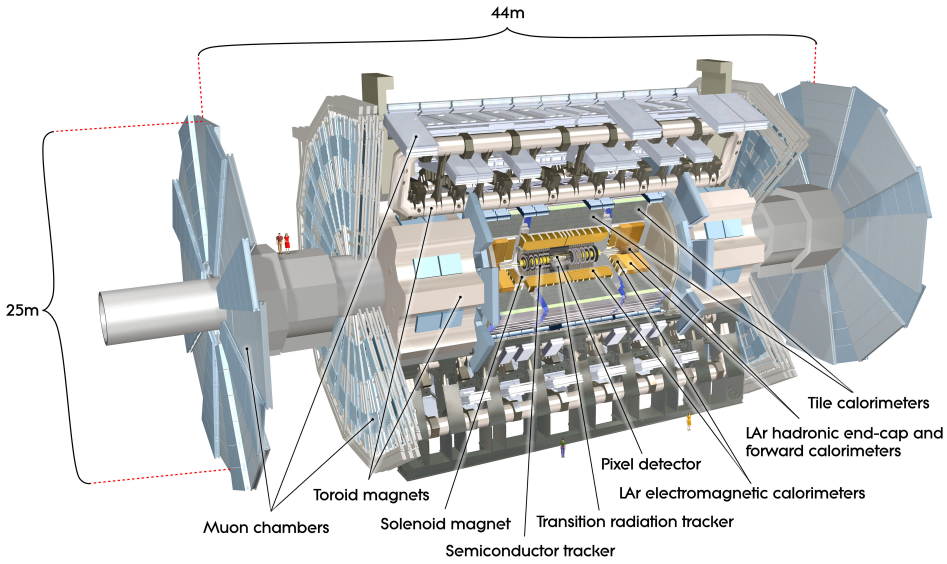

Figure 4.2: Overview of the ATLAS detector and its different components.

Two other variables widely used in the ATLAS experiment are the pseudo-rapidity (η), and the angular distance (ΔR). η is defined as:

$$\eta = \frac{1}{2} \ln \left(\frac{|\vec{P}| + P_z}{|\vec{P}| - P_z} \right). \tag{4.2}$$

which is the same as the rapidity when the mass of the particle goes to zero. It is chosen because the difference in the pseudo-rapidity of two particles $\Delta\eta = \eta_1 - \eta_2$ is independent of Lorentz boosts along the beam axis. It can be re-formulated in terms of the polar angle θ

$$\eta = -\ln \left[\tan \left(\frac{\theta}{2} \right) \right]. \tag{4.3}$$

The second variable, ΔR, between two particles, is defined by

$$\Delta R = \sqrt{\Delta\eta^2 + \Delta\phi^2}, \tag{4.4}$$

where $\Delta\phi$ is the difference in the azimuthal angle between the two particles.

4.2.2 Magnet System

The ATLAS magnet system is unique in many ways. It is a hybrid system of large superconducting magnet systems, with the total length of 26 m and 22 m in diameter (see Figure 4.3).

The first magnet system is the central solenoid which is located around the inner detector and is designed to provide a magnetic field of 2 T in the inner tracker. It is constructed from a single-layer coil that consists of a high-strength Al-stabilised Nb/Ti conductor. It is 5.8 m long and the inner and outer diameters are 2.46 m and 2.56 m, respectively.

The second magnet system is the toroid magnets, which are split into three parts with a barrel part installed around the central calorimeter and two end-caps installed at each end of the detector. Each of these parts has eight identical coils built radially in a symmetric way around the beam-pipe. The

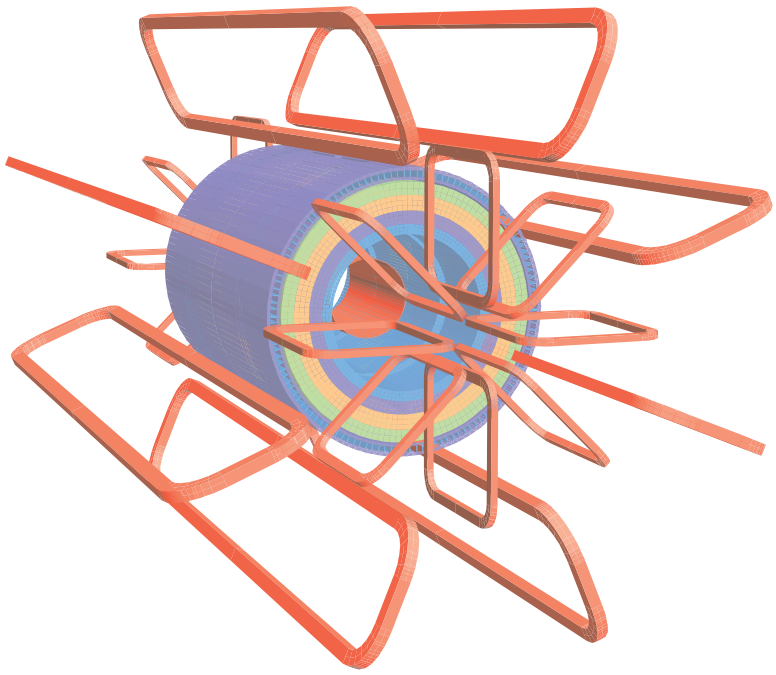

Figure 4.3: The ATLAS magnets, the solenoid and the three toroidal parts: the barrel toroid and two small end-cap toroids

toroid magnets can be operated independently and are designed to produce an average magnetic field (it depends on the radius R and the angle ϕ) of approximately 0.5 T in the barrel region. In the end-cap regions it varies from 0.15 T to 2.5 T.

The four ATLAS magnet parts were designed and built such that the trajectories of charged particles are bent when traversing the tracking devices, which enables the particle momentum measurement and helps in the particle identification.

4.2.3 Inner Detector

The ATLAS inner detector (ID) (see Figure 4.4) is the closest detector system to the LHC beam-pipe starting from 5 cm from the interaction point. It is about 3.5 m long and 1.1 m in radius covering $|\eta| < 2.5$, and embedded in the magnetic solenoid, which makes it possible to measure the charged particle momenta. It also allows the reconstruction of interaction vertices.

The ID has three sub-detectors: the pixel detector, the semiconductor tracker (SCT) and the transition radiation tracker (TRT). Both the pixel and SCT detectors are built to perform precision position measurements, and together with the TRT they can perform a precision position and momentum measurements, and particle identification. The ID has a design momentum resolution [74] given by

$$\frac{\sigma_{P_T}}{P_T} = 0.05\% P_T \oplus 1\% \,, \tag{4.5}$$

where is first term is determined by the intrinsic detector resolution, and the second term represents multiple-scattering effects, the symbol $\oplus$ denotes addition in quadrature. The resolution depends on how the detector material distributed in pseudo-rapidity, η.[2]

[2] The design resolution comes from the track position measurement which can be later converted to a momentum measure-

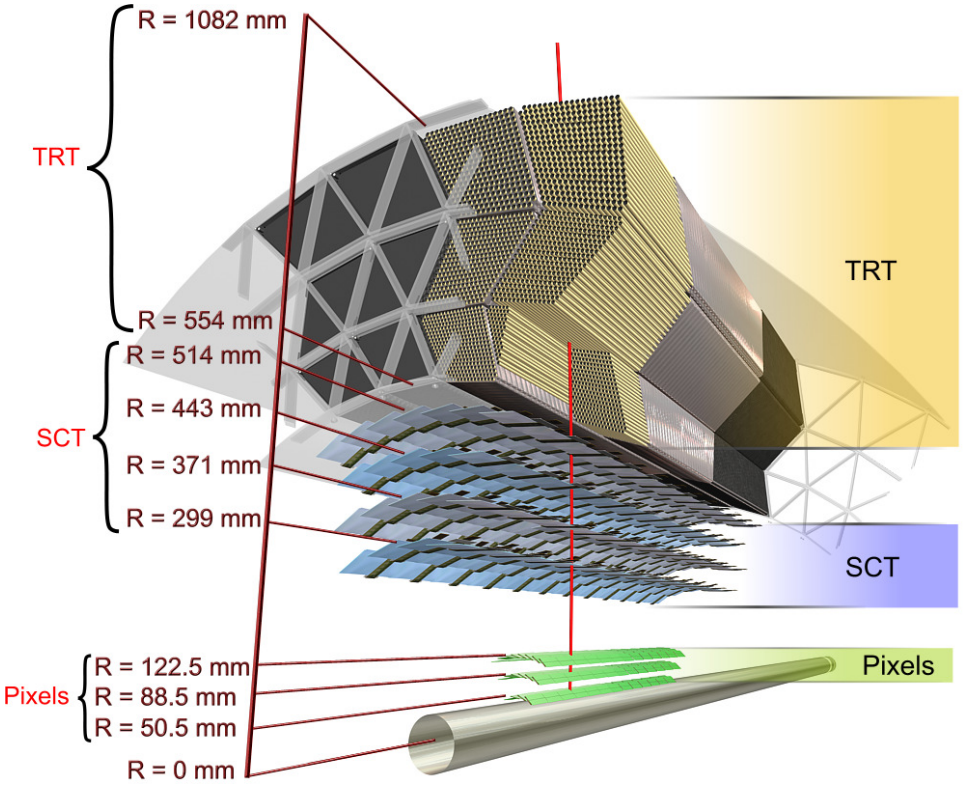

Figure 4.4: Drawing of the inner detector components. The vertical red line represents a track with P_T= 10 GeV and η=0.3 coming from the primary vertex traversing the silicon-pixel layers, the SCT and finally the TRT.

Pixel Detector

The innermost sub-detector is the pixel detector with silicon pixels of 50×450 μm^2. It consists of three radial layers, arranged in concentric cylinders around the beam axis, and three disks in each end-cap wheel perpendicular to the beam axis. In total it contains more than 80.4 million channels distributed over 1744 modules.

The pixel detector provides the most precise position measurements among the ID sub-detectors, with a design accuracy of 10 μm in the R-ϕ direction and 115 μm in the z-direction.

This high accuracy allows the measurement of the tracks with sufficient precision to discriminate between tracks from the primary interaction vertex and tracks from secondary interaction vertices, which helps to identify long-lived hadrons such as B-hadrons.

Semiconductor Tracker

The next ID sub-detector is the semiconductor tracker. It consists of three parts, the barrel region and two end-cap regions, with approximately 6.3 million read-out channels.

In the barrel region, the SCT is built from four cylindrical double-layers of silicon-microstrips. Every layer contains two rows of wafers one with strips parallel to the beam direction measuring the R-ϕ direction and the other with an angle of 40 mrad.

In each end-cap wheel, there are nine layers of disks. Every layer consists of a set of strips running radially and a set of stereo strips at an angle of 40 mrad.

The design accuracy of the SCT is 17 μm (R-ϕ) $\times$ 580 μm (z) in the barrel region and in the end-cap wheels the accuracy is 17 μm (ϕ) $\times$ 580 μm(R).

Transition Radiation Tracker

The transition radiation tracker (TRT) is the third part of the ID and is built from straw tubes with 4 mm in diameter and 144 cm in length in the barrel (37 cm in the end-caps). There are 73 straw layers in the barrel arranged in 3 modules with $-1 < \eta < 1$, and 160 straw planes in each end-caps arranged in 20 disks. Those straws are filled with gas mixture of 70% Xe, 27% CO_2 and 3% O_2.

The barrel and the end-cap TRT parts enable tracking of charged particles with $P_T > 0.5$ GeV up to 150 GeV and $\eta < 2$ with a total 351 000 read-out channels.

Although the TRT has the lowest tracking precision among the ID sub-detectors (130 μm per straw in R-ϕ), it can contribute to high precision measurements of the R-ϕ coordinate by combining the precision measurements from the pixel and SCT detectors to straw hits at larger radius. It can be competitive by compensating its lower precision measurements per straw by the large number of hits and longer measured track length.

In addition to the tracking measurements, the TRT contributes to a very robust pattern recognition and charged particle identification, and also the TRT helps in identifying electrons through the transition radiation effect. Relativistic particles emit photons when they cross boundaries of different refractive indices; the probability of emitting photons depends on the relativistic gamma factor $\gamma = E/m$ of the particle. The TRT was designed to identify particles which emit photons in the X-ray region which can be absorbed by the Xe gas. Electrons can be identified through this effect due to their very high γ factor which comes as a result of their small mass (0.51 MeV) compared to the muon or pion masses (>100 MeV).

ment by using the magnetic field information. For track measurement resolution see Section 6.1.1.

4.2.4 Calorimeter System

The ATLAS calorimeters are designed to stop the particles through electromagnetic and strong interactions. When particles enter the calorimeter, they interact with the material and initiate a particle shower which is then detected. As a consequence, the particle energy can be determined.

In addition to the energy determination, calorimeters can perform a position measurement, which helps in identifying the track trajectory, which can be used later in identifying the particle type and its momentum.

The ATLAS calorimeters are thick enough with many radiation lengths,[3] X_0, and they stop most of the hadrons from arriving to the muon spectrometer and prevent them from being identified as muons. Given the neutrinos do not interact with the detector material and do not leave any signatures to be observed, the four-momentum carried by neutrino is seen as unbalance in the total momentum available in the event, also called missing transverse energy ($\not\!\!E_T$). The ATLAS calorimeters ensure a good measurement of $\not\!\!E_T$, which is an important feature for many physics signatures searches.

The electromagnetic calorimeter is sensitive to electrons and photons while the hadronic calorimeter is designed to absorb strongly interacting particles such as protons and neutrons. The ATLAS calorimeter system is shown in Figure 4.5.

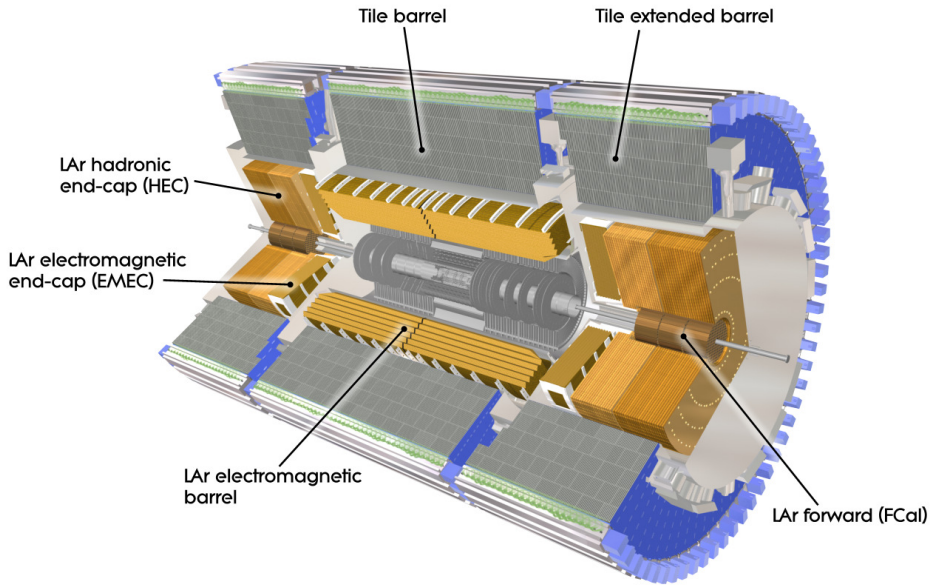

Figure 4.5: The ATLAS calorimeter system.

Electromagnetic Calorimeter

The electromagnetic calorimeter is designed to cover the full azimuthal angle, ϕ, enclosing the central solenoid, and it consists of a barrel that covers $|\eta| < 1.48$ and two end-caps to cover the region of $1.38 < |\eta| < 3.20$.

The electromagnetic calorimeter is built from lead and liquid argon combined where lead acts as an absorber and liquid argon as the active material. The total thickness varies between 22 to 33 radiation

[3] The radiation length is defined as the distance needed to decrease the electron energy to $1/e$ of its original value.

lengths. Between the barrel and end-cap wheels, 1.37< $|\eta|$ <1.58, there is a free space for cables and services for the inner detector.

In the precision measurement region, $0 < |\eta| < 2.5$, we can get an accurate position measurement for particles such as photons and neutral particles. There are three active layers, where the first and the second layer provide the position measurement in η, which can be obtained by small segments in η-direction.

In the region $|\eta| < 1.8$ there is a presampler detector. It consists of an active liquid argon (LAr) layer to correct for the energy lost by electrons and photons upstream of the calorimeter.

Both the barrel and end-cap electromagnetic calorimeters have a design energy resolution [74] of

$$\frac{\sigma_E}{E} = \frac{10\%}{\sqrt{E}} \oplus 0.7\%. \tag{4.6}$$

The electromagnetic calorimeter and the presampler have 1536 and 62208 readout channels, respectively.

Hadron calorimeter

The hadron calorimeter is composed of three separate sub-detectors, the scintillator-tile calorimeter located in the region of $|\eta| < 1.7$, and two end-cap calorimeters using liquid argon (LAr) covering the region of $1.5 < |\eta| < 3.2$.

The tile calorimeter is directly behind the liquid argon electromagnetic calorimeter, where the level of radiation is relatively low. It uses steel as absorber and plastic scintillating tiles as active material. It is divided into the central barrel, 5.8 m in length covering $|\eta| < 1.0$ and two extended barrels, 2.6 m in length and each having an inner radius of 2.28 m and an outer radius of 4.25 m covering $0.8 < |\eta| < 1.7$. The energy resolution that can be achieved by the tile calorimeter [74] is given by

$$\frac{\sigma_E}{E} = \frac{50\%}{E} \oplus 3\%. \tag{4.7}$$

The hadronic end-cap wheels are perpendicular to the beam axis, and are located directly behind the end-cap electromagnetic calorimeter. The wheels are made of copper layers as absorber material filled by an active medium of liquid argon. The readout cells measure $\Delta\eta \times \Delta\phi = 0.1 \times 0.1$ in the region $1.5 < |\eta| < 2.5$ and 0.2×0.2 in the more forward region, resulting in a design energy resolution [74] given by

$$\frac{\sigma_E}{E} = \frac{100\%}{E} \oplus 10\%. \tag{4.8}$$

The hadron calorimeter has 64 modules in total with 9852 readout channels in the barrel region, and 5632 readout channels for each of the end-caps.

4.2.5 Muon Detector System

The muon spectrometer is by far the largest tracking system in ATLAS, extending from a radius of 4.25 m around the calorimeters out to the full radius of the detector (11 m) and stretching out from about 7 m to 23 m from the interaction point on each side in the longitudinal direction, and thus defining the outer perimeter of the ATLAS detector.

Muons have relatively long lifetime, they are heavier than electrons by a factor of 207, and thus lose a very small energy fraction through bremsstrahlung, which makes it easy for them to exit the barrel

and end-cap calorimeters. The muon spectrometer was designed to provide a stand-alone measurement of the muon transverse momentum (from ~3 GeV to 1 TeV) with a precision of approximately 10% for 1 TeV tracks [74].

It is heavily used as a trigger system, see Section 4.2.6. It is used to trigger on muons with high momenta in the region of $|\eta| < 2.4$ over the full azimuthal angle ϕ-range, which plays a role by a distinguishing features in several interesting physics channels. The trigger chambers provide rapid information on muon tracks traversing the detector, allowing the Level-1 trigger (L1) logic to recognise their multiplicity and approximate energy range.

4.2.6 Trigger System

The production cross-section of inelastic proton-proton scattering events at the LHC is is several orders of magnitude higher than the cross-section of physics signatures. Millions of uninteresting collisions happen every second. Taking into account that of ATLAS event occupies in average 1.2 MB on the hard disk, it is far beyond the computing capabilities to record and analyse all interactions.

The trigger system was designed to reduce the number of recorded events by filtering out the uninteresting multijets events while keeping the interesting physics candidates with an efficiency of $\sim O(1)$.

The ATLAS trigger system consists of three levels of event selection, Level-1 (L1) which is a hardware-based trigger, the level-2 (L2) and the event filter (EF), the latter form the high-level trigger (HLT) and are based on computing algorithms.

The L1 trigger searches for particles with high transverse momentum such as muons, electrons, photons, jets, and τ leptons decaying into hadrons, as well as large missing and total transverse energy. It depends on the information from the sub-detectors, such as the muon trigger chambers and calorimeter cells. The L1 trigger reduces the event rate to obtain 75 kHz. For each event passing the L1 trigger a number of regions-of-interest (RoI) in η and ϕ within the detector are identified, the RoI information is used by the L2 trigger. This system requires a good resolution in space and also requires fast processing to keep the time to store the data in the buffers as small as possible.

The L2 trigger uses all the available detector information within the RoI's provided by the L1 trigger. The L2 trigger selection uses specialised algorithms optimised for timing performance, and is designed to reduce the trigger rate to approximately 5 kHz, with an event processing time of about 40 ms .

The event filter is designed to reduce the event selection rate from 5 kHz accepted by the L2 trigger to around 500 Hz of permanent storage acceptance ~600 MB/s. The EF algorithms use the full granularity and precision of calorimeter and muon chamber data, as well as the data from the inner detector. The EF takes the decision to reject the event after its full reconstruction is completed. In addition, it organises the data into streams based on physics object candidates, such as muons, electrons and jets.

4.3 Luminosity Measurement

The instantaneous luminosity, $\mathcal{L}$, is a measure of an accelerator's ability to provide particles (in our case protons) for the collisions. Increasing the $\mathcal{L}$ increases the chance that we see protons interacting with other protons. $\mathcal{L}$ is defined as the number of particles per unit area per unit time of the incident beam multiplied by the number of particles available in the target and for colliders is given by:

$$\mathcal{L} = N \cdot f \cdot \frac{n_1 \cdot n_2}{4\pi\sigma_x\sigma_y}, \tag{4.9}$$

where N is the number of proton bunches, f is the revolution frequency, n_1 and n_2 are the number of protons per bunch, σ_x and σ_y represent the average transverse width and height of the bunches, respectively. The luminosity is measured in units of $\mathrm{cm}^{-2}\mathrm{s}^{-1}$.

Integrating the instantaneous luminosity over time gives the so-called integrated luminosity, $L_{\mathrm{int}} = \int \mathcal{L}\,\mathrm{dt}$, which is a measure of the amount of collected data. To calculate the event rate of a certain physics process, the probability of the process occurring is essential. This probability is given by the cross-section (σ) (see Section 2.3). For a particular cross-section, the number of events N in a given amount of data can be calculated by $N = \sigma \cdot L_{\mathrm{int}}$.

ATLAS monitors the delivered luminosity by measuring the observed interaction rate per bunch crossing independently with a variety of detectors and using several different algorithms. For the luminosity measurement, ATLAS has two further sub-systems located far from the interaction point. The LUCID detector is the first; located at ±17 m from the interaction point, surrounding the beam-pipe at the edge of the cavern. It uses Cherenkov radiation to provide online luminosity measurements. The second sub-detector is ALFA, which is located at a distance of 240 m from the interaction point. It was designed to provide the absolute luminosity measurement, and has not yet been used.

In 2011, the absolute luminosity was determined by using the LHC parameters such as the n_1, n_2, σ_x and σ_y. The beam widths σ_x and $\sigma_y$are determined by using van-der-Meer scans [75], which can be combined with an independent measurement of n_1 and n_2. By scanning the beams across each other, σ_x and σ_y can be extracted and the absolute luminosity can be computed.

4.4 Data Samples

ATLAS and LHC were successfully operated in 2011. On 26.10.2011, the LHC delivered the highest instantaneous luminosity ever recorded at a hadron collider, $\mathcal{L}$=$3.65 \cdot 10^{33}$ $\mathrm{cm}^{-2}\mathrm{s}^{-1}$, recorded with a total number of proton colliding bunches of 1331 at $\sqrt{s}$=7 TeV. Every bunch was in average 50 mm in length and around 20 μm in width at the interaction point, and the number of protons per bunch was $\sim 1.2 \cdot 10^{11}$. The total integrated luminosity delivered by the LHC in 2011 was 5.62 fb^{-1}. ATLAS has recorded 5.25 fb^{-1} with an efficiency of 93%. Figure 4.6 shows the total integrated luminosity over time.

The collision data samples used in this analysis have been collected between 22.03.2011 and 22.08.2011. The data-sets are divided into periods according to the LHC changing parameters, such as the number of proton bunches. The periods considered in this analysis start from period B2 until period K6. The maximum instantaneous luminosity in this period was $\mathcal{L}$=$2.05 \cdot 10^{33}$ $\mathrm{cm}^{-2}\mathrm{s}^{-1}$, with the total number of bunches equal to 1317. The considered data events have been recorded by either electron or muon triggers. These were later filtered using the so-called the Good Run List (GRL), which requires that the LHC beam has good conditions to qualify it for physics analysis. Beside that, all relevant detector parts should be fully operational and flagged as "green". The result integrated luminosity of the data sample is 2.05 fb^{-1}.

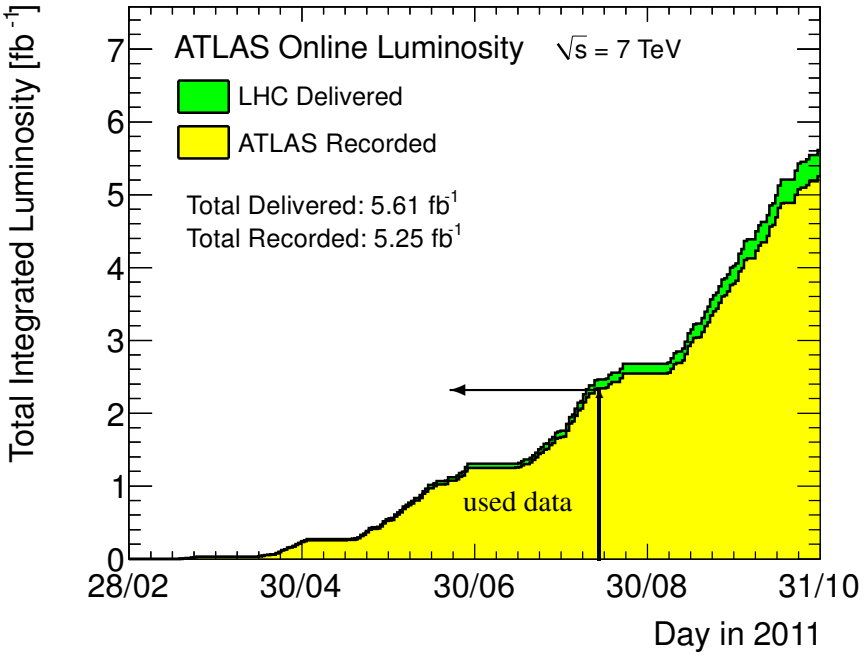

Figure 4.6: The total integrated luminosity as a function of time (2011). The black line indicates the periods used in this analysis.

Chapter 5

Monte Carlo Simulation

A good simulation is required when dealing with complex processes, such as those produced in particle collisions. This requires collision events simulated by computer programs called Monte Carlo (MC) generators. The generated collision events should simulate all physics processes considered in the analysis, because MC events are used to validate the analysis procedures, to calculate the acceptance for the signal channel and to evaluate the contributions from the background processes. In the first section, the MC simulation is discussed, followed by the second section which summarises the MC generators used to simulate different physics processes at ATLAS. The third section explains the signal simulation. The fourth section explains the simulation of the background samples used in this analysis, summarising the predicted cross-sections and their uncertainties for all used processes. The fifth section explains the detector simulation. Finally, the sixth section contains a discussion of the pile-up reweighting applied to reduce the discrepancy between data and MC.

5.1 Monte Carlo Simulation in ATLAS

The full MC simulation at ATLAS is done in many steps. It starts by simulating the collision of two protons, each containing quarks and gluons with a momentum distribution described by the parton distribution function (PDF). This is followed by the hard interaction between the partons, where the interaction of interest is carried out; this corresponds to the process calculated using the matrix element (ME). The collision between partons produces new particles, which might be unstable and have very short life-time. The decay of the short-lived particles is then simulated, where spin and other correlations are transferred from the incoming particles through the intermediate particles to the decay sub-process. Particles may emit or radiate other particles such as photons and gluons, where gluons can split into gluons or quark-antiquark pairs. This leads to a parton shower (PS). At low energy scales $\sim$1 GeV, the strong coupling strength (α_s) is large and confinement becomes effective. Confinement can not be described by perturbation expansion and needs to be modelled. At this energy level, the quark-antiquark pairs becomes strongly connected, and they are transformed into mesons and baryons in a process called hadronisation. Interactions of the remnant partons from the proton are added to the hard interaction. These parton multiple interactions are called the underlying event. In the final step, the decay of the long-lived particles such as τ leptons and B hadrons are simulated.

In the detector simulation, the interaction between all final-state particles (muons, electrons or hadrons such as $\pi^{\pm}$) with the detector material is considered, and the response of the electronics is taken into account. The format of the simulation output is identical to the detector output of collision events. The same reconstruction algorithms are applied to simulated and collision events.

For high instantaneous luminosities, several proton-proton collisions occur in one bunch-crossing (pile-up). These additional collisions are simulated like the primary collisions mentioned above, and overlaid on the detector response.

5.2 Monte Carlo Generators

The aim of the matrix element generators, also called parton-level generators, is to generate events according to the different cross-sections for a fixed number of partons in the final-state. Given a process, they identify the relevant sub-processes and calculate the corresponding amplitudes. The information about the contributing Feynman diagrams is used to calculate the cross-sections and to generate events at parton level. These generators generally do not simulate the PS and hadronsation processes, thus their final states are just leptons, bare quarks and gluons. In order to obtain a sensible description of the production process, the output of ME generators is used as an input for PS generators such as PYTHIA [76] and HERWIG [77].

The PS is an iterative procedure that simulates simplified processes for QCD emissions such as $q \to gq$, $g \to gg$ and $g \to q\bar{q}$ [78]. Each daughter produced may emit additional partons. The PS model uses soft and collinear emission approximations without explicit ME calculations. Instead, the branching fractions are first calculated at LO and the Dokshitzer-Gribov-Lipatov-Altarelli-Parisi (DGLAP) equations [79–81] are used to evolve the emission to different momentum scales. The DGLAP evolution calculations are applicable to QCD and QED, and describe the behaviour of partons at a given momentum scale. In a PS process i.e. $2 \to n$ is factorised into n simple $2 \to 2$ (or $1 \to 2$) processes and multiple soft and collinear emissions. The cross-section of the whole $2 \to n$ process is associated to the cross-section of the core $2 \to 2$ hard process, in the limit that the factorised emissions are soft and collinear. To avoid the confinement effects in the non-perturbative region, a cut-off at energy scales of ~1 GeV is applied. With energies below this scale no soft emissions are simulated. Divergences and their cancellations are handled by Sudakov form factors [82], which expands the DGLAP equations and assures that the probability for a parton to branch never exceeds unity.

The modelling of kinematic distributions for a given process may differ between the MC generators. Usually, NLO matrix element are preferred over LO matrix element MC generators, since the better phenomenological descriptions of the soft emissions are used. Each of the MC generators is tuned to describe better the LHC data. There are two MC tunes for ATLAS: ATLAS minimum bias tune 1 (AMBT1) [83], This is the first tuning of PYTHIA6 to LHC data at $\sqrt{s}$ = 0.9 TeV and $\sqrt{s}$ = 7 TeV. The tune was restricted to events with ≥ 6 charged particles and $|\eta|$ <2.5. The newly tuned MC samples model better the particles P_T and charged multiplicity spectra. The second tune is the ATLAS underlying event tune 1 (AUET1) [84], which was done to tune HERWIG plus JIMMY MC generators. JIMMY is the MC generator used to simulate the underlying processes. This tune was done using ATLAS data at $\sqrt{s}$ = 7 TeV, and it considered the results from AMBT1 ATLAS tune. AUET1 shows a better description of the tracks P_T distributions.

5.3 Signal Simulation

Protos [85] is a LO generator used for the simulation of the direct production of the top quarks via FCNC. To generate the signal MC samples, certain values for the coupling constants $\kappa_{gut}/\kappa_{gct}$ are chosen. Protos uses a different nomenclature for the effective Lagrangian from the one described in Chapter 3, i.e. the coupling constants are defined as:

$$\frac{\zeta^L_{qt}}{m_t} = \frac{\kappa_{gqt}}{\Lambda} f^L_q \quad \text{and} \quad \frac{\zeta^R_{qt}}{m_t} = \frac{\kappa_{gqt}}{\Lambda} f^R_q, \tag{5.1}$$

The $f^{L,R}_q$ are chiral parameters as defined in Chapter 3. The coupling values used to generate the signal samples are ζ^L and ζ^R set to 0.005 and 0, respectively. The ζ^R value is set to 0, since we are interested

in SM- like top-quarks. Two samples are generated, one for the $ug \to t$ channel and the other for the $cg \to t$ channel.

The CTEQ6l1 [86] PDF set is used. The top quark decays as expected in the SM, $t \to bW$. Only the leptonic decay of the W boson is considered. The PS and hadronisation are done with PYTHIA 6.421 [76] and the corresponding AMBT1 tune [83] to the ATLAS data is used. The top quark, W boson and Z boson masses are set to 172.5 GeV, 80.403 GeV and 91.1876 GeV, respectively.

The corresponding cross-sections times the branching fractions of the leptonic decay of the W boson obtained with these coupling values are listed in Table 5.1. The different cross-section values for the

	t	$\bar{t}$	Total
$ug \to t$	7.30 pb	1.29 pb	8.59 pb
$cg \to t$	0.68 pb	0.68 pb	1.36 pb

Table 5.1: The cross-section times branching fractions of the leptonic decays of W boson for the MC generated signal events. The values are determined using the LO Protos generator.

$ug \to t$ and $cg \to t$ channels are explained by the fact that proton has more u quarks than c quarks. In addition, there is a charge asymmetry between the top quark and the antitop quark, this because the antiup quarks and anticharm quarks are produced via the gluon splitting where the same amount of quarks and anti quarks are produced. In addition to production of up quark via the gluon splitting, the up quark is a valance quark where the proton contains up quarks at the ground state.

Since the coupling strength κ_{gqt} is a-priori unknown, the chosen coupling value in the signal simulation should not influence the analysis. This can be ensured by checking the kinematic distributions of MC samples generated using different coupling values. Since the top quark is produced via the FCNC and decays through the SM processes, only the top-quark kinematics need to be checked to show the independence on the chosen coupling values. For this check, two additional MC signal samples have been generated setting $\zeta_{gqt} = 0.05$ and $\zeta_{gqt} = 1 \cdot 10^{-5}$. Figure 5.1 shows the transverse momentum, pseudo-rapidity and the azimuthal angle distribution of the top quark obtained from the three generated samples with different coupling values. The difference are smaller than 1% and within the statistical uncertainty.

5.4 Background Simulation

Several SM processes are expected to have the same final-state particles as the signal events and are considered as a background to the FCNC analysis. The SM decay of the top quark is considered, i.e. $t \to Wb$, where the W boson decays to leptons and neutrinos. The event signature which has been searched for consists of a high P_T b-quark jet, a charged lepton (μ, e) and missing transverse energy, $\not{E}_T$, from the neutrino.

The main background is therefore W/Z+ partons production, especially in association with a heavy flavour (HF) quark, i.e. a b quark or a c quark. The SM single top-quark production is the second dominant background, specially the t-channel. The SM $t\bar{t}$, diboson production and multijets are contributing less to the final state.

5.4.1 W+n Partons and Z+n Partons MC Samples

The W+n partons samples are: W, $Wb\bar{b}$, $Wc\bar{c}$ and Wc with additionally up to 5 partons in the final state. The MC samples have been simulated by the ME generator ALPGEN v2.13 [87], which is interfaced to

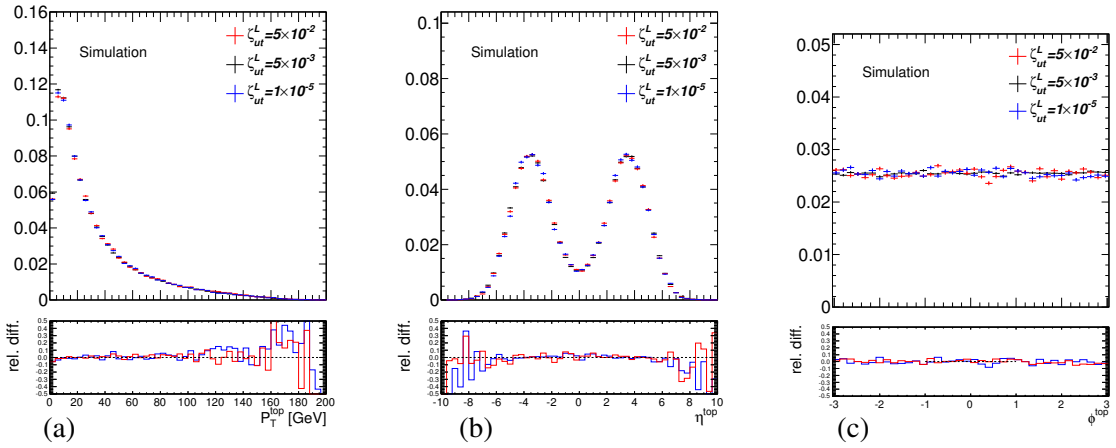

Figure 5.1: a) Transverse momentum b) pseudo-rapidity c) azimuthal angle distributions of the top-quark for three different coupling constants $\zeta_{gqt} = 0.05$, $\zeta_{gqt} = 0.005$ and $\zeta_{gqt} = 1 \cdot 10^{-5}$. It is easily seen that the top-quark kinematics are unaffected by the choice of the coupling value.

the PS generator HERWIG v6.510 [77], and the underlying events are simulated by JIMMY v4.31 [88]. For both the ME calculations and the PS evolution the CTEQ6.1 PDF is used. The corresponding AUET1 HERWIG/JIMMY tune [84] to the ATLAS data is used.

In ALPGEN, some events are simulated twice: once in the inclusive W+n parton samples and the other while simulating the W with associated heavy quark pair production samples. To remove those double-counted events, an overlap removal based on ΔR matching is used. Due to the use of the HF overlap removal, the phase-space populated by the heavy quarks produced in association with the W boson should not be affected by applying the ΔR cut. While using no phase-space cuts is feasible for the associated heavy quark pair production, a transverse momentum cut $P_T(c) > 10$ GeV is introduced for the Wc samples due to the large production cross-section of the process.

Only the leptonic decays of the W and Z bosons are considered and for the Z+n partons the phase space is restricted to $m_{l^+l^-} > 40$ GeV. The W/Z+n partons samples and cross-section values are listed Table 5.2. Note: the production cross-sections of all the other ALPGEN and HERWIG samples are normalised to the corresponding NNLO cross-section prediction given in [89].

Estimation of the W+jets Background

The dominant background process in this analysis is the Wc+0 parton production, where a c quark is identified as a b quark, and needs to be estimated as accurately as possible. The kinematic shapes and acceptances of the Wc+n parton background are taken from MC simulation samples, while the overall normalisation is estimated using the NLO calculations described as follows.

A k-factor is calculated by comparing the NLO and LO calculation using MCFM [90]. The cross-section values and the electroweak parameters used are the same as used in all processes by ATLAS.

- $M_W = 80.403$ GeV
- $M_Z = 91.1876$ GeV
- $m_{\text{top}} = 172.5$ GeV
- $G_F = 1.16637 \cdot 10^{-5}$ GeV^{-1}

Since a P_T cut is applied when the c quark samples are produced, one has to show that the obtained k-factor is unbiased by the value of the chosen P_T cut. This is checked by scanning the cross-section with respect to the P_T of the c quark. The results of the LO and NLO calculations of Wc+n partons using the CTEQ6L1/MSTW08lo and CTEQ6.6/MSTW08nlo PDFS, respectively, can be seen in Figure 5.2. To check reliability of the calculations, the LO cross-section predicted by ALPGEN as tuned for MC10A campaign, is compared with the LO MCFM prediction, and a very good agreement is found.

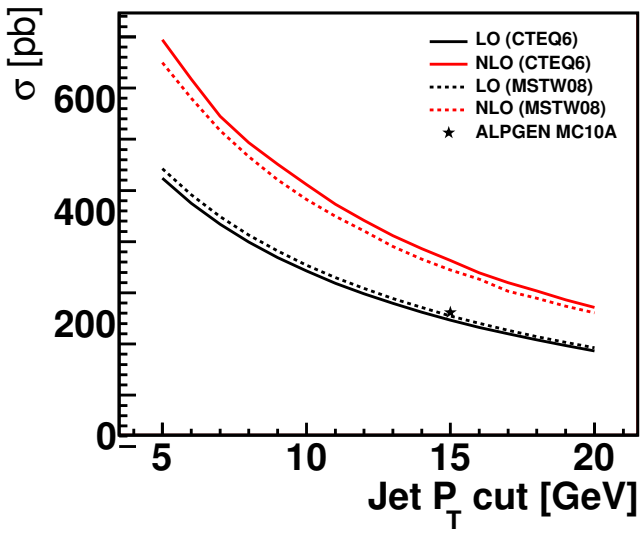

Figure 5.2: Wc cross-section calculated at LO (black) and NLO(red). A comparison between the cross-section calculated with CTEQ6 PDFs (solid) and MSTW8 PDFs (dotted).

The NLO k-factor is obtained from the ratio between the NLO cross-section and the LO cross-section. Figure 5.3a shows the NLO k-factor as a function of the P_T cut applied on c-quark jets. Very small dependence can be seen. Using the CTEQ6L1 PDF set, the k-factor value is 1.52. The uncertainty on the obtained k-factor is estimated from the factorisation normalisation scale dependence of the k-factor, which is evaluated by scanning the factorisation normalisation from 1/4 to 8 times of the nominal value. Figure 5.3b shows the obtained scale factor for different PDF sets as a function of the factorisation normalisation scale. This resulted in 24% cross-section uncertainties, but the actual value used in this analysis is 50%, the choice is taken in order to be consistent with other ATLAS groups, and because the cross-section uncertainties can later be constrained by data when the statistical analysis is applied.

5.4.2 Top Quark MC Samples

For the generation of SM $t\bar{t}$ events, the MC@NLO generator v3.41 [91] and the CTEQ6.6 [92] parton distribution function were used. The parton shower and the underlying event were added using HERWIG v6.510 [77] and JIMMY [88] generators. HERWIG and JIMMY were tuned to ATLAS data by the AUET1 tune. The $t\bar{t}$ cross-section is normalised to the approximate NNLO prediction value of 164.6 pb.

Single top-quark production samples were generated with ACERMC v.3.7 [93] and PYTHIA v.6.4.23 [76]. The t-channel exchange of a virtual W boson has a predicted production cross-section of 64.6 pb, while associated production of an on-shell W boson and a top quark (Wt-channel), has a predicted production cross-section of 15.7 pb. As for the $t\bar{t}$ MC sample, the MC@NLO generator is used to generate single top-quark production through the s-channel, the predicted production cross-section of 4.6 pb. For these

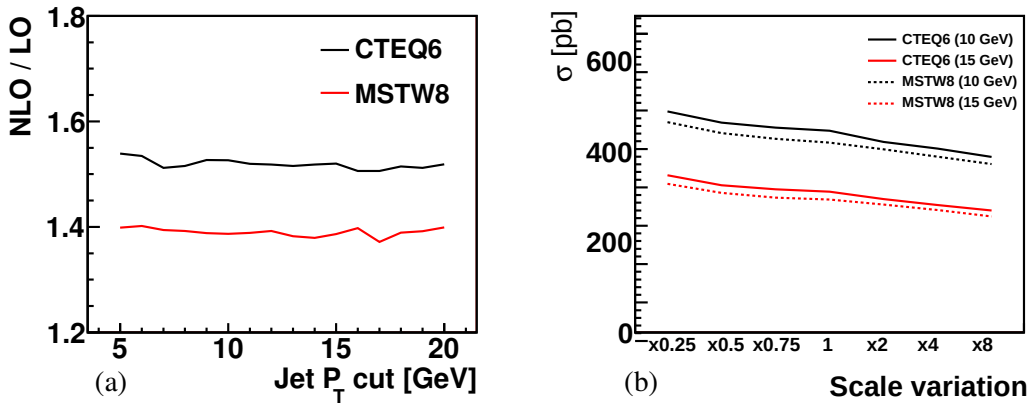

Figure 5.3: a) Wc k-factor with respect to the P_T of the c quark and b) scale dependence using the MCFM built-in functionality.

	σ [pb]	Generator
$Z \to \ell\ell$ + 0 parton	835	ALPGEN+HERWIG
$Z \to \ell\ell$ + 1 partons	168	ALPGEN+HERWIG
$Z \to \ell\ell$ + 2 partons	51	ALPGEN+HERWIG
$Z \to \ell\ell$ + 3 partons	14	ALPGEN+HERWIG
$Z \to \ell\ell$ + 4 partons	4	ALPGEN+HERWIG
$Z \to \ell\ell$ + 5 partons	1	ALPGEN+HERWIG
$W \to \ell\nu$ + 0 parton	8,300	ALPGEN+HERWIG
$W \to \ell\nu$ + 1 partons	1,600	ALPGEN+HERWIG
$W \to \ell\nu$ + 2 partons	460	ALPGEN+HERWIG
$W \to \ell\nu$ + 3 partons	120	ALPGEN+HERWIG
$W \to \ell\nu$ + 4 partons	31	ALPGEN+HERWIG
$W \to \ell\nu$ + 5 partons	8	ALPGEN+HERWIG
$W \to \ell\nu + b\bar{b}$ + 0 parton	57	ALPGEN+HERWIG
$W \to \ell\nu + b\bar{b}$ + 1 partons	43	ALPGEN+HERWIG
$W \to \ell\nu + b\bar{b}$ + 2 partons	21	ALPGEN+HERWIG
$W \to \ell\nu + b\bar{b}$ + 3 partons	8	ALPGEN+HERWIG
$W \to \ell\nu + c\bar{c}$ + 0 parton	153	ALPGEN+HERWIG
$W \to \ell\nu + c\bar{c}$ + 1 partons	126	ALPGEN+HERWIG
$W \to \ell\nu + c\bar{c}$ + 2 partons	62	ALPGEN+HERWIG
$W \to \ell\nu + c\bar{c}$ + 3 partons	20	ALPGEN+HERWIG
$W \to \ell\nu + c$ + 0 parton	980	ALPGEN+HERWIG
$W \to \ell\nu + c$ + 1 partons	312	ALPGEN+HERWIG
$W \to \ell\nu + c$ + 2 partons	77	ALPGEN+HERWIG
$W \to \ell\nu + c$ + 3 partons	17	ALPGEN+HERWIG
$W \to \ell\nu + c$ + 4 partons	4	ALPGEN+HERWIG

Table 5.2: W+n parton MC samples used in the analysis presented in this thesis. These values are the predicted cross sections multiplied by the branching fractions of the leptonic decays of W/Z.

processes the theoretical uncertainties are 8% for $t\bar{t}$ production and 10% for single top-quark production. Table 5.3 contains the cross-section values for the production of the top quark via SM processes.

	σ [pb]	Generator
Wt all decays	15.7	ACERMC+PYTHIA
t-channel (lepton+quarks)	21.3	ACERMC+PYTHIA
s-channel (lepton+quarks)	1.4	MC@NLO+HERWIG
$t\bar{t}$ (lepton+quarks)	89.0	MC@NLO+HERWIG

Table 5.3: Top quark MC samples with the corresponding cross-sections used through out this thesis. For the t-channel, s-channel and $t\bar{t}$ sample, the cross-section values are the predicted values multiplied by the branching fractions of the leptonic decay of W bosons.

5.4.3 Diboson MC Samples

Diboson MC samples (WW, WZ and ZZ) were produced using HERWIG [77]. The samples are produced considering only events with at least one lepton with P_T >10 GeV and $|\eta| < 2.8$. The production cross-sections [89] as predicted by theory are listed in Table 5.4 and have an uncertainty of around 5%. The cross-section values used through out this thesis are the predicted values multiplied by the branching fraction of the leptonic decays of the W/Z boson multiplied by the probability to have a lepton with P_T >10 GeV and $|\eta| < 2.8$.

	σ [pb]	Generator
WW	17.5	HERWIG
WZ	5.5	HERWIG
ZZ	1.3	HERWIG

Table 5.4: Diboson MC samples used in the analysis presented in this thesis with their predicted cross-sections.

5.4.4 Cross-section Uncertainties

The W+n parton and Z+n parton cross-section uncertainties are estimated by the Berends-Giele scaling [94, 95] using the cross-section ratio between the $W(Z) + n + 1$ parton and the $W(Z) + n$ parton, $\frac{\sigma(W(Z)+n+1)}{\sigma(W(Z)+n)}$. The cross-section ratio $\frac{\sigma(W(Z)+n+1)}{\sigma(W(Z)+n)}$ is estimated to have an uncertainty of ±24%. An uncertainty of ±4% is considered for the $W(Z)$+0 parton, which results in 24.3% for $W(Z)$+1 parton. The relative uncertainties on the heavy flavour contributions (HF) are 50% for $Wb\bar{b}$, $Wc\bar{c}$ and Wc+n parton contributions. The HF fraction uncertainty is treated as uncorrelated with the cross-section uncertainty. This allows them to be added in quadrature resulting in 56% scale uncertainty for the W+HF samples. The SM top quark production cross-section uncertainties are taken as 8%, while the cross-section uncertainty of diboson samples is around 5%. Since the diboson samples are treated together with Z+n parton as one background, the same uncertainty (24.3%) is applied on the diboson samples. Table 5.5 summarises the cross-section uncertainties considered in this analysis.

MC samples	Uncertainty(%)
W+light quarks	24
Z+n parton	24
Wc, $Wc\bar{c}$, $Wb\bar{b}$+n parton	56
Single top-quark	8
$t\bar{t}$	10
Diboson	24

Table 5.5: The cross-section uncertainties considered in this analysis.

5.5 Detector Simulation

After the full physics process simulation is done, and the long-lived particles are produced by the MC generators, the response of the detector to the interaction between the final particles and the detector material is simulated. The response of all sub-components of the detector, including resolution effects, inherent inefficiencies in the detector, and the interaction of the particles passing through passive material has to be taken into account in the simulation. Once this is done, the MC event has a data format identical to the one gained from collision data. This allows reconstruction algorithms to work exactly the same way on measured and simulated events.

GEANT4 [96, 97] is a general toolkit for the simulation of the passage of particles through matter. It is used in order to model the tracking volume of the ATLAS detector. This includes all potential interactions of the final-state particles with the detector material, including showering to secondary or tertiary particles, decay products and charge deposition as they travel through the detector. When the charged particles reaches the calorimeter, it has to be showered into many secondary particles. The modelling of all these multiple interactions in the ATLAS detector, which has very high granularity and complexity is a very time consuming procedure (several minutes per event).

The full ATLAS detector simulation consists of the following steps [78].

- All ATLAS sub-detectors are simulated starting from inside to the outside producing hits as an output format. The calorimeter simulation is very detailed in each component and it takes most of the CPU time. Many procedures were investigated and applied in order to reduce the CPU run time and to reduce the memory consumption.

- Hits are transformed into electrical pulses or digits in the digitisation step. A digit is produced when the voltage or current on a particular readout channel rises above a pre-configured threshold within a particular time window. At the digitisation step, the pile-up is simulated as an overlay of several predefined events to save CPU time during simulation and the detector electronic noise is added as well. At this stage the simulation output format is similar to the collision data detector output, except for the presence of the so-called truth information in the simulation which contains the generator information of the particles. The detector output is called the raw data output (RDO) format.

- The same algorithms are applied on the digitised simulation and collision data events to produce particle collections. The particle properties are defined using various reconstruction and clustering algorithms. Often there are many reconstruction algorithms for the same particle types. The output formats are the event summary data format (ESD), the analysis object data format (AOD) or the derived physics data format (DPD).

The ATLAS detector geometry used for the full detector simulation is stored in databases containing the information describing the physical construction and conditions data. The volume dimensions, positions, rotations, element and material properties including densities are stored in the ATLAS geometry database. The magnetic field map is linked to the geometry database. The ATLAS conditions database contains all the information needed to simulate a single data-taking run of the real detector e.g. dead channels and temperatures. The MC10B MC production campaign used the ATLAS official software (Athena), which has release numbers to define the settings used. The used releases for the different steps in the simulation are:

- AtlasProduction 15.6.11.1 - 15.6.13.X for the event generation;
- AtlasProduction 15.6.12.9 - 15.6.13.X for the GEANT4 simulation;
- AtlasProduction 16.6.4.2 - 16.6.3.X for digitisation and reconstruction.

The conditions used are:

- GEANT4 simulation: OFLCOND-SDR-BS7T-02;
- digitisation and reconstruction: OFLCOND-SDR-BS7T-04-13.

5.6 Pile-up Correction

The MC simulation samples which are used in the analysis are generated assuming three bunch trains with 225 ns separation. Within a bunch-train there are 36 proton bunches with 50 ns bunch spacing. The pile-up events were simulated during the digitisation process assuming Poisson distribution for the average number of proton-proton interactions (μ), where the μ in the MC simulation varies from 3 to 20 to describe the various conditions of LHC luminosity. Figure 5.4a shows two distributions of the μ values used in the MC simulation in 2011. MC10A was used for the first MC production campaign, while MC10B was used when all MC samples were reproduced. The μ value in collision data is estimated by the use of integrated luminosity measured in a short period of time called a luminosity block and the total inelastic cross-section for proton-proton collision, $\sigma_{\text{total}} = 71.5$ mb^{-1}. Then

$$\mu = \frac{L_{\text{int}} \times \sigma_{\text{total}}}{N_{\text{bunches}} \times f}, \tag{5.2}$$

where L_{int} is the integrated luminosity of a luminosity block, N_{bunches} is the number of colliding bunches and f is the revolution frequency. Figure 5.4b shows the μ distribution used in the ATLAS data analysed in this thesis.

Since the μ estimated value for the LHC differs from the value used in the MC simulation, all MC events have to be re-weighted to get better description of the data. This is done by the so-called pile-up re-weighting which is discussed again in Chapter 7.

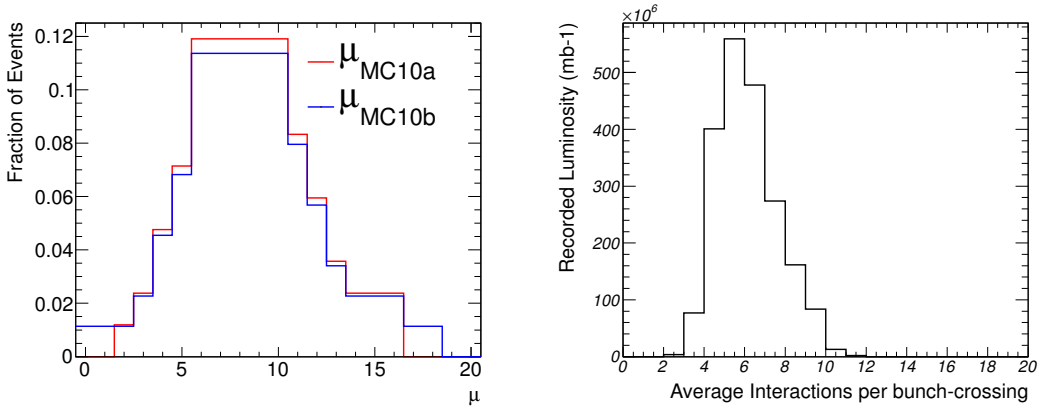

(a) (b)

Figure 5.4: Average number of interactions per bunch crossing (μ) used in a) the MC production and b) obtained in the observed events.

Chapter 6

Particle Reconstruction

The object of the experiment is to determine the particles created in the proton-proton collisions by identifying their decay products. Each subsystem of the ATLAS detector has a key role to play in particle reconstruction and identification. The particles which can be primarily identified and reconstructed are: electrons, photons, muons, τ leptons and hadronic jets which originated from quarks or gluons. Particles which leave no detectable signature in the detector are inferred using energy and momentum conservation, through the calculation of missing transverse momentum $\not{E}_T$. The reconstruction of these particles and calculation of their quantities relies on the more basic observables of tracks left in the inner detector by charged particles and clusters of energy deposits in the calorimeters.

6.1 Basic Quantities

The particle reconstruction begins from well identified tracks left by charged particles in the inner detector (ID) and cluster energy deposits in the calorimeters. Particles such as τ leptons and b-quark jets are identified using more complex information, like the flight distance between the place of the primary proton-proton interaction and the position of the decay.

6.1.1 Track Reconstruction

Charged particles coming from proton-proton collisions follow helical trajectories in the inner detector, because of the magnetic field. Every track is parametrised by $(d_0, z_0, \phi_0, \theta, q/p)$, where d_0 and z_0 are the transverse and longitudinal impact parameters, respectively. The impact parameter is defined as the closest distance to the nominal interaction point. ϕ_0 and θ are the track azimuthal and polar angles, respectively. They are defined at the point of the closest approach to the origin; the point is defined as the perigee. The ratio q/p is the inverse of the particle momentum multiplied by its charge.

Tracks are reconstructed within the inner detector acceptance range $|\eta| < 2.5$, using the inside-out reconstruction algorithm [98]. The track reconstruction begins with silicon clusters deduced from raw hits. Then, three-dimensional space-points are formed from these clusters. Pixel clusters are converted directly into space-points, while SCT clusters from either side of a module are associated to form a single SCT space-point. In track reconstruction, a hit refers to a measurement that has been associated to a track. A hole is an expected measurement given the track trajectory that has not been assigned to the track. Holes can result from material interactions, silicon inefficiency or problems within the pattern recognition. Inactive modules are excluded from the definition of holes [99].

The inside-out sequence is followed by an outside-in sequence that runs on the remaining hits after those hits already used in tracks have been removed. The algorithm starts from the TRT hits and the track is extrapolated to the silicon detector. A second inside-out sequence with less stringent pattern recognition requirement is executed after the outside-in tracking. It aims to construct tracks with $P_T <$ 0.5 GeV and is therefore referred to as low P_T tracking.

The resolution of a track parameter X can be expressed as a function of the track P_T given by:

$$\sigma_X = \sigma_X(\infty)(1 \oplus \frac{P_X}{P_T}), \tag{6.1}$$

where $\sigma_X(\infty)$ is the asymptotic resolution expected at infinite momentum and P_X is a constant representing the value of P_T, for which the intrinsic and multiple-scattering terms are equal for the parameter X under consideration [74].

6.1.2 Cluster Reconstruction in the Calorimeter

Calorimeter clusters are built from energy deposits in the calorimeter cells. There are two clustering algorithms [100]:

- Sliding window clustering algorithm. It builds fixed size clusters from selected seeds, which is fast and useful for objects with a well defined energy deposition pattern, such as electromagnetic showers from electrons and photons (see Section 6.2);

- The topological clustering algorithm. It is more used for hadron reconstruction such as hadronic jets, since hadronic showers have a more varied energy response. It starts by collecting the nearest neighbours around seed cells [101] with a large signal to total noise ratio, i.e. $|E_{\text{cell}}| > 4\sigma$ cell, where σ is the sum of the pile-up and electronic noise. These neighbouring cells are collected independently of the magnitude of their own signal. If the absolute value of their signal significance is above a secondary seed threshold, such that $|E_{\text{cell}}| > 2\sigma$ cell, they are considered as secondary seeds and their direct neighbours are also collected. Finally, all surrounding cells above $|E_{\text{cell}}| > 2\sigma$ threshold are added if no more secondary seeds are among the direct neighbours. This is called the 4/2/0 approach. To prevent overlap of the particle deposits, the clusters are then split between local maxima by a splitting algorithm [102].

6.1.3 Vertex Reconstruction

A vertex is defined as the position where several tracks cross. This can be the interaction point (primary vertex) of the proton-proton collision or the position where long-lived particles such as τ leptons or B hadrons decay (secondary vertex). Good performance of the vertex reconstruction is necessary to identify these long-lived particles and to reduce the non-collision background. This is specially true in case of pile-up, where many collisions occur in the same bunch crossing. The reconstruction of the interaction vertex is based on the reconstruction of charged-particle tracks in the ID.

The vertex reconstruction algorithms [103] work in either an iterative or adaptive mode. In the iterative mode, first a vertex finding is executed where tracks are associated to a vertex, then the vertex if found by looking for the global maximum in the distribution of z coordinates of the tracks, which is computed at the point of closest approach to the beam spot centre. In the adaptive vertex fitter algorithm, a χ^2 fitting technique is used, where the track association to the vertex is done dynamically at the time of the vertex fit, where all vertex candidates compete for the same track. If a track is incompatible with the vertex with more than 7σ, then it is used as a seed for another vertex, this procedure is repeated until no track is left in the event.

The reconstruction of all vertices is followed by the vertex fitting procedure. This is done to reconstruct the position of the primary vertex and its covariance matrix, recalculate the parameters of the incident tracks using the vertex constraint and provide a measure of the goodness of the fit. In addition,

the χ^2 of the refit of the track parameters with the knowledge of the reconstructed vertex is a criterion of track to vertex compatibility.

There are three types of vertices: primary vertices which come from a primary interaction point where the proton-proton collision occurred, pile-up vertices coming from the extra proton-proton collisions and finally secondary vertices which come from hadron and τ-lepton decays.

6.2 Electron Reconstruction

Electrons used in this analysis are reconstructed in the central region of the detector, $|\eta| < 2.5$. The standard electron reconstruction algorithm [104] is used. It starts from cell clusters in the EM calorimeter determined by the sliding window algorithm, which are then associated with reconstructed tracks with P_T >0.5 GeV from the inner detector.

The electron reconstruction starts with the selection of cluster seeds formed by the sliding window algorithm [100], which only takes into account clusters with an energy deposit of more than 2.5 GeV. The seed clusters have a size of 3×5 cells in the middle layer of the calorimeter, where one cell corresponds to $\Delta\eta \times \Delta\phi = 0.025\times0.025$. An electron is reconstructed if one or more tracks from the inner detector are matched to the seed cluster. The η and ϕ coordinates are compared to the corresponding coordinates of the seed cluster. If the difference in ΔR is below a certain threshold, the track is matched to the cluster. For cases with more than one track matched to the cluster, the track with the smallest ΔR is taken. To account for this effect, the $\Delta\phi$ requirement in the track-matching procedure is loosened on the direction in which the extrapolated track bends. After the matching procedure, the EM cluster is recomputed. For the barrel region a sliding window of 3×7 cells is used, while in the end-caps the cluster size is 5×5 in middle layer cell units. The preliminary 3×5 seed cluster is chosen as a subset of the final EM cluster size. In order to obtain the right energy of the electron, several corrections are applied to the final clusters. For the four-momentum of the electron, the energy measurement of the cluster and the η and ϕ coordinates of the track are used. If the track has less than 4 silicon hits, the direction of the electron is also determined from the cluster. The transverse energy is defined by

$$E_T = \frac{E}{\cosh(\eta)}. \tag{6.2}$$

The largest background to the isolated electrons is coming from hadronic jets that pass the electron reconstruction algorithms; these are referred to as fake electrons. In order to reduce the multijet background, a set of rectangular cuts based on calorimetry and tracking information are applied as described in [105]. These cuts are described by the *isEm* variable, which is optimised to provide three levels of selections: *loose*, *medium*, and *tight*. Each level applies stronger cuts than the previous one, to further reduce the multijet background.

The loose electron selection is based on shower shape variables from the second sampling layer of the EM calorimeter, along with hadronic leakage information. The hadronic leakage is defined as the ratio of the E_T reconstructed in the first layer of the hadronic calorimeter in a window of $\Delta\eta\times\Delta\phi = 0.2\times0.2$ to the E_T reconstructed in the EM calorimeter.[1] In addition to the criteria applied to select loose electrons, medium electrons require energy deposits in the strip layer of the EM calorimeter, higher track quality and a better match between the reconstructed track and the energy deposit cluster in the calorimeter.

The tight electron requirements are optimised to exploit the full potential of electron identification with the purpose of specifically rejecting charged hadrons, by using the ratio between the measured

[1] Electrons may deposit a small amount of energy in the hadronic calorimeter, typically less than 2%, either due to their low energy or because of the presence of the cryostat wall for energetic electrons.

cluster energy and track momentum (E/p), and the fraction of high-threshold hits in the TRT. Background electrons from photon conversions are removed by requiring the presence of a hit on the track in the pixel vertexing layer and rejecting candidates with a matching conversion vertex. They also comprise tighter track-matching cuts and impact parameter cuts. For robustness, cut choices and thresholds are based on the level of understanding of the detector performance.

6.3 Jet Reconstruction

The ATLAS calorimeters have very high granularity and several samplings in depth over $|\eta| < 3.2$. The forward calorimeters, which cover the region $3.2 < |\eta| < 4.9$, provide sufficient granularity to reconstruct jets with small polar angles with reasonable accuracy and efficiency. The *topoclusters* described in Section 6.1.2 are used as inputs to the jet finding algorithm, the anti-k_T algorithm [106].

The anti-k_T algorithm constructs, for each input object (energy cluster or particle track) i, two quantities: the distance measure between two objects (d_{ij}), and the similar distance between the object and the beam d_{iB}. d_{ij} and d_{iB} are calculated as follows [101]:

$$\begin{aligned} d_{ij} &= \min(P_{T,i}^{-2}, P_{T,j}^{-2}) \frac{(\Delta R)_{ij}^2}{R^2} \\ d_{iB} &= P_{T,i}^{-2}, \end{aligned} \tag{6.3}$$

where

$$(\Delta R)_{ij}^2 = (y_i - y_j)^2 + (\phi_i - \phi_j)^2 , \tag{6.4}$$

$P_{T,i}^{-2}$ is the transverse momentum of object i with respect to the beam direction, ϕ_i and y_i are its azimuthal angle and rapidity, respectively. The variable R is a resolution parameter which sets the relative distance at which jets are resolved from each other as compared to the beam. Jets used in this analysis are reconstructed with $R = 0.4$, thus the jet reconstruction algorithm is called *AntiKt4TopoJets*.

The algorithm takes the list of all the d_{ij} and d_{iB} values,

- if the smallest entry is a d_{ij}, objects i and j are combined and the list is updated;
- if the smallest entry is a d_{iB}, this object is considered a final jet and is removed from the list.

In a very small fraction of events which are caused by coherent noise bursts in the electromagnetic calorimeter, jets might be incorrectly reconstructed from a few noisy cells [107]. These jets are characterised by cells with bad calorimeter reconstruction quality and with large reconstructed energy, causing large fractions of jet energy in only the electromagnetic calorimeter (f_{EM}). The calorimeter quality is a measure of the difference in the sampling of the measured pulse and the reference pulse shape that is used to reconstruct the cell energy. In order to deal with jets that have a large portion of their energy accounted for by coherent noise, the variable f_{quality} is defined, which is the fraction of jet energy from bad-quality calorimeter cells. Bad quality jets in the electromagnetic calorimeter are defined if $|f_{\mathrm{quality}}| > 0.8$ and $f_{\mathrm{EM}} > 0.95$.

The reconstructed jets are calibrated to the energy scale measured by the electromagnetic calorimeter. This is done using a Monte Carlo based correction factor, which on average brings the measured jet P_T to the particle level in the simulations. It is done using the jet response $R(P_T, \eta)$, which is a function of the jet transverse momentum, P_T, and jet pseudo-rapidity, η, where $R(P_T, \eta)$ is defined as follows:

$$R(P_T, \eta) = P_T^{\mathrm{jet}} / P_T^{\mathrm{MC\ truth}} , \tag{6.5}$$

where $P_T^{\text{MC truth}}$ is the jet P_T from the MC generator and P_T^{jet} is the jet P_T after the jet energy calibration. The calibrated jet energy is then given by

$$P_T^{\text{jet,calib}} = \frac{P_T^{\text{jet,EM}}}{R(P_T, \eta)} \,. \tag{6.6}$$

6.4 b-quark Jet Identification

One of the most important signatures of top quark events is the existence of a b-quark jet. These are identified and used to reduce the background and to increase the purity of the selected signal samples. b-quark jet identification is possible because of the properties of B hadrons which are produced in b-quark hadronisation: B hadrons have a relatively long lifetime $\sim 10^{-12}$ s, which results in long flight path length (L$\sim$ 3 mm); when the B hadron decays, it creates a secondary vertex with measurable impact parameter and relatively high mass. In addition, B hadrons decay into leptons; however, this property is not used in the algorithms described below.

The *JetFitterComNN* [108] algorithm, which is a combination of the *IP3D* and *JetFitter* algorithms, is used for b-tagging in this analysis. The *IP3D* tagger uses a likelihood ratio technique to distinguish b-quark jets from light-quark jets. The signed impact parameter significance and longitudinal impact parameter significance of the track associated to a jet are compared to MC distributions for b- and light-quark jet hypotheses. *JetFitter* uses a Kalman filter to find the position of the b and the c vertices to give an approximate flight path for the different hadrons. Discrimination between b-, c- and light-quark jets is done with a likelihood using the flight-length significance of the vertices and additional variables such as the invariant mass of tracks associated with a vertex. The combined tagger *JetFitterComNN* uses an artificial neural network to combine the outputs of both taggers in addition to variables describing the topology of the hadron decay chain. The neural network is trained with MC simulated samples.

The available working points (the threshold to identify a jet as a b-quark jet) for identifying b-quark jets from the b-tagging performance group correspond to 60% b-tagging efficiency or more. But, since the dominant background in this analysis is Wc+n partons, a working point with lower b-quark jet tagging efficiency and high light-quark jet rejection[2] serves better for having a high signal to background ratio. An additional working point at 2.4 is chosen to identify the b-quark jet. It has smaller b-tagging efficiency than 60%, it is approximately 56%, but with much higher light-quark jet rejection around 520. These values are derived from $t\bar{t}$ MC simulations using jets reconstructed by the *AntiKt4TopoJets* algorithm. Figure 6.1 shows the expected number of events after applying all event selections (see Chapter 7) for the signal and the background processes as a function of the possible working points. The horizontal lines represent the expected number of events using *SV0*[3] b-tagging algorithm at 50% b-tagging efficiency, while the dashed vertical line represents the default *JetFitterComNN* working point at 2 which is delivered by the b-tagging performance group, and the solid vertical line represents the new working point at 2.4. This plot shows the big improvement in the Wc+n partons rejection by moving from 2 to 2.4 working point, while the drop in the FCNC signal acceptance is very small.

[2] The tagging efficiency is defined as the fraction of true b-quark jets tagged by the b-tagging algorithm. The mis-tagging rate is the fraction of light-quark jets identified as b-quark jets by the b-tagging algorithm, the light-quark jets rejection is just the inverse of mis-tagging rate.

[3] SV0 is a simpler algorithm, which uses the secondary vertex information to identify b-quark jets.

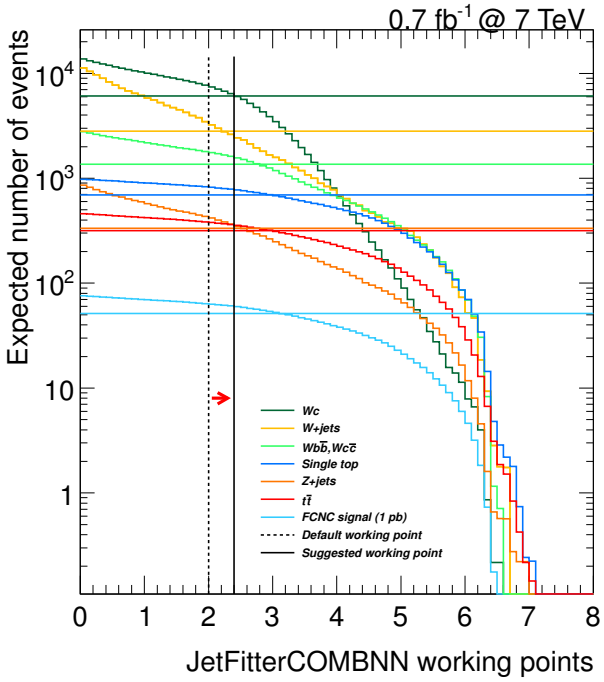

Figure 6.1: Number of expected events for various backgrounds for different working points of the JetFitterComNN. The horizontal lines correspond to the expected number of events for the 50% b-tagging efficiency working point of the SV0 algorithm.

6.5 Muon Reconstruction

The muon objects used in this analysis are combined muons, which are reconstructed by matching *standalone* muons constructed by the muon spectrometer and muon tracks built using the ID information [109].

Standalone muons are reconstructed using the Muonboy [110] construction algorithm. The muon construction starts by building track segments by a straight line fit performed on 4 to 8 RPC and TGC hits in the muon stations that overlap with the region of activities around hits with a size of $\Delta\eta \times \Delta\phi = 0.4 \times 0.4$. These track segments are used in a global track fit as described in Section 6.1, where the resulting tracks are fitted using the drift time measurements. The reconstructed muon tracks are then extrapolated to the beam-pipe where the primary interaction occurred. This track extrapolation helps to reduce the muon momentum mis-measurement caused by the energy loss in the detector material in front of the muon spectrometer. The muon electric charge and momentum are measured using the bend in the muon track trajectory due the the effect of the magnetic field produced by the magnetic toroids, where the possible measured momentum varies between 3 GeV and 3 TeV covering a range of $|\eta| \leq 2.7$.

To combine the *standalone* muons with muon tracks built using the ID information, the Staco reconstruction algorithm is used [110]. Here, pairs of tracks from the ID and muon spectrometer are combined if they are very close in η and ϕ. If there is more than one possible combination, a χ^2 fit is performed to chose the best combination. The combined muon has more precisely measured momentum, in particular when the muon has a low P_T, while the η coverage is reduced from $|\eta| \leq 2.7$ to $|\eta| \leq 2.5$ because of the ID covered region.

6.6 Missing Transverse Energy

Many physics channels have one or more neutrinos in the final-state. Neutrinos have an extremely small probability of interaction with the detector material.[4] The energy and momentum carried by neutrinos are not measured directly in the detector, but they can be calculated by using the energy and momentum conservation laws.

A good measurement of the missing energy (E^{miss} or $\not{E}$) is required in the search of new physics, since neutrinos or other undetectable particles (predicted by extensions to SM theories) are predicted to exist in final-state products. Also an accurate E^{miss} measurement is important for reducing the multijet background and as well as the the accurate reconstruction the top-quark events, when the W boson coming from the top quark decays to a lepton and a neutrino ($t \to Wb \to lvb$). At LHC, due to the composite nature of protons, the initial momenta of the colliding partons along the beam axis are unknown, which makes the calculation of the total energy available at the interaction impossible. However, the initial momentum transverse to the beam axis is approximately zero, so the missing momentum in the $x-y$ plane can be calculated. So the missing momentum in the transverse plane to the beam axis (E_T^{miss} or $\not{E}_T$) is the quantity of choice.

The $\not{E}_T$ reconstruction is based on the energy deposited in each calorimeter cell calibrated to an associated reconstructed particle and an estimate of energy lost by particles in the cryostat. An additional correction is needed for muons which do not deposit much energy in the calorimeters. The total $\not{E}_T$ is the sum of all these contributions, and the x and y components are calculated from the direction of $\not{E}_T$ with respect to the beam-line.

$$\not{E}_T = \sqrt{\not{E}_x^2 + \not{E}_y^2}, \tag{6.7}$$

$$\not{E}_{x,y} = \not{E}_{x,y}^{\text{Calo}} + \not{E}_{x,y}^{\text{Cryo}} + \not{E}_{x,y}^{\text{Muon}}, \tag{6.8}$$

where

$$\begin{aligned} \not{E}_{x,y}^{\text{Calo}} &= -\sum_{\text{TopoCells}} E_{x,y}, \\ \not{E}_{x,y}^{\text{Cryo}} &= -\sum_{\text{Cryo}} E_{x,y}, \\ \not{E}_{x,y}^{\text{Muon}} &= -\sum_{\text{Muons}} E_{x,y}. \end{aligned} \tag{6.9}$$

To suppress noise effects, only the calorimeter cells that are associated to a *TopoCluster* contribute to $\not{E}_{x,y}^{\text{Calo}}$. Muons detected by both the inner detector and the muon spectrometer (combined muons) are considered, and the muon momentum measured only by the muon spectrometer is included in the $\not{E}_T$ calculation. This to ensure that energy lost by muons in the calorimeter is not double counted.

The final step in the $\not{E}_T$ calculation is the refined calibration of cells associated to objects, because of the identified objects are calibrated with better accuracy than the energy deposits. The identified objects that are associated to the $\not{E}_T$ calculation are: electrons, photons, muons, τ leptons and quark jets. If a cell belongs to more than one object, then the highest ranked object is only associated to it. Thus the components of the refined $\not{E}_T$ become

$$\not{E}_{x,y}^{\text{RefFinal}} = \not{E}_{x,y}^{\text{RefEle}} + \not{E}_{x,y}^{\text{RefGamma}} + \not{E}_{x,y}^{\text{RefTau}} + \not{E}_{x,y}^{\text{RefJets}} + \not{E}_{x,y}^{\text{RefMuon}} + \not{E}_{x,y}^{\text{Cellout}}, \tag{6.10}$$

[4] The reconstruction of missing transverse energy is well described in Reference [74].

where the Cellout term refers to *TopoCluster* cells that are not assigned to any object. Fake $\not\!\!E_T$ defined as the difference between reconstructed and true $\not\!\!E_T$, can be caused by many sources: dead cells in the calorimeter, electronic noise, particles escaping in the beam direction, errors in determining the interaction vertices. Muons with high P_T escaping outside the acceptance region of the detector and large losses of deposited energy in inactive materials can also cause a mis-measurement of the $\not\!\!E_T$, these two effects can effectively limit the $\not\!\!E_T$ reconstruction performance.

Chapter 7

Event Selection

In experiments, the goal is to obtain physics results with the lowest possible uncertainty. This can be done by understanding the performance of the detector, the reconstruction algorithms, and by maximising the signal-to-background ratio. The latter is performed by applying extra criteria to select the candidate events. After passing the event-filter (EF), the extra selection criteria are applied in three steps: first, general quality cuts are applied on data and MC samples to select the candidate events; second, objects such as electrons, muons and hadron jets are selected according to the quality they have; finally, events are selected according to the measurement that is going to be performed. The first and the second steps can be the same for all analyses looking for similar signatures, such as those done by the ATLAS top working group.

This chapter is divided into four sections: in the first section the general quality cuts are discussed, in the second section, electron, muon and hadron jet selections, in the third section, the final cuts are applied to select the FCNC candidate events according to their physics signature. In the last section the event yield and control plots are shown.

7.1 Pre-Selection

7.1.1 Data Event Selection

As mentioned in Chapter 4, the data used in this analysis were collected between 22.03.2011 and 22.08.2011, with a total integrated luminosity of 2.05 fb^{-1} at $\sqrt{s}$=7 TeV. The data has been divided into 6 periods, which the ATLAS status and the LHC parameters such as the luminosity and the number of proton bunches in between changed, which affected the expected number pile-up events. Table 7.1 shows the data periods with the integrated luminosity of each of them. In addition, Table 7.1 indicates the 3.7% uncertainty on luminosity measurement.

Period	L_{int} [pb^{-1}]
B-D	166 ± 6
E-H	870 ± 32
I	305 ± 11
J	212 ± 8
K	500 ± 19
Total	2052± 76

Table 7.1: Data periods considered in this analyses with their corresponding integrated luminosity.

Data events are selected if they have been recorded during the ATLAS good runs, where the proton beams were in good conditions and qualified for physics analyses, as well as all ATLAS sub-detectors

flagged as green. This check is done by comparing the event's run number and its luminosity block with a list containing all qualified runs.

Further requirements are applied on events to be selected: events have to be recorded by an EF trigger, which can be an electron or muon trigger. Table 7.2 shows the EF triggers used to select collision data events. If the event passes the electron trigger, it is considered as a good candidate to perform electron channel analysis, while events passing the muon trigger are considered for the muon channel.

Period	Electron trigger	Muon trigger
B-D	EF_e20_medium	EF_mu18
E-H	EF_e20_medium	EF_mu18
I	EF_e20_medium	EF_mu18
J	EF_e20_medium	EF_mu18_medium
K	EF_e22_medium	EF_mu18_medium

Table 7.2: Data periods considered in this analyses with the corresponding triggers.

The difference between EF_mu18 and EF_mu18_medium trigger in muon channel is the Level 1 requirement. Both EF_mu18 and EF_mu18_medium require a muon spectrometer track with at least 18 GeV of estimated transverse momentum, but the EF_mu18_medium item requires all three layers of the trigger system, whereas EF_mu18 requires only two.

EF_e20_medium is an EF trigger fired by a medium electron candidate with $P_T > 20$ GeV. A medium electron is identified using shower shape variables in the second electromagnetic calorimeter layer, hadronic leakage variables, and a track roughly matched to a cluster. In addition, first layer calorimeter shape cuts, track quality requirements and a tighter track-cluster matching are required for medium electron selection.

The LAr calorimeter may have some inefficiencies during the data acquisitions, mostly due to the isolated high-voltage (HV) system trips and electronic noise. These inefficiencies can partially be recovered later when the data is reprocessed. A collision data event with a LAr noise bursts are dealt with an event veto.

7.1.2 MC Event Selection

Preselection treatment is also applied on MC events. The MC samples have been simulated at the end of 2010 with the best guess of LHC parameters. The assumed bunch spacing is 225 ns, while the achieved value by LHC is 50 ns, which means that the pileup interactions are underestimated. In addition, the ATLAS LAr calorimeter electronic readout system suffered from a problem during the data taking from period E to period H. This was due to a failure in three front-end electronic boards (FEB), which cover a region of $0.64 < \phi < 0.74$ and $0 < \eta < 1.4$ affecting 870 pb^{-1} of data. This problem was not considered in the MC samples production, and this region has to be treated differently when it comes to data and MC comparisons, as explained later.

Since LHC and ATLAS performance changed over the time, a simple correction or weighting is not applicable. To solve this problem, there are two approaches: first, new MC simulations to consider all these problems and LHC upgrades. This approach is very time consuming and was discarded for the time being. Second, split the MC samples into sub-samples, where each sub-sample should describe a data period by using proper weights and scale factors. The second approach is technically implemented by drawing a uniform random number at the beginning with the range between 0 and 2052. The period is then chosen according to the recorded integrated luminosity.

In principle, the same trigger used to select the collision events should be used to select the simulated MC events, but since not all triggers are available in MC samples, it was decided to use the trigger which was used to describe the data period with the highest integrated luminosity. The trigger used to select events in the electron channel is `EF_e20_medium`, while `EF_mu18` trigger is used to select events for muon channel. Later, scale factors are used to compensate discrepancies in the acceptance between MC and collision data events.

Other quality cuts are applied to select events:

- only proton-proton collision data events are selected while events triggered by cosmic particles are rejected by requiring at least a primary or a pile-up vertex with at least 5 associated tracks;
- the event is rejected if there is a jet with $P_T > 20$ GeV identified as a bad jet using the jet quality criteria: where the bad jet is defined as a jet not associated to in-time real energy deposits in the calorimeters caused by different sources varies from hardware problems in the calorimeter, the LHC beam conditions, and the atmospheric muons producing showers;

Pile-up Re-weighting

Since the number of pile-up interactions in simulation is different from collision data, MC events are reweighted by using the average number of pile-up interactions, μ, as described in Section 5.6. By knowing the data period which the MC event should describe (as mentioned in the previous section), the average data μ value is compared to the μ value of the MC event, then an appropriate weight is applied to the MC event.

At this point, the MC event has two weights: the pile-up and the MC weight. The MC weight comes from the ME generators, which is 1 for almost of the MC generators used in this analysis, except the MC@NLO generator, where the event has a weight either 1 or -1. 13% of the events have a negative weight. The total number of available events (N_{total}) in a MC sample is given by the sum over the weights,

$$N_{\text{total}} = \sum_{\text{Events}} w_{\text{MC}} \times w_{\text{pile-up}} \,. \tag{7.1}$$

For MC processes, N_{total} and the corresponding cross-section, σ, are used to calculate a scale factor called lumi-weight, which is used later to get the expected number of events and to scale all histograms to the prediction. Equation 7.2 shows how the luminosity scale factor calculated from the N_{total} and σ.

$$\text{lumi-weight} = \frac{L_0 \times \sigma}{N_{\text{total}}} \,, \tag{7.2}$$

where L_0 is the target luminosity.

Heavy Favour Overlap Removal

In ALPGEN, there are cases where the same heavy flavour quark, b or c, final state arises in multiple samples [111, 112]. For example, an event with a Wc or WU (U = light quark) final state may be generated both in the Wc+n parton and $Wc + n$+1 parton samples. When combining multiple ALPGEN samples together, it is therefore necessary to veto certain classes of events in each of the samples to avoid double-counting. In case of b-quark production this double-counting can largely be avoided by choosing the $b\bar{b}$ phase space cuts identical to the MLM matching parameters: the matching of matrix element (ME) partons and jets from the parton shower (PS). However, in case the of c-quark jets, the

overlap will be larger since the W+n parton samples contain massless c-quarks in the ME. An alternative approach exploits the different strengths of the ME and the PS. The ME is better suited for large opening angles between the quarks, in contrast the PS describes the collinear gluon splitting much better. In this case one has to find matching procedure based on the opening angles between the two quarks or on a matching to reconstructed jets. In this procedure the removal criterion is based on the distance ΔR between two heavy flavour quarks (ΔR-based overlap removal). The matching distance was chosen to be the same as the cone size of the jet algorithm, i.e. $\Delta R < 0.4$.

7.2 Object Selection

After the preselection quality cuts, the four-vectors of all objects are identified. Then, selection criteria are applied to reduce the background. The selections are applied on objects in the following order: electron, jets, and then muons.

7.2.1 Electron Selection

The offline selection criteria are applied on electrons as follows:

- Electron passes tight definition.
- $P_T > 25$ GeV. The 25 GeV value is chosen to ensure high trigger efficiency.
- $|\eta_{\text{clus}}| < 2.47$, where η_{clus} indicates the electron cluster position in the electromagnetic calorimeter.
- A veto is placed on electrons in the calorimeter barrel-endcap overlap region, $1.37 < |\eta_{\text{clus}}| < 1.52$, where there is limited calorimeter instrumentation.
- Hadronic jets can deposit energy in the calorimeter which can fake electrons. Real electrons produced from the heavy flavour decays, together with photon pair production are the major backgrounds for electrons coming the W-boson decay. Since electrons from the W-boson decay are typically isolated from hadronic jet activity, isolation criteria are required. Electrons with the minimum calorimeter activity (calorimeter isolation) and only few tracks (track isolation) in an η-ϕ cone around the electron track are selected. The following cuts are applied:
  - the ratio between the electron transverse energy and its P_T within a cone size of ΔR=0.3 around the electron direction is less than 0.15, $E_T(\Delta R < 0.3)/P_T < 0.15$;
  - the ratio between the scalar sum of transverse momenta of all tracks inside ΔR=0.3 and electron P_T is less than 0.10, $P_T(\Delta R < 0.3)/P_T < 0.10$.
- Finally, if the event belongs to the period E-H, then the electron should not be in the region where the LAr problem is, this is checked by using the electron cluster variables (η_{clus},ϕ_{clus}).

7.2.2 Jet Selection

The jets used in this analysis are reconstructed using the anti-k_T algorithm [106] with a radius parameter $R = 0.4$, using *topoclusters* from the 4/2/0 clustering algorithm as inputs to the jet finding (*AntiKt4TopoJets*). The jet is then calibrated from the raw electromagnetic scale using a MC based correction factor, which on average brings the measured jet P_T to the particle level in the simulations.

Jets are considered if:

- they have transverse momentum, P_T greater than 25 GeV;
- they are in the central region of the detector, $|\eta| < 2.5$;
- the closest distance in ΔR between the jet and the closest selected electron has to be greater than 0.2 ($\Delta R > 0.2$), as the overlapping jets and the electrons are very likely to correspond the same physics object.

7.2.3 Muon Selection

Muons are considered if they pass the following criteria:

- A set of inner detector requirements are applied and the muon track quality must satisfy:
  - the muon track should have at least one hit in the pixel B-layer, if it expected a hit;
  - the number of hits in the pixel detector plus number of crossed dead pixel sensors should be greater than one;
  - the number of hits in the SCT detector plus number of crossed dead SCT sensors should be greater than or equal to six;
  - the number of muon track holes in both pixel and SCT detector (see Section 6.1.1) is less than three;
  - few TRT requirements are needed. In the region of $|\eta| < 1.9$, the number of hits in the TRT is ≥ 6, and the number of TRT hits that are classified as "outliers"[1] must be less than 90% of the total number of TRT hits on the track. The latter cut is also applied for the region of $|\eta| \geq 1.9$ if only the number of hits in the TRT is ≥ 6.
- They are reconstructed from both muon spectrometer hits and inner detector tracks (combined muons) and they are classified as tight muons.
- The transverse momentum of the muon is greater than 25 GeV.
- The absolute pseudo-rapidity is less than 2.5.
- To reject muons from the heavy flavour decay which are typically within hadronic jets, the muon is required to have minimal surrounding calorimeter and track activity. These muons are called isolated muons. The following cuts are applied:
  - The ratio between the muon transverse energy and its P_T within a cone size of ΔR=0.3 around the muon direction is less than 0.15; $E_T(\Delta R < 0.3)/P_T < 0.15$;
  - the ratio between the scalar sum of transverse momenta of all tracks inside ΔR=0.3 and muon P_T is less than 0.10, $P_T(\Delta R < 0.3)/P_T < 0.10$.

  where the E_T and P_T variables are defined as the transverse energy and scalar sum of transverse momenta of additional tracks inside a cone of size of $\Delta R = 0.3$, respectively.
- Additionally, a muon overlapping with a high P_T jet with ($P_T > 20$ GeV) in cone size of $\Delta R = 0.4$ is removed.

[1] An outlier hit is a hit in the TRT which is initially assigned to the track and not used in the track fit, because of the large uncertainty. This hit may be used for particle identification.

7.3 Final Event Selection

Once the event passes the preselection criteria and all good objects are selected, the final event selection is applied:

- Since the leptonic decay of the W boson is considered, the event should contain one and only one electron or muon for the electron or muon channels, respectively. This cut rejects events with no or with more than 1 lepton, such as multijet and Z+jets backgrounds, respectively. Events with an electron and a muon are rejected. This to reduce the $t\bar{t}$ when both top quarks decay to lepton plus jets and to ensure two statistically independent samples.

- Events with significant amount of $\not\!\!E_T$ are accepted: $\not\!\!E_T > 25$ GeV. This cut reduces the Z+jets background by 83% as well as the multijet background.

- Leptons in multijet events do not come from real W bosons. They typically have the characteristics of low $\not\!\!E_T$ and low transverse W boson mass ($m_T(W)$), where the $m_T(W)$ is defined as

$$m_T(W) = \sqrt{2P_T^{\text{lep}} \cdot \not\!\!E_T \left(1 - \cos(\Delta\phi(\overrightarrow{P}^{\text{lep}}, \overrightarrow{\not\!\!E_T})\right)}. \tag{7.3}$$

  To reduce the multijet background, an event is required to pass the triangular cut which is defined as $m_T(W) + \not\!\!E_T > 60$ GeV. This cut has an efficiency for the FCNC signal process of 95.4%, while the estimated efficiency for the multijet background is less than 8%.

- Events with exactly one jet with $P_T > 25$ GeV are accepted. This cut is good at reducing the background processes with two or more jets in the final state. This cut has an efficiency of 3% for $t\bar{t}$ events, 13% for W+jets processes and 22% for the single top-quark processes, while it has an efficiency of 55% for the FCNC signal processes.

  Since the requirement of b-quark jets is not yet applied, the set of events passed all the above mentioned cuts define the pretagged sample.

- Finally, the event is accepted if it has a b-quark jet identified by the *JetFitterComNN* b-tagging algorithm using the working point of 2.4. This cut is extremely good at reducing the background, for example: W+light jets background has an efficiency of 0.33%, Z+jets has an efficiency of 0.8%, this is higher than W+jets because Z+heavy flavour background are included in the sample, Wc+n parton background has an efficiency of 6%, while $t\bar{t}$, single top-quark and the FCNC signal have an efficiency around 40% each. The low cut efficiency of the top-quark samples is explained by:

  – b-tagging scale factors (see Section 7.5) are less than one, which lowers the cut efficiency from 57% to around 50%;

  – light-quark jet contamination in the top-quark samples, these light quark jets have very low tagging efficiency.

  The set of events passed all the above mentioned cuts define the b-tagged sample.

7.4 Multijet Background Estimation

The multijet background fraction is determined in the electron and muon channel, using a binned likelihood fit to the $\not\!\!E_T$ distribution. The multijet background shape is modelled using events with

jets constructed as electrons (electron-like jets) selected from jet-triggered collision data (jet-electron model) [113]. The kinematic shapes of the W+jets and other background processes are taken from MC simulation samples. The fit is performed after applying all selection criteria, but removing the $\not\!\!E_T$ selection criteria. Using the jet-electron model, the number of multijet background events in the region of $\not\!\!E_T > 25$ GeV is determined. As a cross-check, a binned likelihood fit is performed on less sensitive variables such as $m_T(W)$.

Table 7.3 provides the estimate of the multijet background in the electron and muon channel for the one jet bin in the pretagged and b-tagged samples.

	Pretagged events	b-tagged events
Electron	41691 ± 1013	796 ± 78
Muon	20216 ± 741	785 ± 77

Table 7.3: Estimate of the multijet background for the pretagged and b-tagged samples. The quoted numbers are the expected number of events in the signal region. The given uncertainties are the statistical uncertainties from the likelihood fit.

The fitted $\not\!\!E_T$ distributions for the pretagged and b-tagged samples for electrons and muons are shown in Figure 7.1. These distributions show the good descriptions of the data after performing the likelihood fit and a big confidence is built in the jet-electron model.

As systematic uncertainty, a very conservative approach is taken and 50% of the measured multijet background is considered, this can be later constrained when the statistical analysis is done.

7.5 Scale Factors

To get better agreement between observed and simulated distributions, events with electrons, muons and b-quark jets are scaled up and down using scale factors determined from the data itself [114].

Trigger, identification, and reconstruction scale factors for tight electrons have been measured with the data using W+jets and Z+jets samples and tag-and-probe methods [115]. The MC-to-data correction factors derived from these studies are provided in eight bins of η and six bins of P_T.

The muon identification efficiencies also have been measured from the Z-boson data samples and correction factors have been derived in 10 bins in η-ϕ space using a method described in [116]. The scale factor is around one for most bins with an uncertainty of around 4%.

To obtain better agreement between observed and simulated distributions, discrepancies coming from the use of b-tagging algorithm are reduced using correction factors applied on b-tagged MC samples only. The scale factors depend on whether the b-tagged jet is a true b-quark jet or a mis-tagged jet from a light quark. This needs the knowledge of the original quark which produces the jet (truth information). In addition, the scale factor has a dependency on the jet P_T, while its uncertainty has a dependency on the jet P_T as well as the jet η.

After applying all event selections and using all scale factors, each event has five weights. The total number of events surviving the event selection is the sum over all events including their weight as given in Equation 7.4 and 7.5. The pretagged sample is only corrected by the first four weights (b-tagging scale factors are not included). Since the electron and muon channels are statistically independent (an event can not be contained in both at the same time), either muon scales or electron scales are applied. The predicted number of events passing all cuts (n_{total}) for a given sample, is given by the sum over all event weights as given by

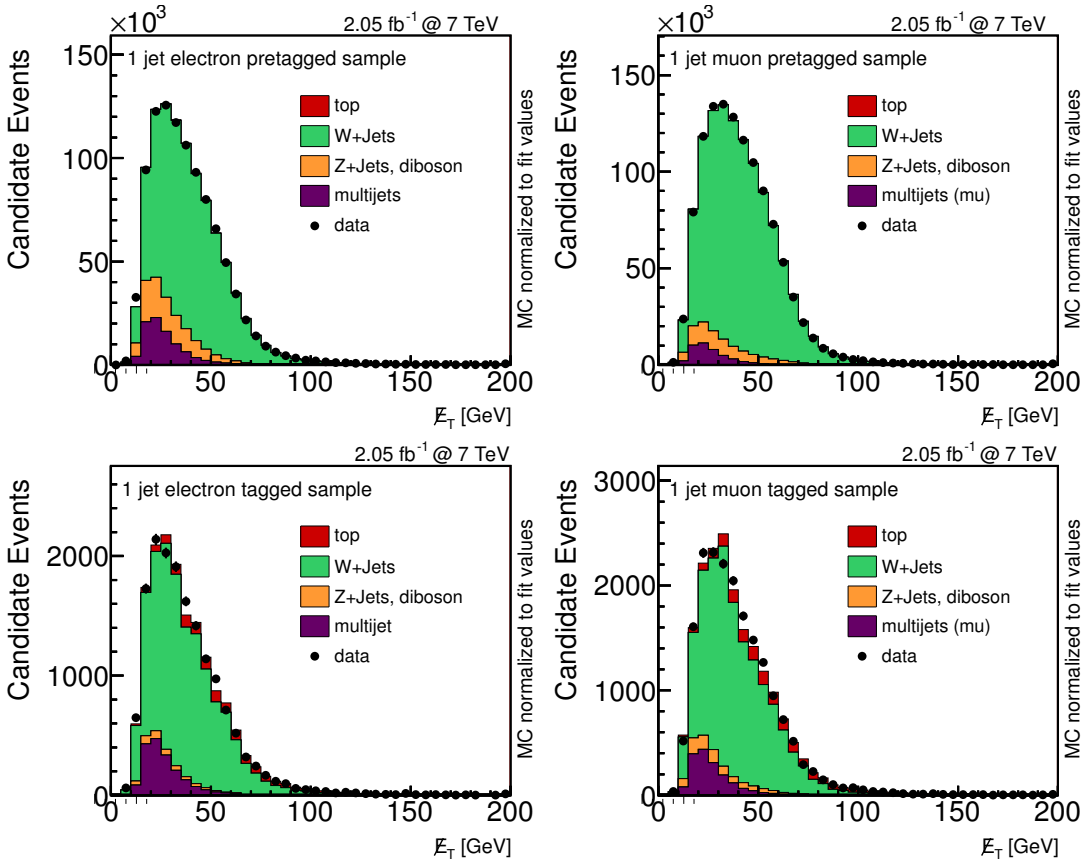

Figure 7.1: $\not\!\!E_T$ distribution for the W+1 jet pretagged and b-tagged data-sets. A binned likelihood fit is performed to determine the fraction of multijet events and W+1 jet in the sample.

$$n_{\text{total}} = \sum_{\text{Events}} w_{\text{MC}} \times w_{\text{pile-up}} \times w_{\text{electron}} \times w_{\text{btagging}} \,, \tag{7.4}$$

for the electron channel and

$$n_{\text{total}} = \sum_{\text{Events}} w_{\text{MC}} \times w_{\text{pile-up}} \times w_{\text{muon}} \times w_{\text{btagging}} \,, \tag{7.5}$$

for the muon channel.

7.6 Yield and Control Plots

The number of observed and expected background events for a luminosity of 2.05 fb^{-1} are listed in Table 7.4 for pretagged events and in Table 7.5 for b-tagged events. The number of expected signal events is given for an assumed cross-section of 1 pb. Apart from the multijet background, all event yields are calculated using the acceptance from MC samples normalised to the theoretical cross-sections given in Chapter 5. The uncertainties are statistical uncertainties and cross-section uncertainties as described in Chapter 5, and the multijet background uncertainty is 50% as given. The contribution of the statistical uncertainties is very small ~1% or less, since very large MC samples were generated. It can be easily seen that the dominant background after requiring the b-quark jet is the Wc+jets then W+light jets, and with less contribution coming from the $Wb\bar{b}$+jets and single top-quark backgrounds. Overall, the difference between the number of observed and predicted events is very small and covered by the uncertainties. With the big uncertainties and small expected signal, the analysis needs to be improved by using more available information such as the shape differences between the predicted and the observed distributions.

	Electron			Muon			Combined		
FCNC single top	117	±	1	134	±	1	252	±	1
SM single top	1680	±	170	1840	±	190	3500	±	400
$t\bar{t}$	800	±	80	860	±	90	1660	±	170
W+light jets	635300	±	152500	817990	±	196340	145300	±	348800
$Wb\bar{b}/Wc\bar{c}$+jets	23200	±	12700	28900	±	15900	52100	±	28600
Wc+jets	91400	±	50270	109670	±	60320	201100	±	110600
Z+jets/diboson	38810	±	9320	44200	±	10600	83000	±	19000
multijet	41700	±	20800	20220	±	10110	62000	±	31000
Total background	832800	±	162700	1023700	±	206500	1857000	±	369000
Observed	750358			948628			1698986		

Table 7.4: Number of observed data events and the expected number of background events for the pretagged samples. The numbers of expected events for the signal are assuming a production cross-section of 1 pb. The uncertainties given include the statistical uncertainty as well as the theoretical uncertainty on the cross-section and the uncertainty of the multijet background normalisation.

The kinematic distributions of the identified lepton, reconstructed jet, $\not{E}_T$ and $m_T(W)$ are shown in Figure 7.2 before requiring the b-quark jet. These distributions are normalised to the observed number of events in order to check if the W+light jet MC samples can model the observed data. The same distributions are also shown in Figure 7.3 for the b-tagged sample, where the b-quark jet is required.

	Electron			Muon			Combined		
FCNC single top	53	±	1	60	±	1	113	±	1
SM single top	700	±	70	760	±	80	1460	±	150
$t\bar{t}$	310	±	30	340	±	40	660	±	70
W+light jets	2100	±	500	2500	±	600	4700	±	1100
$Wb\bar{b}/Wc\bar{c}$+jets	1300	±	700	1500	±	800	2700	±	1500
Wc+jets	5480	±	3020	6600	±	3600	12100	±	6700
Z+jets/diboson	190	±	50	510	±	120	700	±	170
multijet	800	±	400	800	±	400	1600	±	800
Total background	10900	±	3170	13000	±	3800	24000	±	7000
Observed	11704			14519			26223		

Table 7.5: Number of observed data events in the FCNC single top-quark production analysis and the expected number of background events for the b-tagged samples. The numbers of expected events for the signal are assuming a production cross-section of 1 pb. The uncertainties given include the statistical uncertainty as well as the theoretical uncertainty on the cross-section and the uncertainty of the multijet background normalisation.

The hatched band indicates the statistical uncertainty from the simulated samples size and cross-section uncertainties as well as the multijet background normalisation uncertainty, see Table 5.4.4; these uncertainties are added in quadrature.

The same distributions separated for the electron and muon channel are shown in Appendix A. Overall, a very good agreement between the observed and predicted distributions is seen. No signal can be observed in these distributions and more information is needed to make conclusions. A complex analysis is described in the next chapter, where many variables are combined to produce a very powerful distribution to separate the signal from the background.

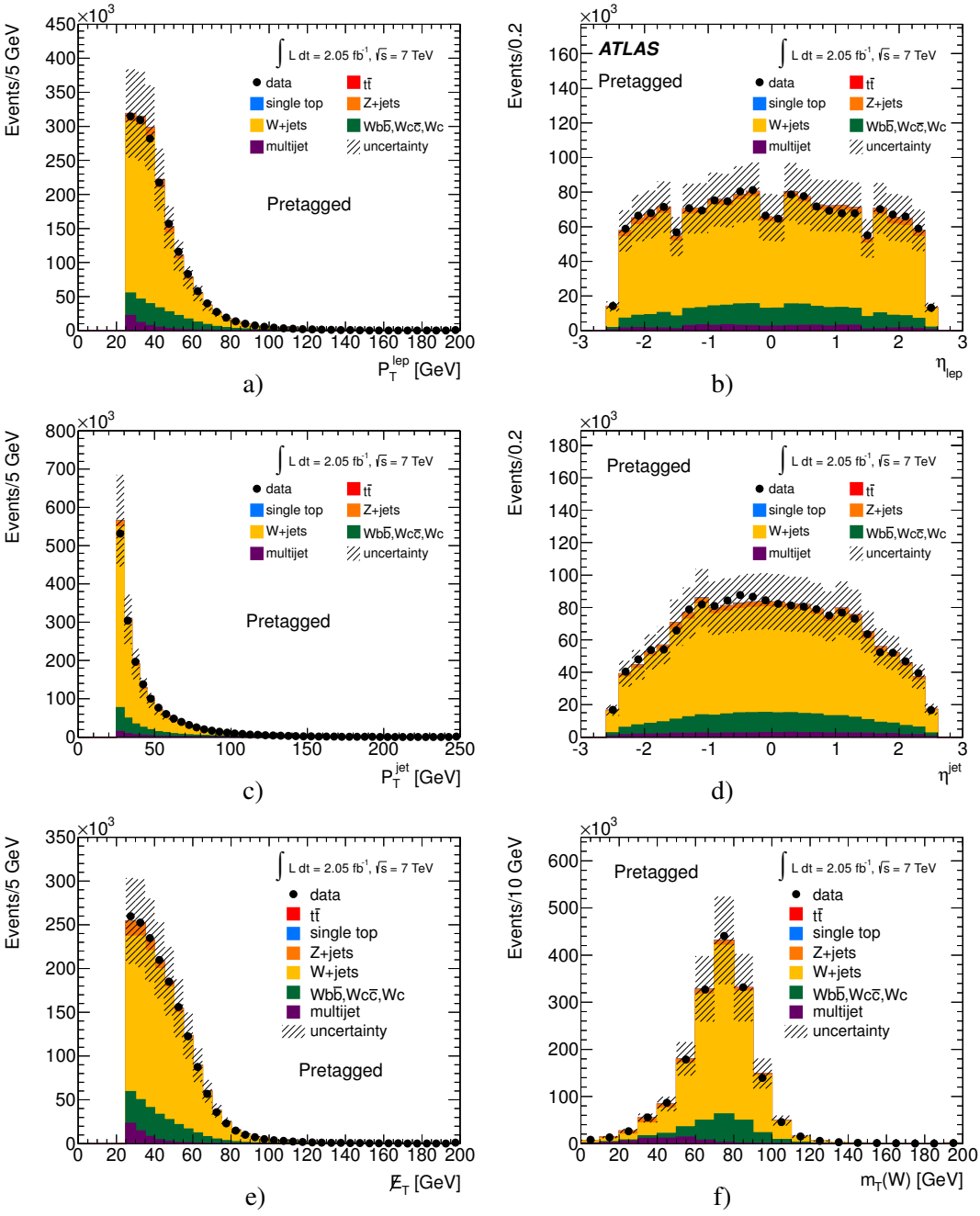

Figure 7.2: Kinematic distributions before *b*-tagging, normalised to the number of observed events, for the electron and muon channel combined: a) transverse momentum and b) pseudo-rapidity of the lepton, c) transverse momentum and d) pseudo-rapidity of the jet, e) missing transverse energy and f) transverse W-boson mass. The hatched band indicates the statistical uncertainty and the uncertainty on the background normalisation.

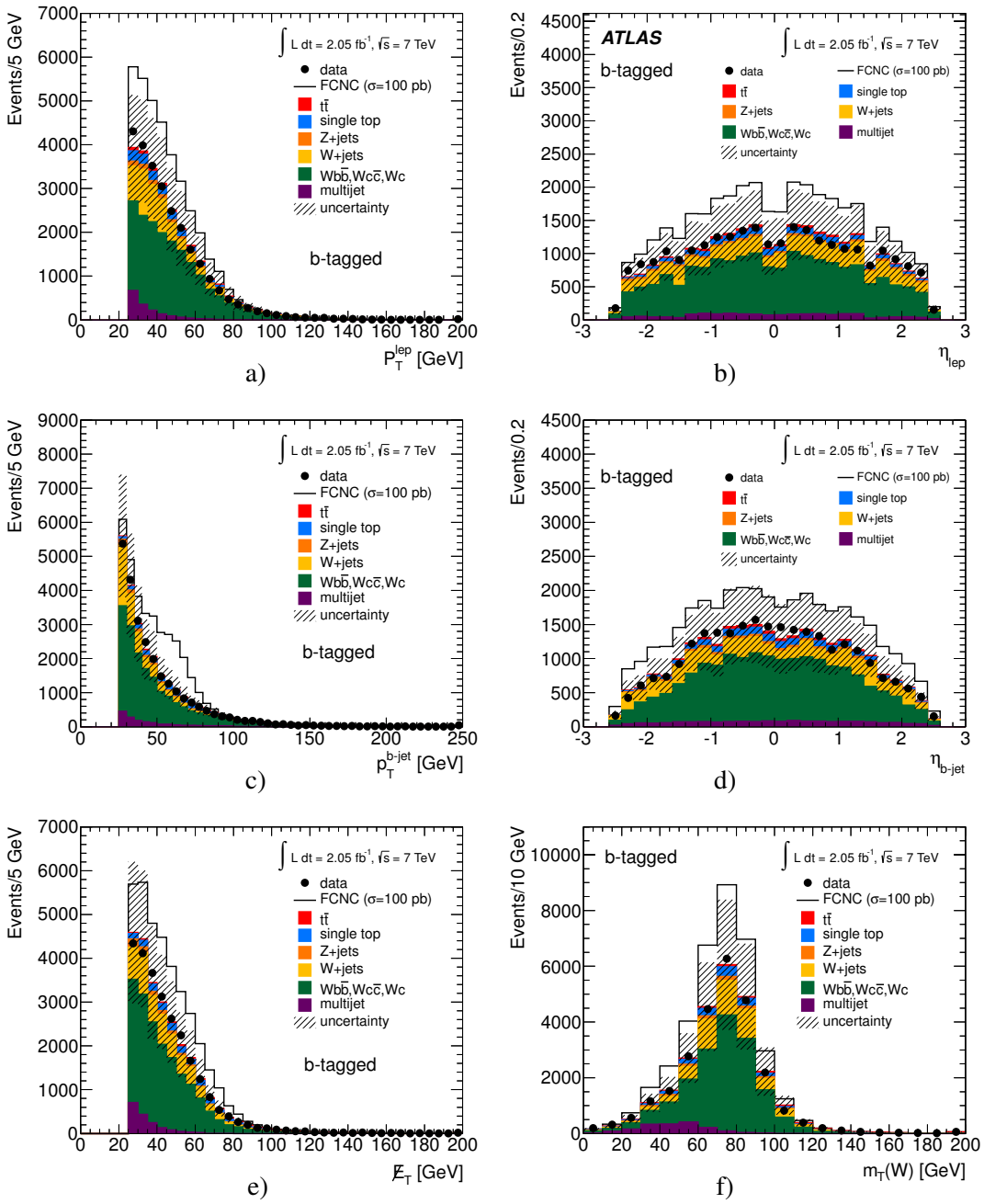

Figure 7.3: Kinematic distributions after *b*-tagging, normalised to the number of observed events, for the electron and muon channels combined: a) transverse momentum and b) pseudo-rapidity of the lepton, c) transverse momentum and d) pseudo-rapidity of the b-tagged jet, e) missing transverse energy and f) transverse W-boson mass. The signal contribution is shown stacked on top of the backgrounds, with a normalisation corresponding to a cross-section of 100 pb. The hatched band indicates the statistical uncertainty and the uncertainty on the background normalisation.

Chapter 8

Neural Networks

In the search for top-quark production through FCNC processes, a cut-and-count analysis is difficult and will give vey bad sensitivity, due to the large number of background events and the big uncertainties associated to them. Therefore, a multivariate analysis technique (MVA) is necessary. High performing algorithms, such as neural networks, are optimal for this task.

8.1 Introduction

The neural network (NN) which used in this analysis is three-layer feed-forward algorithm implemented in the NeuroBayes® package [13, 117].[1] The first layer of the neural network consists of one node for each input variable plus extra nodes. These extra nodes (bias nodes) have a constant value of 1, and are generally useful to help the NN to converge. The second layer consists of an arbitrary number of nodes usually equal to the number of nodes in the first layer. Finally, the third layer contains one node with a continuous output (O) between -1 and 1, where the output tends to -1 for background and +1 for signal. The performance of the neural network is improved by the implemented Bayesian regularisation techniques that can help to avoid the overtraining.[2]

The neural network output is calculated as follows,

$$O = S\left(\sum_{j=0}^{l} w_j \cdot S\left(\sum_{i=0}^{k} w_{ij} \cdot x_i + \mu_{0i}\right)\right), \tag{8.1}$$

where x_i is the input value of the variable i, and the indices k and l are the number of the nodes of the first and the second layer, respectively. w_{ij} is the weight of the connection between the node i of the first layer and node j of the second layer, μ_{0i} is the weight that connects the bias node with the nodes in the second layer.

$S(x)$ is the transfer function which gives the output value of each node. It is determined by a symmetric transformed sigmoid function as given by

$$S(x) = \frac{2}{1 + e^{-x}} - 1. \tag{8.2}$$

The sigmoid function transfers values from the interval of $[-\infty, +\infty]$ to the interval of $[-1, +1]$ as can be seen in Figure 8.1.

When the neural network is trained to classify events as signal or background events, the difference between the target value, +1 for the signal and -1 for the background, and neural network output is

[1] The discussion in Section 8.1 is relevant to the implementation of the neural network algorithm in the NeuroBayes® package. Other implementations differ in how they preprocess the variables, the transfer function and the error functions they minimise.

[2] In Reference [118] from page 49 to page 51, the neural network algorithm is nicely described.

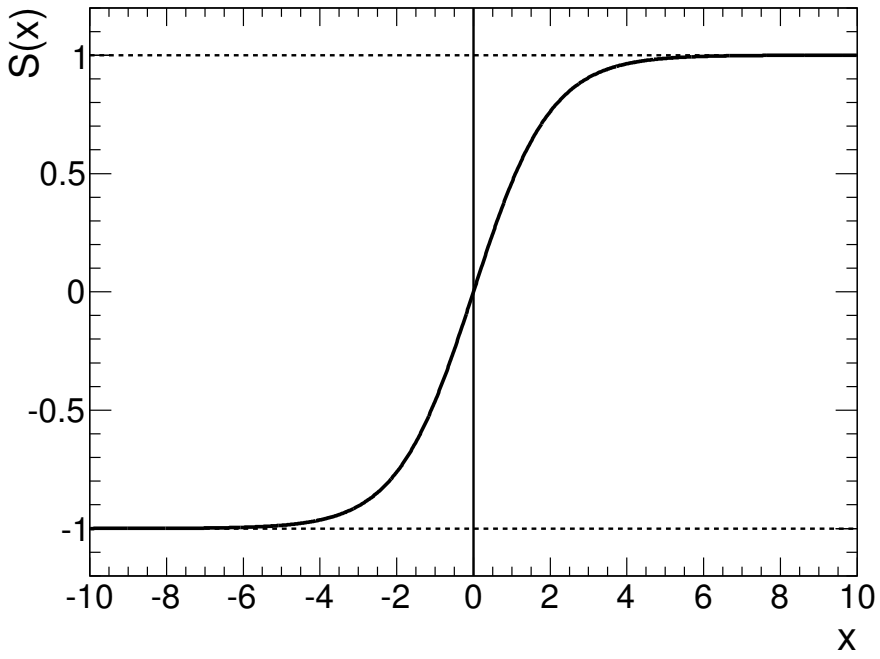

Figure 8.1: The sigmoid function $S(x)$ as given by Equation 8.2.

minimised. The numerically minimised function is the entropy loss function which is given as follows

$$E(w) = \sum_n \log(\frac{1}{2} \cdot (1 + T_n \cdot O_n + \varepsilon)), \tag{8.3}$$

where T_n is target value for the output node in event n, O_n is neural network output value as described before and ε is a regularisation constant added to avoid numerical problems when minimising the error loss function. It becomes zero after a few iterations.

8.1.1 Preprocessing of the Variables

As can be seen in Figure 8.1, the sigmoid function is sensitive to a small range around zero, and for very large ($x \to \infty$) or very small ($x \to -\infty$) values, a saturation is reached. Thus, it would be optimal to transform the input variables to be distributed between -1 and +1 before they are fed to the neural network. The variable transformation is done automatically by NeuroBayes® and it is helpful to reduce the effect of the extreme values in one variable which can completely saturate neurons and thus dominate the NN output. Using the inverse of the integrated χ^2 function, the transformed variables are then converted into Gaussian distributions, with mean equal to zero and width equal to one. This is to ensure that the inputs to the next layers are Gaussian distributed with mean zero and width one.

The preprocessed input variables are decorrelated by diagonalising their covariance matrix using Jacobi rotations; then by dividing the rotated input vectors by their square root of the corresponding eigenvalues which transforms the covariance matrix into a unit matrix. The preprocessing can deal with: continuous variables such as transverse momentum; and discreet variables such as the lepton charge.

After the correlation matrix is computed, one variable at the time is removed from the input set of variables and the correlation to the target is computed again. The variables are then sorted according to the loss of the correlation to target caused by their removal. The least significant variable is the variable causes the least loss of correlation to target and is removed from the list of input variables. The significance of this variable is calculated by the loss of the correlation caused by variable removal multiplied by $\sqrt{n}$, where n is the sample size. After removing the least significant variable, the $(n-1)$ correlation matrix is calculated and procedure is repeated and the significance is calculated for another variable. After the preprocessing is performed and the variables significance list is computed, the irrelevant variable can be removed from the training process which can be done automatically by applying a significance threshold on the variables used to train the NN.

8.2 Neural Network Training

To get an optimal result from the neural network training, it is necessary to consider all background processes. The relative contribution of a background process should be considered, which can be done by using the corresponding cross-sections. The samples used to train the NN are scaled in such a way that the FCNC single top-quark production process has the same number of events as the total considered background samples. The relative fractions of all considered background processes are computed by using their expected number of events after requiring a b-quark jet, as can be seen in Table 7.5.

The NN first layer consists of 12 nodes, one for each input variable used in the training, the extra node is the bias node. The second layer consists of 13 hidden nodes, and the third layer is built from 1 output node.

8.2.1 Input Variables

The input variables are chosen in an iterative process. First, many variables are used to train a preliminary NN. This means, that all input variables are preprocessed, as discussed in Section 8.1.1, and the respective correlations to the target are determined, providing a list of input variables ordered according to their importance. In a second step, the relevant variables with the biggest separation power are investigated by comparing data and MC distributions. Since the NN benefits from the correlation between the input variables, the correlation is also checked. The correlation between variables in MC events is compared with the correlation between variable in data.

The signal event signature is simple, and consists of only three particles in the final state. The input variables are limited and can be categorised as: simple variables measured directly in the detector; others which are reconstructed from the measured quantities and require the knowledge about the four-vectors (P) of the W boson and the top quark; and finally, variables describing the event shape.

The top quark is the heaviest elementary particle known, and it is much heavier than the W and Z bosons. As a consequence, the top quark decay products are very energetic and typically have higher momenta than the particles coming from W and Z boson decays. On the other hand, the top quark is predicted to be produced through FCNC processes without additional particles, this leads to extremely small top-quark transverse momentum ($P_T^{\text{top}} \sim 0$) compared to the top-quark transverse momenta produced via SM processes. This makes the top-quark P_T (P_T^{top}) and the P_T of all its decay products good variables to separate the signal from the W+jets, Z+jets backgrounds as well as from the SM top-quark backgrounds.

Figure 8.2a) shows the P_T distributions of the reconstructed top quarks from the FCNC and back-

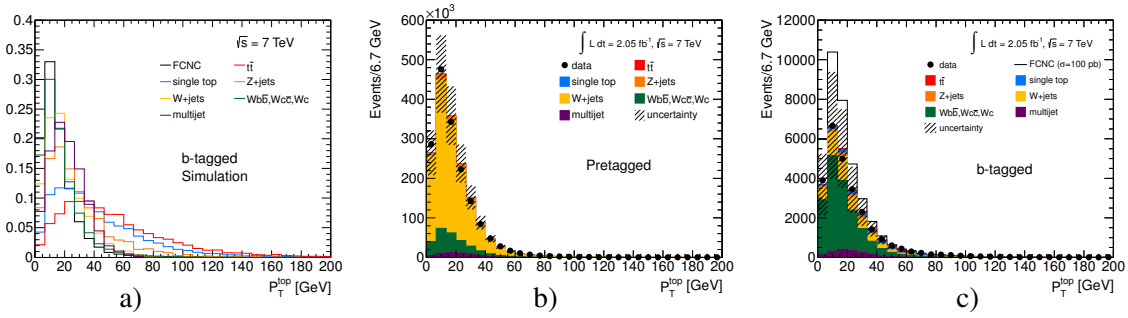

Figure 8.2: The reconstructed top-quark P_T distributions for the combined muon and electron channel: a) MC distributions for signal and background in the b-tagged sample normalised to unity. b) Data and MC distributions in the pretagged sample. c) Data and MC distributions in the b-tagged sample where the FCNC cross-section is assumed to be 100 pb for visibility. In b) and c) the MC distributions are normalised to the data. The hatched bands indicate the statistical and the background normalisation uncertainties added in quadrature.

ground processes,[3] these distributions are normalised to unity. It can be seen that the P_T of the FCNC top quark is smaller than the P_T of the top quarks produced via the SM processes, while the wide P_T^{top} distribution comes from the momentum conservation since the top quark can radiate gluons before it decays. Figure 8.2b) shows the reconstructed P_T^{top} distributions of the observed data and MC processes in pretagged samples, while and Figure 8.2c) show P_T^{top} distribution in b-tagged samples, where the FCNC top quark cross-section is assumed to be 100 pb to be visible and stacked on top of the background. The agreement between observed data and MC distributions is easily seen.

Since the FCNC single-top quark is produced with very small P_T, the W boson and the b-quark coming from its decay are back to back a large relative angle $\sim\pi$ [rad] in the x-y plane, while the decay products of the top quark produced via SM processes have smaller relative angles due to the higher top-quark momentum. Because the W boson coming from the top-quark decay has very high momentum, its decay products are highly boosted and have small relative angles, and are back-to-back in the x-y plane to the b-quark jet originated from the top-quark decay. In contrast, W or Z bosons from non-top-quark processes are produced with much smaller momenta, and thus their decay products have big relative angles compared to the decay products of the W boson coming from the top-quark decay. All relative angles between available particles in the event are explored to improve the performance of the NN.

More variables are investigated to reduce the background, for example the reconstructed top-quark mass (m_{top}), which is very good to help against the non-top-quark backgrounds. The FCNC processes are predicted to produce four times more single-top quarks than antitop quarks, see Table 5.1, whereas in SM single top-quark production and all other SM backgrounds this ratio is at most two. The lepton electric charges reflecting the top-quark charge are expected to have very good separation power against all SM backgrounds.

As described above, all possible variables such as momenta, relative angles, pseudo-rapidity, and particles masses, lepton electric charge are explored. The variables with highest separation power after including the correlation are chosen. All variables used to train the NN are required to describe well the data before and after requiring a b-quark jet. All chosen variables are described below.

[3] The reconstruction of the top-quark four-momentum from the observed objects will be discussed later in this chapter.

Simple Input variables

The lepton transverse momenta (P_T^{lep}), the b-quark jet transverse momentum ($P_T^{b\text{-jet}}$), the b-quark jet pseudo-rapidity ($\eta_{b\text{-jet}}$), the ΔR between the lepton and the b-quark jet (ΔR(lep,b-jet)) and the lepton electric charge are chosen to train the NN. The mass of the reconstructed b-quark jet ($M_{b\text{-jet}}$) is a very good at distinguishing between the true jet originated from a b-quark and mis-tagged jets which have lower mass. The shape distributions of the above listed variables are shown in Figure 8.3.

Top Quark Reconstruction

Variables such as m_{top} require the knowledge of the top-quark four-vector (P^{top}) and W-boson four-vector (P^W). P^{top} is reconstructed from the knowledge of b-quark jet four-vector ($P^{\text{b-jet}}$) and P^W, as shown in the following equation:

$$P^{\text{top}} = P^W + P^{\text{b-jet}}\,. \tag{8.4}$$

Because only the leptonic decay of the W boson is considered, the W-boson four-vector is the sum of the lepton and neutrino four-vectors (P^ν) as given by

$$P^W = P^{\text{lep}} + P^\nu. \tag{8.5}$$

The neutrino has extremely low probability to interact with the detector material and thus can not be detected directly. The amount of the transverse momentum carried by the neutrino is interpreted as missing transverse momentum, and can be reconstructed as described in Section 6.6. The missing part of the neutrino four-vector is the longitudinal component along the z-axis (P_z^ν), which can be obtained by using the mass constraint of the W boson

$$(P^W)^2 = (P^{\text{lep}} + P^\nu)^2 = M_W^2\,, \tag{8.6}$$

where the M_W is the W-boson mass, 80.398 GeV [19].

The solution of the quadratic equation given in Equation 8.6 in terms of the P_z^ν can be expressed as follows

$$P_z^\nu = \frac{\alpha \cdot P_z^{\text{lep}} \pm \sqrt{\alpha^2 - P_T^{\text{lep}} \cdot \not{E}_T}}{P_T^{\text{lep}}}\,, \tag{8.7}$$

where α is given by

$$\alpha = \frac{M_W^2}{2} + \overrightarrow{P_T}^{\text{lep}} \cdot \overrightarrow{\not{E}_T}\,. \tag{8.8}$$

When the quantity under the square root is positive ($\alpha^2 \geq P_T^{\text{lep}} \cdot \not{E}_T$), then there are two real solutions, and the smallest one in magnitude is taken, since the W boson is expected to be produced with small rapidity. For about 30% of the events, Equation 8.7 has imaginary solutions ($\alpha^2 < P_T^{\text{lep}} \cdot \not{E}_T$), which is interpreted as a mis-measurement of $\not{E}_T$. In this case, $m_T(W) > M_W$. Ignoring the square root in Equation 8.7 violates Equation 8.6, and the measured values of $\not{E}_T$, $\not{E}_x$ and $\not{E}_y$ can not be taken as the components of the neutrino momentum. If $m_T(W)$ is fixed to be $m_T(W) = M_W$, which corresponds to a vanishing of the square root in Equation 8.7, a quadratic dependence of $\not{E}_x$ on $\not{E}_y$ appears. Technically this is resolved by introducing a new scale factor β, which is defined by

$$\beta = \frac{M_W^2}{2 \cdot P_T^{\text{lep}} \cdot \not{E}_T - \overrightarrow{P_T}^{\text{lep}} \cdot \overrightarrow{\not{E}_T}}. \tag{8.9}$$

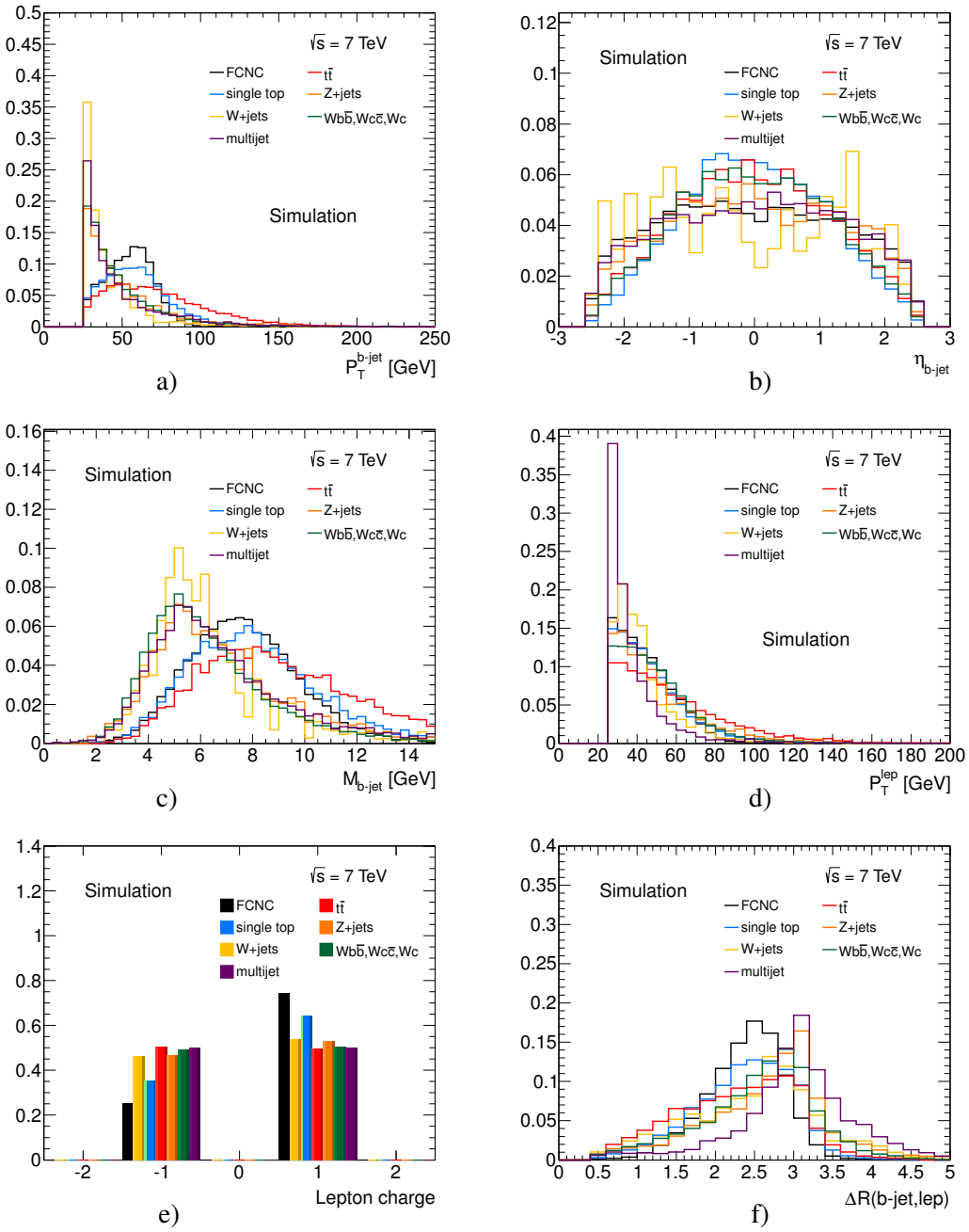

Figure 8.3: Kinematic distributions of the simple variables used to train the NN. These distributions are normalised to unity: a) is the transverse momentum of the b-quark jet $P_T^{b\text{-jet}}$ b) the pseudo-rapidity of the b-quark jet $\eta_{b\text{-jet}}$ c) the b-quark jet mass $M_{b\text{-jet}}$ d) the transverse momentum of the lepton P_T^{lep} e) the lepton electric charge and f) the ΔR between the lepton and the b-quark jet, ΔR(lep,b-jet). These distributions are for the b-tagged sample.

β is used to scale $\not{E}_x$, $\not{E}_y$ and $\not{E}_T$, and then α is recalculated as shown in Equation 8.8. Following that, P_z^ν is found by considering only the offset part of the Equation 8.7.

Figure 8.4a) and Figure 8.4b) shows the $m_T(W)$ distributions for the MC and the observed data before

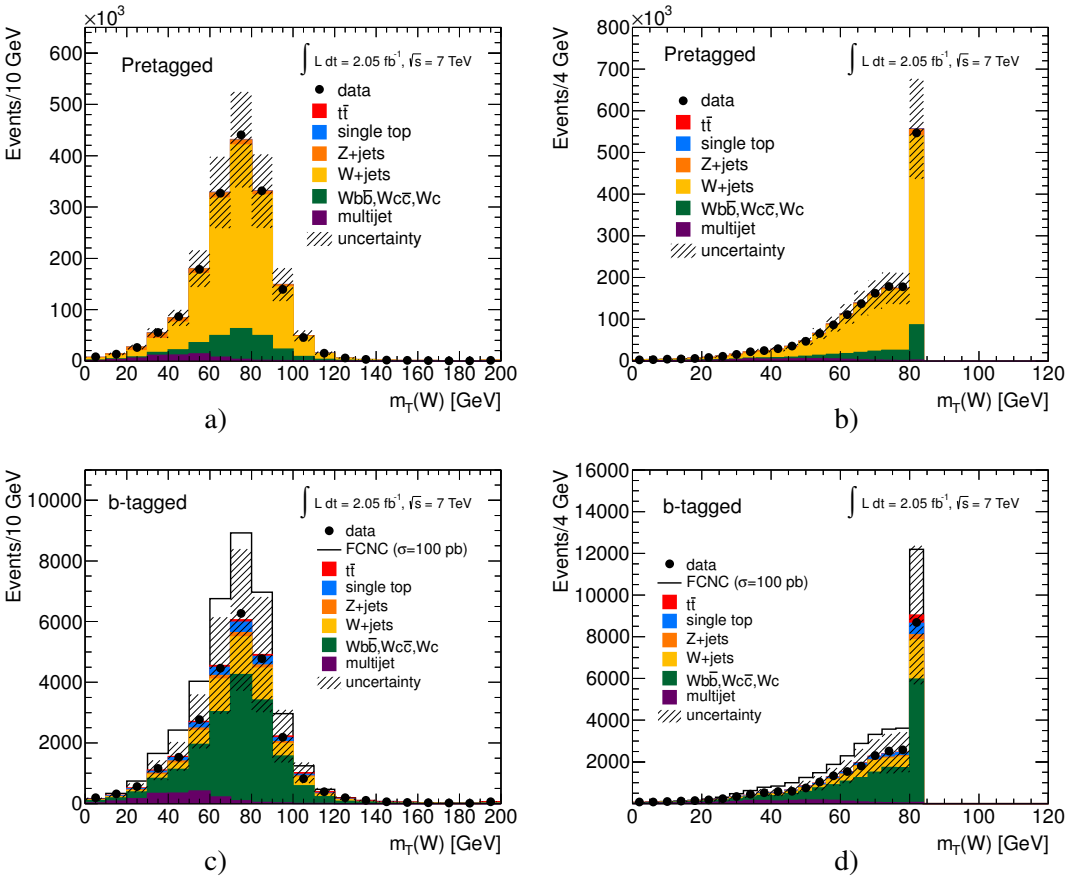

Figure 8.4: Distribution of the transverse mass of the W boson: a) in the pretagged before determining P_z^ν, b) in the pretagged after determining P_z^ν, c) in the b-tagged sample before determining P_z^ν, d) in the tagging after determining P_z^ν. MC distributions are normalised to data, the signal cross-section is assumed to be 100 pb. The hatched bands indicate the statistical and the background uncertainties added in quadrature.

and after determining the P_z^ν for the pretagged sample. It can be seen in Figure 8.4a) that $m_T(W)$ can be greater than M_W, while in Figure 8.4b) where the $m_T(W) \leq M_W$ constraint is applied and the β scale factor is introduced, a clear cut at $m_T(W) = M_W$ is seen. Figure 8.4c) and Figure 8.4d) shows the same distributions, but for the b-tagged samples, where the FCNC cross-section is assumed to be 100 pb and stacked on top of the background. The background distributions are scaled to the observed data, and the agreement between MC and data is demonstrated in pretagged and b-tagged samples.

By reconstructing the neutrino four-vector, the W-boson and top-quark four-vectors can be reconstructed as shown in Equation 8.5 and Equation 8.4, respectively.

More variables are investigated and chosen to be used to train the NN: the transverse momentum of the reconstructed W boson (P_T^W), the relative azimuthal angle $\Delta\phi$ and the ΔR between the reconstructed W boson and b-quark jet; $\Delta\phi(W, b\text{-jet})$ and $\Delta R(W, b\text{-jet})$, respectively. Two more variables are used as input variables, the top-quark mass and the W-boson helicity, which is defined as the cosine angle between the lepton in the W-boson rest frame and the W-boson direction in the top-quark rest frame. Figure 8.5

shows P_T^W, $\Delta\phi(W, b\text{-jet})$, $\Delta R(W, b\text{-jet})$, m_{top} and the W-boson helicity distributions; the distributions are normalised to unity.

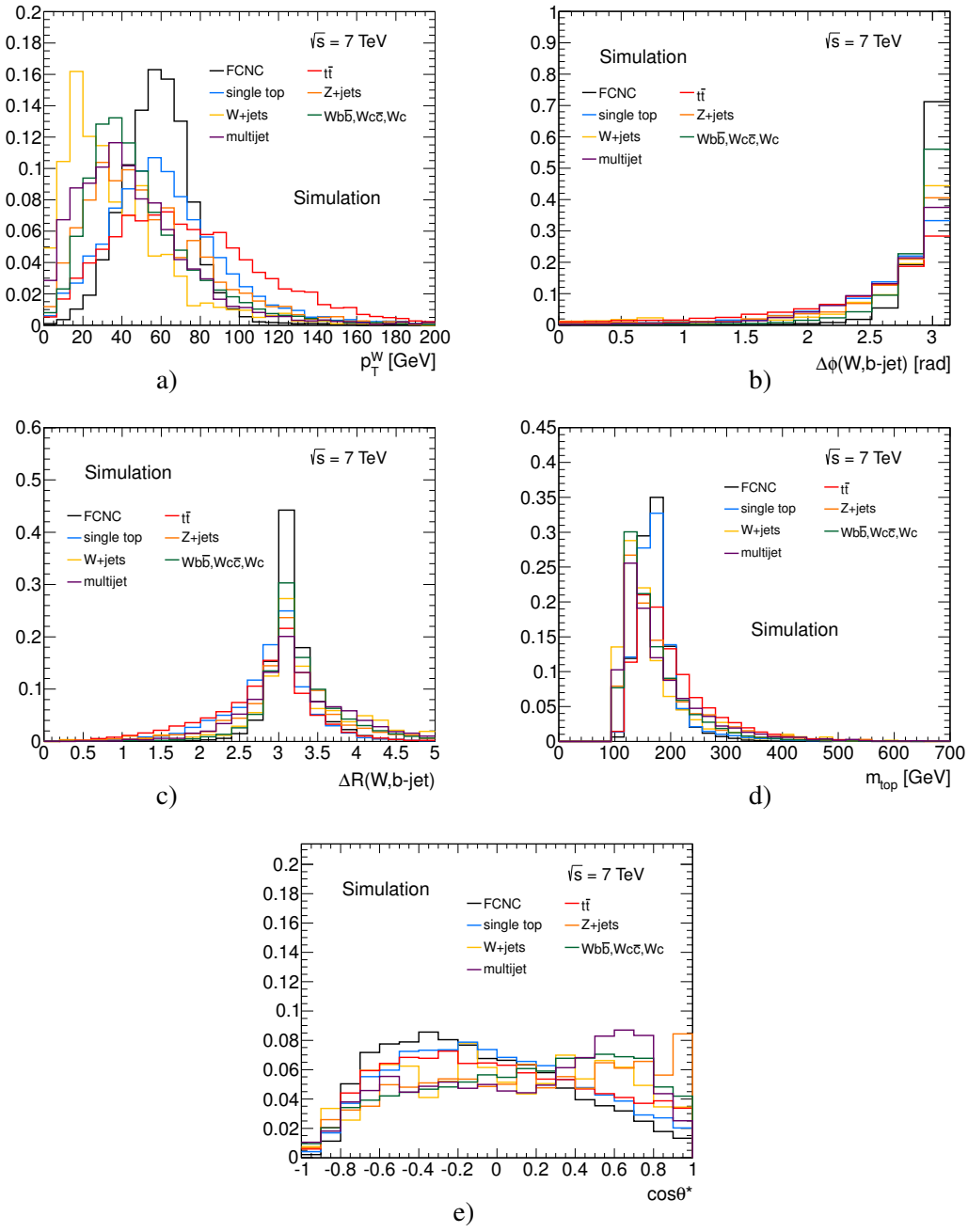

Figure 8.5: Shape distributions of the constructed variables used to train the NN. These distributions are normalised to unity. a) is the transverse momentum of the reconstructed W boson, P_T^W, b) the $\Delta\phi$ between the b-quark jet and the W boson, c) the ΔR between the b-quark jet and the W boson, d) the reconstructed top-quark mass, m_{top} and e) the W helicity.

The 11 variables used to train the NN are listed with their significance to the output in Table 8.1. As seen in the Table 8.1, the most important variable is the transverse momentum of the W boson, which

Variable	Significance (σ)
P_T^W	57
ΔR(lep,b-jet)	28
Lepton charge	22
m_{top}	20
$M_{b\text{-jet}}$	15
$\eta_{b\text{-jet}}$	12
$\Delta\phi(W, b\text{-jet})$	11
P_T^{lep}	12
$P_T^{b\text{-jet}}$	6.5
W-boson helicity	5.7
$\Delta R(W, b\text{-jet})$	5.0

Table 8.1: Variables used in the training of the neural network ordered by their importance.

is highly correlated to the top-quark mass and momentum, the ΔR between the b-quark jet and the W boson, and the lepton electric charge.

Figure 8.6a) shows the linear correlations between the input variables. The final configuration of the

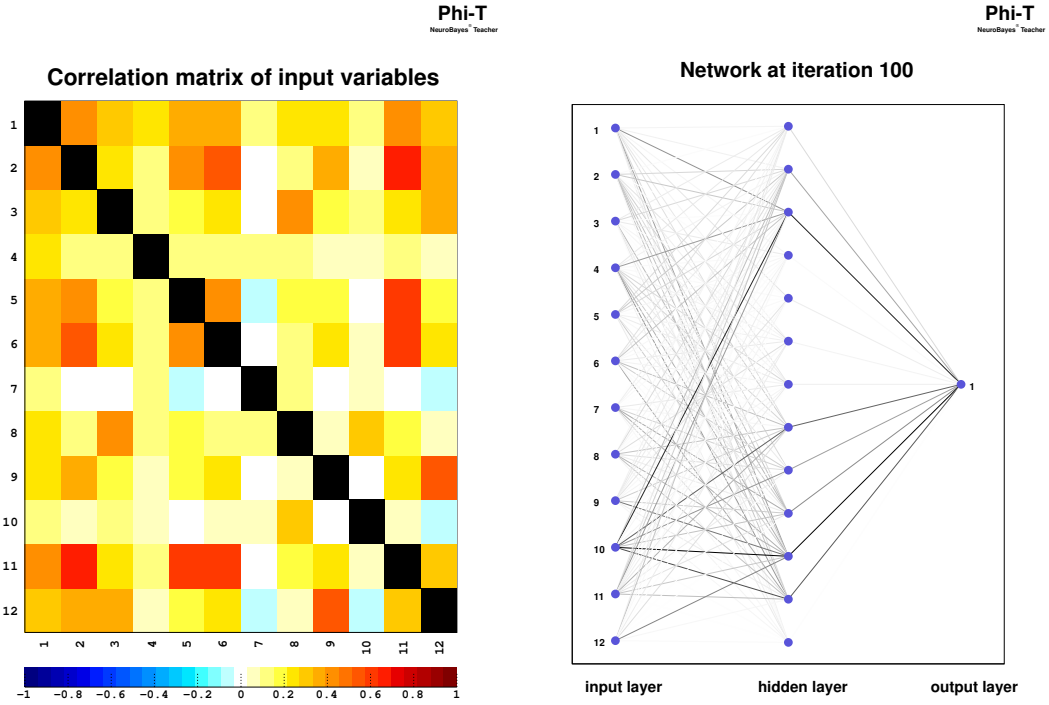

a) b)

Figure 8.6: a) Correlation matrix between the different input variables. b) Final network configuration. The width of the lines correspond to the weights between the nodes. Meaning of variables and numbers given in Table 8.2.

network is shown in Figure 8.6b). The width of the connections between the nodes corresponds to the weight between them. The labels in these plots is shown in Table 8.2.

No.	Variable	No.	Variable
1	Bias node	7	$\eta_{b\text{-jet}}$
2	P_T^W	8	W-boson helicity
3	ΔR(lep,b-jet)	9	$\Delta R(W, b\text{-jet})$
4	Lepton charge	10	P_T^{lep}
5	$M_{b\text{-jet}}$	11	$P_T^{b\text{-jet}}$
6	m_{top}	12	$\Delta\phi(W, b\text{-jet})$

Table 8.2: Numbering of the variables used in the training of the neural network.

Neural Network Overtraining Test

The MVA algorithms such as the NN sometimes due to the small sizes of training samples, suffer from learning the events kinematics by heart, which worsen the result and can lead to a bias if the network is applied to analyse the collision data. The overtraining in NeuroBayes is constantly checked during the training process; i.e. after each iteration, the entropy error function is recalculated and minimised. For this analysis, 80% of the MC events are used to train the NN, the other 20% of MC events are used for testing.[4] The values of the error function for training and test samples are shown in Figure 8.7. An

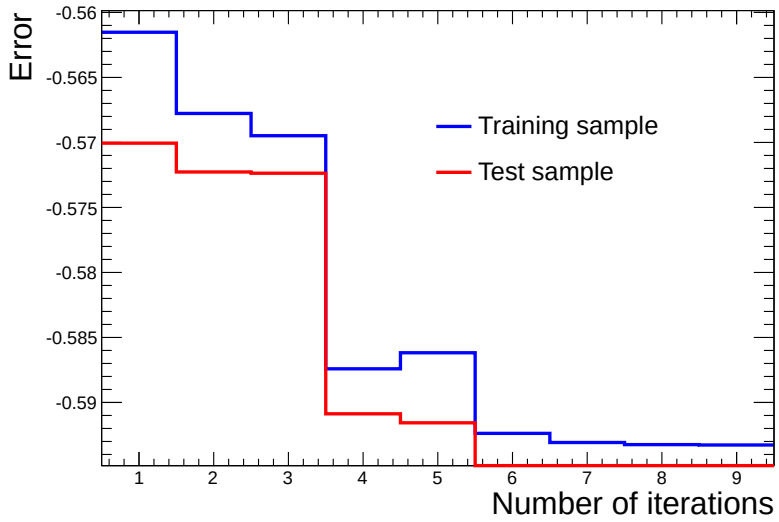

Figure 8.7: Entropy error function during the training of the neural network. In blue is the training sample and in red is the test sample. The training is finished after 9 iterations.

increase of the value of the error on the test sample, would indicate an overtraining. The errors went down all the time, and the training was finished after 9 iterations when the error ran into a plateau and could not be further minimised. Indeed, no indication of overtraining is seen.

[4] The ratios 80% and 20% are chosen, because of the limited statistics of the MC samples available for training and the need to make the training sample as big as possible.

Training Results

The neural network output of signal events accumulate around +1, while background events accumulate at outputs around -1. This can be seen in Figure 8.8a). The quality of the training is checked by plotting the signal purity as a function of the neural network output as can be seen in Figure 8.8b).

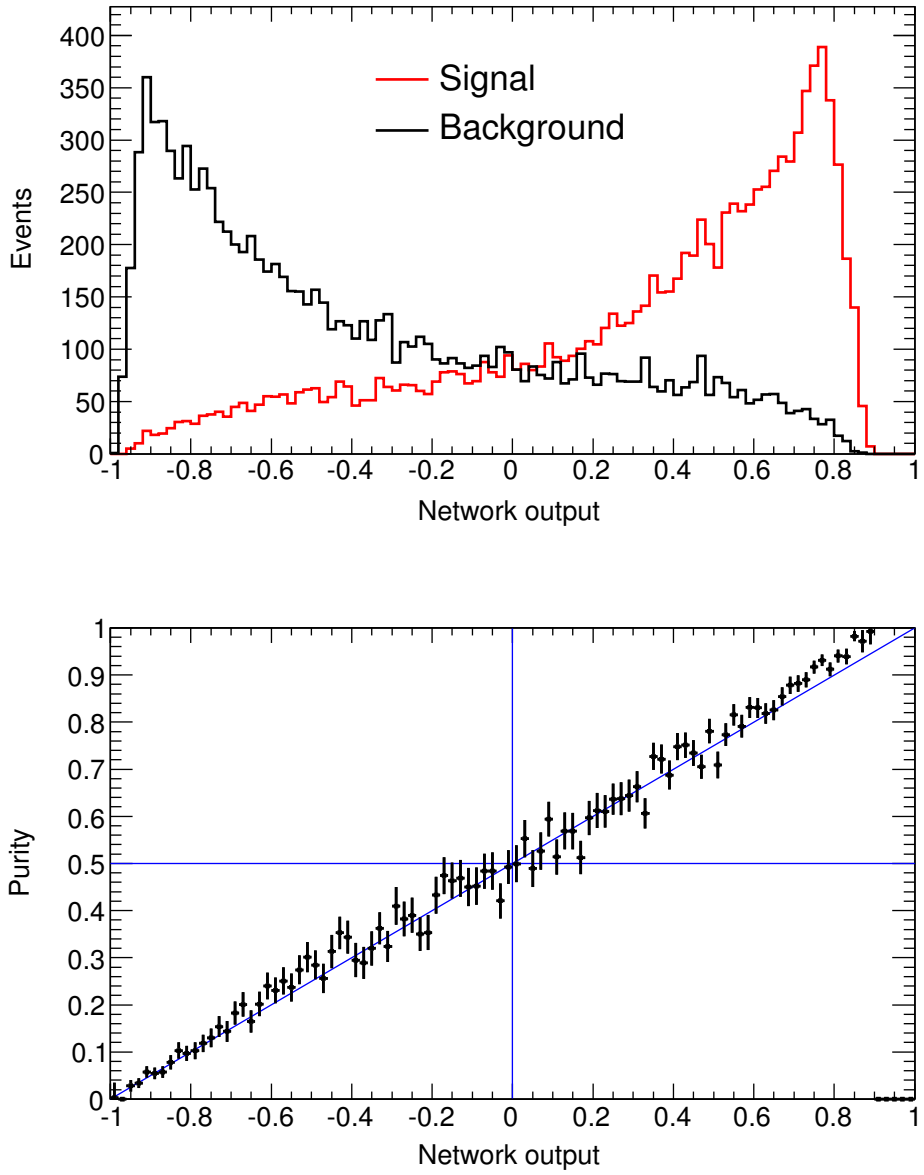

Figure 8.8: The upper plot shows the NN output distributions for signal (red) and background (black) events. The lower plot shows the signal purity in each bin as a function of the NN output. The expected linear behaviour is observed demonstrating that the network is well trained.

The signal purity is defined as the ratio between the number of signal events and the signal plus

background events in a bin. If the NN is well trained, then $E(w)$ is minimal, i.e. $\frac{dE}{dO} = 0$. It is shown in Reference [117] that the purity for a well trained network at the minimum is a linear function of the network output, O, as follows

$$P = \frac{O + 1}{2}, \tag{8.10}$$

which can be interpreted as a probability to observe signal events as a function of the NN output. Thus, for a well trained network, all the points should lie on the diagonal as can be seen in the purity plot.

8.2.2 Data and MC Comparison

Since the neural network is trained with simulated events, it is important to check if the input variables are modelled correctly. Data and MC distributions are compared in Figures 8.9, 8.10 and 8.11. All MC distributions are normalised using their predicted cross-section values, Multijet background is normalised by the electron-jet fit results, see Section 7.4. All MC distributions have an extra scale factor such that the total background is normalised to the data, which is useful to compare the shapes. The FCNC signal distribution is stacked on top of the backgrounds, with a normalisation corresponding to a cross-section value of 100 pb. The hatched band indicates the statistical uncertainty and the uncertainty of the background normalisation. The left plots show the MC distributions for the pretagged sample and the right distributions are for the b-tagged samples. P_T^{lep}, $P_T^{b\text{-jet}}$ and $\eta_{b\text{-jet}}$ have already been shown in Figure 7.2 and Figure 7.3 for the pretagged and b-tagged samples, respectively. These distributions are for the muon and electron channels combined, while the distributions for the electron and muon channels separated are shown in Appendix A.1 and Appendix A.2, respectively.

Additionally, since the neural network takes the advantage of the correlation between the input variables to distinguish the signal from the background events, the modelling of the corresponding correlations are checked. The correlation between variable x_i and x_j is checked using the correlation coefficient κ_{ij} [118] defined as

$$\kappa_{ij} = \frac{x_i - \bar{x}_i}{\sigma_{x_i}} \cdot \frac{x_j - \bar{x}_j}{\sigma_{x_j}}, \tag{8.11}$$

where $\bar{x}_i$ is the mean of variable x_i and σ_{x_i} is the corresponding standard deviation. In this analysis, the κ_{ij} coefficients are checked by comparing the MC and collision data distributions, since more information can be inferred from the distributions to judge the data modelling. Figure 8.12 shows the distributions of the correlation coefficients between the best input variables used to train the NN, where the good agreement between the background and observed data distributions is seen. The rest of the correlation coefficient distributions between less contributing variables to the NN output are shown in Appendix B.

8.3 Results and Data Modelling

To construct the background shape templates, it is necessary to combine background processes whose output distributions look very similar and are difficult to distinguish. Based on this concept, some of the processes are merged into one template with a fraction given by their cross-section estimate (see Chapter 5). Six background templates are created to describe the background processes: $t\bar{t}$, the SM single top-quark processes, W+light jets, W+heavy flavour (Wcc, Wbb, Wc+n partons), Z+jets including the diboson samples and multijet background. The FCNC single top-quark production is modelled by one template.

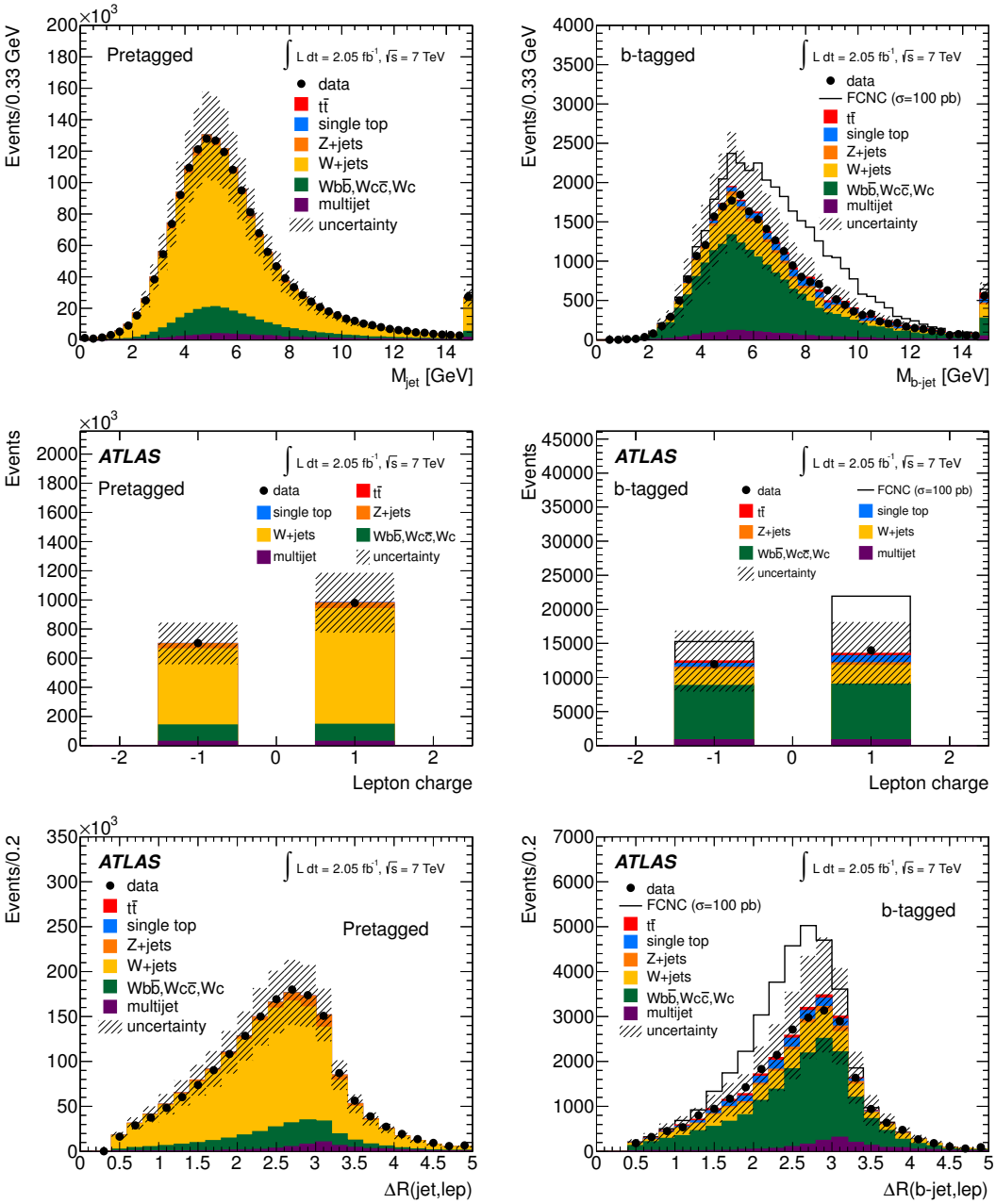

Figure 8.9: Kinematic distributions the muon and electron combined channel: left) the kinematic distributions for the pretagged samples; right) the kinematic distributions for the *b*-tagged samples. The MC is normalised to the number of observed events. From top to bottom: the reconstructed jet mass, lepton charge and ΔR between the jet and lepton. The signal contribution is stacked on top of the backgrounds, with a normalisation corresponding to a cross-section of 100 pb. The hatched band indicates the statistical uncertainty and the uncertainty on the background normalisation added in quadrature.

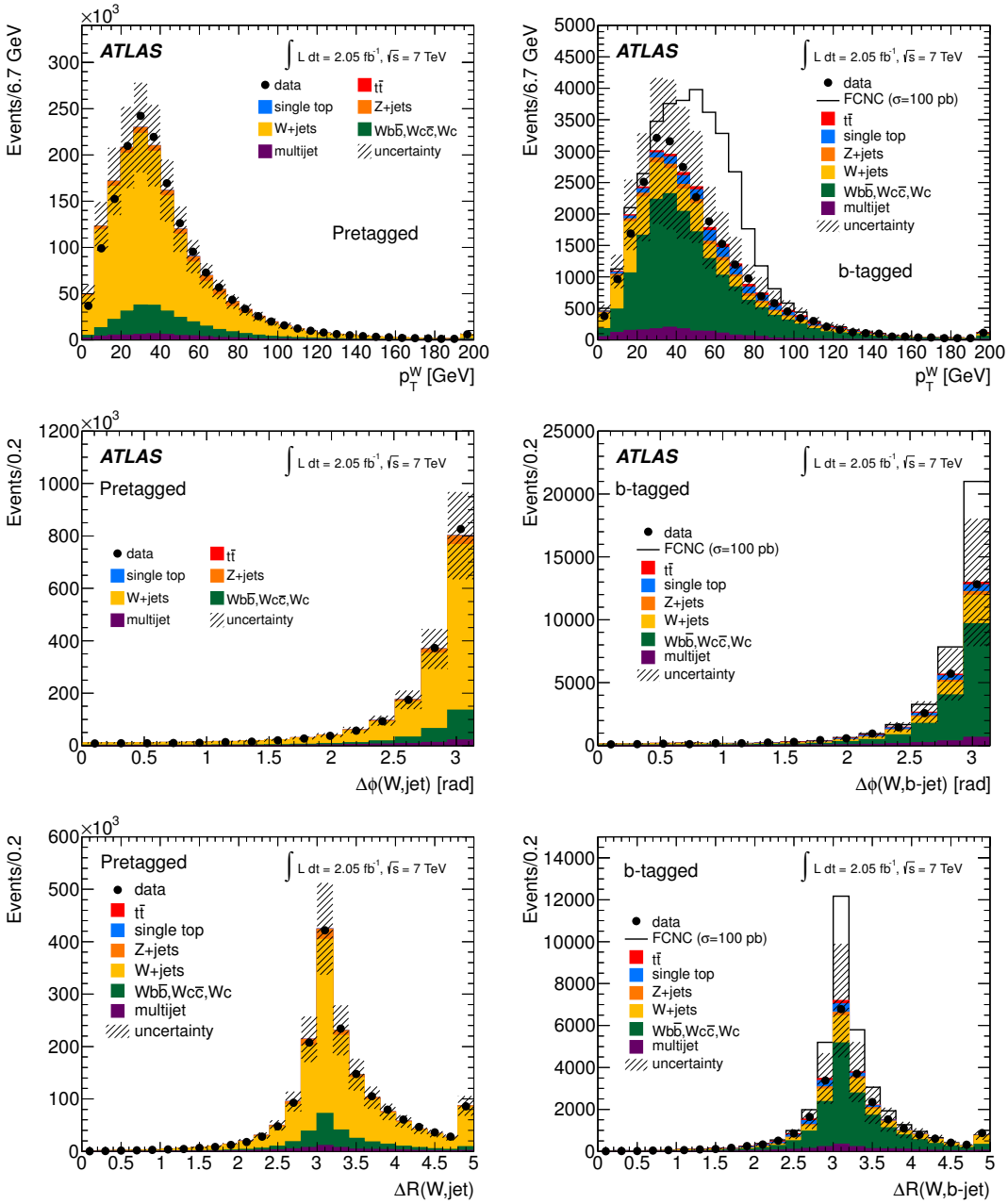

Figure 8.10: Kinematic distributions for the muon and electron combined channel: left) the kinematic distributions for the pretagged samples; right) the kinematic distributions for the b-tagged samples. The MC is normalised to the number of observed events. From top to bottom: the P_T of reconstructed W boson, $\Delta\phi$ between the W boson and the jet and ΔR between the W boson and the jet. The signal contribution is stacked on top of the backgrounds, with a normalisation corresponding to a cross-section of 100 pb. The hatched band indicates the statistical uncertainty and the uncertainty on the background normalisation added in quadrature.

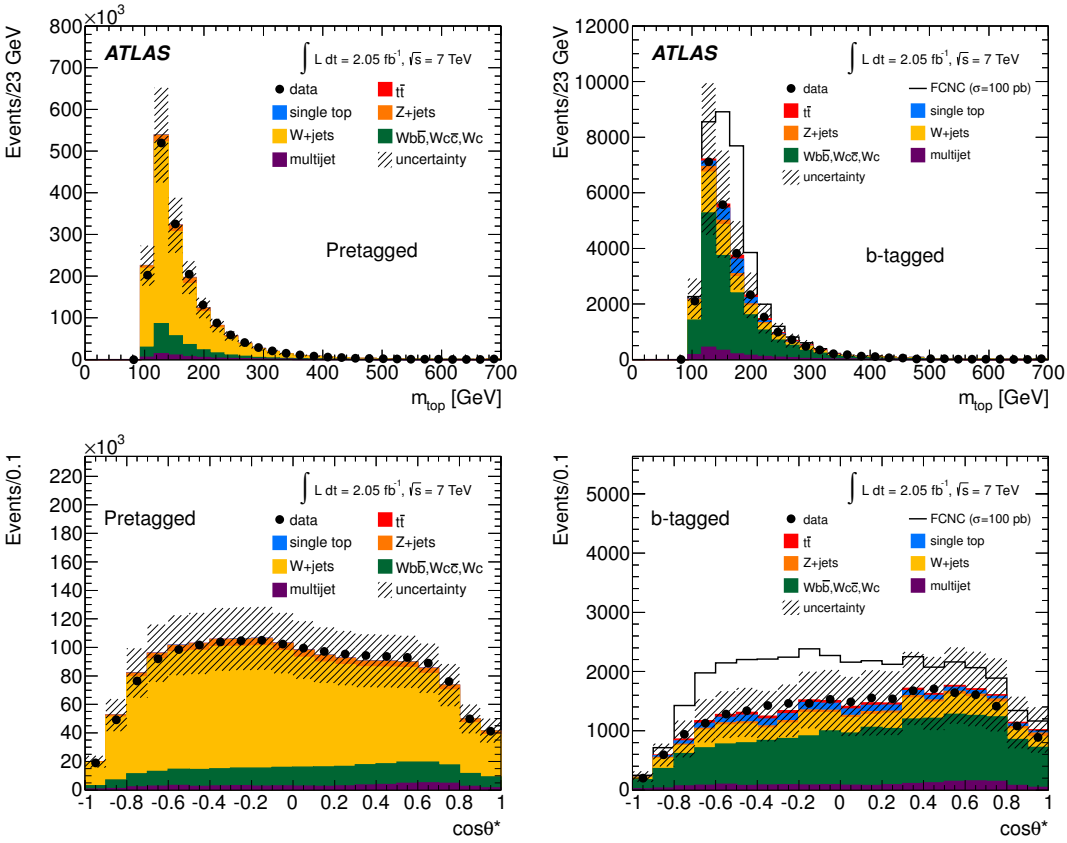

Figure 8.11: Kinematic distributions for the muon and electron combined channel: left) the kinematic distributions for the pretagged samples; right) the kinematic distributions for the *b*-tagged samples. The MC is normalised to the number of observed events. From top to bottom: m_{top} and the W helicity. The signal contribution is stacked on top of the backgrounds, with a normalisation corresponding to a cross-section of 100 pb. The hatched band indicates the statistical uncertainty and the uncertainty on the background normalisation added in quadrature.

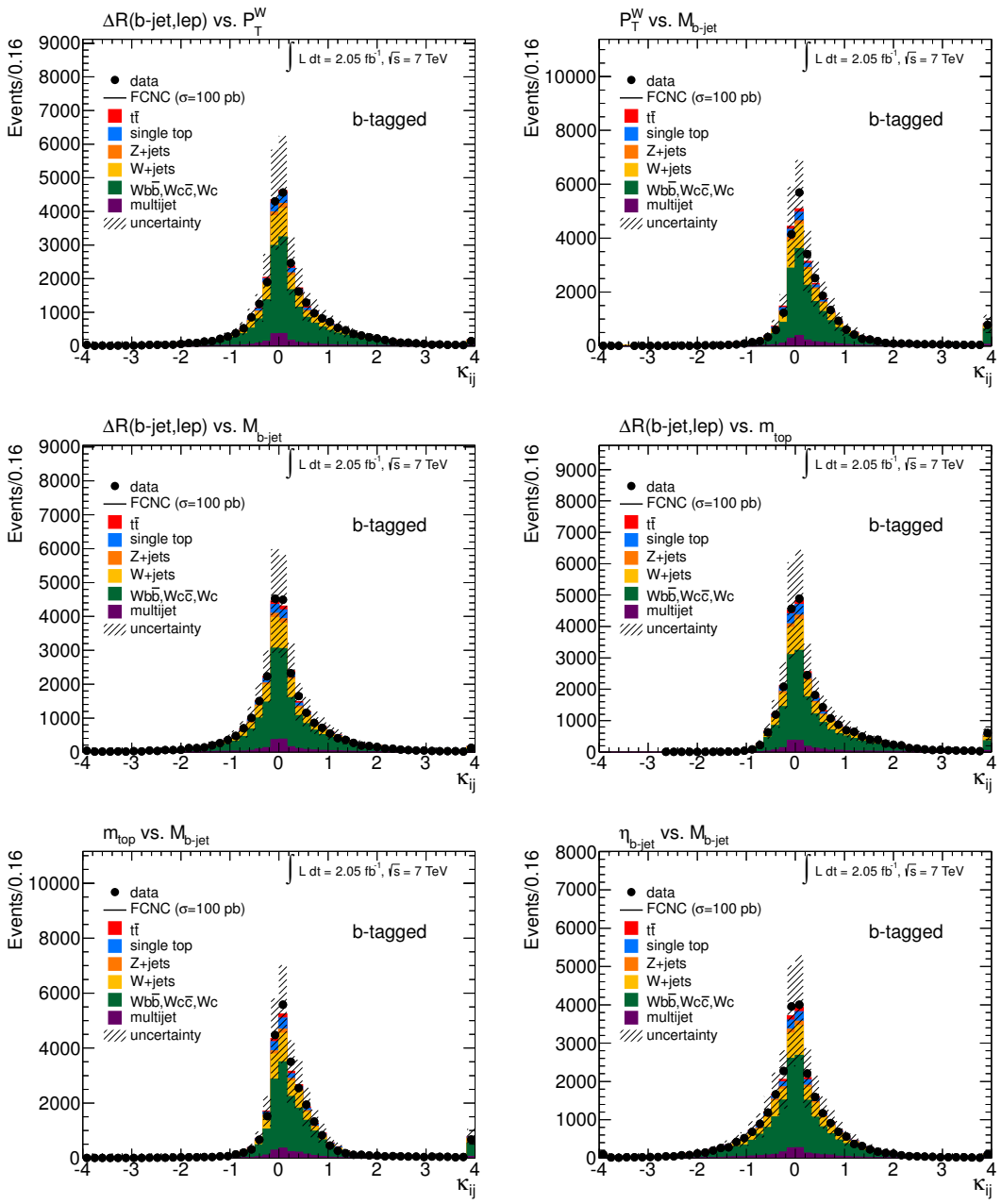

Figure 8.12: Correlation coefficients k_{ij} between various input variables used in the neural network in the b-tagged sample, where the background distributions are normalised to the number of observed events. The hatched band indicates the statistical and the background normalisation uncertainties added in quadrature.

Figure 8.13a) shows the neural network output distributions for the signal and background normalised to unity. These distributions are for the muon and electron combined channel from the *b*-tagged sample. It can be seen that the NN is powerful in separating the background processes from the signal process with an exception from the SM single top-quark (*t*-channel when the associated light-quark jet is missing) which has slightly similar features. Figure 8.13b) shows the NN output distributions for MC and observed data combining muon and electron channels in the *b*-tagged samples. The background distribution is normalised to observed data and the signal cross-section is assumed to be 100 pb and stacked on top of the background. The hatched band indicates the statistical and the background normalisation uncertainties added in quadrature, and the good agreement between the observed data and the MC background distributions is demonstrated. The same distributions for muon and electron channels separately are shown in the Appendix C.2.

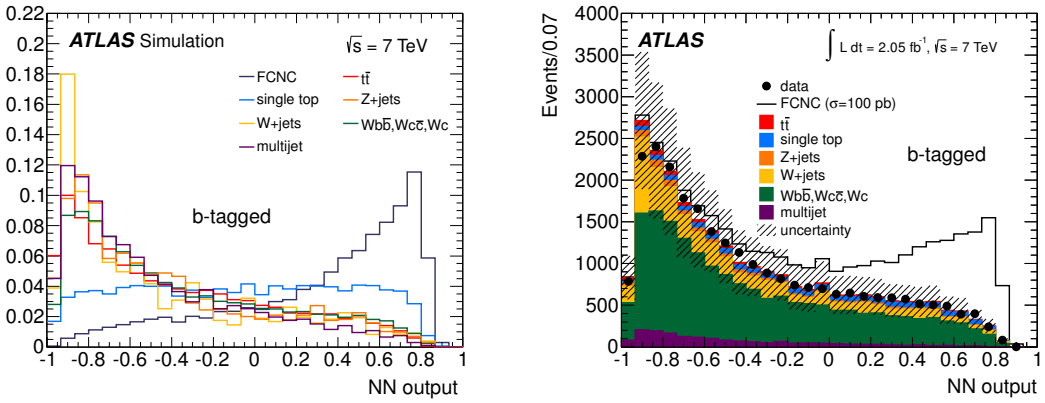

a) b)

Figure 8.13: a) Signal and background output distributions normalised to unity, b) Observed signal and simulated background output distributions normalised to the number of data events in the *b*-tagged sample. The signal process is stacked on top the background after scaling it to a cross-section of 100 pb. The hatched band indicates the statistical and background normalisation uncertainties.

8.4 Tests Performed to Validate the NN

8.4.1 Pretagged Network as a Cross-Check

The actual fractions of the background processes in nature are a-priori unknown and it is necessary to demonstrate that the NN can describe all background shapes. As a cross-check, the NN which is trained by using the *b*-tagged sample is applied on the pretagged sample, which has different background composition and is enriched with the W+light jets background. Figure 8.14a) shows the NN distribution for the pretagged sample, while Figure 8.14b) zooms on the high NN output region where the signal in the *b*-tagged sample is expected to be. Both distributions are for the muon and electron combined channel; the very good agreement between data and MC is clear. The same distributions for muon and electron channels separately are shown in Appendix C.1.

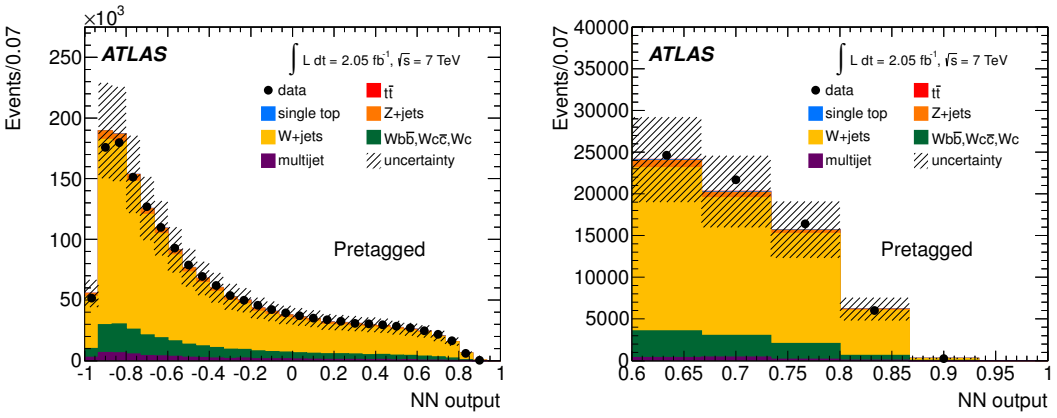

Figure 8.14: Distributions of the neural network output for the pretagged sample combining muon and electron channels: a) The observed data and MC background distribution normalised to the number of data events; b) Zoom into the high NN output region where the signal is expected to be in the *b*-tagged sample. The hatched band indicates the statistical and background uncertainties added in quadrature.

8.4.2 Pile-up

Because the pile-up conditions changed during the data taken in 2011, it is important to show that the analysis is insensitive to pile-up. This is checked by testing the NN sensitivity to the number of primary and pile-up vertices. Therefore, data samples are split into two sub-samples according to the number of primary vertices available in an event. The first sub-sample is the low pile-up region with fewer than six primary vertices per event, the other region contains all events which have six or more primary vertices. The default NN, which has been trained by using the MC samples with the full range of number of primary vertices, is applied on these two subset samples. To compare the different data NN output distributions, first, they are normalised to unity and then compared to the nominal shape by calculating the relative differences as shown in Figure 8.15. Indeed, no observed dependency on the pile-up condition is seen.

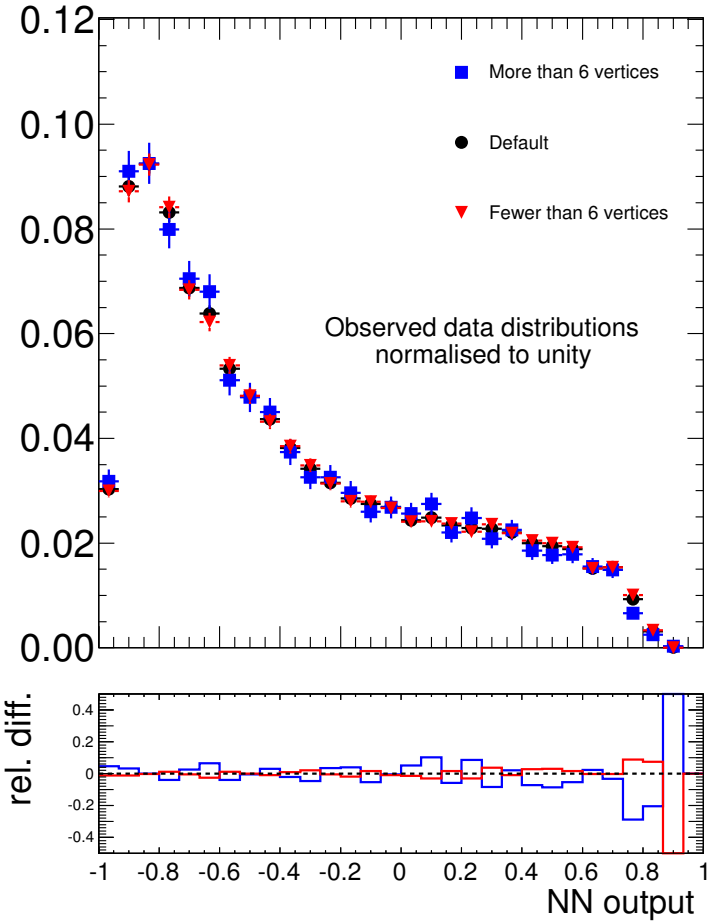

Figure 8.15: Distributions of the neural network output of the data samples for different pile-up conditions. The distributions are normalised to unity.

Chapter 9

Systematic Uncertainties

The uncertainties in modelling the physics processes and detector effects are called the systematic uncertainties. They are called systematic uncertainties because they keep repeating themselves no matter how many times the measurement is done. Systematic uncertainties are different from statistical uncertainties, which can be decreased by collecting more data. The systematic uncertainties can affect both the rate of predicted signal and background events as well as the shape of the template histograms used in the statistical analysis of the observed data distribution.

In this analysis, a binned likelihood method is used to extract the signal and to measure its cross-section, where the neural network output distributions are used as the histogram templates. Thus, the uncertainties in the background normalisation and any mis-modelling in the NN distributions have to be considered and taken into account. In this chapter, systematic uncertainties which may affect the NN output distributions are described, since the background normalisation uncertainties are described in Section 5.4.4. These systematics are implemented following the standard ATLAS procedures [119].

9.1 Object Energy Scale and Momentum Resolution

These systematic uncertainties are due to the residual differences in P_T and E between data and MC simulations for reconstructed electrons, muons and jets. The systematic effects are evaluated by shifting the P_T and E by their uncertainties (1 σ), and the missing transverse energy is recalculated. The objects and event selections are then reapplied to measure the effect on the expected number of events and the kinematic distributions.

Lepton Momentum Scale and Resolution

The $Z \rightarrow \ell^-\ell^+$ processes are used to measure the lepton momentum scale at the particle level and the resolution. Correction factors and associated uncertainties are derived to match the simulated P_T distribution to the observed distribution in the collision data.

Electron energy in simulated MC events is observed to be different from that in data. The difference is reduced by rescaling the electron energy of the data events, while no correction is applied on electron energy for the MC events; thus, an uncertainty rises from the different treatment. The correction factor and its upward and downward uncertainties are dependent on E and η of the electron energy deposit in the calorimeter.

Since the electron momentum resolution in MC samples is observed to be smaller than in data, the momentum of an electron with P_T range between 10 GeV and 1 TeV is smeared. The smearing factor is a random number drawn from Gaussian distribution with mean and width dependent on E and η of the electron energy deposit in the calorimeter. A systematic uncertainty is associated to this treatment. The electron momentum is smeared then three times, once to assign the upward fluctuation and the other smearing to assign the downward fluctuation.

Similarly, the muon momentum resolution in MC is found to be better than in data. This difference is reduced by smearing the muon momentum in MC events. A systematic uncertainty is assigned due to the treatment. The systematic effect is evaluated by smearing the muon momentum four times: first, the muon momentum measured in the ID is smeared by 1σ twice, once for the upward fluctuation and the other for downward fluctuation; then, the muon momentum measured in muon spectrometer is smeared by 1σ again to assign the upward and downward fluctuations.

Jet Energy Scale (JES)

The accurate knowledge of the jet energy scale and resolution are of key importance for precise measurements and have an important impact on the measurement of the missing transverse energy. The JES uncertainty is derived by using the information from test-beam data, LHC collision data and simulation. The uncertainty varies between 2.5% and 8% in the central region and 3.5% and 14% in the forward region of the detector dependent on the P_T and η of the jet [120]. This includes uncertainties in the flavour composition (gluon, light quark, heavy quark) of the samples; this is because the JES is determined from the light-quark and gluon jets. An additional uncertainty of the jet energy is considered because of the mis-measurements coming from the overlapping with other jets that have $P_T > 7$ GeV.

Additionally, uncertainties due to the pile-up are considered and estimated to be as large as 5% (7%) in the central (forward) region of the detector depending on the jet P_T. An additional jet energy scale uncertainty is considered for the identified b-quark jets due to differences between light-quark and gluon jets as opposed to jets containing B hadrons. This uncertainty varies between 0.8% and 2.5% depending on the jet P_T.

Jet Energy Resolution

The Jet Energy Resolution (JER) is measured by the dijet balance method. Events with two jets are selected in this method and the jet P_T resolution is derived from the momentum conservation in the x-y plane. The imbalance in the P_T of the two jets is called the P_T asymmetry which is fitted by using a Gaussian function to characterise the asymmetry distribution and to determine the jet P_T resolution. It was found that the jet energy resolution as predicted by the simulations is observed to be less than in data [121]. Thus, the jet energy in MC samples is smeared by a Gaussian function with mean and width dependent on the jet P_T and η to match the observed resolution of the jet energy in the collision data.

Because the jet energy is smeared only in MC samples, a systematic uncertainty is considered due to the different treatment. The systematic uncertainty is calculated by smearing the jet energy in MC twice: one to assign the upward fluctuation and the other smearing to assign the downward fluctuation.

The relative uncertainties in the expected event yields due to the energy and momentum object uncertainties are shown in Table 9.1. It can be seen that the JES has a big impact on the $t\bar{t}$ and on the single top-quark processes. This is because they have different flavour compositions (they have at least one b-quark jet) and high jet multiplicity. The JES has an effect on the number of jets passing the jet selection criteria, as a result, the number of events passing the event selection criteria (the event is accepted if it has only one jet passes the jet selection) is different. The JES has a smaller impact on the FCNC process, because most of the FCNC events have one jet, thus the migration from the zero-jet events to one-jet events has approximately the same effect as the migration from the one-jet events to two-jet events, and vice versa for the downward fluctuation. The large impact of the JES and the JER on the W+jets background is because of the small W+jets MC sample which has a large statistical uncertainty, around 10%. The lepton energy scale and momentum resolution have negligible effect on all MC processes.

	Electron energy scale	Electron resolution	JES	JER	Muon momentum resolution	JES	JER
W+jets	$^{+0.0}_{-2.8}$	$^{-0.3}_{-0.9}$	$^{+9}_{-15}$	$^{+0.3}_{+0.1}$	$^{+0.4}_{-0.2}$	$^{+18}_{-11}$	$^{+15}_{+11}$
W+HF	$^{+0.5}_{-2.0}$	$^{-0.1}_{-0.5}$	$^{+0.7}_{-1.4}$	$^{-0.5}_{-0.4}$	$^{+0.1}_{-0.1}$	$^{-0.4}_{-1.0}$	$^{-0.8}_{-0.5}$
$t\bar{t}$	$^{+0.3}_{-0.2}$	$^{+0.0}_{-0.1}$	$^{-19}_{+23}$	$^{-0.5}_{-0.5}$	$^{0.0}_{0.0}$	$^{-19}_{+24}$	$^{-0.6}_{-0.5}$
Single top	$^{+0.7}_{-0.9}$	$^{-0.2}_{-0.0}$	$^{-11}_{+11}$	$^{-1.2}_{-1.3}$	$^{+0.0}_{-0.1}$	$^{-12}_{+14}$	$^{-0.9}_{-0.5}$
Z+jets	$^{+0.5}_{-0.2}$	$^{+1.9}_{-0.2}$	$^{+4.6}_{-0.8}$	$^{+0.2}_{+1.5}$	$^{+0.2}_{+0.1}$	$^{+4.1}_{-2.2}$	$^{+0.9}_{+2.9}$
FCNC	$^{+0.5}_{-0.6}$	$^{+0.1}_{+0.1}$	$^{-2.9}_{+1.3}$	$^{-1.6}_{-1.5}$	$^{-0.3}_{+0.5}$	$^{-4.1}_{+2.8}$	$^{-0.7}_{-0.6}$

Table 9.1: The relative difference in percent of the event yields caused by the P_T and E uncertainties. Left for the electron channel and right for the muon channel.

Appendix D.1 contains the NN output distributions for signal and backgrounds processes and it shows the shifts in the distributions caused by the energy and momentum uncertainties.

9.2 Object Reconstruction Efficiencies

These systematic uncertainties are due to the residual differences between data and MC simulations, on electron, muon and jets reconstruction efficiencies.

Lepton Reconstruction

The mis-modelling of electron or muon trigger, reconstruction and selection efficiencies in simulations are corrected by scale factors derived from measurements of the efficiency in data. $Z \to \mu\mu$ ($Z \to ee$ and $W \to e\nu$) decays are used to obtain scale factors as functions of the lepton kinematics. The uncertainties are evaluated by varying the lepton scale factors by their uncertainties and the shifts of the event yields are then calculated for the signal and for the backgrounds. The scale factor uncertainties are around 3%.s

Jet Reconstruction Efficiency

The jet reconstruction efficiency is estimated using minimum bias and QCD dijet events. An uncertainty of 2% is assigned based on the agreement between efficiencies measured in data and simulations [122]. The impact of the jet reconstruction efficiency is evaluated by randomly dropping jets with $P_T > 20$ GeV from the events and by determining the variation of the yields from the nominal samples. This uncertainty is one-sided systematic.

b-tagging Efficiency

The b-tagging efficiencies and mis-tagging rates for the *JetFitterCombNN* b-tagger are measured in data [108]. Jet P_T- and η-dependent scale factors are applied to MC simulated events to reduce the inconsistency with data, have uncertainties which range from 8% to 16% for the b-quark jet tagging

efficiency scale factor, and 23% to 45% for light-quark jets mis-tagging rate scale factors.

The relative uncertainties in the expected event yields due to the uncertainties on correction scale factors are shown in Table 9.2. In Appendix D.2 all template distributions for signal and backgrounds are shown including the plus and minus 1σ shift due the uncertainties in the correction scale factors.

	Jet reco. eff.	e trigger, eff. and ID	b-tag, mis-tag	Jet reco. eff.	μ trigger, eff. and ID	b-tag, mis-tag
W+jets	+0.0	±3.4	±17	+0.0	±1.1	±15
W+HF	+0.0	±3.4	±18	−0.0	±1.4	±18
$t\bar{t}$	+0.2	±3.3	±12	+0.2	±2.2	±12
Single top	+0.1	±3.3	±11	+0.1	±.4	±11
Z+jets	+0.5	±3.4	±13	+0.3	±1.6	±12
FCNC	−0.0	±3.4	±11	+0.0	±1.1	±11

Table 9.2: The relative difference in percent of the event yield caused by the uncertainties of the object correction scale factors. The uncertainty on the b-tagging efficiency is added in quadrature to the uncertainty on the mis-tagging rate. Left for the electron channel and right for the muon channel.

9.3 Monte Carlo Generators and PDF Uncertainties

Systematic effects from MC modelling are estimated by comparing different generators and varying parameters for the event generation.

Parton Showering

The effect of parton-shower modelling is evaluated by comparing two ACERMC samples interfaced to HERWIG and PYTHIA, respectively. The uncertainty due to the PS mis-modelling is only evaluated for the single top-quark background because it is one of the dominant backgrounds and it is difficult for NN to separate it completely from the FCNC signal. This is due to the similar kinematics of the single top-quark background and the FCNC signal. This uncertainty is a one-sided systematic.

ISR/FSR

The amount of initial- (ISR) and final-state radiation (FSR) can affect the FCNC top-quark kinematics and can change the jet multiplicity, which can later affect the cross-section measurement. The uncertainty coming from the choice of the ISR/FSR parameters is estimated by varying parameters in ACERMC [123] interfaced to PYTHIA. The parameters are varied in a range comparable to those used in the ATLAS Perugia Soft/Hard tune variations [124] and the largest deviation from the nominal sample is taken as the systematic uncertainty. The PYTHIA ISR and FSR varied parameters are:

- ISR: PARP(64) and PARP(67). The variable PARP(64) controls the running coupling (α_s) as a function of the squared transverse momentum evolution scale, with the default value of 1. Para-

meter PARP(67) has a default value of 4 and controls the Q^2 scale of the hard scattering to define the maximum parton virtuality allowed in Q^2 showers.

- FSR: PARP(72) and PARJ(82). PARP(72) controls the value used in running α_s for time-like parton showers with the default value of 0.192 GeV. Parameter PARJ(82) controls the invariant mass cut-off, m_{min}, of the parton showers, below which partons are not assumed to radiate. This parameter has a default value of 1 GeV.

The new parameter values for the ISR/FSR samples are given as follows:

- ISR down: PARP(67)=0.5, PARP (64)=4 · D,
- ISR up: PARP(67)=6, PARP (64)=0.25 · D,
- FSR down: PARP(72)=0.5 · D, PARJ(82)=2 · D,
- FSR up: PARP(72)=2 · D, PARJ(82)=0.5 · D,

where D is the default parameter value mentioned above. The ISR/FSR uncertainties are applied to all single top-quark processes including the signal FCNC process, but is not evaluated for the $t\bar{t}$ background since it is one of the least contributing backgrounds to the yield and the NN can easily separate it from the signal, reducing its effect on the signal cross-section measurement.

The uncertainties in the event yield caused by the ISR/FSR are summarised in Table 9.3. It can be seen that ISR has large impact on both FCNC signal and single top-quark processes, since it can change the number of jets available in the events as well as it can change the kinematics of the top quark. More ISR increases the number of jets, thus the acceptance is expected to be less for both processes, while the higher drop in the single top-quark event acceptance is due to the fact it has higher jet multiplicity. Less ISR results in the smaller number of jets in an event which results in higher single top-quark acceptance due to its higher jet multiplicity. But less ISR has an opposite effect resulting in a big drop in the FCNC signal acceptance which can be understood by the following: the probability of losing the only jet in the event (for example by the jet selection) is higher than the probability of reducing the number of jets in an event which has more than one jet to only one jet.

The same thing is applied on the FSR, where the number of jets in an event can be different due by different amount of FSR. This has a small impact on single top-quark, while a large impact on FCNC is observed especially when the FSR is increased.

PDF Sets

The choice of parton density functions (PDF) can change the FCNC top-quark kinematics and cross-sections as well as the asymmetry between top-quark antitop-quark production. The impact of the choice of PDF can be estimated by generating new MC samples. However, because this approach is very time consuming, the PDF uncertainties are estimated by re-weighting the MC events according to various PDF uncertainty eigenvector sets (CTEQ66, MSTW2008 [125]). The results of different eigenvectors are combined following the procedure described in [126]. This uncertainty is applied to all top-quark processes including the FCNC process.

The relative differences in the expected event yields caused by the uncertainties coming from MC mis-modelling are summarised in Table 9.3, while in Appendix D.3 the template shits caused by the uncertainties coming from MC mis-modelling and from the multijet mis-modelling are shown.

	ISR	FSR	PDF	MC generator	ISR	FSR	PDF	MC generator
$t\bar{t}$	–	–	$^{+5}_{-5}$	–	–	–	$^{+7}_{-7}$	–
Single top	$^{-12}_{+17}$	$^{+0.2}_{-0.2}$	$^{+2.8}_{-2.8}$	+13	$^{-10}_{+21}$	$^{+2.3}_{-0.6}$	$^{+2.4}_{-2.4}$	+15
FCNC	$^{-3}_{-11}$	$^{-22}_{+6}$	$^{+0.5}_{-0.5}$	–	$^{-3}_{-9}$	$^{+19}_{+2}$	$^{+0.4}_{-0.4}$	–

Table 9.3: The relative difference in percent of the event yield caused by the uncertainties coming from the MC mis-modelling. Left for the electron channel and right for the muon channel.

9.4 Other Systematic Uncertainties.

W+jets Kinematics Modelling

W+jets is the dominant background, and it is very important to study its impact on the FCNC analysis. Because of the large cross-section with very big uncertainty, the different modelling of the W+jets kinematics has to be taken into account. The shape uncertainty is estimated using truth-level samples, in which the ALPGEN parameters are varied with respect to the ATLAS nominal parameter set, and new samples are generated and their event kinematics are compared. It has been found that the P_T of the leading jet (the jet with highest P_T) is a good estimator of the event kinematics. The W+jet shape systematic can be given as a functions of the leading-jet P_T. The function is derived with truth-level kinematic cuts corresponding to the final event selection. The P_T-dependent function for a jet multiplicity of one is parametrised as first order polynomial,

$$f(P_T) = 1.015 \cdot P_T - 0.00045 \ \ [\text{GeV}] \,. \tag{9.1}$$

This function is used to give events extra weights, where the difference between the new shapes and nominal shapes is considered as the shape systematic. This systematic uncertainty is studied to evaluate the impact of the kinematic shape mis-modelling on the analysis, thus no rate uncertainty is considered.

Multijet Background Shape Uncertainty

The expected number of multijet background events is estimated to have an uncertainty of 50%. The miss-modelling of the multijet kinematic distributions is estimated by dividing the jet-electron data samples into two regions: A low pile-up region which contains events with vertices $n_{\text{vtx}} < 6$, and a high pile-up region which contains events with $n_{\text{vtx}} >= 6$. From these multijet event categories, new multijet neural network distributions are created.

Calorimeter Readout (LAr Hole)

Due to a hardware failure, one rectangular region of the ATLAS LAr calorimeter could not be read out in a subset of the data. Data events in which a jet is close to the affected calorimeter region and passes a P_T threshold of 20 GeV are rejected. MC simulated events with jets of P_T >20 GeV close to the affected region are reweighted by a factor equal to the fraction of the integrated luminosity of data for which the calorimeter hardware problem is not present. A systematic uncertainty is evaluated by varying

the P_T-threshold by ±4 GeV. Table 9.4 shows the relative difference in the expected event yield, while Appendix D.4 show all template shifts caused by the uncertainty coming from LAr problem treatment.

	LAr hole	LAr hole
W+jets	$^{+0.0}_{-0.2}$	$^{+0.1}_{-0.3}$
W+HF	$^{+0.3}_{-0.4}$	$^{+0.2}_{-0.4}$
Z+jets	$^{+0.2}_{-0.1}$	$^{+0.4}_{-0.6}$
Single top	$^{+0.5}_{-0.5}$	$^{+0.1}_{-0.2}$
$t\bar{t}$	$^{+0.1}_{-0.3}$	$^{+0.7}_{-0.6}$
FCNC	$^{+0.2}_{-0.3}$	$^{+0.1}_{-0.2}$

Table 9.4: The relative difference in percent of the event yield caused by the uncertainties coming from the treatment of LAr hole problem. Left for the electron channel and right for the muon channel.

Chapter 10

Results

A Bayesian statistical analysis [127, 128] using a binned likelihood method is applied on the neural network output distributions for the electron and the muon channel to measure or to set an upper limit on the FCNC single top-quark production cross-section. In the first section of this chapter, the Bayesian statistical analysis and the binned likelihood which are used to calculate the upper limit are introduced. The way statistical and systematic uncertainties are included in likelihood is presented. In the second section, the expected limit which is used as a measure for the a-priori sensitivity of the analysis is described. In the third section, the final result is presented. Moreover, the effect of each individual systematic uncertainty on the result is shown. A conversion from the observed limit on the single top-quark production via the FCNC cross-section to a limit on the FCNC coupling constants and branching fractions is given. In the fourth section, a discussion of the quality of the statistical analysis is presented.

10.1 Statistical Analysis

10.1.1 Bayesian Approach

In this analysis, the full distribution of the neural network output is used. For a given bin, the likelihood to observe a yield (D_j), if the mean expected yield (d_j) is given by the Poisson distribution:[1]

$$L(D_j|d_j) = \frac{d_j^{D_j} e^{-d_j}}{\Gamma(D_j + 1)}\,, \tag{10.1}$$

where Γ is the Gamma function. The Poisson distribution is written in this form to be applicable for non-integer counts which can occur when studying the expected limits, where yield D_j is set to the predicted yield. The expected number of events d_j is the sum of the predicted contributions from the signal and all n background sources in bin j as follows

$$d_j = a_j + \sum_i^n b_{ij}\,, \tag{10.2}$$

where the $a_j = \alpha_j \sigma \mathcal{L}$, with α_j is the efficiency to observe a signal count in the j^{th} bin for a given integrated luminosity $\mathcal{L}$ and a given signal cross-section, σ. b_{ij} is the background yield for the source i in bin j.

[1] The detailed description of the implementation of Bayesian statistics can be found in the manual of the *top_statistics* packaged used to perform this analysis.

For a distribution of observed data events, the likelihood is the product of all single bin likelihoods:

$$L(\mathbf{D}|\mathbf{d}) \equiv L(\mathbf{D}|\sigma, \mathbf{a}, \mathbf{b}) = \prod_{j=1}^{N} \frac{d_j^{D_j} e^{-d_j}}{\Gamma(D_j + 1)}\,, \tag{10.3}$$

where $\mathbf{D}$ and $\mathbf{d}$ represent the observed and the expected number of events distributed over N bins, respectively. This is valid, because the probability of observing a d_j events in a given bin is independent of observing events in the other bins. Similarly, in case of more than one statistically independent channel, the combined likelihood for all channels is a product of the single-channel likelihoods.

Bayes theorem states that

$$P(H(\sigma, \mathbf{a}, \mathbf{b})|\mathbf{D}) = \frac{P(\mathbf{D}|H(\sigma, \mathbf{a}, \mathbf{b})) \cdot \pi(\sigma, \mathbf{a}, \mathbf{b})}{P(\mathbf{D})}\,, \tag{10.4}$$

where

- $P(H(\sigma, \mathbf{a}, \mathbf{b})|\mathbf{D})$ is the posterior probability, or the degree of belief that hypothesis $H(\sigma, \mathbf{a}, \mathbf{b})$ is true given the $\mathbf{D}$ yield;
- $P(\mathbf{D}|H(\sigma, \mathbf{a}, \mathbf{b}))$ is the conditional probability or the likelihood of seeing the $\mathbf{D}$ yield if the hypothesis $H(\sigma, \mathbf{a}, \mathbf{b})$ is true;
- $\pi(\sigma, \mathbf{a}, \mathbf{b})$ is the prior probability which reflects our degree of belief that $H(\sigma, \mathbf{a}, \mathbf{b})$ is a true hypothesis;
- $P(\mathbf{D})$ is marginal probability of $\mathbf{D}$. This is the same for all possible hypotheses being considered.

The prior probability $\pi(\sigma, \mathbf{a}, \mathbf{b})$ encodes the best knowledge available of the parameters σ, $\mathbf{a}$ and $\mathbf{b}$. It assumes that any prior knowledge of $\mathbf{a}$ and $\mathbf{b}$ is independent of the signal cross-section, σ, and therefore one can factorise the prior probability as:

$$\pi(\sigma, \mathbf{a}, \mathbf{b}) \quad = \quad \pi(\mathbf{a}, \mathbf{b})\, \pi(\sigma)\,. \tag{10.5}$$

The prior density for the signal cross-section is assumed to be flat in σ given as follows

$$\pi(\sigma) = \begin{cases} \frac{1}{\sigma_{\max}} & 0 < \sigma < \sigma_{\max} \\ 0 & \text{otherwise.} \end{cases} \tag{10.6}$$

Since the chosen signal prior is an improper probability function, its range is constrained with an upper bound $\sigma_{\max}$, where $\sigma_{\max}$ is a numerical value chosen large enough to make the posterior go to zero such that

$$\int_0^{\sigma\max} P(H(\sigma, \mathbf{a}, \mathbf{b}|\mathbf{D})\mathrm{d}\sigma = 1\,. \tag{10.7}$$

The lower bound starts from zero since the cross-section is always greater than or equal to zero.

The posterior probability density (PDF) is computed and then integrated with respect to the parameters $\mathbf{a}$ and $\mathbf{b}$ to obtain the posterior density as a function of the signal cross-section, given the observed distribution of counts $\mathbf{D}$:

$$P(\sigma|\mathbf{D}) = \frac{1}{\mathcal{N}\sigma_{\max}} \int\int L(\mathbf{D}|\sigma, \mathbf{a}, \mathbf{b})\pi(\mathbf{a}, \mathbf{b})\, \mathrm{d}\mathbf{a}\, \mathrm{d}\mathbf{b}\,. \tag{10.8}$$

where $\mathcal{N}$ is the overall normalisation to make Equation 10.7 true.

A Bayesian upper limit $\sigma_{\text{C.L.}}$ at confidence level (C.L.) is a solution of

$$\int_0^{\sigma_{\text{C.L.}}} p(\sigma|\mathbf{D}) \quad = \quad \text{C.L.}\,. \tag{10.9}$$

When evidences of observing the searched signal are not enough to confirm the observation, the upper limit is calculated.

10.1.2 Systematic Uncertainties

The uncertainties are divided into two types: normalisation systematic uncertainties described in Section 5.4.4, and shape systematic uncertainties that are described in Chapter 9. The systematic uncertainties are included in the likelihood using the direct sampling method in which a large number of samples of systematic shifts is created. A separate likelihood distribution is obtained for each sample, and the final posterior is then the sum over all likelihoods divided by the number of samples.

For each individual systematic uncertainty, a random number is drawn from a Gaussian distribution with mean equal to zero and width equal to one $g(0,1)_s$, this number represents the shift caused by that systematic uncertainty s. The Gaussian random number is used to calculate the yield shift, Δd_{ijs} for all bins from all sources in all channels, where the yield shift is determined by the quadratic approach [129] given by

$$\Delta d_{ijs} = g(0,1)_s \times \left[\frac{\delta^+_{ijs} + \delta^-_{ijs}}{2} + g(0,1)^2_s \cdot \frac{\delta^+_{ijs} - \delta^-_{ijs}}{2} \right], \tag{10.10}$$

where Δd_{ijs} is the yield shift in the bin j from the source i caused by systematic s. The δ^+_{ijs} and δ^-_{ijs} are the upward and downward fluctuations in bin j from source i calculated from the input MC distributions. The quadratic approach of calculating the yield shift is used since the upward and downward fluctuations can be different, or even the systematic uncertainty can be one-sided with only upward or downward fluctuations.

In each bin, the background or signal yield is then simply a sum over all systematic shifts given as follows

$$d'_{ij} = d_{ij} + \sum_s \Delta d_{ijs}\,, \tag{10.11}$$

where d'_{ij} is used to calculate the new likelihood. If the yield d'_{ij} is negative due to large negative systematic shifts, then the bin is set to zero. If the number of bins with negative values exceed a threshold, then the complete set of random numbers for this sample are redrawn.

10.1.3 Monte Carlo Statistics

The MC samples used to model the signal and background yield are limited in size, and thus have uncertainties connected to the number of available events. The statistical uncertainty is treated as independent bin to bin and source to source and thus does not have a common Gaussian prior. Rather, it needs to be applied independently for each source and bin. This results in a very large phase space for the MC integration, which requires a large number of samples. Such a large number of samples are very CP time consuming. However, since the uncertainty is related to the number of events in each MC sample, a Gamma distribution can be used to model the MC statistical uncertainty. This allows an algebraic expression to be used for the integral over the MC statistical uncertainty. It is implemented by extending the likelihood of Equation 10.1 to include the Gamma prior for the yield d_j with statistical uncertainty,

$\sigma_{d_j^{MC}}$, in bin j,

$$L(D_j|d_j) = \int L(D_j|d_j, \sigma_{d_j^{MC}}) \mathrm{d}\sigma_{d_j^{MC}}, \quad (10.12)$$
$$= \frac{y_j^{D_j}}{(y_j+1)^{D_j+k_j+1}} \frac{1}{\beta(D_j+1, k_j)},$$

where $k_j = (d_j/\sigma_{d_j^{MC}})^2$, $y_j = d_j/k_j$, and β is the beta function. The expression makes it possible to achieve the aimed statistical precision without the need of increasing the number of systematic samples.

10.2 Expected Limit

When analysis methods (for example statistical methods) are applied to real data, the obtained posterior density distribution may look reasonable. However, this does not guarantee that the methods are not biased and perform as expected. It is necessary to study the behaviour of the used methods using pseudo-data samples with characteristics as close as possible to those of the collision data. In this analysis, the expected limit is determined using the Asimov dataset [130], where the number of pseudo-data events is fixed to the prediction bin by bin. Then the cross-section upper limit is calculated in the same way as for the observed data sample. Additionally, pseudo-data samples are used to check the effect of each individual systematic uncertainties, this is done by including only one systematic uncertainty, and then the expected limit is calculated.

The expected upper limit at 95% C.L. is calculated for two cases: the nominal case, by including the MC statistics, theoretical cross-section and multijet background uncertainties; and by including all the systemic uncertainties. Figure 10.1a) shows the predicted signal posterior PDF distribution for the nominal case, while the Figure 10.1b) shows the signal posterior PDF distribution after including all systemic uncertainties. For the nominal case, the expected upper limit is 2.3 pb at 95% C.L. and by including all systematic uncertainties, the expected cross-section upper limit at 95% C.L. increased to 2.4 pb.

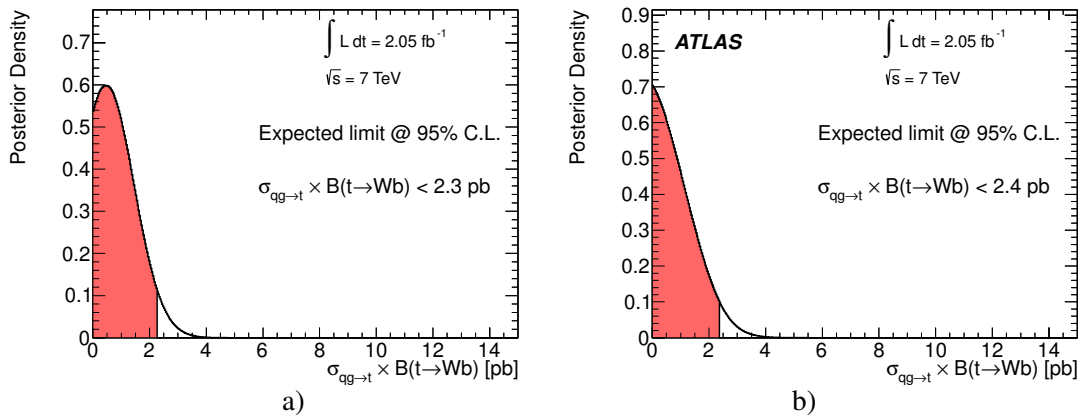

Figure 10.1: Distribution of the posterior PDF function of the Asimov dataset used to calculate the expected upper limit. a) including only the uncertainties on the theoretical cross-section and multijet background uncertainties, b) including all systematic uncertainties. The red shaded area covers 95% of the area.

The influence of each individual shape systematic uncertainty on the expected upper limits is investigated. This is done by just adding one uncertainty at a time to the nominal set of systematic uncertainties. The resulting upper limits are summarised in Table 10.1.

Source	Expected upper limit @ 95% C.L. [pb]
Normalisation uncertainties	2.3
Luminosity	2.3
Jet energy scale	1.7
Jet reco. efficiency	2.3
Jet energy resolution	2.3
b-tagging, mis-tagging	2.9
Electron trigger, eff. and ID	2.3
Electron energy scale	2.3
Electron energy resolution	2.2
Muon trigger, eff. and ID	2.3
Muon momentum resolution	2.2
LAr hole	2.3
PDF	2.3
ISR	2.4
FSR	2.4
W+jets shape	2.3
MC generator	2.3
All systematics	2.4

Table 10.1: The effect of each systematic uncertainty considered on the expected upper limits at 95% C.L. on anomalous FCNC single top-quark production $qg \to t \to b\ell\nu$.

It can be seen that most of the systematic uncertainties have negligible impact on the expected upper limit keeping the upper limit 2.3 pb which is the same as the nominal case. Also it can be seen that some systematic uncertainties increase the upper limit to 2.9 pb such as b-tagging efficiency and mis-tagging rate uncertainties, while some other systematic uncertainties push the upper limit down to 2.2 pb such as electron momentum resolution and muon momentum resolution. The systematic uncertainty which decreases the upper limit most is the JES uncertainty that pulls the limit down to 1.7 pb. These values can be understood by considering the most probable value of the posterior PDF, which can be shifted up or down due to asymmetric systematic uncertainty with different effects on the background than on the signal, in return changing the upper cross-section limit. This can be clearly seen when the most probable value shifts from 0.4 pb in case of the nominal list of systematic uncertainties to 0 pb after considering the JES. Similarly, when the b-tagging efficiency and mis-tagging rate uncertainties are added, the most probable value shifts from 0.4 pb to 0.7 pb increasing the upper limit to 2.9 pb. This makes the JES and b-tagging efficiency the most dominant systematic uncertainties affecting the signal posterior PDF.

10.3 Observed Limit

The probability that the single top-quark production via the FCNC process allowed in nature is given as a function of the production cross-section, which is given by the FCNC signal posterior PDF distribution.

No signal of the FCNC single top-quark production has been observed, thus an upper limit at 95% C.L. is calculated to be 3.5 pb as shown in Figure 10.2a). This is done by including statistical, theoretical cross-section and multijet background uncertainties. Including all uncertainties, the upper limit at 95% C.L. on the signal cross-section is calculated to be 3.9 pb as seen in Figure 10.2b). In both cases, the

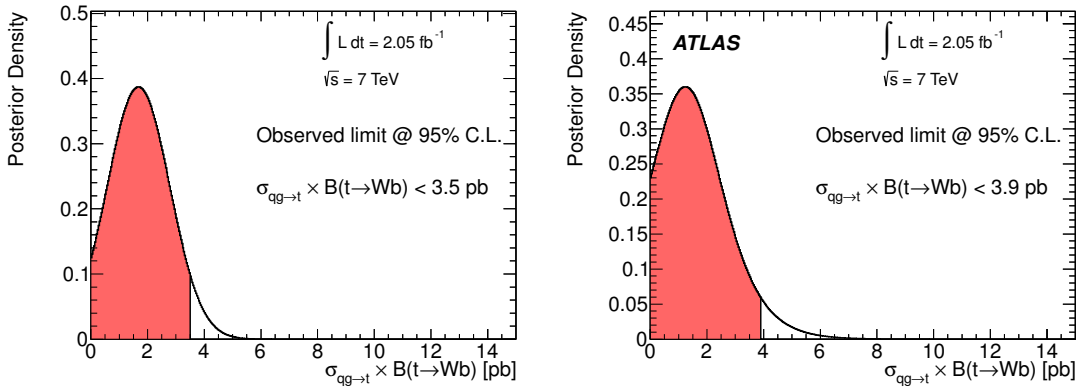

Figure 10.2: a) The signal posterior PDF of the observed events including cross-section and multijet uncertainties. b) The signal posterior PDF of the observed events including all systematic uncertainties. The red area covers 95% of the area.

signal posterior PDF peaks at a value grater than zero, which is interpreted as the measured signal cross-section of yield 1.7 pb and 1.2 pb for the nominal list of systematic uncertainties and all systematic uncertainties included, respectively. These values have small significances and are interpreted as an upward fluctuations of the backgrounds. A summary of the expected and observed upper limits at 95% C.L. is given in Table 10.2.

	Expected limit	Observed limit
Only normalisation uncertainties	2.3 pb	3.5 pb
All systematics	2.4 pb	3.9 pb

Table 10.2: Expected and the observed upper limits at 95% C.L. on the anomalous FCNC single top-quark production $qg \to t \to b\ell\nu$.

To get an idea about the possible systematic uncertainties allowed by the collision data, by integrating the likelihood as done when the signal posterior PDF is calculated, but replacing the signal parameters by the systematic shift for a particular systematic uncertainty. The integrals over the priors for the signal **a** and the backgrounds **b** excluding integrating over systematic shift, s. The systematic posterior PDF distributions are used to get an idea of how each systematic uncertainty is present in the data and to correct the background normalisation. The latter is done using the cross-section systematic uncertainties. Table 10.3 summarises the background output scales with their relative uncertainties obtained from the collision data.

It can be seen that the collision data is best described when the cross-sections of the W+jets and W+HF are scaled by 0.7 and 1.3, respectively. Also, one can see that the background cross-section output uncertainties are smaller than the input uncertainties given in Table 5.5, this is because of constraints applied by the data on the background fluctuations. This is demonstrated by the good agreement between the observed data and MC as shown in Figure 10.3a). It shows the NN distribution for the observed data

Process	Factor	Uncertainty
Single top	0.97	0.10
W+jets	0.73	0.13
W+HF	1.29	0.14
Z+jets	1.03	0.23
$t\bar{t}$	0.96	0.11
Multijet (electron)	1.14	0.38
Multijet (muon)	0.90	0.42

Table 10.3: A summary of the background output scales with their relative uncertainties obtained from the collision data.

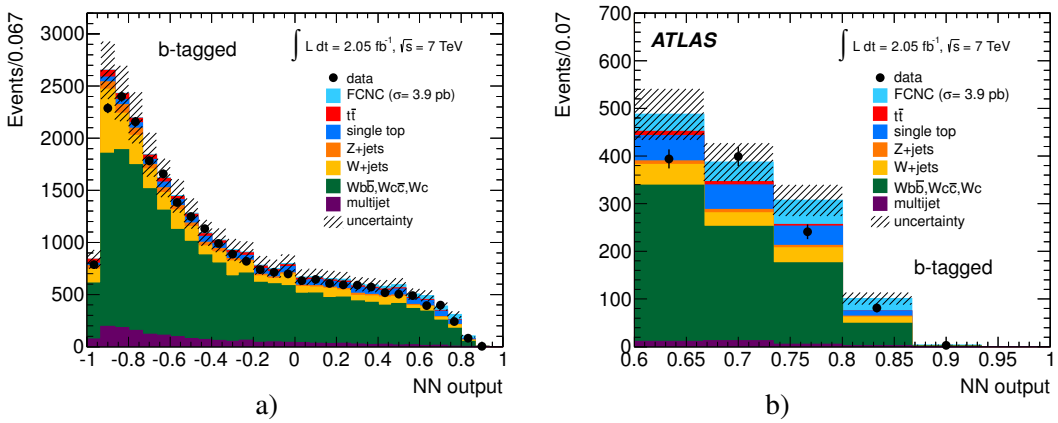

Figure 10.3: a) Neural network output distribution scaled to the measured cross-sections for all processes. The FCNC single top-quark production is scaled to the observed upper limit. b) The same as in a), with a zoom on the region of the high NN output. The hashed band indicates the background uncertainties obtained by the statistical analysis.

superimposed with the MC distributions normalised by the output scales given in Table 10.3, while the signal distribution is normalised to the observed limit at 95% C.L.. The hatched bands indicate the background uncertainties obtained by the statistical analysis. Figure 10.3b) is a zoom of Figure 10.3a) showing the high NN output region where the FCNC signal is expected to be; it is clearly seen that the collision data can be described only by the background processes.

Using the NLO predictions for the FCNC single top-quark production cross-section that have been introduced in Section 3.1, the measured upper limit on the production cross-section is converted into a limit on the coupling constants $\frac{\kappa_{ugt}}{\Lambda}$ and $\frac{\kappa_{cgt}}{\Lambda}$. Using Equation 3.15 and assuming $\frac{\kappa_{cgt}}{\Lambda} = 0$ it is found that $\frac{\kappa_{ugt}}{\Lambda} < 6.9 \cdot 10^{-3}$ TeV^{-1}. Assuming $\frac{\kappa_{ugt}}{\Lambda} = 0$ it is found that $\frac{\kappa_{cgt}}{\Lambda} < 1.6 \cdot 10^{-2}$ TeV^{-1}. Figure 10.4 shows the distribution of the upper limit for all possible couplings at 95% C.L..

Similarly, using the NLO calculation, the upper limits on the coupling constants are converted to limits on branching fractions. Using Equation 3.16, one find Br($t \to ug$) $< 5.7 \cdot 10^{-5}$ assuming Br($t \to cg$) = 0, and Br($t \to cg$) $< 2.7 \cdot 10^{-4}$ assuming Br($t \to ug$) = 0. Figure 10.5 shows the distribution of the upper limit for all possible branching fractions at 95% C.L..

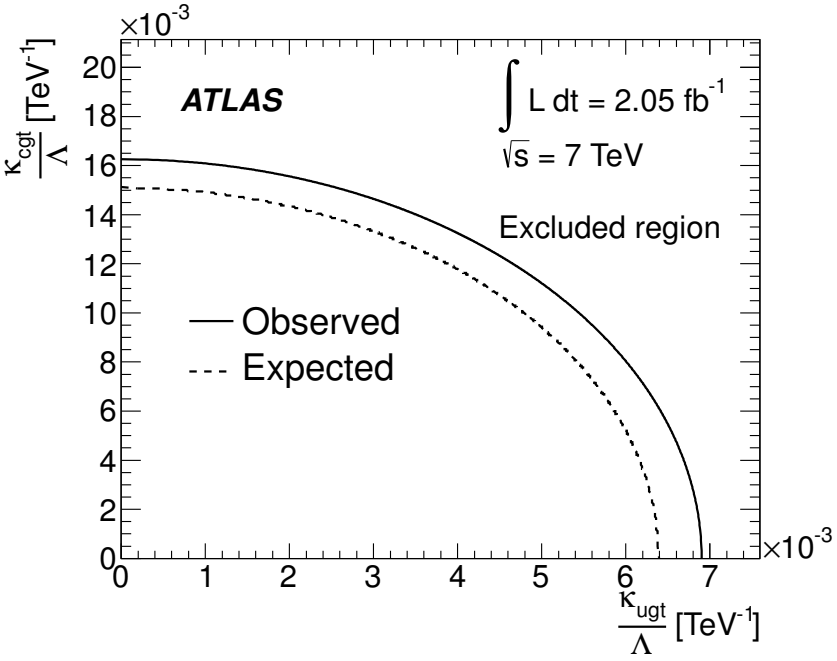

Figure 10.4: The plot shows the upper limit at 95% C.L. on the coupling strengths $\frac{\kappa_{ugt}}{\Lambda}$ and $\frac{\kappa_{cgt}}{\Lambda}$. The solid curve show the observed upper limits, while the dashed curve represent the predicted upper limits.

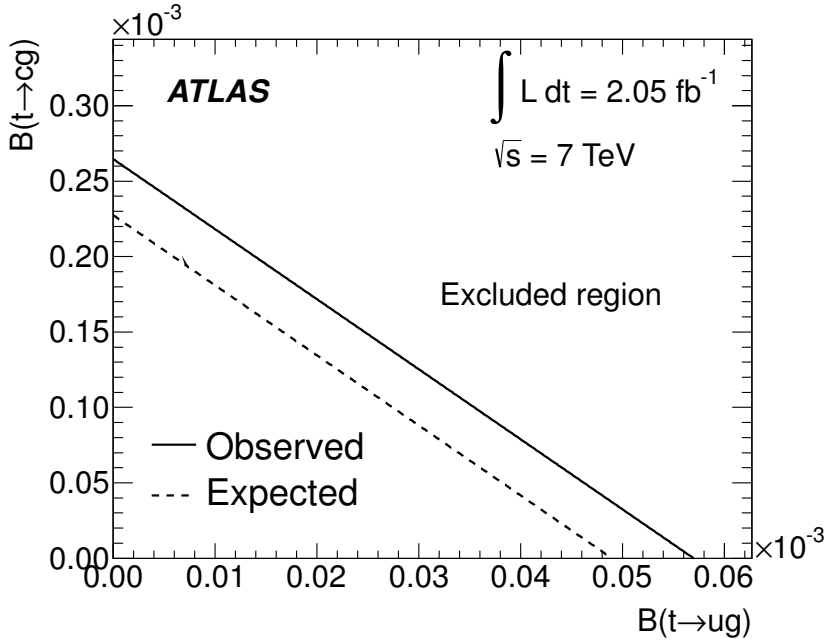

Figure 10.5: The plot shows the upper limit at 95% C.L. on fractions of $t \to ug$ and $t \to cg$. The solid line show the observed upper limits, while the dashed line represent the predicted upper limits.

10.3.1 Diagnostic Plots

It is necessary to know how the sampling of each individual systematic uncertainty is done, and how this is affected by the truncation procedure. The random numbers used in preparing the samples considered in the limit calculation are filled in histograms, one for each systematic source. Figure 10.6 shows the systematic sampling for background normalisation uncertainties. It is easily seen that samples have Gaussian shapes and the truncation effect is negligible.

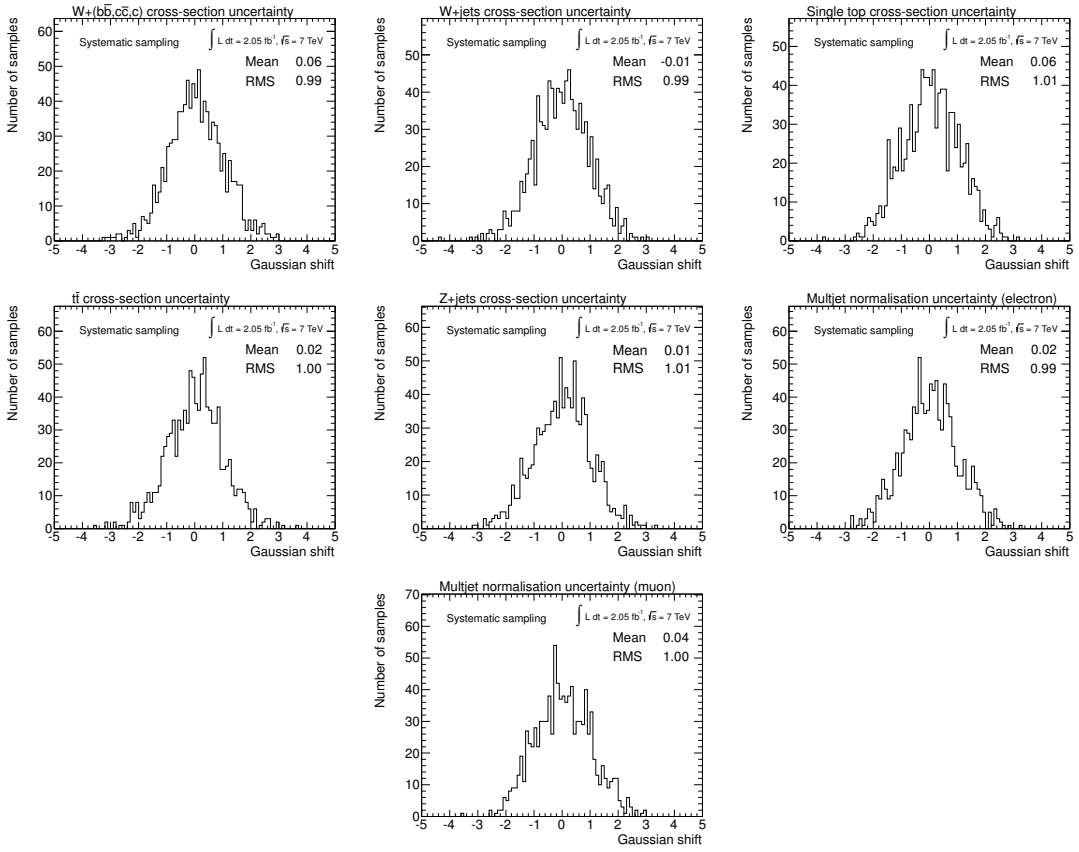

Figure 10.6: Distribution of shift $g(0,1)_s$ systematic samples for the search for single top-quark production via FCNC.

The two dimensional histograms of the signal cross-section versus the systematic shift for a particular systematic uncertainty are checked. These distributions show whether a given systematic uncertainty has any effect on the measured signal cross-section. Figure 10.7 shows this distribution for the background normalisation uncertainties. The figure shows a small correlation between the background normalisation uncertainties and the possible FCNC signal cross-section.

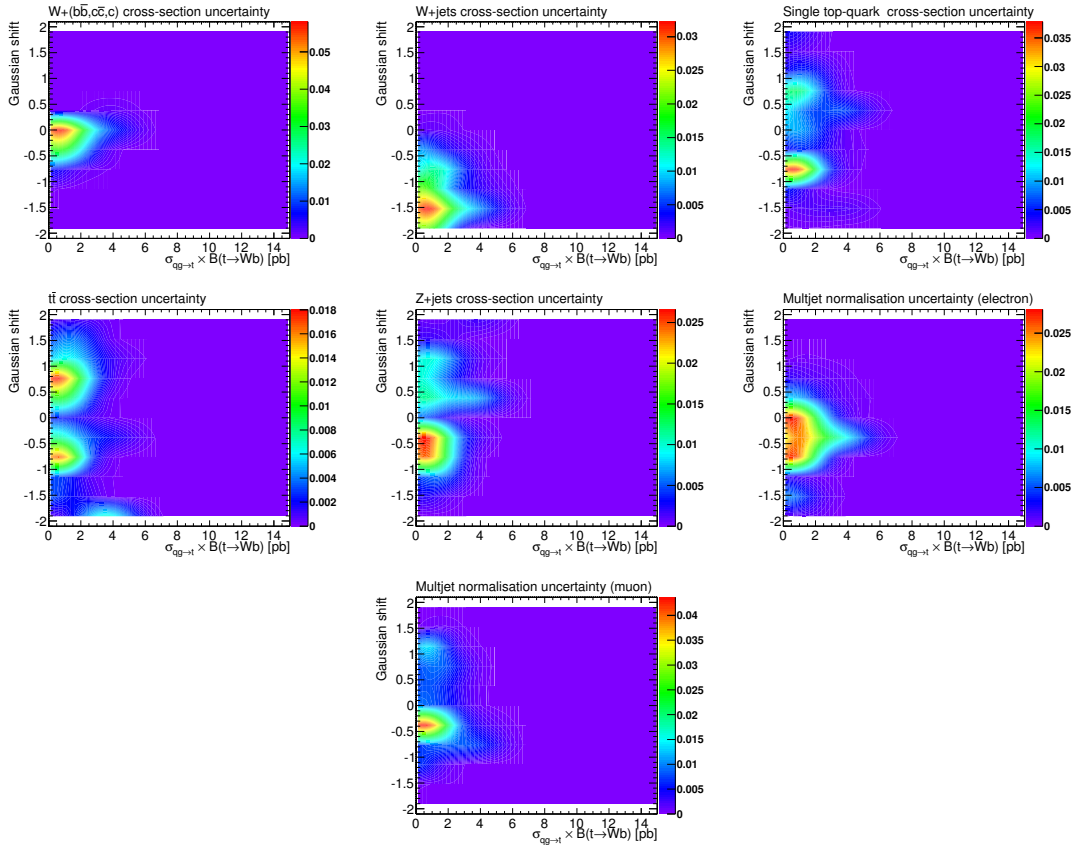

Figure 10.7: Posterior for the signal cross-section and the systematic shifts due to background normalisation uncertainties. The colours correspond to bins of equal probability.

Chapter 11

Summary

A data sample of 2.05 fb^{-1} collected by the ATLAS detector in 2011 and containing events with an isolated electron or muon, missing transverse momentum and a b-quark jet has been used to search for single top-quark production via FCNC at the LHC.

A neural network classifier [13] that combines a three-layer feed-forward neural network with a complex robust preprocessing was used. The network infrastructure consists of one input node for each input variable plus one bias node, 13 nodes in the hidden layer, and one output node which gives a continuous output in the interval $[-1, 1]$.

A Bayesian statistical analysis [127, 128] using a binned likelihood method was used to set an upper limit on the FCNC single top-quark production cross-section. The neural network output distributions were used as the histogram templates. Systematic uncertainties and their correlations across channels were included with a direct sampling approach where the same Gaussian shift was applied to each source, channel, and bin for a given systematic uncertainty. The posterior probability density function (PDF) was obtained by creating a large number of samples of systematic shifts. A separate likelihood distribution was obtained for each sample, and the final posterior PDF is then the sum over all of the individual likelihoods.

The signal posterior PDF gives the probability of the signal hypothesis as a function of the signal cross-section. Since no significant rate of FCNC single top-quark production was observed, an upper limit is set by integrating the posterior PDF. To estimate the a-priori sensitivity, the Asimov dataset [131], which is treated in the same way as the observed dataset was used. The resulting expected upper limit at 95% C.L. on the anomalous FCNC single top-quark production cross-section including all systematic uncertainties is 2.4 pb, while the observed upper limit at 95% C.L. is 3.9 pb.

Using the NLO predictions for the FCNC single top-quark production cross-section, the measured upper limit on the production cross-section was converted into a limit on the coupling constants $\frac{\kappa_{ugt}}{\Lambda}$ and $\frac{\kappa_{cgt}}{\Lambda}$. Assuming $\frac{\kappa_{cgt}}{\Lambda} = 0$ it is found that $\frac{\kappa_{ugt}}{\Lambda} < 6.9 \cdot 10^{-3}$ TeV^{-1} and assuming $\frac{\kappa_{ugt}}{\Lambda} = 0$ it is found that $\frac{\kappa_{cgt}}{\Lambda} < 1.6 \cdot 10^{-2}$ TeV^{-1}. Using the NLO calculation, upper limits on the branching fraction $\mathrm{Br}(t \to ug) < 5.7 \cdot 10^{-5}$ assuming $\mathrm{Br}(t \to cg) = 0$, and $\mathrm{Br}(t \to cg) < 2.7 \cdot 10^{-4}$ assuming $\mathrm{Br}(t \to ug) = 0$ are derived.

In summary, the limits set on the coupling constants $\frac{\kappa_{ugt}}{\Lambda}$ and $\frac{\kappa_{cgt}}{\Lambda}$ and the branching fractions $\mathrm{Br}(t \to ug)$ and $\mathrm{Br}(t \to cg)$ represent the world's best limit to date on FCNC single top-quark production processes for $qg \to t$ and improve on the previous best limits [15] by factors of 4 and 15, respectively.

Appendix A

Kinematic Distributions

A.1 Data and MC Comparison in the Electron Channel

A.1.1 Kinematic Plots for the Pretagged Sample

The kinematic distributions of the identified lepton and reconstructed jet are shown in Figure A.1. Figure A.2 shows the kinematic distributions of $\not{E}_T$, $m_T(W)$, the reconstructed W-boson P_T, $\Delta\phi$ between W boson and the jet, ΔR between W boson and the jet, ΔR between electron and the jet, the reconstructed top-quark mass m_{top}, the reconstructed top-quark P_T and the W-boson helicity. The background is normalised to the observed number of events in order to check the modelling of the shapes in a high statistics sample. The hatched band indicates the statistical and background normalisation uncertainties added in quadrature.

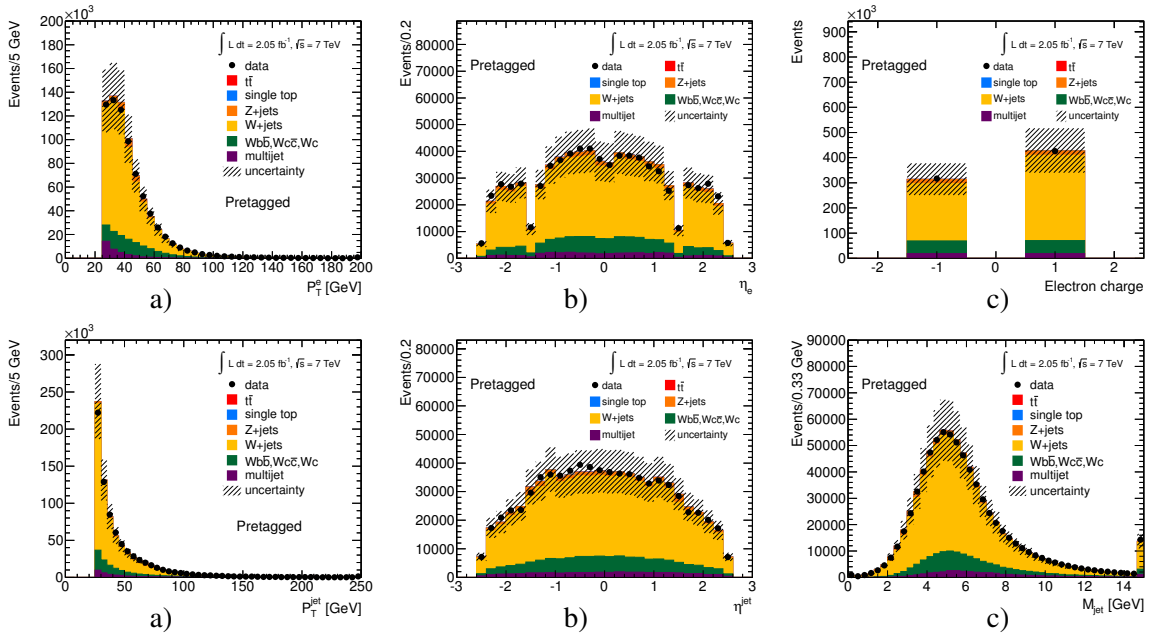

Figure A.1: Kinematic distributions for pretagged samples normalised to the number of observed events: a) electron P_T, b) electron η, c) electron electric charge, d) P_T of the jet, e) η of the jet and f) the invariant mass of the jet. The hatched band indicates the statistical and background normalisation uncertainties added in quadrature.

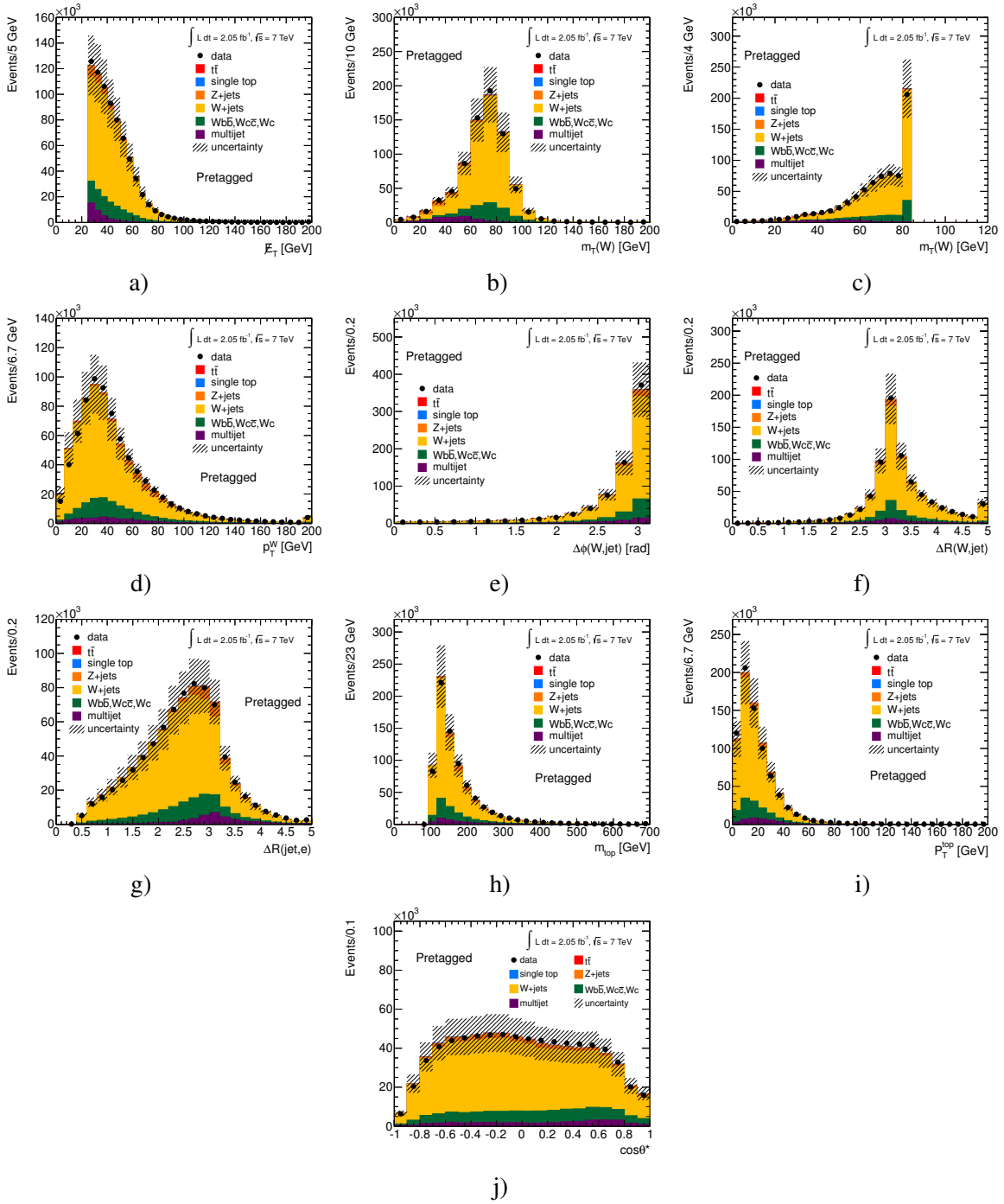

Figure A.2: Kinematic distributions for pretagged samples in the electron channel normalised to the number of observed events: a) Missing transverse momentum, b) transverse W-boson mass before determining the neutrino P_z , c) transverse W-boson mass after determining the neutrino P_z, d) the reconstructed W-boson P_T, e) $\Delta\phi$ between W boson and the jet, f) ΔR between W boson and the jet, g) ΔR between electron and the jet ,h) the reconstructed top-quark mass, i) the reconstructed top-quark P_T and j) the W-boson helicity. The hatched band indicates the statistical and background normalisation uncertainties added in quadrature.

A.1.2 Kinematic Plots for the b-tagged Samples

The kinematic distributions of the identified lepton and reconstructed jet are shown in Figure A.3. Figure A.4 shows the kinematic distributions of $\not{E}_T$, $m_T(W)$, the reconstructed W-boson P_T, $\Delta\phi$ between W boson and the jet, ΔR between W boson and the jet, ΔR between electron and the jet, the reconstructed top-quark mass m_{top}, the reconstructed top-quark P_T and the W-boson helicity. The background is normalised to the observed number of events and the FCNC cross-section is assumed to be 100 pb and stacked on top of the background. The hatched band indicates the statistical and background normalisation uncertainties added in quadrature.

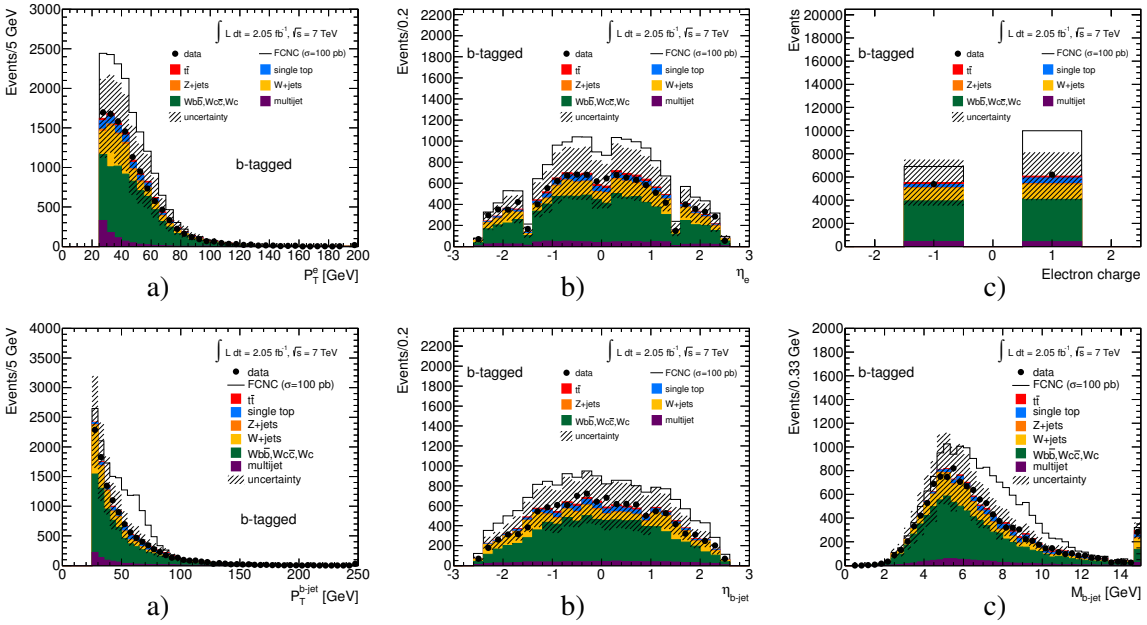

Figure A.3: Kinematic distributions for b-tagged samples normalised to the number of observed events: a) electron P_T, b) electron η, c) electron electric charge, d) P_T of the jet, e) η of the jet and f) the invariant mass of the jet. The hatched band indicates the statistical and background normalisation uncertainties added in quadrature.

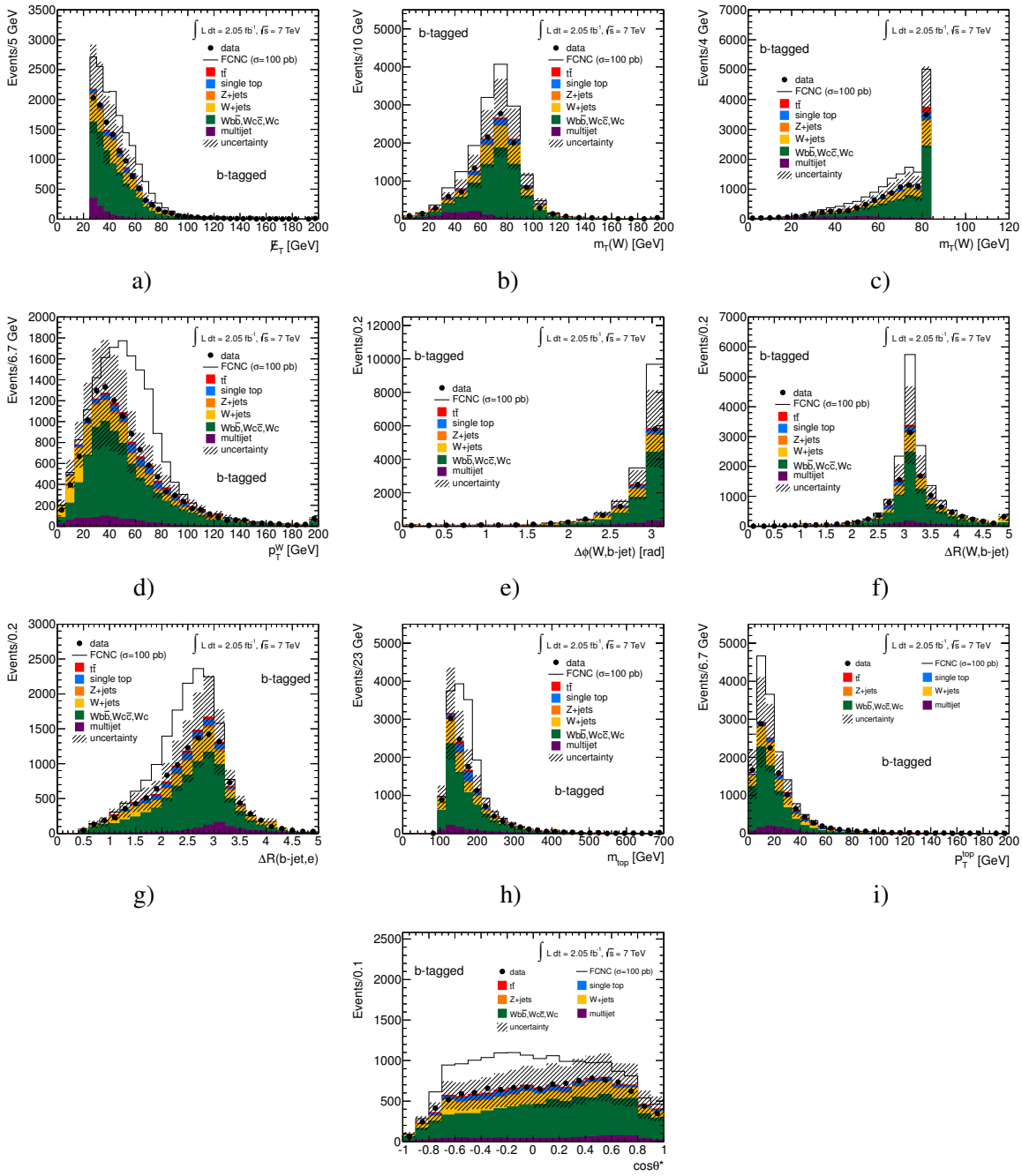

Figure A.4: Kinematic distributions for *b*-tagged samples in the electron channel normalised to the number of observed events: a) Missing transverse momentum, b) transverse W-boson mass before determining the neutrino P_z , c) transverse W-boson mass after determining the neutrino P_z, d) the reconstructed W-boson P_T, e) $\Delta\phi$ between W boson and the jet, f) ΔR between W boson and the jet, g) ΔR between electron and the jet ,h) the reconstructed top-quark mass, i) the reconstructed top-quark P_T and j) the W-boson helicity. The hatched band indicates the statistical and background normalisation uncertainties added in quadrature.

A.2 Data and MC Comparison in the Muon Channel

A.2.1 Kinematic Plots for the Pretagged Sample

The kinematic distributions of the identified lepton and reconstructed jet are shown in Figure A.5. Figure A.6 shows the kinematic distributions of $\not\!\!E_T$, $m_T(W)$, the reconstructed W-boson P_T, $\Delta\phi$ between the W boson and the jet, ΔR between the W boson and the jet, ΔR between the electron and the jet, the reconstructed top-quark mass, m_{top}, the reconstructed top-quark P_T and the W-boson helicity. The background is normalised to the observed number of events in order to check the modelling of the shapes in a high statistics sample. The hatched band indicates the statistical and background normalisation uncertainties added in quadrature.

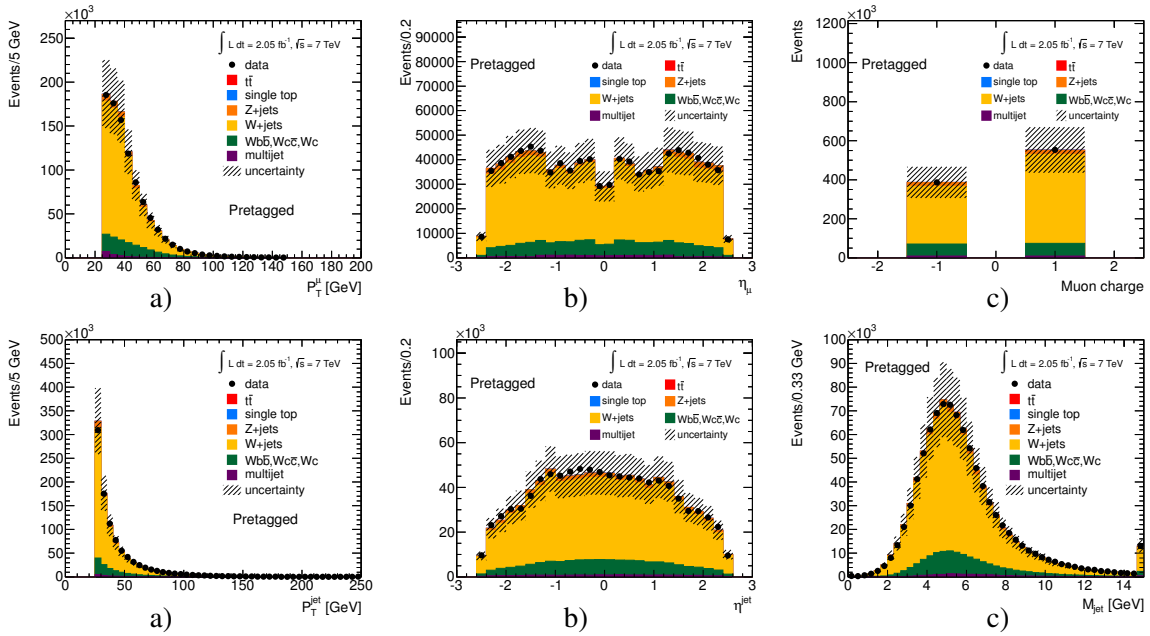

Figure A.5: Kinematic distributions for pretagged samples normalised to the number of observed events: a) muon P_T, b) muon η, c) muon electric charge, d) P_T of the jet, e) η of the jet and f) the invariant mass of the jet. The hatched band indicates the statistical and background normalisation uncertainties added in quadrature.

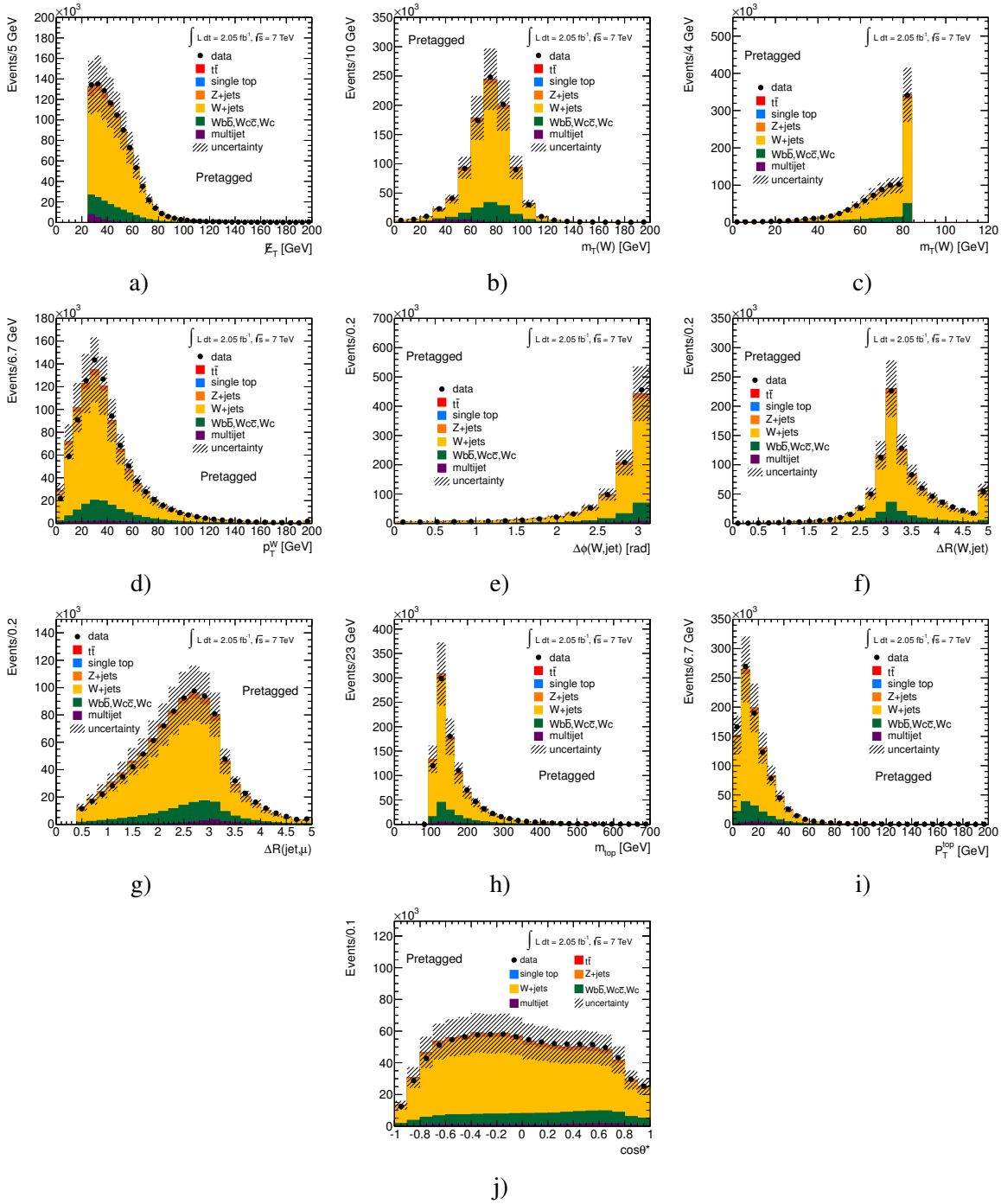

Figure A.6: Kinematic distributions for pretagged samples in the muon channel normalised to the number of observed events: a) Missing transverse momentum, b) transverse W-boson mass before determining the neutrino P_z , c) transverse W-boson mass after determining the neutrino P_z, d) the reconstructed W-boson P_T, e) $\Delta\phi$ between W boson and the jet, f) ΔR between W boson and the jet, g) ΔR between muon and the jet, h) the reconstructed top-quark mass, i) the reconstructed top-quark P_T and j) the W-boson helicity. The hatched band indicates the statistical and background normalisation uncertainties added in quadrature.

A.2.2 Kinematic Plots for the b-tagged Samples

The kinematic distributions of the identified lepton and reconstructed jet are shown in Figure A.7. Figure A.8 shows the kinematic distributions of $\not{E}_T$, $m_T(W)$, the reconstructed W-boson P_T, $\Delta\phi$ between W boson and the jet, ΔR between W boson and the jet, ΔR between electron and the jet, the reconstructed top-quark mass m_{top}, the reconstructed top-quark P_T and the W-boson helicity. The background is normalised to the observed number of events and the FCNC cross-section is assumed to be 100 pb and stacked on top of the background. The hatched band indicates the statistical and background normalisation uncertainties added in quadrature.

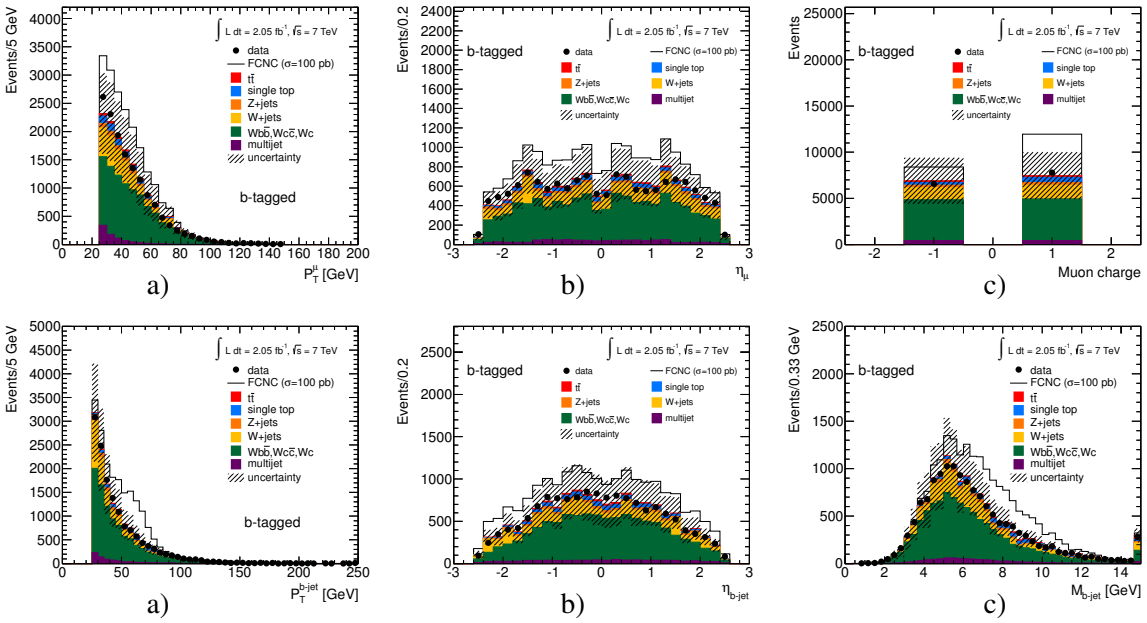

Figure A.7: Kinematic distributions for b-tagged samples normalised to the number of observed events : a) muon P_T, b) muon η, c) muon electric charge, d) P_T of the jet, e) η of the jet and f) the invariant mass of the jet. The hatched band indicates the statistical and background normalisation uncertainties added in quadrature.

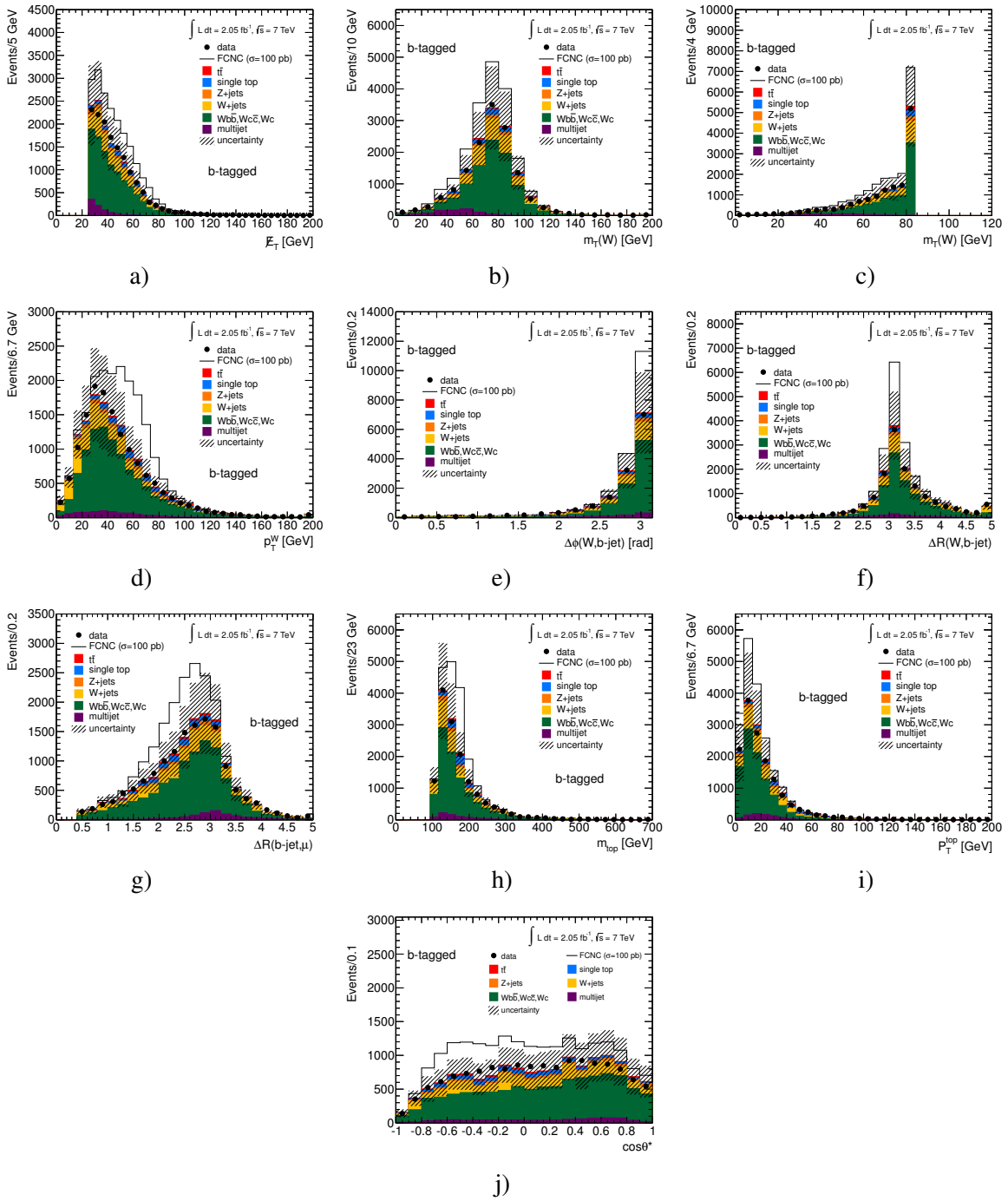

Figure A.8: Kinematic distributions for *b*-tagged samples in muon channel normalised to the number of observed events: a) Missing transverse momentum, b) transverse W-boson mass before determining the neutrino P_z , c) transverse W-boson mass after determining the neutrino P_z, d) the reconstructed W-boson P_T, e) $\Delta\phi$ between W boson and the jet, f) ΔR between W boson and the jet, g) ΔR between muon and the jet ,h) the reconstructed top-quark mass, i) the reconstructed top-quark P_T and j) the W-boson helicity. The hatched band indicates the statistical and background normalisation uncertainties added in quadrature.

Appendix B

Correlations

Comparison of data and MC in the correlation coefficient distributions between the input variables used to train the neural network.

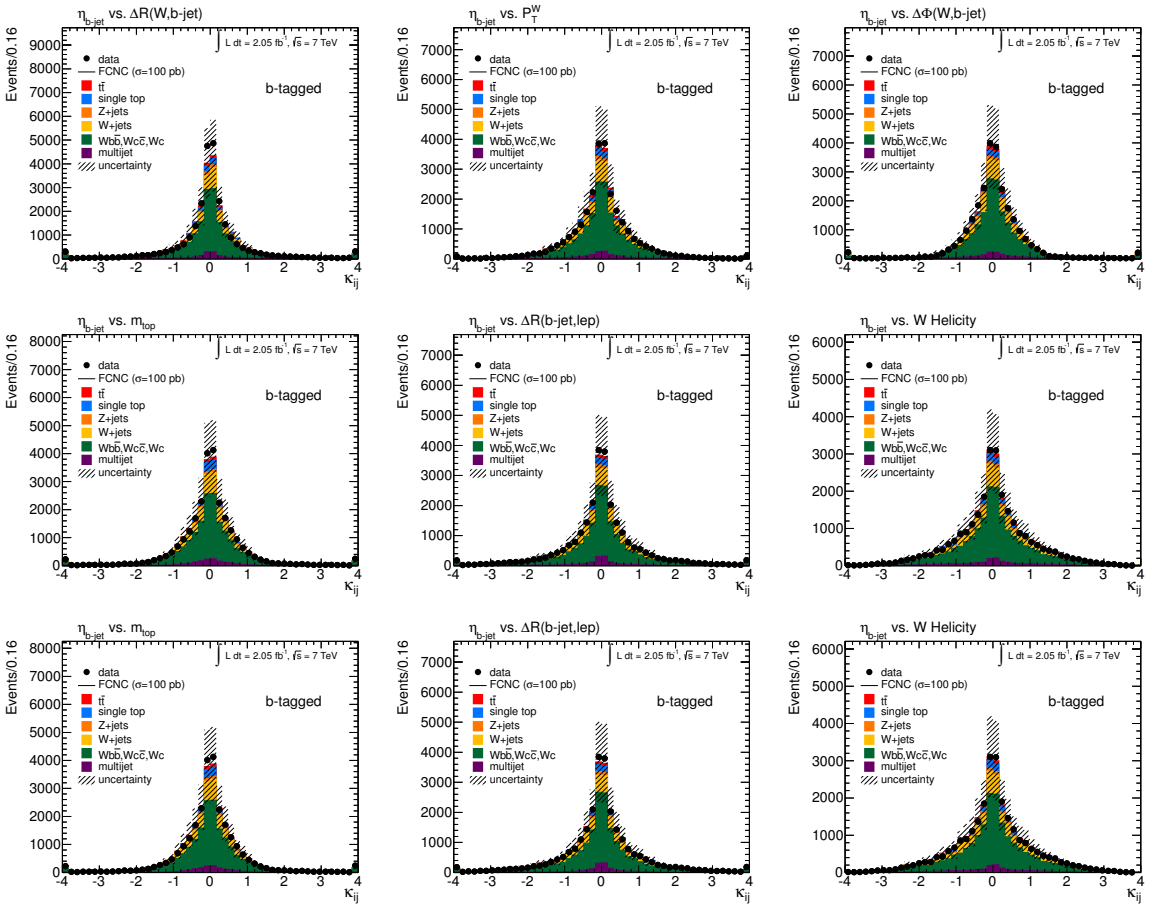

Figure B.1: Correlation plots.

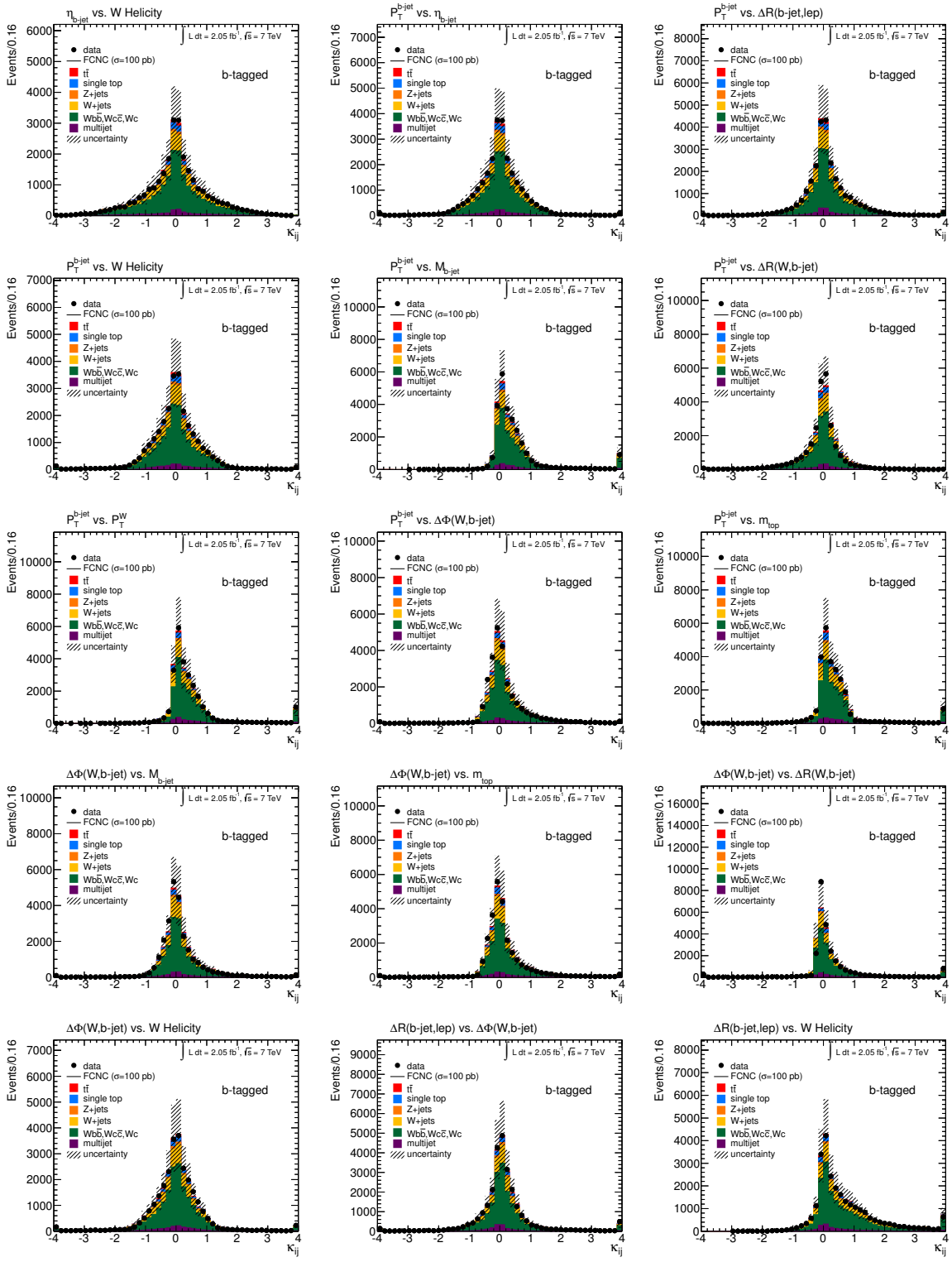

Figure B.2: Correlation plots.

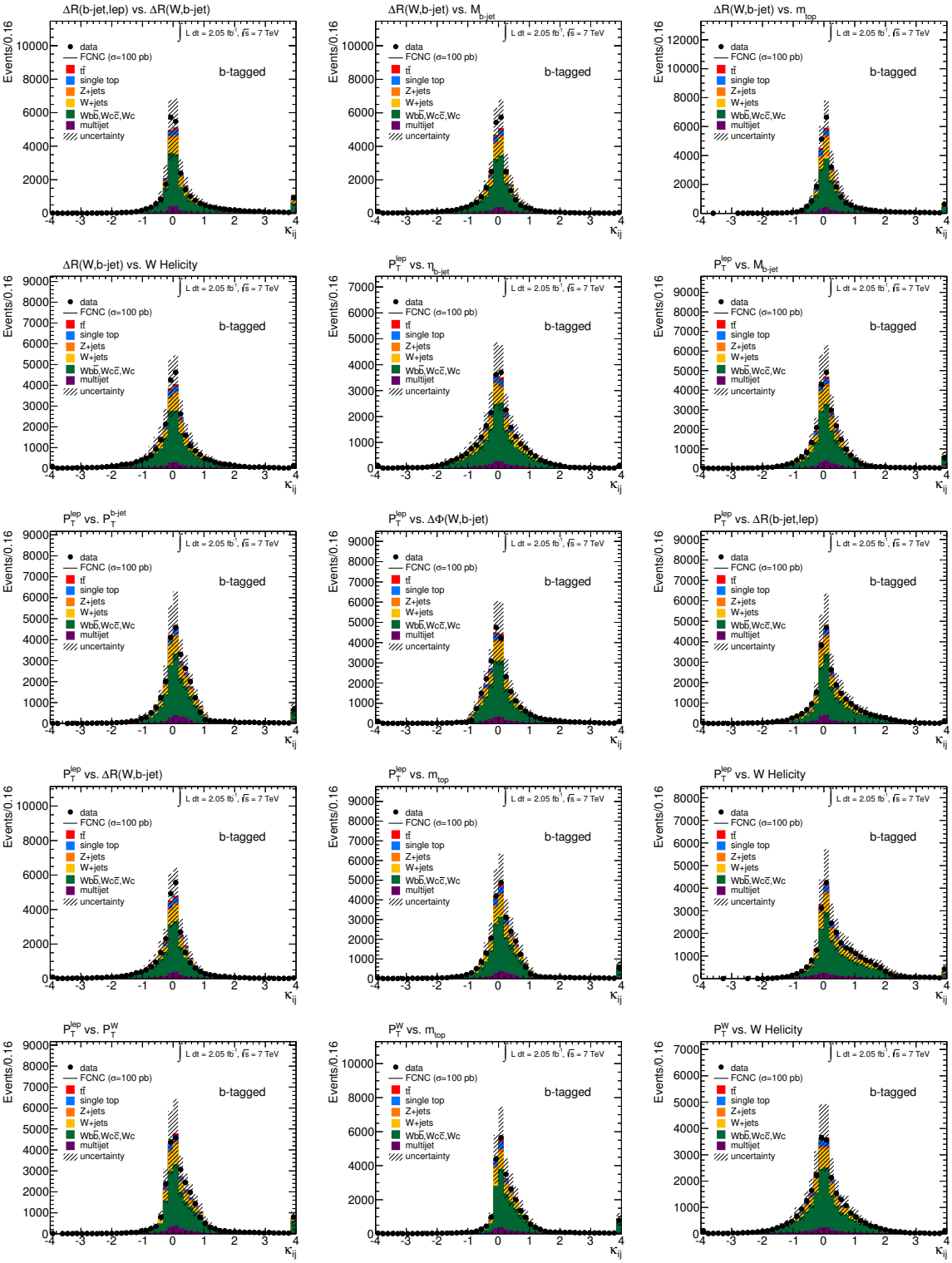

Figure B.3: Correlation plots.

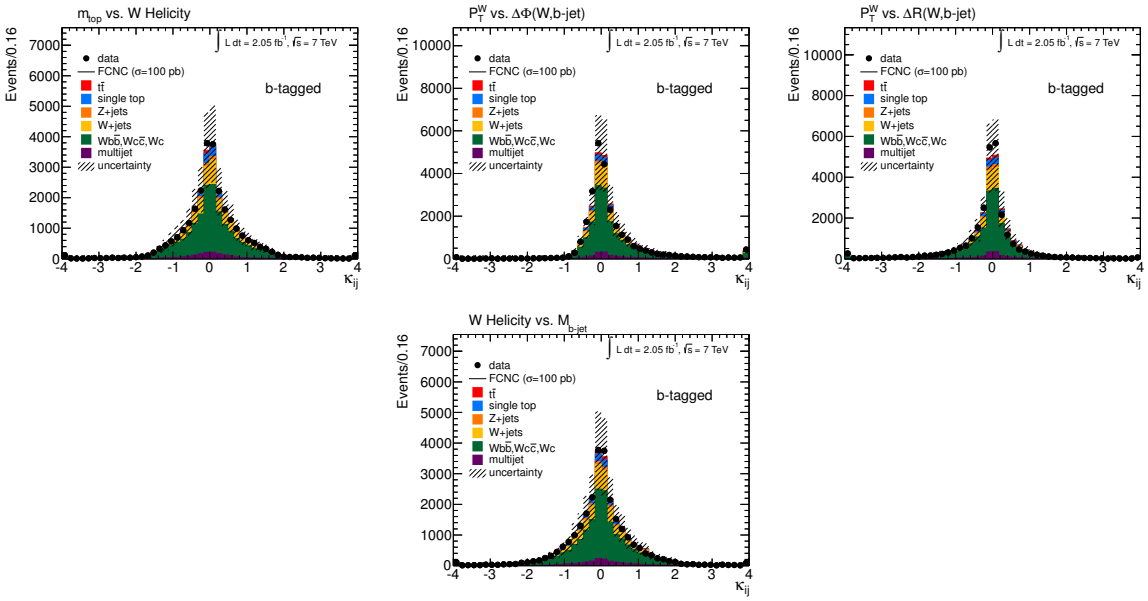

Figure B.4: Correlation plots.

Appendix C

Neural Network Output Distributions

C.1 Pretagged Sample

Neural network output distributions in the pretagged samples for the muon and the electron channels separately.

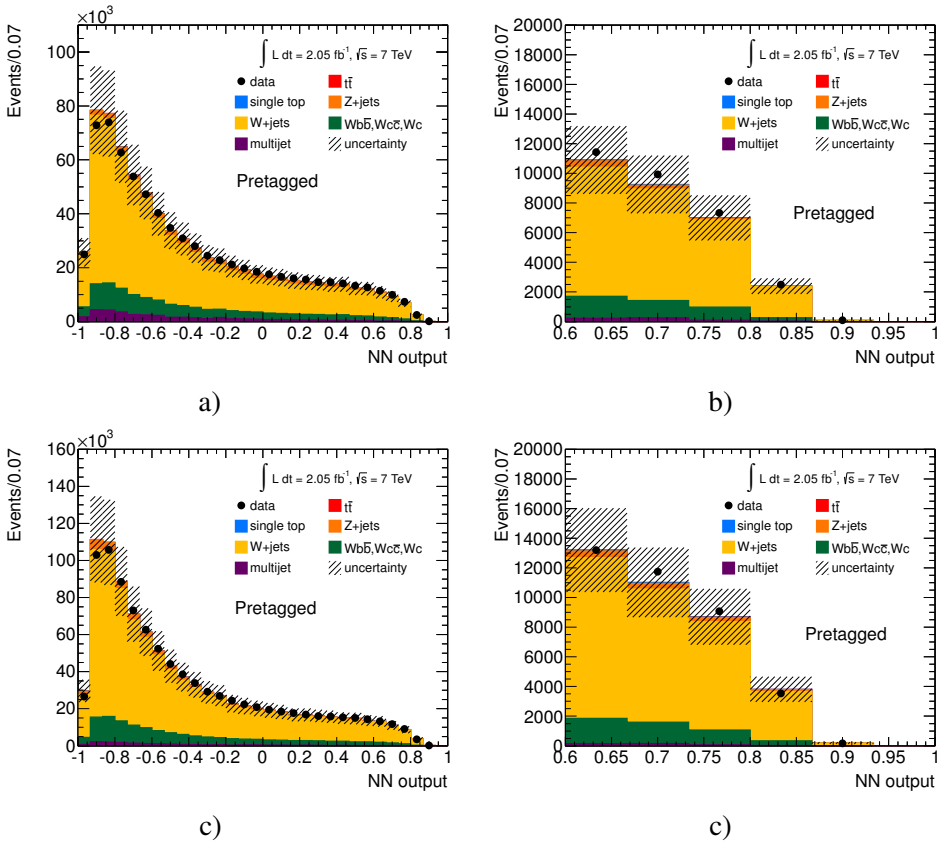

Figure C.1: Distributions of the neural network output for the pretagged sample: a) The observed data and MC background distribution normalised to the number of data events; b) Zoom into the high NN output region where the signal is expected to be in the *b*-tagged sample; c) The observed data and MC background distribution normalised to the number of data events; d) Zoom into the high NN output region where the signal is expected to be in the *b*-tagged sample. a) and b) for electron channel, c) and d) for muon channel. The hatched band indicates the statistical and background normalisation uncertainties added in quadrature.

C.2 b-tagged Samples

Neural network output distributions in the *b*-tagged sample for the muon and electron channels separately.

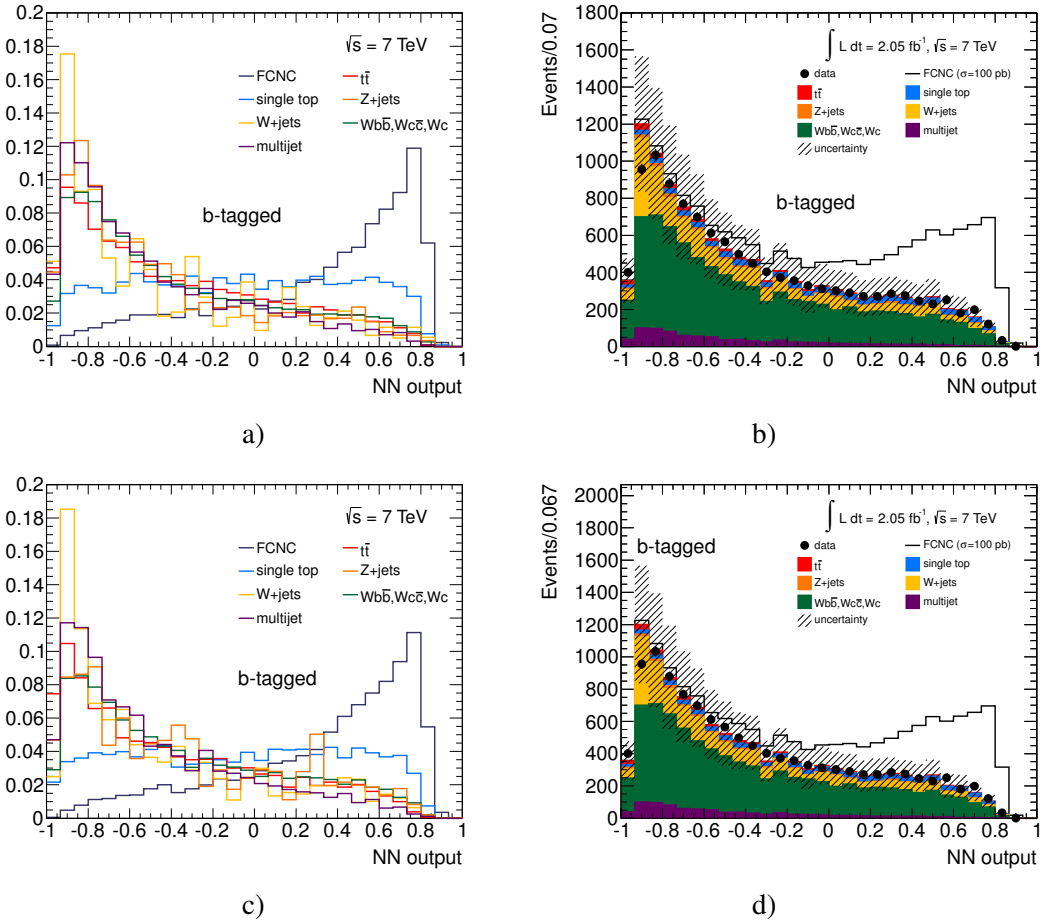

Figure C.2: a) Signal and background output distributions normalised to unity for the muon channel, b) observed signal and simulated background output distributions normalised to the number of data events in the *b*-tagged sample for the muon channel, c) signal and background output distributions normalised to unity for the electron channel, b) observed signal and simulated background output distributions normalised to the number of data events in the *b*-tagged sample for the electron channel. The signal process is stacked on top the background after scaling it to a cross-section of 100 pb. The hatched band indicates the statistical and background normalisation uncertainties.

Appendix D

Shifts in the NN outputs

This section contains the NN output distributions for the nominal case and after including the systematic uncertainties for the muon and the electron channels combined. Only processes that might be affected by the systematic uncertainties are shown. Every plot contains two parts: the upper part which contains the NN output distributions for the nominal and after including the upward and downward fluctuations normalised to the unity, while the lower part contains the relative difference between the shifted distributions and the default one.

D.1 Object Energy Scale and Momentum Resolution

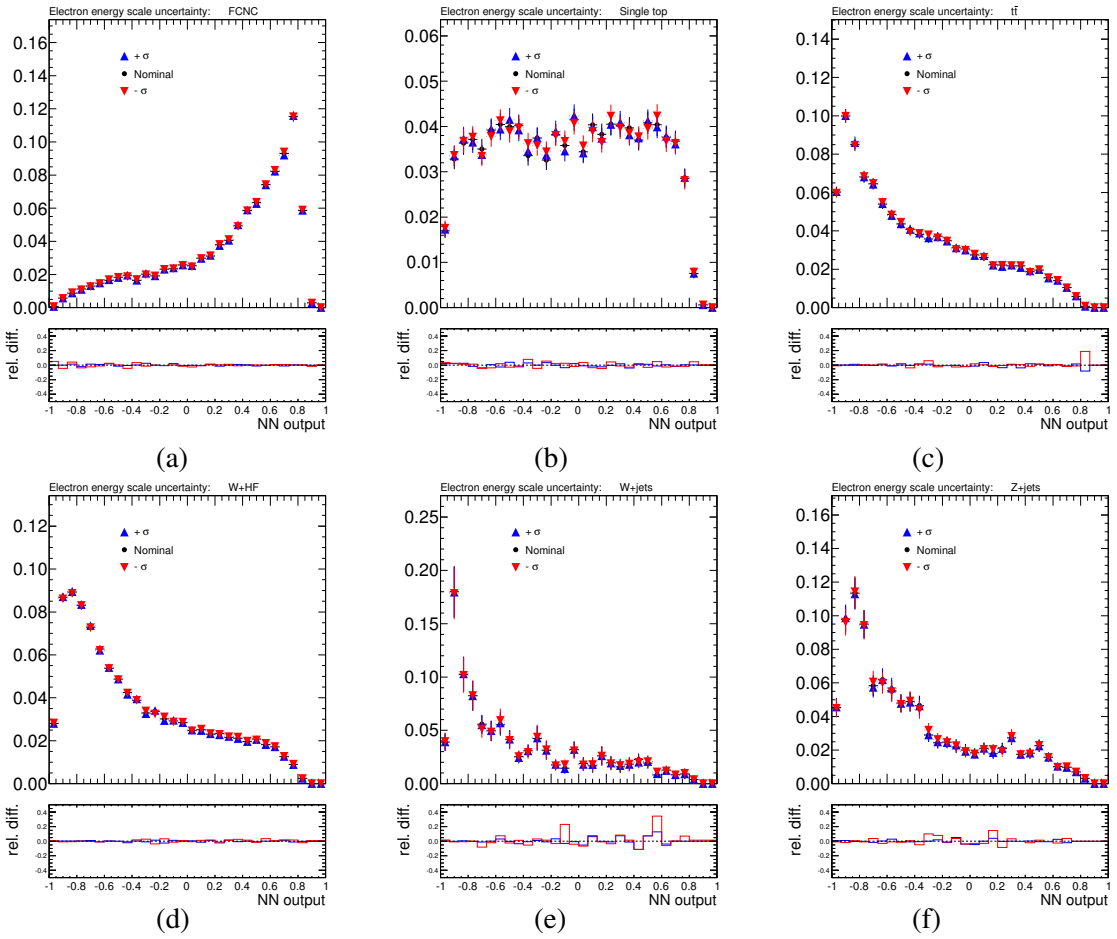

Figure D.1: Shifts in the NN outputs caused by the uncertainty of the electron energy scale. a) For FCNC, b) SM single top-quark, c) $t\bar{t}$, d) W+HF jets, e) W+light jets and f) Z+jets.

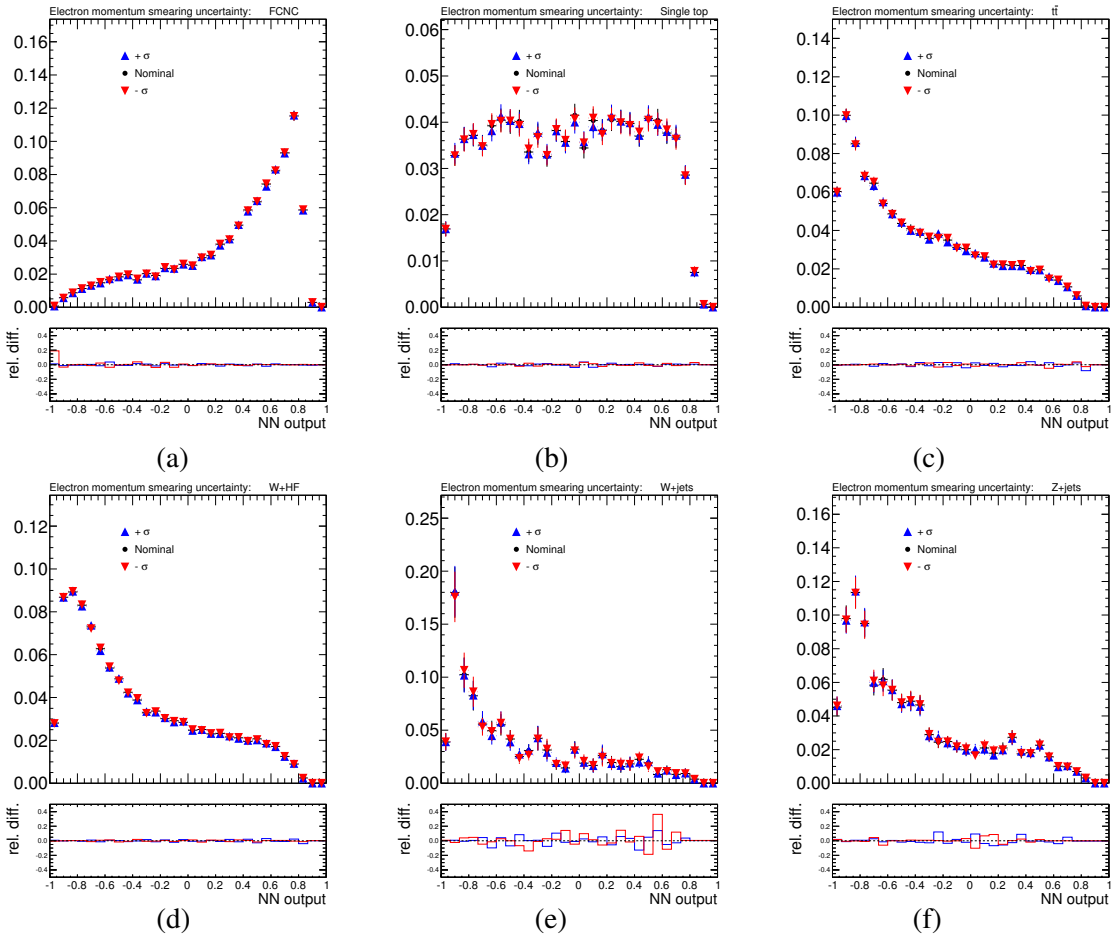

Figure D.2: Shifts in the NN outputs caused by the uncertainty of the electron momentum resolution. a) for FCNC, b) SM single top-quark, c) $t\bar{t}$, d) W+HF jets, e) W+light jets and f) Z+jets.

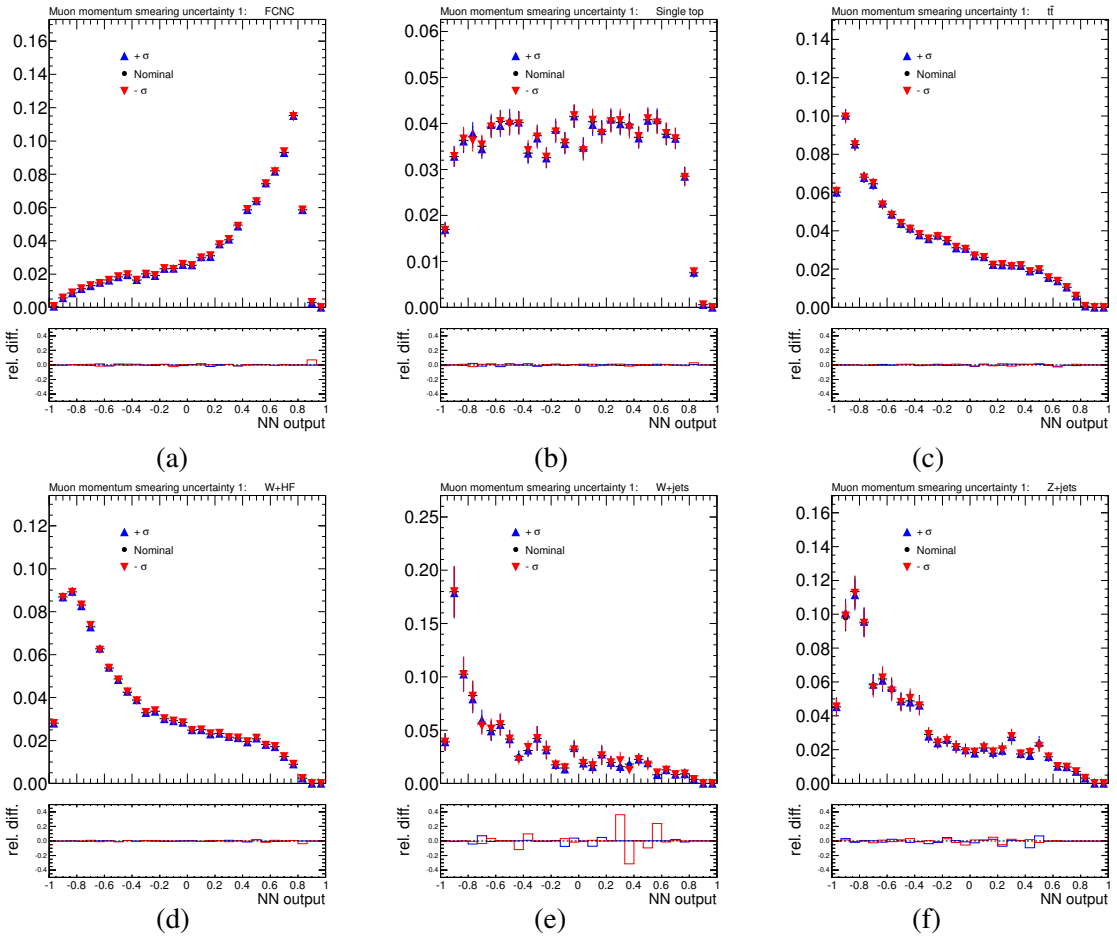

Figure D.3: Shifts in the NN outputs caused by the uncertainty of the muon momentum resolution. a) for FCNC, b) SM single top-quark, c) $t\bar{t}$, d) W+HF jets, e) W+light jets and f) Z+jets.

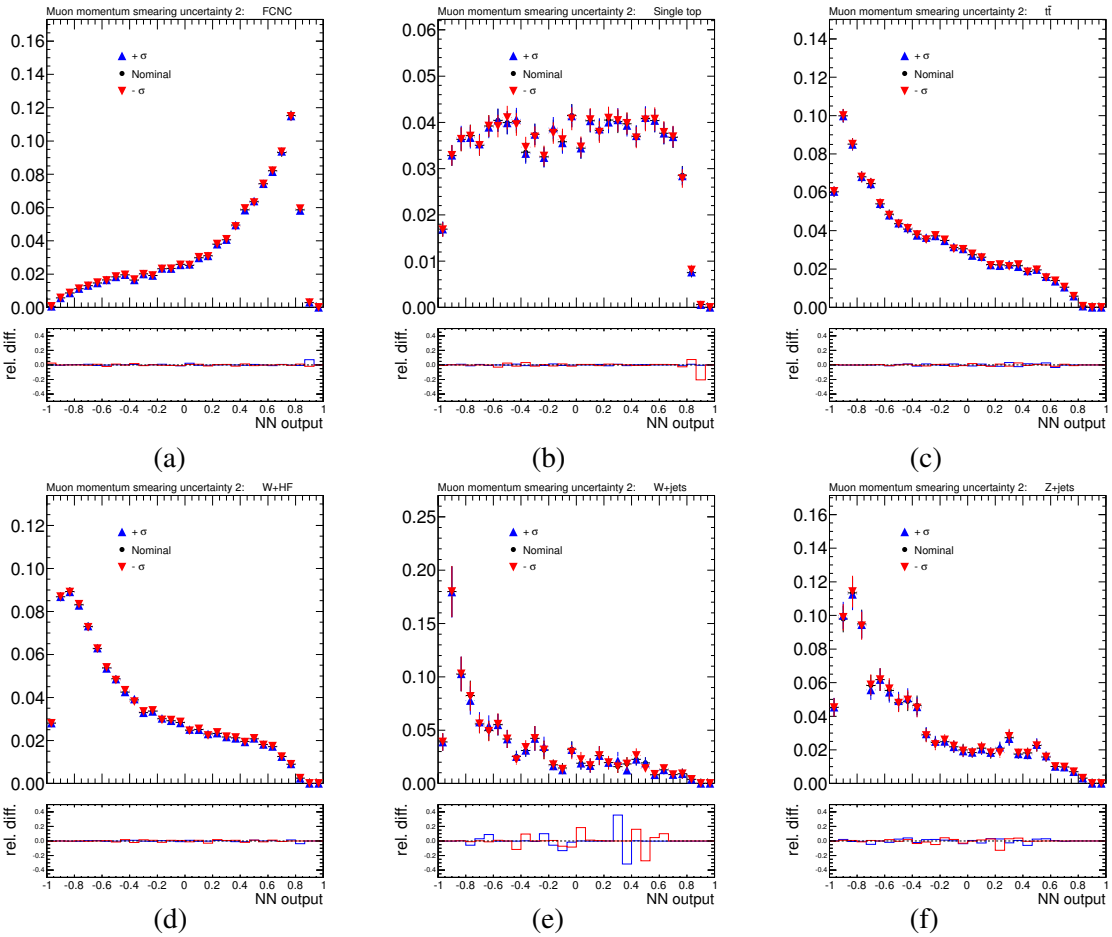

Figure D.4: Shifts in the NN outputs caused by the uncertainty of the muon momentum resolution. a) for FCNC, b) SM single top-quark, c) $t\bar{t}$, d) W+HF jets, e) W+light jets and f) Z+jets.

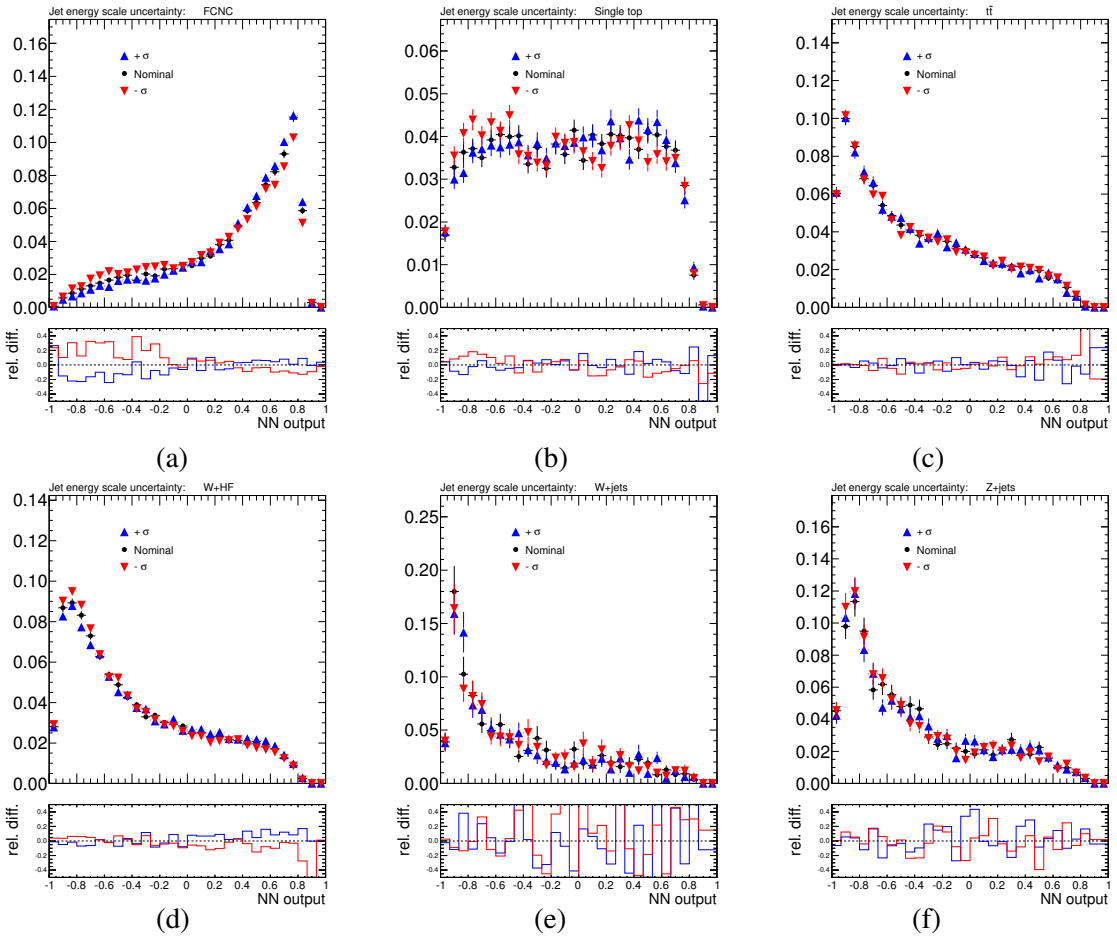

Figure D.5: Shifts in the NN outputs caused by the uncertainty on the jet energy scale. a) for FCNC, b) SM single top-quark, c) $t\bar{t}$, d) W+HF jets, e) W+light jets and f) Z+jets.

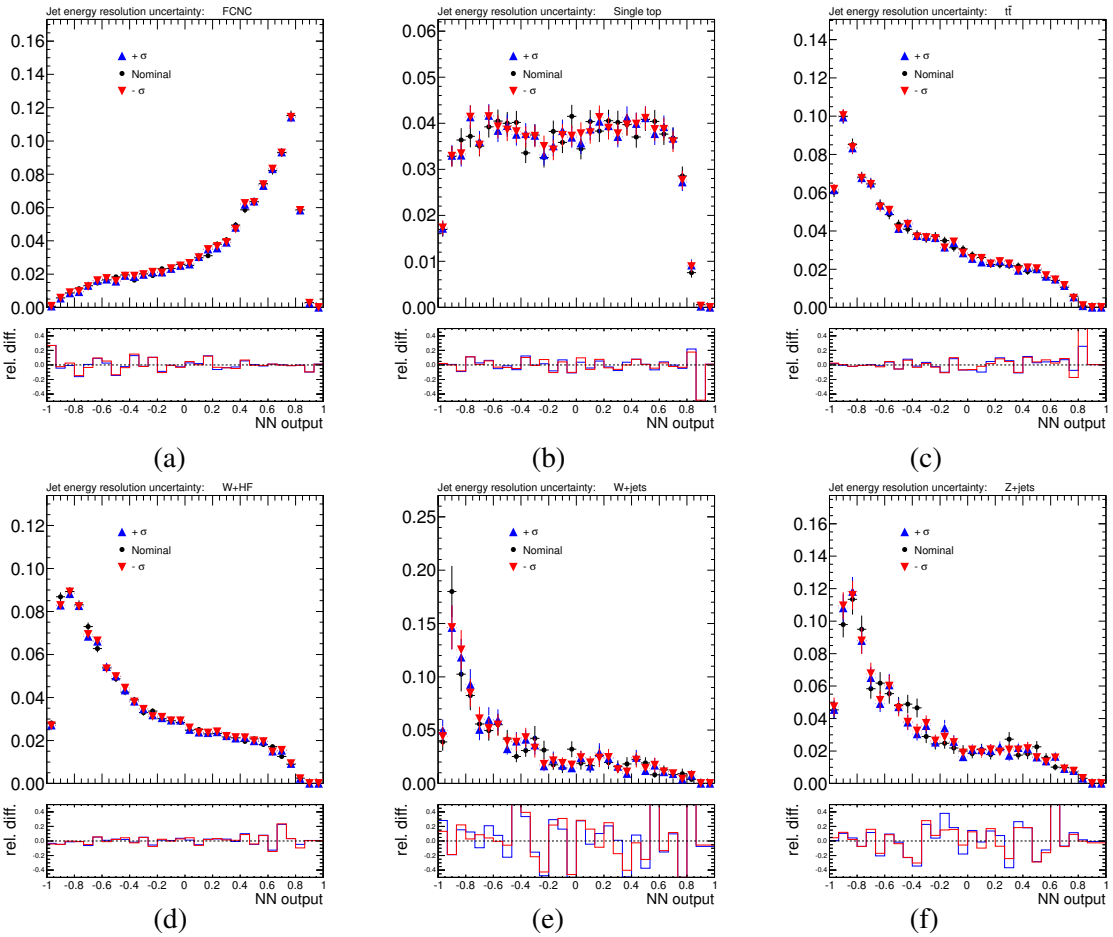

Figure D.6: Shifts in the NN outputs caused by the uncertainty of the jet energy resolution. a) for FCNC, b) SM single top-quark, c) $t\bar{t}$, d) W+HF jets, e) W+light jets and f) Z+jets.

D.2 Object Reconstruction Efficiencies

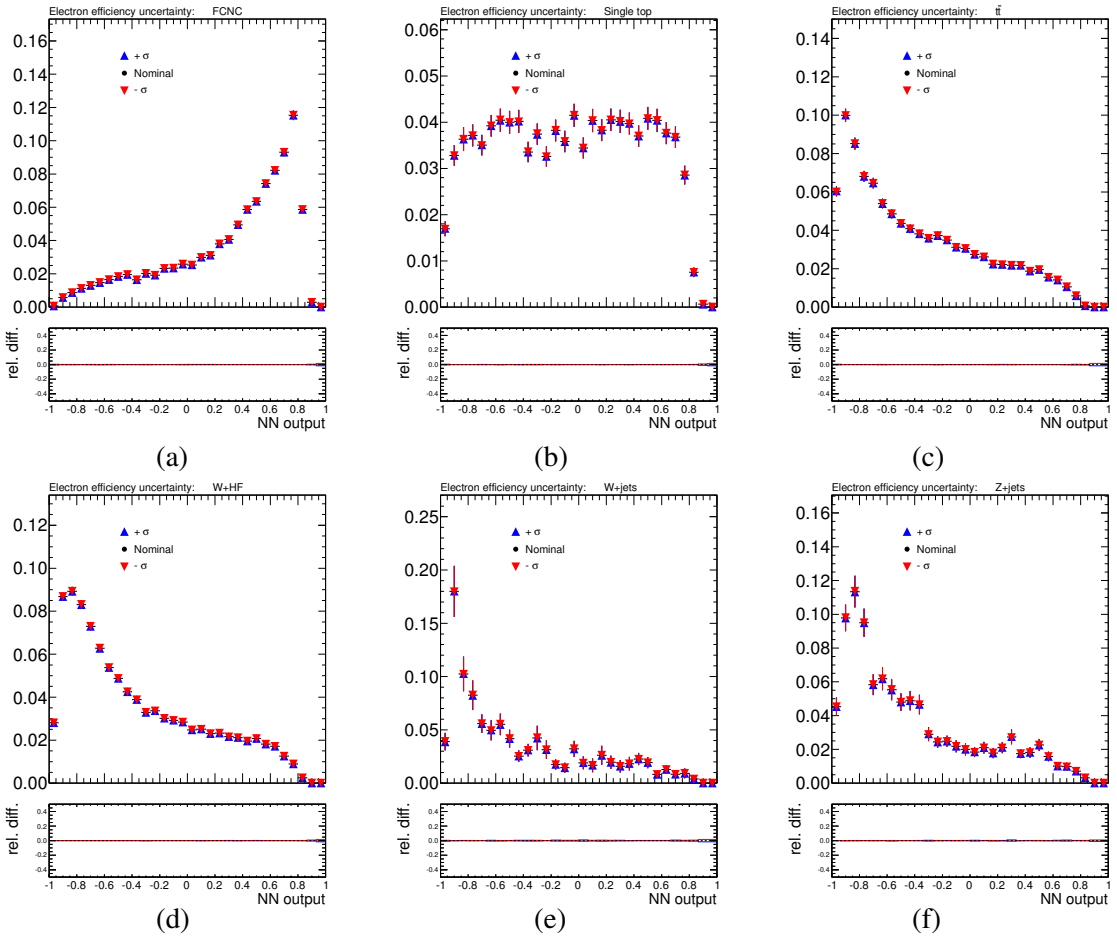

Figure D.7: Shifts in the NN outputs caused by the uncertainty of electron correction scale factors. a) for FCNC, b) SM single top-quark, c) $t\bar{t}$, d) W+HF jets, e) W+light jets and f) Z+jets.

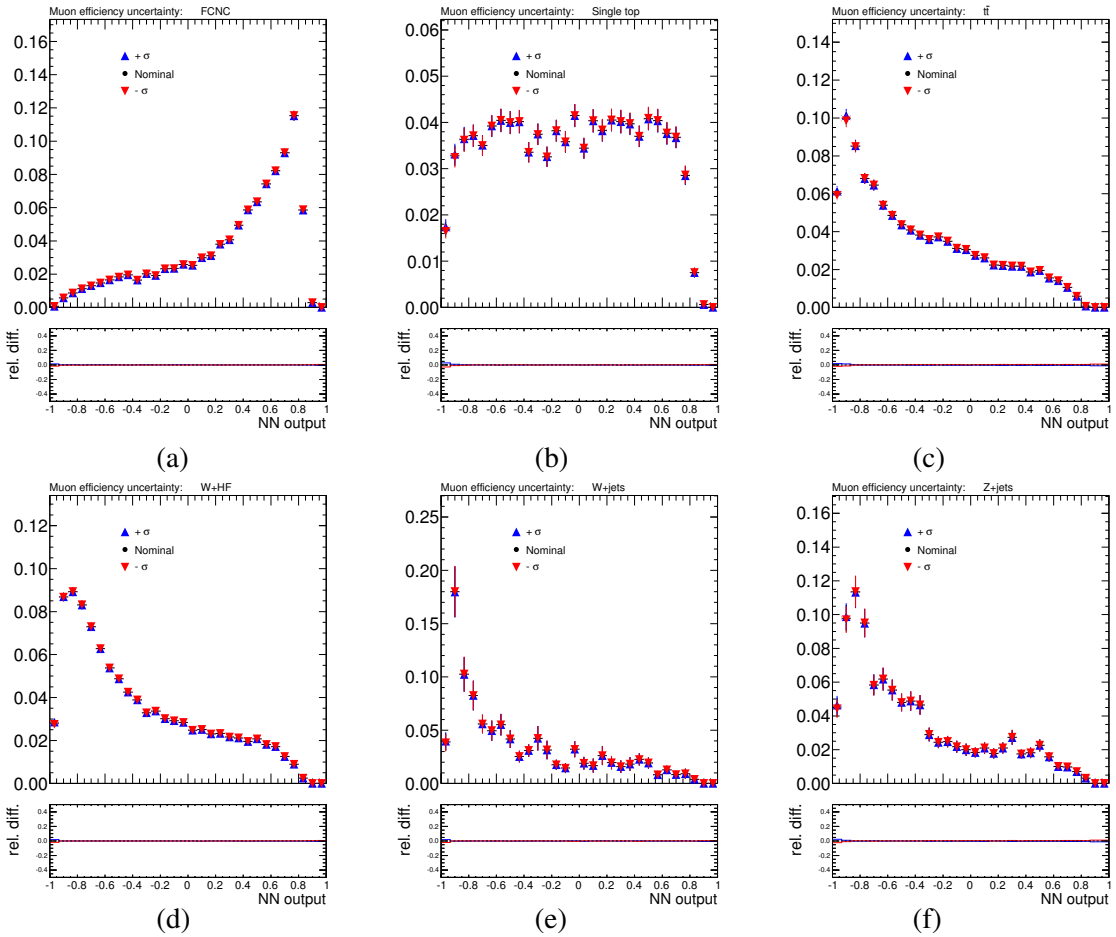

Figure D.8: Shifts in the NN outputs caused by the uncertainty of the muon correction scale factors. a) for FCNC, b) SM single top-quark, c) $t\bar{t}$, d) W+HF jets, e) W+light jets and f) Z+jets.

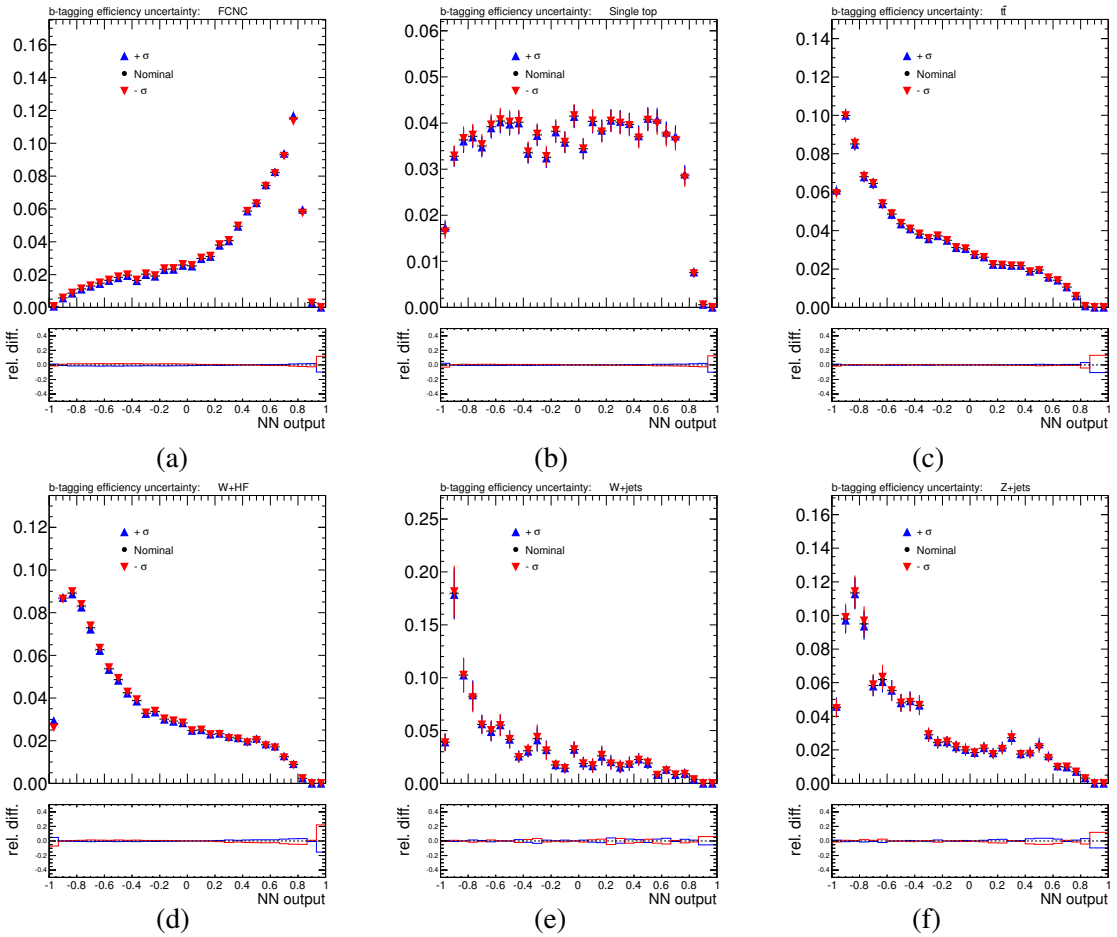

Figure D.9: Shifts in the NN outputs caused by the uncertainty of the b-tagging efficiency. a) For FCNC, b) SM single top-quark, c) $t\bar{t}$, d) W+HF jets, e) W+light jets and f) Z+jets.

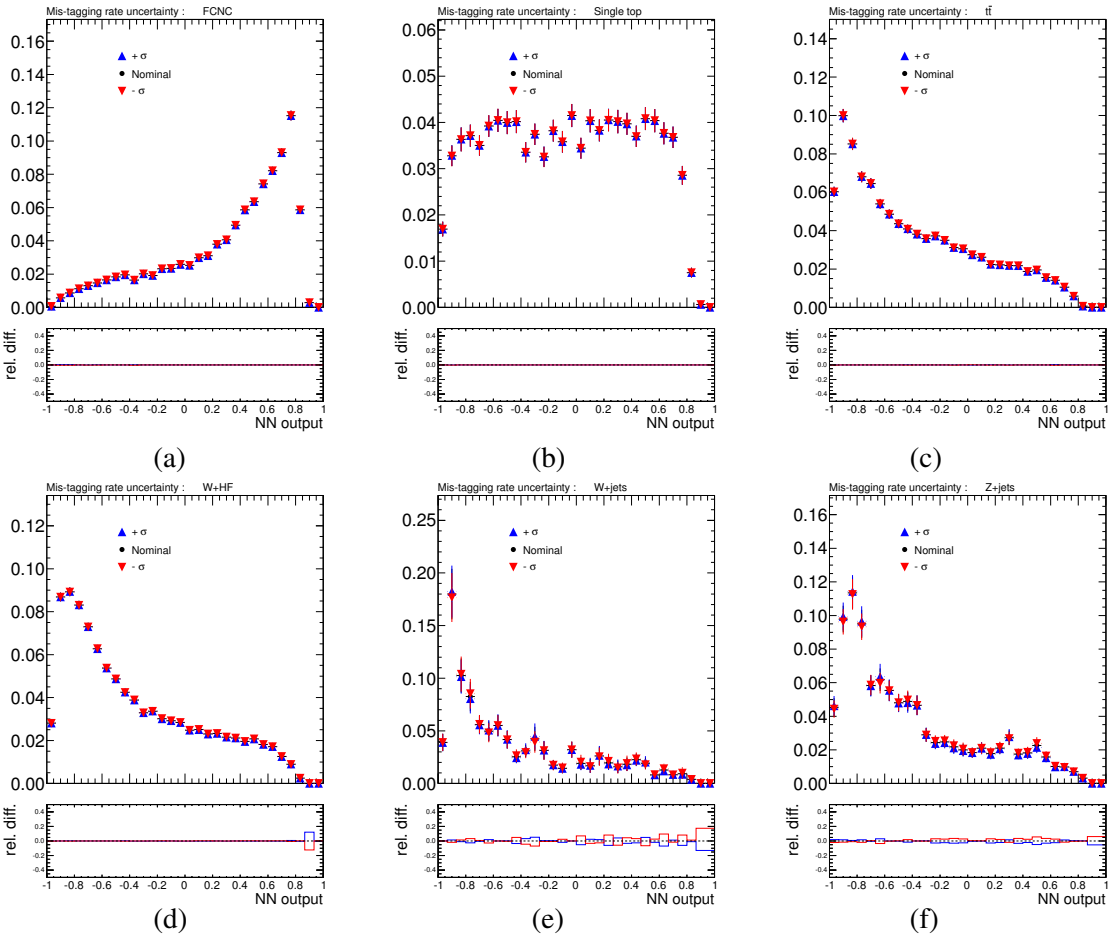

Figure D.10: Shifts in the NN outputs caused by the uncertainty of light-quark jet mis-tagging. a) For FCNC, b) SM single top-quark, c) $t\bar{t}$, d) W+HF jets, e) W+light jets and f) Z+jets.

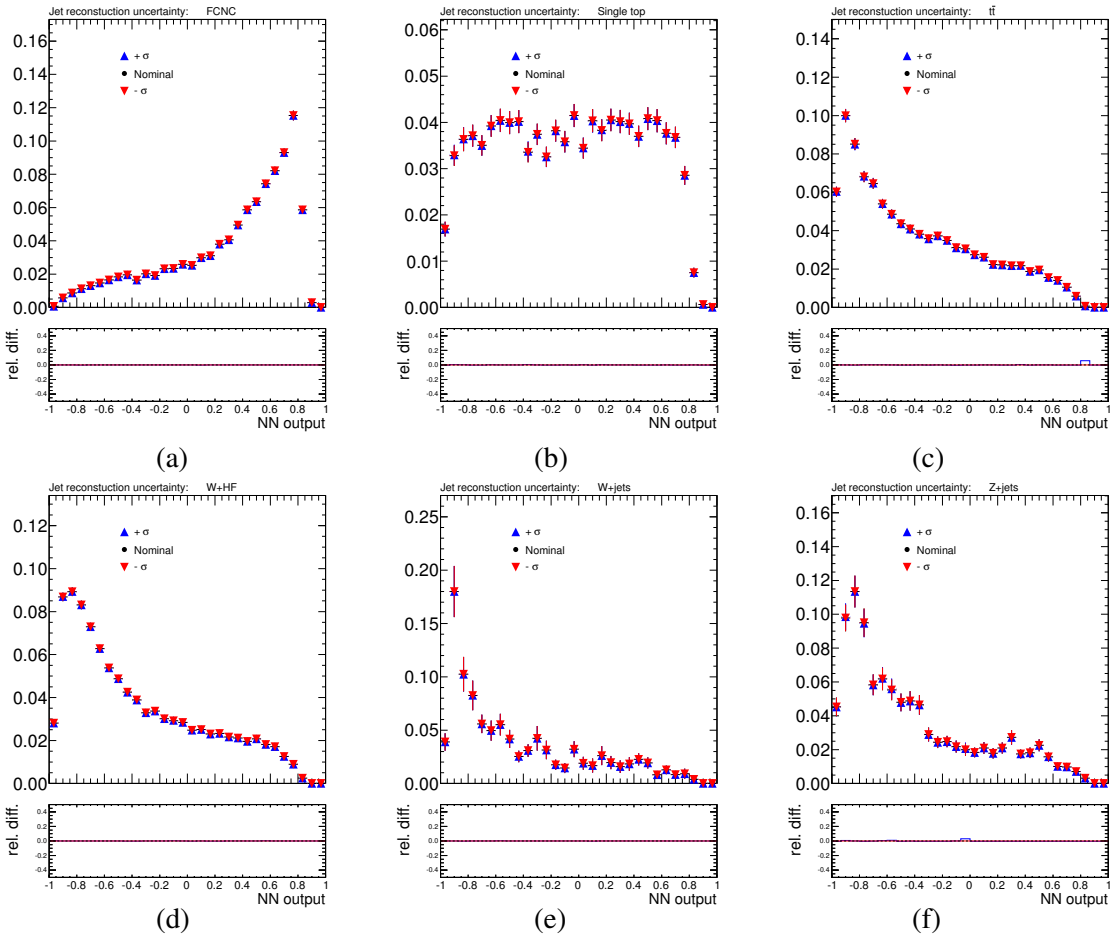

Figure D.11: Shifts in the NN outputs caused by the uncertainty of the jet reconstruction. a) For FCNC, b) SM single top-quark, c) $t\bar{t}$, d) W+HF jets, e) W+light jets and f) Z+jets.

D.3 Monte Carlo Generators and PDF Uncertainties

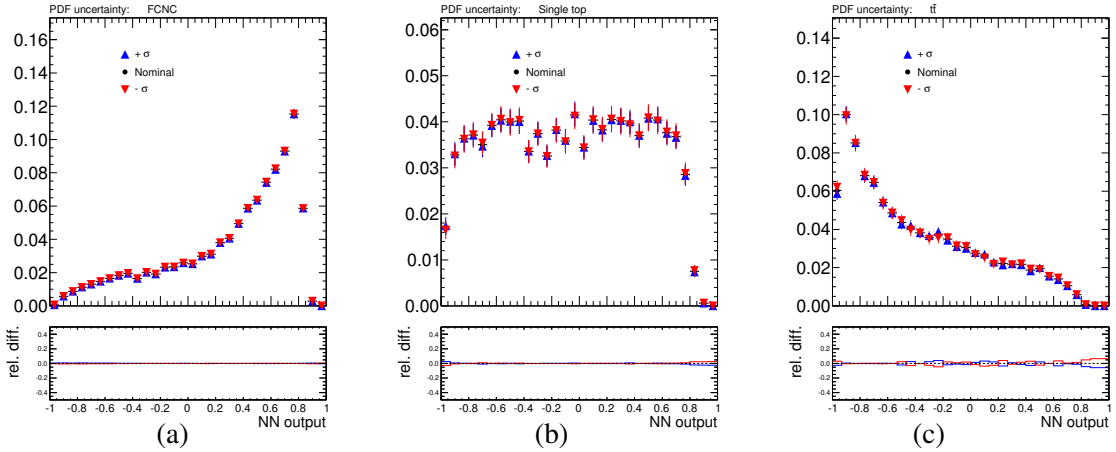

Figure D.12: Shifts in the NN outputs caused by the PDF uncertainties. a) For FCNC, b) SM single top-quark and c) $t\bar{t}$.

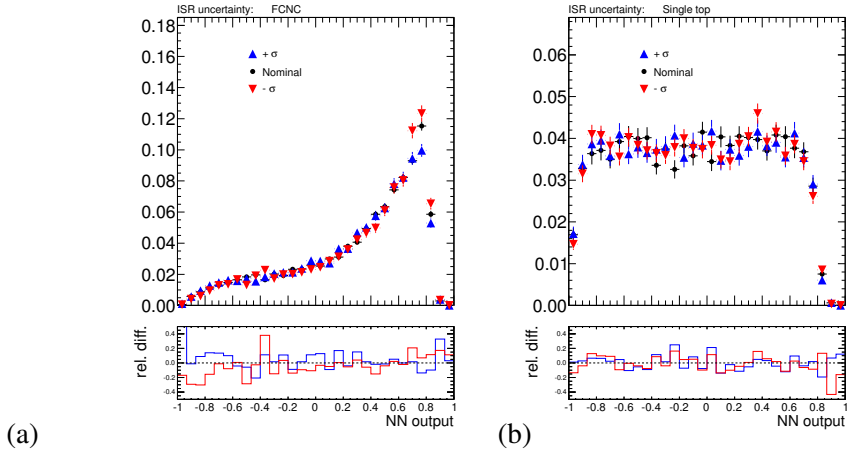

Figure D.13: Shifts in the NN outputs caused by the ISR uncertainty. a) For FCNC and b) SM single top-quark.

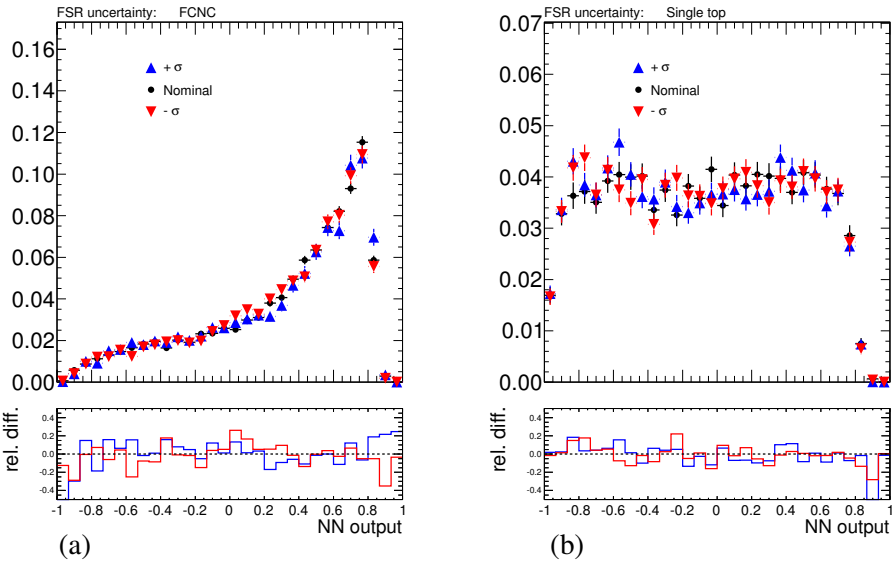

Figure D.14: Shifts in the NN outputs caused by the FSR uncertainty. a) For FCNC and b) SM single top-quark.

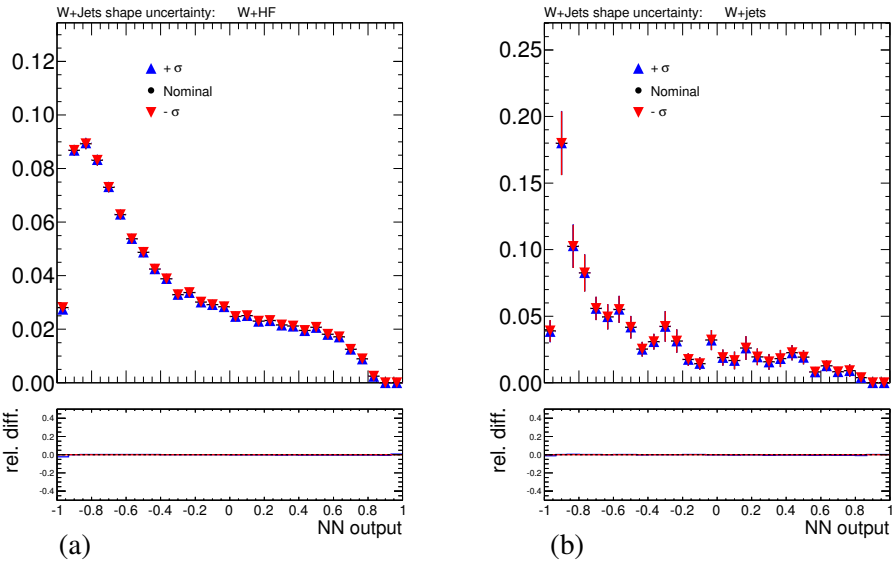

Figure D.15: Shifts in the NN outputs caused by the uncertainty of the W+jets kinematics. a) W+light jets and b) W+HF jets.

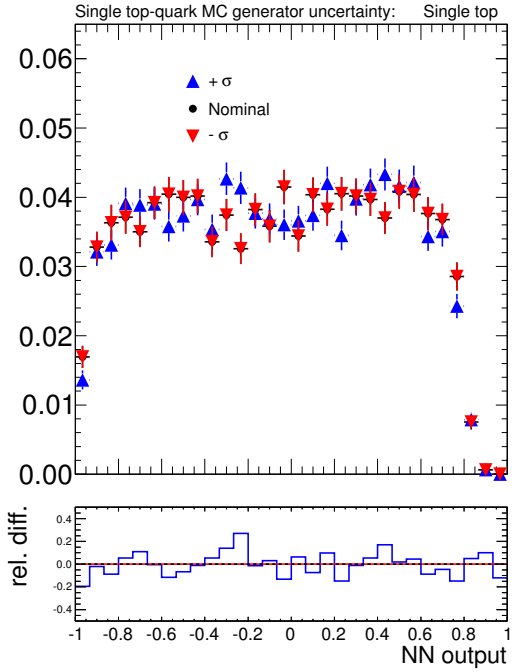

Figure D.16: Shifts in the NN outputs caused by the uncertainty of the single top-quark MC simulation. This is one-side systematic uncertainty.

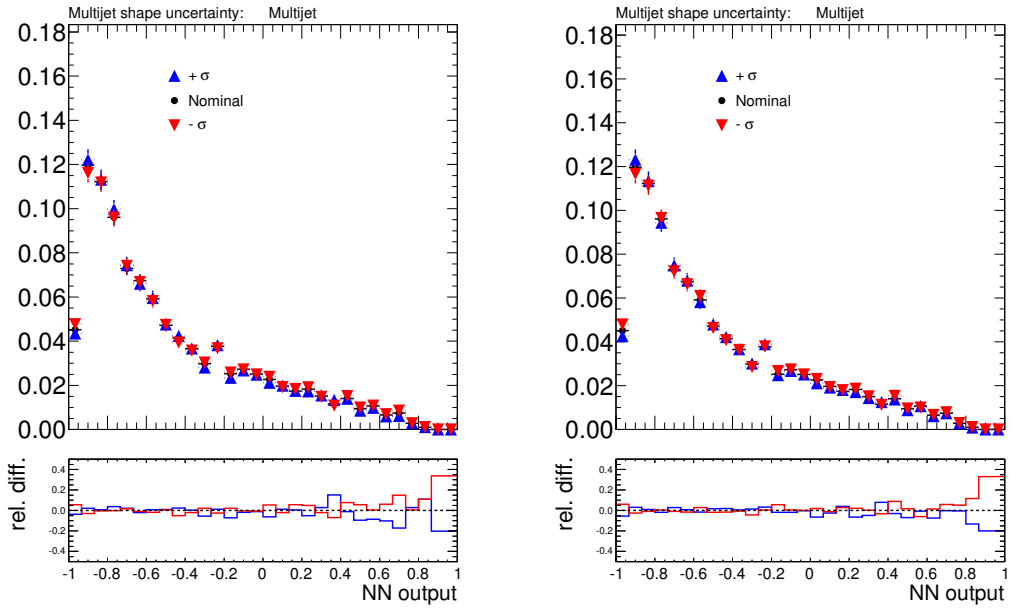

Figure D.17: Shifts in the NN outputs caused by the different multijet background shape modelling. a) For electron channel and b) muon channel.

D.4 LAr Hole

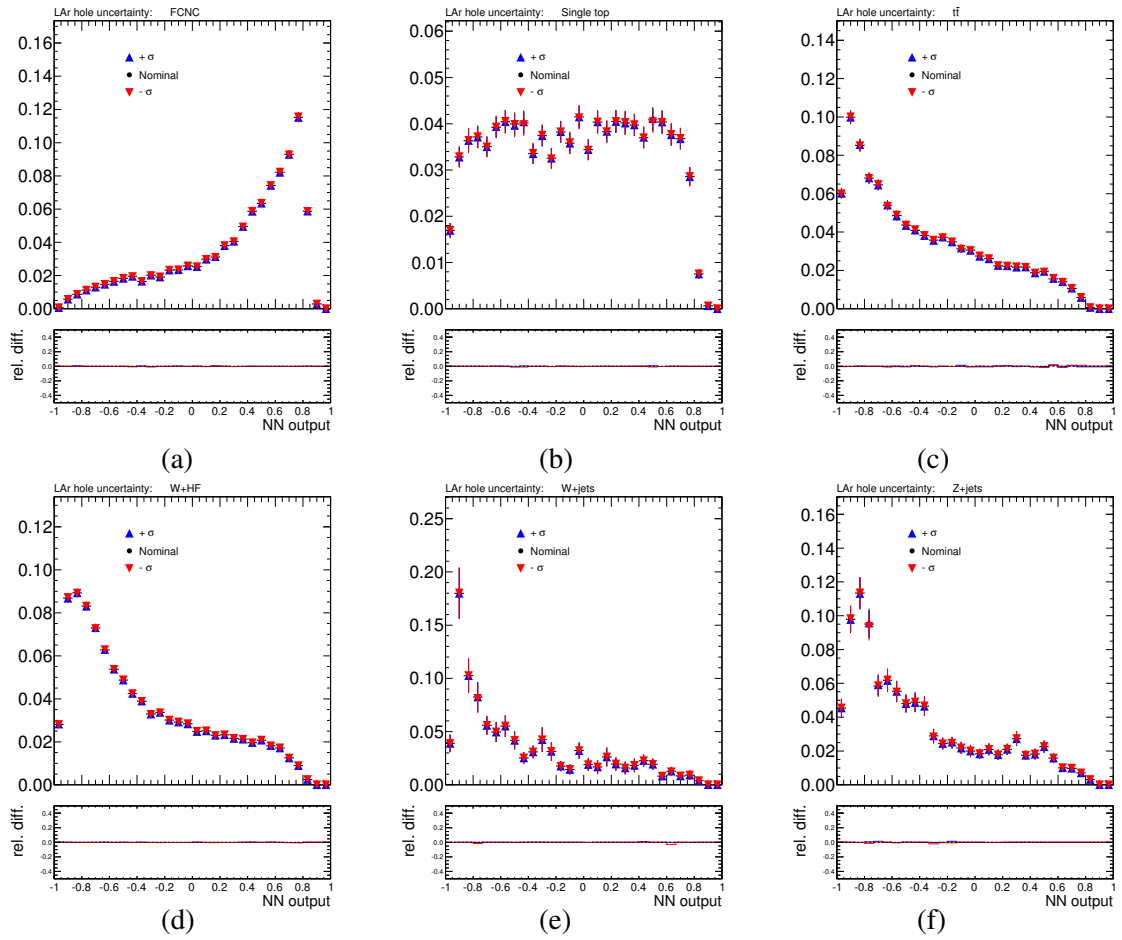

Figure D.18: Shifts in the NN outputs caused by the calorimeter problem treatment. a) For FCNC, b) SM single top-quark, c) $t\bar{t}$, d) W+HF jets, e) W+light jets and f) Z+jets.

Bibliography

[1] CDF and D0 Collaborations,
'Combination of CDF and D0 results on the mass of the top quark using up to 5.8 fb^{-1} of data' (2011), arXiv:1107.5255 [hep-ex].

[2] ATLAS Collaboration, 'Measurement of the Top Quark Pair Production Cross Section in pp Collisions at $\sqrt{s} = 7$ TeV in Dilepton Final States with ATLAS',
Phys. Lett. B707 (2012) 459–477, arXiv:1108.3699 [hep-ex].

[3] CMS Collaboration, 'Measurement of the $t\bar{t}$ production cross section in pp collisions at 7 TeV in lepton + jets events using b-quark jet identification', *Phys. Rev.* D84 (2011) 092004.

[4] CDF Collaboration, 'First observation of electroweak single top quark production',
Phys. Rev. Lett. 103 (2009) 092002, DOI: 10.1103/PhysRevLett.103.092002,
arXiv:0903.0885 [hep-ex].

[5] D0 Collaboration, 'Model-independent measurement of t-channel single top quark production in $p\bar{p}$ collisions at $\sqrt{s} = 1.96$ TeV' (2011), arXiv:1105.2788 [hep-ex].

[6] ATLAS Collaboration, 'Measurement of the t-channel Single Top-Quark Production Cross Section in 0.70 fb^{-1} of pp Collisions at $\sqrt{s} = 7$ TeV with the ATLAS detector',
tech. rep. ATLAS-CONF-2011-101, Geneva: CERN, 2011.

[7] CMS Collaboration, 'Measurement of the t-channel single top quark production cross section in pp collisions at $\sqrt{s} = 7$ TeV', *Phys. Rev. Lett.* 107 (2011) 091802,
DOI: 10.1103/PhysRevLett.107.091802, arXiv:1106.3052 [hep-ex].

[8] S. L. Glashow and others, 'Weak interactions with lepton-hadron symmetry',
Phys. Rev. D2 (1970) 1285–1292, DOI: 10.1103/PhysRevD.2.1285.

[9] J. A. Aguilar-Saavedra, 'Top flavour-changing neutral interactions: Theoretical expectations and experimental detection', *Acta Phys. Polon.* B35 (2004) 2695–2710,
arXiv:hep-ph/0409342.

[10] R. A. Coimbra and others, 'Dimension six FCNC operators and top production at the LHC',
Phys. Rev. D79 (2009) 014006, DOI: 10.1103/PhysRevD.79.014006,
arXiv:0811.1743 [hep-ph].

[11] CDF Collaboration, 'Search for the flavor changing neutral current decay $t \to Zq$ in $p\bar{p}$ collisions at $\sqrt{s} = 1.96$ TeV', *Phys. Rev. Lett.* 101 (2008) 192002,
DOI: 10.1103/PhysRevLett.101.192002, arXiv:0805.2109 [hep-ex].

[12] D0 Collaboration, 'Search for flavor changing neutral currents in decays of top quarks' (2011),
arXiv:1103.4574 [hep-ex].

[13] M. Feindt and U. Kerzel, 'The NeuroBayes neural network package',
Nucl. Instrum. Meth. A559 (2006) 190–194, DOI: 10.1016/j.nima.2005.11.166.

[14] ATLAS Collaboration,
'Search for FCNC single top-quark production at $\sqrt{s} = 7$ TeV with the ATLAS detector',
Phys. Lett. B712 (June 2012) 351–369, arXiv:1203.0529 [hep-ex].

[15] D0 Collaboration, 'Search for flavor changing neutral currents via quark-gluon couplings in single top quark production using 2.3 fb^{-1} of $p\bar{p}$ collisions', *Phys. Lett.* B693 (2010) 81–87, DOI: 10.1016/j.physletb.2010.08.011, arXiv:1006.3575 [hep-ex].

[16] S. Glashow, 'Partial-symmetries of weak interactions',
Nuclear Physics 22.4 (Feb. 1961) 579–588, ISSN: 00295582,
DOI: 10.1016/0029-5582(61)90469-2,
URL: http://dx.doi.org/10.1016/0029-5582(61)90469-2.

[17] M. Mann, 'A Schematic model of baryons and mesons', *Phys. Lett.* 8 (1964) 214–215.

[18] M. G. Mann and others, 'The axial vector current in beta decay', *Nuovo Cim.* 16 (1960) 705.

[19] K. Nakamura and Particle Data Group, 'Review of particle physics',
Journal of Physics G: Nuclear and Particle Physics 37.7A (2010) 075021,
URL: http://stacks.iop.org/0954-3899/37/i=7A/a=075021.

[20] E. Noether, 'Invariant Variation Problems', *Gott.Nachr.* 1918 (1918) 235–257,
DOI: 10.1080/00411457108231446,10.1080/00411457108231446,
arXiv:0503066 [physics].

[21] P. W. Higgs, 'Broken symmetries, massless particles and gauge fields',
Phys. Lett. 12 (Sept. 1964) 132–133, DOI: 10.1016/0031-9163(64)91136-9,
URL: http://dx.doi.org/10.1016/0031-9163(64)91136-9.

[22] P. W. Higgs, 'Broken symmetries and the masses of gauge bosons',
Phys. Rev. Lett. 13.16 (Oct. 1964) 508–509, DOI: 10.1103/PhysRevLett.13.508,
URL: http://dx.doi.org/10.1103/PhysRevLett.13.508.

[23] C. Rubbia, 'Discovery of W^+W^- and Z^0 bosons' (1984).

[24] M. Kobayashi and others, 'CP-Violation in the Renormalizable Theory of Weak Interaction',
Prog. Theor. Phys. 49 (1973) 652–657, DOI: 10.1143/PTP.49.652.

[25] Durham university, *HEPDATA*, URL: http://hepdata.cedar.ac.uk/pdf/pdf3.html.

[26] CDF Collaboration, 'Evidence for Top Quark Production in $p\bar{p}$ Collisions at $\sqrt{s} = 1.8$ TeV',
Phys. Rev. Lett. 73 (1994) 225–231, DOI: 10.1103/PhysRevLett.73.225,
arXiv:9405005 [hep-ex].

[27] D0 Collaboration, 'Observation of the Top Quark', *Phys. Rev. Lett.* 74 (1995) 2632–2637,
DOI: 10.1103/PhysRevLett.74.2632, arXiv:9503003 [hep-ex].

[28] ATLAS Collaboration, 'Measurement of the top quark-pair production cross section with ATLAS in pp collisions at $\sqrt{s} = 7$ TeV', *Eur. Phys. J* C71 (2011) 1577,
DOI: 10.1140/epjc/s10052-011-1577-6, arXiv:1012.1792 [hep-ex].

[29] CMS Collaboration, 'First Measurement of the Cross Section for Top-Quark Pair Production in Proton-Proton Collisions at $\sqrt{s} = 7$ TeV', *Phys. Lett.* B695 (2011) 424–443,
arXiv:1010.5994 [hep-ex].

[30] U. Langenfeld and others, 'New results for $t\bar{t}$ production at hadron colliders' (2009),
arXiv:0907.2527 [hep-ph].

[31] S. Moch and others,
'Theoretical status and prospects for top-quark pair production at hadron colliders',
Phys. Rev. D78 (2008) 034003, DOI: 10.1103/PhysRevD.78.034003,
arXiv:0804.1476 [hep-ph].

[32] N. Kidonakis, 'Next-to-next-to-leading-order collinear and soft gluon corrections for t-channel single top quark production', *Phys.Rev.* D83 (2011) 091503,
DOI: 10.1103/PhysRevD.83.091503, arXiv:1103.2792 [hep-ph].

[33] N. Kidonakis, 'Two-loop soft anomalous dimensions for single top quark associated production with a W^- or H^-', *Phys. Rev.* D82 (2010) 054018,
eprint: arXiv:1005.4451[hep-ph].

[34] N. Kidonakis, 'NNLL resummation for s-channel single top quark production',
Phys. Rev. D81 (2010) 054028, eprint: arXiv:1001.5034[hep-ph].

[35] D0 Collaboration, 'Observation of single top quark production',
Phys. Rev. Lett. 103 (2009) 092001, DOI: 10.1103/PhysRevLett.103.092001,
arXiv:0903.0850 [hep-ex].

[36] K. Nakamura and others, 'Review of particle physics', *J. Phys.* G37 (2010) 075021,
DOI: 10.1088/0954-3899/37/7A/075021.

[37] G. Eilam and others,
'Rare decays of the top quark in the standard and two Higgs doublet models',
Phys. Rev. D44 (1991) 1473–1484,
DOI: 10.1103/PhysRevD.44.1473,10.1103/PhysRevD.59.039901.

[38] F. del Aguila and others, 'Constraints on top couplings in models with exotic quarks',
Phys. Rev. Lett. 82 (1999) 1628–1631, DOI: 10.1103/PhysRevLett.82.1628,
arXiv:hep-ph/9808400.

[39] J. A. Aguilar-Saavedra, 'Effects of mixing with quark singlets',
Phys. Rev. D67 (2003), Erratum-ibid. D **69** (2004) 099901 035003,
DOI: 10.1103/PhysRevD.67.035003, arXiv:hep-ph/0210112.

[40] J. A. Aguilar-Saavedra and others, 'Rare top decays $t \to c\gamma, t \to cg$ and CKM unitarity',
Phys. Lett. B553 (2003) 251–260, DOI: 10.1016/S0370-2693(02)03230-6,
arXiv:hep-ph/0210360.

[41] D. Atwood and others,
'Phenomenology of two Higgs doublet models with flavor changing neutral currents',
Phys. Rev. D55 (1997) 3156–3176, DOI: 10.1103/PhysRevD.55.3156, arXiv:9609279.

[42] D. Atwood and others,
'Probing flavor changing top-charm-scalar interactions in e^+e^- collisions',
Phys.Rev. D53 (1996) 1199–1201, DOI: 10.1103/PhysRevD.53.1199,
arXiv:9506243 [hep-ph].

[43] S. Bejar, 'Loop Induced Flavor Changing Neutral Decays of the Top Quark in a General Two-Higgs-Doublet Model', *Nucl.Phys.* B600 (2001) 21–38,
DOI: 10.1016/S0550-3213(01)00044-X, arXiv:0011091 [hep-ph].

[44] T. P. Cheng and others,
'Mass Matrix Ansatz and flavor nonconservation in models with multiple Higgs doublets',
Phys. Rev. D35 (1987) 3484, DOI: 10.1103/PhysRevD.35.3484.

[45] B. Grzadkowski and others, 'Neutral current flavor changing decays for the Z boson and the top quark in two Higgs doublet models', *Phys. Lett.* B268 (1991) 106–111, DOI: 10.1016/0370-2693(91)90931-F.

[46] M. E. Luke and others,
'Flavor changing neutral currents in the Higgs sector and rare top decays',
Phys. Lett. B307 (1993) 387–393, DOI: 10.1016/0370-2693(93)90238-D,
arXiv:hep-ph/9303249.

[47] J. J. Cao and others, 'SUSY-induced FCNC top-quark processes at the Large Hadron Collider',
Phys. Rev. D75 (2007) 075021, DOI: 10.1103/PhysRevD.75.075021,
arXiv:hep-ph/0702264.

[48] D. Delepine and others, 'Top flavour violating decays in general supersymmetric models',
Phys. Lett. B599 (2004) 62–74, DOI: 10.1016/j.physletb.2004.08.025,
arXiv:hep-ph/0406264.

[49] G. M. de Divitiis and others,
'Flavour changing top decays in supersymmetric extensions of the standard model',
Nucl. Phys. B504 (1997) 45–60, DOI: 10.1016/S0550-3213(97)00476-8,
arXiv:9704244 [hep-ph].

[50] J. Guasch and others,
'FCNC top quark decays: A door to SUSY physics in high luminosity colliders',
Nucl. Phys. B562 (1999) 3–28, DOI: 10.1016/S0550-3213(99)00579-9,
arXiv:9906268 [hep-ph].

[51] C. S. Li and others, 'Rare decay of the top quark in the minimal supersymmetric model',
Phys. Rev. D49 (1994), Erratum-ibid.D56:3156,1997 293–298,
DOI: 10.1103/PhysRevD.49.293.

[52] J. J. Liu and others, '$t \to cV$ via SUSY FCNC couplings in the unconstrained MSSM',
Phys. Lett. B599 (2004) 92–101, DOI: 10.1016/j.physletb.2004.07.062,
arXiv:hep-ph/0406155.

[53] J. L. Lopez and others, 'New supersymmetric contributions to $t \to cV$',
Phys. Rev. D56 (1997) 3100–3106, DOI: 10.1103/PhysRevD.56.3100,
arXiv:9702350 [hep-ph].

[54] J. M. Yang and others, 'Flavor-changing top quark decays in R-parity violating SUSY',
Phys. Rev. D58 (1998) 055001, DOI: 10.1103/PhysRevD.58.055001,
arXiv:hep-ph/9705341.

[55] G. Lu and and others,
'The rare top quark decays $t \to cV$ in the topcolor-assisted technicolor model',
Phys. Rev. D68 (2003) 015002, DOI: 10.1103/PhysRevD.68.015002,
arXiv:hep-ph/0303122.

[56] CDF Collaboration, 'Search for top-quark production via flavor-changing neutral currents in W+1 jet events at CDF', *Phys. Rev. Lett.* 102 (2009) 151801,
DOI: 10.1103/PhysRevLett.102.151801, arXiv:0812.3400 [hep-ex].

[57] A. Heister and others,
'Search for single top production in e^+e^- collisions at $\sqrt{s}$ up to 209 GeV',
Phys. Lett. B543 (2002) 173–182, eprint: hep-ex/0206070.

[58] J. Abdallah and others,
'Search for single top production via FCNC at LEP at $\sqrt{s}$ = 189 GeV - 208 GeV',
Phys. Lett. B590 (2004) 21–34, eprint: hep-ex/0404014.

[59] Abbiendi, G. and others, 'Search for single top quark production at LEP2',
Phys. Lett. B521 (2001) 181–194, eprint: hep-ex/0110009.

[60] P. Achard and others, 'Search for single top production at LEP',
Phys. Lett. B549 (2002) 290–300, eprint: hep-ex/0210041.

[61] The LEP Exotica WG, *Search for single top production via flavour changing neutral currents: preliminary combined results of the LEP experiments*, eprint: LEPExoticaWG2001-01.

[62] F. D. Aaron and others, 'Search for Single Top Quark Production at HERA',
Phys. Lett. B678 (2009) 450–458, DOI: 10.1016/j.physletb.2009.06.057,
arXiv:0904.3876 [hep-ex].

[63] F. Abe and others, 'Search for flavor-changing neutral current decays of the top quark in $p\bar{p}$ collisions at $\sqrt{s}$ = 1.8 TeV', *Phys. Rev. Lett.* 80 (1998) 2525–2530,
DOI: 10.1103/PhysRevLett.80.2525.

[64] S. Chekanov and others, 'Search for single-top production in ep collisions at HERA',
Phys. Lett. B559 (2003) 153–170, eprint: hep-ex/0302010.

[65] M. Beneke and others, 'Top quark physics in Proceedings of the 1999 CERN Workshop on SM physics (and more) at the LHC' (2000), arXiv:hep-ph/0003033.

[66] A. A. Ashimova and S. R. Slabospitsky,
'The constraint on FCNC coupling of the top quark with a gluon from ep collisions',
Phys. Lett. B668 (2008) 282–285, DOI: 10.1016/j.physletb.2008.08.065,
arXiv:hep-ph/0604119.

[67] A. Aktas and others, 'Search for single top quark production in ep collisions at HERA',
Eur. Phys. J. C33 (2004) 9–22, eprint: hep-ex/0310032.

[68] E. Malkawi and others, 'Top-Charm Strong Flavor-Changing Neutral Currents at the Tevatron',
Phys. Rev. D54 (9 Nov. 1996) 5758–5762, DOI: 10.1103/PhysRevD.54.5758,
URL: http://link.aps.org/doi/10.1103/PhysRevD.54.5758.

[69] M. Hosch and others,
'Direct Top Quark Production at Hadron Colliders as a Probe of New Physics',
Phys.Rev. D56 (1997) 5725–5730, DOI: 10.1103/PhysRevD.56.5725,
arXiv:hep-ph/9703450 [hep-ph].

[70] J. Gao and others, 'Searching for anomalous top quark production at the early LHC',
Phys. Rev. Lett. 107 (2011) 092002, DOI: 10.1103/PhysRevLett.107.092002,
arXiv:1104.4945 [hep-ph].

[71] J. J. Zhang and others, 'Next-to-leading order QCD corrections to the top quark decay via model-independent FCNC couplings', *Phys. Rev. Lett.* 102 (2009) 072001,
DOI: 10.1103/PhysRevLett.102.072001, arXiv:0810.3889 [hep-ph].

[72] M. P. Tait and others,
'Single Top Quark Production as a Window to Physics Beyond the Standard Model',
Phys.Rev. D63 (2000) 014018, DOI: 10.1103/PhysRevD.63.014018,
arXiv:hep-ph/0007298 [hep-ph].

[73] L. Evans and P. Bryant, 'LHC Machine', *JINST* 3 (2008) S08001, DOI: 10.1088/1748-0221/3/08/S08001.

[74] ATLAS Collaboration, 'The ATLAS experiment at the CERN Large Hadron Collider', *JINST* 3 (2008) S08003, DOI: 10.1088/1748-0221/3/08/S08003.

[75] ATLAS Collaboration, 'Updated Luminosity Determination in pp Collisions at $\sqrt{s} = 7$ TeV using the ATLAS Detector', *ATLAS-CONF-2011-011* (2011).

[76] T. Sjostrand and others, 'PYTHIA 6.4 physics and manual', *JHEP* 05 (2006) 026, DOI: 10.1088/1126-6708/2006/05/026, arXiv:hep-ph/0603175.

[77] G. Corcella and others, 'HERWIG 6: An event generator for hadron emission reactions with interfering gluons (including supersymmetric processes)', *JHEP* 0101 (2001) 010, eprint: hep-ph/0011363.

[78] J. Schaarschmidt, *The Discovery Potential of Neutral Supersymmetric Higgs Bosons with Decay to Tau Pairs at the ATLAS Experiment*.

[79] V. N. Gribov and others, 'Deep inelastic ep scattering in perturbation theory', *Sov. J. Nucl. Phys.* 15 (1972) 438–450.

[80] G. Altarelli and others, 'Asymptotic Freedom in Parton Language', *Nucl. Phys.* B126 (1977) 298, DOI: 10.1016/0550-3213(77)90384-4.

[81] Y. L. Dokshitzer, 'Calculation of the structure functions for deep inelastic scattering and e^+e^- annihilation by perturbation theory in Quantum Chromodynamics', *Sov. Phys. JETP* 46 (1977) 641–653.

[82] V. V. Sudakov, 'Vertex parts at very high-energies in Quantum Electrodynamics', *Sov.Phys.JETP* 3 (1956) 65–71.

[83] ATLAS Collaboration, 'UPDATE: charged particle multiplicities in pp interactions at $\sqrt{s} =$ 0.9 TeV and 7 TeV measured with the ATLAS detector at the LHC. diffractive limited phase-space and new ATLAS Monte Carlo tune', tech. rep. ATLAS-COM-CONF-2010-031, CERN, May 2010.

[84] ATLAS Collaboration, *First tuning of HERWIG/JIMMY to ATLAS data*, ATL-PHYS-PUB-2010-014, 2010.

[85] J.A. Aguilar-Saavedra, 'Zt, γt and t production at hadron colliders via strong flavour-changing neutral couplings', *Nucl. Phys.* B837 (2010) 122–136, DOI: 10.1016/j.nuclphysb.2010.05.005, arXiv:1003.3173 [hep-ph].

[86] J. Pumplin and others, 'New generation of parton distributions with uncertainties from global QCD analysis', *JHEP* 0207 (2002) 012, arXiv:hep-ph/0201195.

[87] M. L. Mangano and others, 'ALPGEN, a generator for hard multiparton processes in hadronic collisions', *JHEP* 0307 (2003) 001, arXiv:hep-ph/0206293 [hep-ph].

[88] J. M. Butterworth and others, 'Multiparton interactions in photoproduction at HERA', *Z. Phys.* C72 (1996) 637–646, DOI: 10.1007/s002880050286, arXiv:hep-ph/9601371.

[89] ATLAS Collaboration,
'Single boson and diboson production cross sections in pp collisions at $\sqrt{s}$ = 7 TeV',
tech. rep. ATL-COM-PHYS-2010-695, Geneva: CERN, Aug. 2010.

[90] J. M. Campbell and others, 'Update on vector boson pair production at hadron colliders',
Phys. Rev. D60 (1999) 113006, arXiv:hep-ph/9905386v2.

[91] S. Frixione and others, 'Single-top production in MC@NLO', *JHEP* 03 (2006) 092,
DOI: 10.1088/1126-6708/2006/03/092, arXiv:hep-ph/0512250.

[92] P. M. Nadolsky and others, 'Implications of CTEQ global analysis for collider observables',
Phys. Rev. D78 (2008) 013004, DOI: 10.1103/PhysRevD.78.013004,
arXiv:0802.0007 [hep-ph].

[93] B. Kersevan and others, 'The Monte Carlo event generator AcerMC version 2.0 with interfaces
to PYTHIA 6.2 and HERWIG 6.5' (2004), arXiv:hep-ph/0405247.

[94] F. A. Berends and others, 'On the production of a W and jets at hadron colliders',
Nucl. Phys. B357 (1991) 32–64, DOI: 10.1016/0550-3213(91)90458-A.

[95] S. D. Ellis and others, 'W's, Z's and jets', *Phys. Lett.* B154 (1985) 435,
DOI: 10.1016/0370-2693(85)90425-3.

[96] S. Agostinelli and others, 'GEANT4: A simulation toolkit',
Nucl. Instrum. Meth. A506 (2003) 250–303, DOI: 10.1016/S0168-9002(03)01368-8.

[97] ATLAS Collaboration, 'The ATLAS simulation infrastructure',
Eur. Phys. J. C70 (2010) 823–874, DOI: 10.1140/epjc/s10052-010-1429-9,
arXiv:1005.4568 [physics.ins-det].

[98] T. Cornelissen and others,
'Concepts, design and implementation of the ATLAS new tracking (NEWT)',
tech. rep. ATL-SOFT-PUB-2007-007. ATL-COM-SOFT-2007-002,
Geneva: CERN, Mar. 2007.

[99] ATLAS Collaboration,
'Tracking Results and Comparison to Monte Carlo simulation at $\sqrt{s}$ = 900 GeV',
tech. rep. ATLAS-COM-CONF-2010-011, Geneva: CERN, Feb. 2009.

[100] W. Lampl and others, 'Calorimeter clustering algorithms: description and performance',
tech. rep. ATL-LARG-PUB-2008-002. ATL-COM-LARG-2008-003,
Geneva: CERN, Apr. 2008.

[101] ATLAS Collaboration, 'Study of Jet Shapes in Inclusive Jet Production in pp Collisions at $\sqrt{s}$
= 7 TeV using the ATLAS Detector', *Phys.Rev.* D83 (2011) 052003,
arXiv:1101.0070 [hep-ex].

[102] ALEPH Collaboration, DELPHI Collaboration, L3 Collaboration, OPAL Collaboration, LEP
Electroweak Working Group, SLD Heavy Flavor Group, 'A combination of preliminary
electroweak measurements and constraints on the standard model' (2002),
arXiv:0212036 [hep-ex].

[103] ATLAS Collaboration, 'Performance of primary vertex reconstruction in proton-proton
collisions at $\sqrt{s}$ = 7 TeV in the ATLAS experiment', tech. rep. ATLAS-CONF-2010-069,
Geneva: CERN, July 2010.

[104] ATLAS Collaboration,
'Expected Performance of the ATLAS Experiment - Detector, Trigger and Physics' (2009), arXiv:0901.0512 [hep-ex].

[105] ATLAS Collaboration, 'Electron and photon reconstruction and identification in ATLAS: expected performance at high energy and results at 900 GeV',
tech. rep. ATLAS-CONF-2010-005, Geneva: CERN, June 2010.

[106] G. P. Salam and others, 'A practical seedless infrared-safe cone jet algorithm',
JHEP 05 (2007) 086, arXiv:0704.0292 [hep-ph].

[107] ATLAS Collaboration, 'Data-quality requirements and event cleaning for jets and missing transverse energy reconstruction with the ATLAS detector in proton-proton collisions at a center-of-mass energy of 7 TeV' (2010), ATLAS-CONF-2010-038.

[108] ATLAS Collaboration, 'Commissioning of the ATLAS high-performance *b*-tagging algorithms in the 7 TeV collision data', tech. rep. ATLAS-CONF-2011-102, Geneva: CERN, July 2011.

[109] ATLAS Collaboration, 'Preliminary studies for the measurement of the inclusive muon spectrum in pp collisions at $\sqrt{s} = 7$ TeV with the ATLAS detector',
tech. rep. ATLAS-COM-CONF-2010-035, Geneva: CERN, May 2010.

[110] S. Hassani, 'A muon identification and combined reconstruction procedure for the ATLAS detector at the LHC using the (Muonboy, STACO, MuTag) reconstruction packages',
NIM A572 (2007) 77–79.

[111] B. Alvarez and others, 'Measurement of Single Top-Quark Production in the Lepton+Jets Channel in pp Collisions at $\sqrt{s} = 7$ TeV', tech. rep. ATL-COM-PHYS-2011-058,
Geneva: CERN, Jan. 2011.

[112] Allwood-Spires and others,
'Monte Carlo samples used for top physics: Top Working Group Note IX',
tech. rep. ATL-COM-PHYS-2010-836, Supporting document for top paper,
Geneva: CERN, Oct. 2010.

[113] K. Becker and others, 'Mis-identified lepton backgrounds in top quark pair production studies for EPS 2011 analyses', tech. rep. ATL-COM-PHYS-2011-768, Geneva: CERN, June 2011.

[114] ATLAS single-top group, *Electron scale factors*,
URL: https://svnweb.cern.ch/trac/atlasoff/browser/PhysicsAnalysis/TopPhys/TopPhysUtils/TopElectronSFUtils/trunk/electron_SF_EPS_sgtop.h.

[115] ATLAS Top Group, 'Lepton trigger and identification for the Winter 2011 top quark analyses',
tech. rep. ATL-COM-PHYS-2011-123, Geneva: CERN, Jan. 2011.

[116] ATLAS Collaboration, 'Performance of primary vertex reconstruction in proton-proton collisions at $\sqrt{s} = 7$ TeV in the ATLAS experiment', ATL-CONF-2010-069 (2010).

[117] M. Feindt, 'A Neural Bayesian Estimator for Conditional Probability Densities' (2004), arXiv:0402093[physics.data-an].

[118] A. Papaikonomou, 'Search for single top-quark production via flavor-changing neutral currents with the CDF II experiment' (2009).

[119] ATLAS Collaboration, 'Measurement of the top quark-pair cross-section with ATLAS in pp collisions at $\sqrt{s} = 7$ TeV in the single-lepton channel using *b*-tagging',
ATLAS-CONF-2011-035 (2011).

[120] ATLAS Collaboration, 'Jet energy scale and its systematic uncertainty in proton-proton collisions at $\sqrt{s}$ = 7 TeV in ATLAS 2010 data', *ATLAS-CONF-2011-032* (2011).

[121] ATLAS Collaboration, 'Jet energy resolution from in-situ techniques with the ATLAS detector using proton-proton collisions at a center-of-mass energy $\sqrt{s}$ = 7 TeV' (2011), eprint: ATL-COM-PHYS-2011-240.

[122] ATLAS Collaboration, 'Jet energy resolution and selection efficiency relative to track jets from in-situ techniques with the ATLAS detector using proton-proton collisions at a center-of-mass energy $\sqrt{s}$ = 7 TeV', *ATLAS-CONF-2010-054* (2010).

[123] B. P. Kersevan and others, 'The Monte Carlo event generator AcerMC version 2.0 with interfaces to PYTHIA 6.2 and HERWIG 6.5' (2004), eprint: hep-ph/0405247.

[124] P. Z. Skands, 'Tuning Monte Carlo Generators: The Perugia Tunes', *Phys. Rev.* D82 (2010) 074018, DOI: 10.1103/PhysRevD.82.074018, arXiv:1005.3457 [hep-ph].

[125] A. D. Martin and others, 'Parton distributions for the LHC', *Eur. Phys. J.* C63 (2009) 189–285, arXiv:0901.0002 [hep-ph].

[126] Allwood-Spiresand and others, 'Monte Carlo samples used for top physics', tech. rep. ATL-PHYS-INT-2010-132, Geneva: CERN, Dec. 2010.

[127] D0 Collaboration, 'A recipe for the construction of confidence limits', tech. rep. FERMILAB-TM-2104, 2000.

[128] E. T. Jaynes, *Probability theory: the logic of science*, ed. by G. L. Bretthorst, Cambridge University Press, 2003.

[129] R. Barlow, 'Asymmetric errors', *eConf* C030908 (2003) WEMT002, arXiv:physics/0401042 [physics].

[130] I. Asimov, *The complete stories*, Isaac Asimov, Doubleday, 1992, ISBN: 9780385420785.

[131] G. Cowan and others, 'Asymptotic formulae for likelihood-based tests of new physics', *Eur. Phys. J.* C71 (2011) 1554, DOI: 10.1140/epjc/s10052-011-1554-0, arXiv:1007.1727 [physics.data-an].

List of Figures

List of Tables